Università degli Studi dell'Insubria

Dipartimento di Scienza e Alta Tecnologia

Tesi di Dottorato in
Scienze Chimiche ed Ambientali

Stochastic Coarse-grained Simulations of Polyelectrolytes in Aqueous Solutions

Supervisor
Prof. Massimo Mella

Candidate
Andrea Tagliabue

XXXIII Cycle - 2018/2020

Università degli Studi dell'Insubria
Dipartimento di Scienza e Alta Tecnologia

Tesi di Dottorato in
Scienze Chimiche ed Ambientali

Stochastic Coarse-grained Simulations of Polyelectrolytes in Aqueous Solutions

Supervisor
Prof. Massimo Mella

Candidate
Andrea Tagliabue

XXXIII Cycle – 2018/2020

Contents

*This chapter has been adapted from: Tagliabue, A., Izzo L., Mella M., Impact of Charge Correlation, Chain Rigidity, and Chemical Specific Interactions on the Behavior of Weak Polyelectrolytes in Solution, *Journal of Chemical Physics B*, 123, 42, 8872–8888 (2019).

*This chapter has been adapted from: Tagliabue, A., Izzo L., Mella M., Impact of Charge Correlation, Chain Rigidity, and Chemical Specific Interactions on the Behavior of Weak Polyelectrolytes in Solution, *Journal of Physical Chemistry B*, 123, 42, 8872–8888, 2019.

*This chapter has been adapted from: Mella M., Tagliabue A., Mollica L., Izzo L., Monte Carlo Study of the Effects of Macroion Charge Distribution on the Ionization and Adsorption of Weak Polyelectrolytes and Concurrent Counterion Release, *Journal of Colloid and Interface Science*, 560, 667-680, (2020)

*This chapter has been adapted from: Mella M., Tagliabue A., Izzo L., On the Distribution of Hydrophilic Polyelectrolytes and their Counterions around Zwitterionic Micelles: the Possible Impact on the Charge Density in Solution *Soft Matter*, Advanced article (doi.org/10.1039/D0SM01541E),

*This chapter has been adapted with permission from Tagliabue A., Izzo L., Mella M., *Journal of Chemical Physics B* 2020, 124, 14, 2930–2937. Copyright 2020 American Chemical Society. All rights reserved.

*This chapter has been adapted from: Tagliabue A., Landsgesell J., Mella M., Holm, C., Can Oppositely Charged Polyelectrolyte Stars Form a Gel? A Simulational Study, *Soft Matter*, Accepted article (doi.org/10.1039/D0SM01617A), © Reproduced by permission of The Royal Society of Chemistry. All rights reserved.

Chapter 1

Introduction

Polyelectrolytes are polymers whose repeating units (monomers) bear one (or even more) electrolyte group. We distinguish between *strong* and *weak* polyelectrolytes. The former bear quenched charges along the chain, either negative (*polyanions*) or positive (*polycations*); thus, they are considered as fully "dissociated" (at least, as a first approximation). Conversely, ionization equilibrium of weak polyelectrolytes (*weak Brønsted polyacids* if negatively charged, *weak Brønsted polybases* otherwise) is defined by solution properties such as pH, ionic strength or presence of co-solutes. Polyelectrolytes bearing both cationic and anionic (either weak or strong) groups are called *polyampholytes*.

Both strong and weak polyelectrolytes have many applications [1, 2], mostly related to modifying the stability of aqueous solutions, colloidal solutions, emulsions, gels [3–5], etc. They can also be used to functionalize nanoparticles (NPs); the latter can be either neutral (thus, polyelectrolytes can be tethered to the NP surface via the formation of covalent bonds) or oppositely charged with respect to the polyelectrolyte (in which case "patchy" NPs can form via electrostatic interactions [6–15]). Moreover, polyelectrolytes are often used to disperse NPs in aqueous solution due to both their power in screening electrostatics and their capability to bind more NPs, acting as bridging agent [15,16] and, hence, forming NPs–polyelectrolytes networks.

Polyelectrolytes are also target materials for biochemical and biomedical applications. For example, they are studied as building blocks for vesicles or micelles deputed to drug delivery [17–24], whereas polyelectrolyte brushes can be used for controlled drug release [3, 25–27], and other applications [28]. Worth noticing,

many biomacromolecules are polyelectrolytes: e.g., glycosaminoglycans, proteins, and polyaminoacids in general are weak polyampholytes, whereas DNA and RNA act, *de facto*, as strong polyanions due to the presence of fully dissociated phosphate groups.

For a weak polyelectrolyte we define the dissociation degree α (neutral $:= 0 \leq \alpha \leq 1 =:$ fully ionized) as the ratio between the number of ionized groups and the number of total weak electrolyte groups carried by the chain. Physical properties of polyelectrolyte solutions are usually strongly affected by α [12,29–42] (and vice versa):

- vicinal ionizable groups are always close to each other and strongly interact due to chain connectivity, so that their titration behavior is much more complex than the one of small molecules (e.g., free monomers able to wander in solution). In fact, the energy penalty arising from having two dissociated neighbor monomers (carrying the same charge) suppresses further ionization. Thus, monomers linked to form, e.g., a weak polyacid usually show a depressed acidity with respect to non-bonded monomers.

- Even location along the chain may impact on group acidity, with monomers lying on the terminal segments of a linear weak polyelectrolyte resulting more acid than the ones lying internally due to a reduced interaction with neighbor ionizable groups.

- Weak polyelectrolytes usually undergo a marked swelling (i.e., their average size, or extension, increases), and become more rigid as they dissociate, due to the electrostatic repulsion occurring between charged monomers.

- The latter phenomena are partially counterbalanced by the releases of counterions in solution, which screen the electrostatic interaction between monomers along a chain or between different charged chains. Moreover, counterions release affects solution properties such as mobile ions activity, electrical conductivity, ionic strength, Debye length, etc. (so that the latter strongly depends on α).

- The same role is played by monovalent background salts, the latter screening Coulomb interactions favoring polyelectrolytes ionization while, at the same time, reducing their tendency to swell. Furthermore, multivalent

(counter)ions tend to markedly condense on charged polymers coordinating several monomers each, and resulting in polyelectrolyte collapse [43–45].

On the other hand, polyelectrolytes titration behavior depends not only on the chemical nature of monomers (i.e., on their pK) but also on the conformational and topological structure of the polymer itself, with, e.g., linear species presenting different behaviors with respect to star-shaped (or, in general, branched [26, 27, 46–54]) ones (*vide infra* Chapters 3 and 5), or even circular weak polyelectrolytes showing a pH–responsiveness that depend on their knotted topology (*vide infra* Chapter 7).

Another factor that can impact on polyelectrolytes behavior is the possibility to form chemical specific interactions between monomers lying on a chain or even between different chains. As an example, the formation of (charged) hydrogen bond in (dimethylamino)ethyl methacrylate (DMAEMA)–based polyelectrolytes [12] resulted to markedly modify both titration behavior and conformations of such polyelectrolytes, helping to rationalize the higher charge density found on plaques of water-insoluble methyl methacrylate and DMAEMA co-polymers [26, 27].

Summarizing, there is a very intricate (hence, interesting) dependency between polyelectrolytes microscopic detail and bulk (i.e., macroscopic) properties of their solutions. To date, several gaps seem to be present in simulation literature of these systems. In this work we thus present a selection of puzzling systems simulated with the aim to shed some more light on this topic. To do so, we performed stochastic (either based on Monte Carlo or Langevin sampling algorithm) coarse-grained simulation, taking into account the reactivity of weakly ionizable groups by means of the constant-pH [32, 42, 55] method and a primitive restricted electrolyte model. Albeit in literature one can find large amount of scientific works, both experimental and theoretical/computational, about polyelectrolytes and their aqueous solutions, there were several unclearified aspects regarding the physico-chemical behavior of these systems; in particular during this dissertation we will focus on the following points:

- chemical specific interactions, such as (charged) hydrogen bonds or multivalent ion coordination were expected to markedly impact on polyelectrolytes (and their solutions) behavior; however, scientific works describing how

these kind of interactions can modify both microscopic and thermodynamical properties of polyelectrolyte solutions are scarce;

- whereas there are many computational studies regarding strong polyelectrolytes interacting with charged object (functionalized nanoparticles, colloids, charged vescicles or micelles, surfaces, etc.), there is a lack in similar studies but regarding weak polyelectrolytes. Moreover, the coarse-grained representation of such charges object usually employ a very minimalist description (i.e., most of the time they're are simulated as simple charged spheres with a proper excluded volume), the latter does not taking into account important effets such as colloid polarizability, or the possibility to charged species composing vescicles or micelles to redistribute on the latter surface when interacting with other charges species.

- The vast majority of computational studies on weak polyelectrolytes regard linear species and, to a lesser extent, their star-shaped counterparts. The impact of different "architectures" (dendrimers, rings, comb-like chains, etc.) or topologies (e.g, the presence of knots or concatenations) seemed, to the best of our knowledge, to be almost completely absent.

- With respect to covalently-bonded gels, for the so-called physical gels, whose polymeric building blocks cross-links exploiting weaker interactions (e.g., hydrogen bonds, hydrophobic forces or electrostatics interactions) there was a lack of both experimental and theoretical/computational studies, despite their promising properties (e.g., network responsiveness stimuli such as pH, ionic strength, or changes in solvent, or even self-healing abilities). In particular, to the best of our knowledge no simulational studies were published on the possibility to form gel-like phases by mixing oppositely charged star polyelectrolytes.

This thesis is organized as follows. In Chapter 2 we discuss and describe in detail both the model implemented to simulate polyelectrolytes in (aqueous) solution and the simulation protocols implemented, paying particular attention to methods used to take into account the equilibria of weakly ionizable species, and the calculation of both polyelectrolytes and solution properties.

In Chapter 3, we present and discuss simulations on the titration behavior (and its consequent impact on both polyelectrolyte conformations and solutions properties) of both linear and star-shaped systems confined inside spherical capsids (SC). From these, it emerges that absorption of weak polyelectrolytes impacts on properties such as ionization, conformations, and counterion condensation that are important in several areas of applied and fundamental science. Thus we used a weak polyelectrolyte model and Monte Carlo (MC) simulations to investigate how the mentioned properties depend on the pH or on the size of a spherical confinement permeable to counterions but not to polyelectrolytes; the latter have either linear or star-like topologies, and may be allowed or not to form charged hydrogen bonds (c-H-bonds) between ionized and neutral monomers. Average ionization decreases upon increasing arms number at constant number of monomers; it instead increases with arms length in large SC due to counterions screening. The way SC size, chains rigidity and pH values interrelate to define the ionization revealed to be more intricate due to arms pairing or clustering when c-H-bonds can form. The impact of ionization on the confinement free energy has been also estimated, highlighting that c-H-bonding may enhance absorption compared to neutral chains.*

In Chapter 4, we discuss titration simulations of weak short linear polyelectrolytes simulated with the aim to understand how polyelectrolyte concentration, chain rigidity and the possible formation of intra- and inter-chain c-H-bonds impact on ionization and conformations of short weak polyacid chains, their counterion distribution and system Helmholtz energy. We observed that increasing polyelectrolyte concentration resulted in an enhanced acidity for all the cases investigated due to the increased screening of chain charges by counterions, and, when possible, in the formation of inter-chain c-H-bonds. We also evidenced that polyelectrolytes able to form c-H-bonds can populate simultaneously two conformational states (unfolded and clustered) in a range of pH, the transition between the two appearing to be first order-like. Thus, to better understand how properties of two chains are modified by their relative distance, we performed

*The latter paragraph has been adapted from: Tagliabue A., Izzo L., Mella M., Absorbed Weak Polyelectrolytes: Impact of Confinement, Topology, and Chemically Specific Interactions on Ionization, Conformation Free Energy, Counterion Condensation, and Absorption Equilibrium, *Journal of Polymer Science Part B: Polymer Physics*, 57, 491-510 (2019).

window sampling simulations, which highlighted non-trivial features in the ionization and conformational behaviors. As byproducts of such simulations, we obtained also the potential of mean force between two chains; from this emerged that the reversible work needed to reach a specific inter-chain distance does not always increase with the pH, especially for semi-rigid chains able to interact via c-H-bonds when the latter are brought at short distances.[†]

Adsorption of weak polyelectrolytes on charged nanoparticles, and concurrent effects such as spatial partitioning of ions may be influenced by details of the polyelectrolyte structure (e.g., linear or star-like) and size, by the mobility of the nanoparticle surface charge, or the valence of its counterions. Thus, in Chapter 5, we discuss ionization and complexation of both linear and star-shaped weak polyelectrolytes adsorbed on oppositely charged spherical macroions. Importantly, nanoparticle surface charge has been represented either as a single colloid-centered total charge or as surface-tethered mobile monovalent charges. The degree of condensation of polymer counterions on the polyelectrolytes resulted also substantially higher in presence of the former type of colloid, with a concurrent decrease of osmotic coefficient values, and this is due to the fact that it tends to adsorb a lower number of star-like species' arms with respect to the "polarizable" counterpart. [‡]

As there are experimental evidences that, despite their charge neutrality, micelles composed of surfactants with zwitterionic headgroups selectively accumulate anions at their hydrophobic core/solution interphase due to electrostatic interactions if headgroup positive moieties are the innermost (the latter a tendency that may be markedly enhanced if polyanions substitute simple anions), in Chapter 6 we extended the study of complexes formed between polyelectrolytes and colloids to the case of strong polyacids interacting with zwitterionic micelles. Structural and energetic properties are thus obtained to highlight the impact of connecting simple ions into polyions on the interactions between electrolytes

[†]The latter paragraph has been adapted from: Tagliabue, A., Izzo L., Mella M., Impact of Charge Correlation, Chain Rigidity, and Chemical Specific Interactions on the Behavior of Weak Polyelectrolytes in Solution, *Journal of Physical Chemistry B*, 123, 42, 8872–8888 (2019).

[‡]The latter paragraph has been adapted from: Mella M., Tagliabue A., Mollica L., Izzo L., Monte Carlo Study of the Effects of Macroion Charge Distribution on the Ionization and Adsorption of Weak Polyelectrolytes and Concurrent Counterion Release, *Journal of Colloid and Interface Science*, 560, 667-680, (2020)

and zwitterionic micelles. Despite the presence of the latter, polyanions conserve their conformational properties. A marked increase in the concentration of charged species inside the micellar corona is, instead, found when polyions are present independently of their charge sign or the headgroup structure. Thus, polyelectrolytes act as "shuttle" for all charged species, with the potential of increasing reactions rates involving the latter due to mass effects. Besides, results for the polyions/micelles mixing free energy and Helmholtz energy profiles indicate that the critical micelle concentration is impacted minimally by hydrophilic polyelectrolytes, an outcome that is in agreement with experiments. This finding is entirely due to weak enthalpic effects while mixing hydrophilic polyions and micelles. Finally, a strong reduction in the screening of the micelle negative charge, acquired following the adsorption of anions in the corona and due to counterions layering just outside it (the so called "Chameleon effect"), is forecasted when polyanions substitute monovalent anions[§].

In Chapter 7, stochastic simulations are used to investigate the conformational behavior of knotted weak polyacid rings as a function of the pH. Differently from the common expected ionization→repulsion→expansion scheme upon increasing pH, results suggest a non-monotonic behavior of the gyration radius R_g^2. Polyelectrolyte re-contraction at high ionization is induced by the weakening of Coulomb repulsion due to counterions condensation on the polyelectrolyte, and appears more marked the more complex is the knot topology. Comparing with polyelectrolyte species of identical ionization but with quenched charges, weak (i.e., annealed) polyacids present tighter knots due to their ability of localizing neutral monomers inside the knotted portion of the chain. Increasing solvent Bjerrum length enhances counterions localization lowering the pH at which polyacids start decreasing their average size. A similar effect is also obtained increasing the amount of "localizable" cations by adding background monovalent salts, whereas divalent ions induce polyelectrolyte collapse.[¶]

[§]The latter paragraph has been adapted from: Mella M., Tagliabue A., Izzo L., On the Distribution of Hydrophilic Polyelectrolytes and their Counterions around Zwitterionic Micelles: the Possible Impact on the Charge Density in Solution *Soft Matter*, just accepted article (doi.org/10.1039/D0SM01541E), © Reproduced by permission of The Royal Society of Chemistry.

[¶]The latter paragraph has been adapted from: Tagliabue A., Izzo L., Mella M., Interface Counterion Localization Induces a Switch Between Tight and Loose Configurations of Knotted Weak Polyacid Rings Despite Intermonomer Coulomb Repulsions, *Journal of Physical Chemistry B*, 124, 14, 2930–2937 (2020). © 2020, American Chemical Society. All rights reserved.

Polyelectrolytes (and polymer in general) can be cross-linked in order to form networks and gels. When they are soluble in water they are called "hydrogels". These gels possess a huge swelling capacity in aqueous solution and are capable to absorb water in amounts of up to a few hundred times their dry mass. Chemically cross-linked gels presents covalent bonds, so their structure is immutable. However, chemical cross-linking is not the only way to form a gel. In fact, there are the so called "physical (hydro)gels" that exploit weak interactions (such as hydrogen bonds, hydrophobic forces, van der Waals or ionic interactions) to form reversible (even, self-healing) networks [56–61]. In Chapter 8, we show how stochastic simulations can be used to study the self assembly of an equimolar mixture of mono-dispersed oppositely charged di-block four-armed polyelectrolyte stars, the latter carrying a tunable number of charged terminal monomers. By varying the polymer concentration we computed PV diagrams and determined the free-swelling equilibrium concentration with respect to a pure water reservoir as a function of the charged block length. Then, we investigated various structural properties of the resulting equilibrium structures, like the number of ionic bonds, dangling arms, isolated stars, and cluster sizes. The ionic bonds feature a broad distribution of the number of arms involved and also display a distribution of net charges peaked around the neutral ionic bond. The main result of our study is that we observe that for charged block length equal to 4 and 5 ionized beads the resulting macro-aggregate spans the box and forms a network phase. Furthermore, we investigated the restructuring dynamics of ionic bonds, the results suggesting both the presence of short bond lifetimes and a high frequency of ballistic association/dissociation events. In other words, bonds resulted strong enough to yield a stable gel phase but remain sufficiently weak to allow network restructuring under thermal fluctuations.

Finally, in Chapter 9 we draw general conclusions and we discuss the possible outlooks of our research.

The results discussed in Chapters 3, 4, 5, and 6 have been obtained performing Monte Carlo simulations in the constant-pH ensemble [32, 42, 55] by means of a FORTRAN code developed by the Candidate in collaboration with Dr. Massimo Mella. Differently, systems discussed in Chapters 7 and 8 have been simulated via the software package ESPResSo [62].

Chapter 2

Theoretical Background

2.1 Coarse-grained simulations of polymers and polyelectrolytes

Coarse-grained simulations aim to study *in silico* complex systems, e.g. polymers, biomolecules such as proteins, nucleic acid or membranes, functionalized nanoparticles, etc., by simplifying their description maintaining a level of detail sufficient to compute the properties of interest while reducing the amount of computational resources needed.

In our work, we implement a coarse-grained description of polyelectrolytes solution, the so called "polyelectrolyte primitive model", in order to investigate the complicate relationships occurring between conformational and structural properties of polyelectrolyte species in solution and, e.g., their ionizability, their ability to interact between each other and form supramolecular aggregates, etc. Our coarse-graining approach can be schematized as follows (see also Figure 2.1 for a pictorial scheme):

i. polymeric chains are represented via "beads & springs" models, in which each monomer (or group of monomers) is represented by soft-sphere with its own excluded volume and connected to the adjacent bead(s) via an interaction potential, the latter mimicking the presence of a covalent (hence, unbreakable) bond;

ii. strong polyelectrolytes' charged monomers and mobile ions (that is, polyelectrolyte counterions or background salts) are represented by spheres with

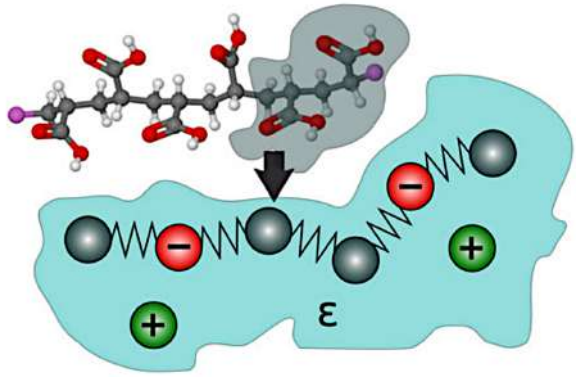

Figure 2.1: Scheme of a coarse-grained representation of a polyelectrolyte in implicit solvent. Reprinted by permission from Springer Nature: Progress in Colloid and Polymer Science 140, Molecular Simulations of Hydrogels, Peter Košovan, Tobias Richter, and Christian Holm, © Springer International Publishing Switzerland 2013.

a point charge positioned in their center of mass;

iii. the state of weakly ionizable monomers can be switched from neutral to charged and *vice versa*, and their reactivity (as acids or bases) is taken into account by means of the constant-pH ensemble (*vide infra* Section 2.2.2);

iv. the solvent is treated as a uniform dielectric continuum, i.e. no explicit water molecules are simulated, and electrostatic interactions are tuned by setting the value of the solvent relative permittivity ε_r or its Bjerrum length l_B;

v. depending on the case, all particles are enclosed in a spherical cell (the so called "cell model", *vide infra* Section 2.1.2) or in a cubic box with periodical boundary conditions in all the three Cartesian directions.

From this schematization, it follows that our simulations regarding strong polyelectrolytes are performed in the canonical ensemble, whereas when weakly ionizable species are present simulations are performed in a semi-grand canonical ensemble (or, more specifically, in the constant pH ensemble, *vide infra* Section 2.2.2).

2.1.1 Interaction potentials

2.1.1.1 Excluded volume interactions

In order to simulate particles excluded volume and to prevent particles overlaps (especially in the case of oppositely charged interacting species), the interaction between two particles is simulated via a tunable potential (U_{excV}). The most general expression for such pairwise interaction potential is the generic Lennard-Jones interaction:

$$U_{\mathrm{gLJ}}(r_{ij}) = \begin{cases} \epsilon \left[b_1 \left(\frac{\sigma}{r_{ij}} \right)^{e_1} - b_2 \left(\frac{\sigma}{r_{ij}} \right)^{e_2} + c_{\mathrm{shift}} \right] & \text{if } r_{ij} < r_{\mathrm{cut}} \\ 0 & \text{otherwise} \end{cases} \tag{2.1}$$

In the expression, σ is the sum of the radii of the interacting particles i and j, r_{ij} is their distance, ϵ is the potential depth, whereas b_1 and b_2 are adaptable parameters. The most used combination is $b_1 = b_2 = 4$, $e_1 = 12$, and $e_2 = 6$, resulting in the canonical Lennard-Jones (LJ) potential:

$$U_{\mathrm{LJ}}(r_{ij}) = \begin{cases} 4\epsilon \left[\left(\frac{\sigma}{r_{ij}} \right)^{12} - \left(\frac{\sigma}{r_{ij}} \right)^{6} + c_{\mathrm{shift}} \right] & \text{if } r_{ij} < r_{\mathrm{cut}} \\ 0 & \text{otherwise.} \end{cases} \tag{2.2}$$

The latter is the "work-horse" potential of particle-based coarse-grained simulations. Since it is attractive at large distances (or equal to 0 for $r_{ij} \geq r_{\mathrm{cut}}$), while it is strongly repulsive at short r_{ij} values, it is the most implemented model to simulate van der Waals interactions. At $r_{ij} = \sigma$, $U_{\mathrm{LJ}}(\sigma) = 4\epsilon c_{\mathrm{shift}}$, whereas the minimum of the potential is attained at $r = 2^{\frac{1}{6}}\sigma$, i.e. $U_{\mathrm{LJ}}\left(2^{\frac{1}{6}}\sigma\right) = (4c_{\mathrm{shift}} - 1)\epsilon$.

One popular interaction potential implemented in order to simulate particles as purely repulsive soft spheres is the Weeks-Chandler-Anderson (WCA) potential [63]:

$$U_{\mathrm{WCA}}(r_{ij}) = \begin{cases} 4\epsilon \left[\left(\frac{\sigma}{r_{ij}} \right)^{12} - \left(\frac{\sigma}{r_{ij}} \right)^{6} + \frac{1}{4} \right] & \text{if } r_{ij} < 2^{\frac{1}{6}}\sigma \\ 0 & \text{otherwise.} \end{cases} \tag{2.3}$$

In the WCA interaction, the curve is truncated at the minimum of the potential ($r_{\mathrm{cut}} = 2^{\frac{1}{6}}\sigma$), and it is shifted so that the value of the potential at the minimum is equal to 0. WCA interactions are usually implemented when the dielectric is

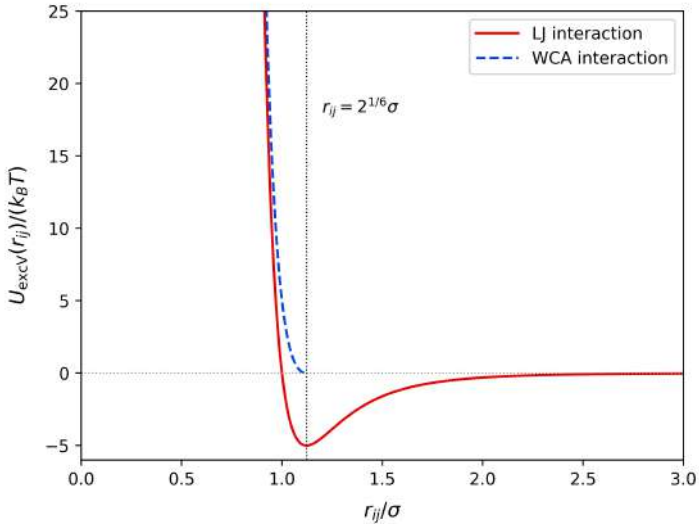

Figure 2.2: Classic (unshifted) LJ and WCA interactions, with $\sigma = 1$ and $\epsilon = k_BT$. The vertical dotted black indicate the value of the minimum of the LJ potential, whereas the horizontal dotted gray line is only a guide to the eye to discern positive and negative values.

a good solvent for the particles; on the contrary, poor solvent conditions could be modeled by implementing classical LJ interactions, so that particles tend to cluster together reducing the surface in contact with the dielectric. Examples of LJ and WCA interactions are shown in Figure 2.2.

2.1.1.2 Covalent bonding interactions

In order to treat polymeric systems, we need to connect each pair of adjacent monomers i and j with a potential $U_{\text{bond}}(r_{ij})$ that simulate the presence of an unbreakable (but nevertheless stretchable) covalent bond between the two beads. The most used stretching potentials are the "harmonic bond" ($U_{\text{bond}}(r_{ij}) = U_{\text{harm}}(r_{ij})$) and the "finite extensible non-linear elastic" (FENE) bonding potential [64], $U_{\text{bond}}(r_{ij}) = U_{\text{FENE}}(r_{ij})$.

Harmonic bond The harmonic potential is the simplest way to simulate non-rigid covalent bonds and it is defined as

$$U_{\text{harm}}(r_{ij}) = \frac{1}{2} k_{\text{bond}} (r_{ij} - r_0)^2, \tag{2.4}$$

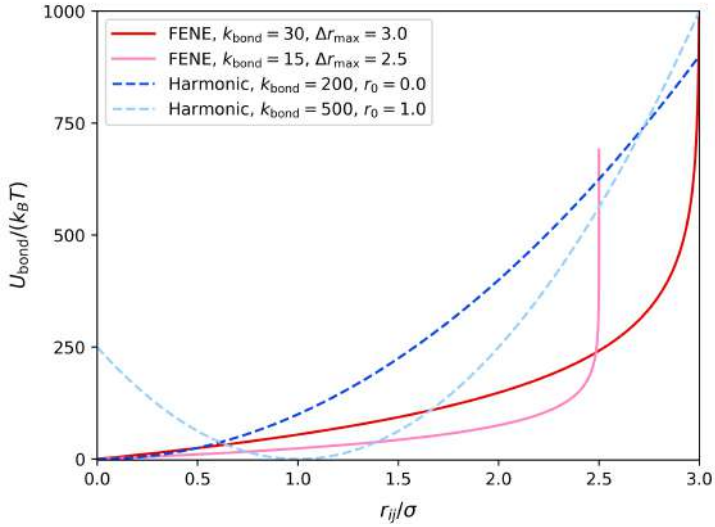

Figure 2.3: Examples of covalent bonding potentials. For the FENE interactions we set $r_0 = 0$.

where k_{bond} is the bonding force constant and r_0 is the equilibrium position. Examples of harmonic bonding potential are reported in Figure 2.3.

FENE bond The FENE potential [64] is defined as

$$U_{\text{FENE}}(r_{ij}) = -\frac{1}{2} k_{\text{bond}} \Delta r_{\text{max}}^2 \ln\left[1 - \left(\frac{r_{ij} - r_0}{\Delta r_{\text{max}}}\right)\right], \tag{2.5}$$

where k_{bond} is the bonding force constant, Δr_{max} is the maximum allowed displacement, and r_0 is the equilibrium position; parameters are usually set to 0 in order to have $U(r_0 \equiv 0) = 0$. Differently from the harmonic potential, the FENE bond diverges at the chosen maximum bond length, and the bond is considered broken if (for any reason) $r_{ij} > \Delta r_{\text{max}}$.

Examples of both harmonic and FENE potentials are reported in Figure 2.3. In each simulation set we will present during our discussion, the choice between one of the two bonding interactions has been made exclusively to facilitate the comparison of the results obtained by us with those already present in the literature.

2.1.1.3 Angular interactions

In order to increase the rigidity of a polymer chain, besides stretching interactions one can also add an angular potential (or bending potential) which has the effect to impose an equilibrium angle θ_0 between three adjacent monomers i, j, and k. The easiest way to introduce such a potential is to implement an angular harmonic potential

$$U_{\text{ang}}(\theta_{ijk}) = \frac{1}{2} k_{\text{ang}} (\theta_{ijk} - \theta_0)^2. \tag{2.6}$$

In the formula θ_{ijk} is the angle between the three monomers and k_{ang} is the bending force constant.

2.1.1.4 Electrostatics interaction

Within the framework of the cell model (*vide* Section 2.1.2), electrostatics interactions can be calculated via the classic pairwise Coulomb potential:

$$U_{\text{Coul}}(r_{ij}) = \frac{1}{4\pi\varepsilon_0\varepsilon_r} \frac{q_i q_j}{r_{ij}}, \tag{2.7}$$

where q_i and q_j are the point charges carried by particles i and j, whereas ε_0 and ε_r are, respectively, the vacuum dielectric constant and the relative permittivity of the solvent. The latter is not treated explicitly in our models, but it is instead represented by an unpolarizable dielectric continuum. Unless otherwise specified, our simulations are done at $T = 298$ K in aqueous solutions, hence $\varepsilon_r \simeq 78$. If periodic boundary conditions have to be taken into account in all the three Cartesian directions, the electrostatic contribution can be evaluated efficiently by numerical methods like such as the P^3M algorithm [65–67] or the Wolf's method [68, 69].

2.1.1.5 Simulating charged hydrogen bonds

In order to simulate the impact of charged hydrogen bonds on polyelectrolytes behavior, we employ a many-body interactions potential U_{MB} previously introduced by Mella et al. [12, 37]. The latter consist in a density-dependent additive term of the total potential mimicking the formation of charged hydrogen bonds [70–73] (c-H-bonds) between neutral and ionized monomers.

Parameters defining this type of interaction are the cutoff radius r_{MB} below which charged and neutral monomers are considered to be interacting, the strength of the stabilizing interaction potential per interacting pair ξ_{MB}, and the maximum number of c-H-bonds that neutral and charged monomers can form, $n_{\mathrm{MB}}^{(\mathrm{n})}$ and $n_{\mathrm{MB}}^{(\mathrm{c})}$ respectively. In fact, in order to represent the formation of c-H-bonds so that the model is, at least, qualitatively correct, one has to bear in mind that there is a maximum number of possible contacts that can be formed between a charged monomer and its neutral counterparts. For example, an ammonium ion obtained by protonating a tertiary amine can form only one of such contacts, while up to two contacts are allowed for a secondary amine [70, 71, 74, 75]. Obviously, there is also an intrinsic limit to the number of c-H-bonds that a neutral group can form (most likely related to the number of lone pairs available); thus, H_2O can form two such bonds, while NH_3 is limited to one. For the same reasons, (undissociated) carboxylic acids can form one charged contact, while carboxylates can form two of them. Albeit such characteristic could be introduced, in principle, by using orientation–dependent forces, we opted for conserving the simplicity of the original polyelectrolyte model provided by representing monomers as spheres.

The original version of the c-H-bonds–mimicking potential [12] was built adding the following density-dependent energy term to the total potential:

$$U_{\mathrm{MB}} = \sum_{j}^{N_{\mathrm{chain}}} \sum_{i}^{L} \tilde{e}(\rho_i) \tag{2.8}$$

In Equation 2.8, i represents the position of a charged monomer along a chain j, the latter composed by L beads in total, and

$$\rho_i = \sum_{\mu} H[r_{\mathrm{MB}} - r_{i\mu}] \tag{2.9}$$

is the number of neutral groups that may be "c-H-bonded" to the charged group i. In Equation 2.9, $H[x]$ is the Heaviside function, μ indicates a neutral group (belonging to the same chain j of i or to another one), while r_{MB} is the critical distance used to define the possibility for the μ neutral group of forming ($r_{i\mu} \leq r_{\mathrm{MB}}$) or not ($r_{i\mu} > r_{\mathrm{MB}}$) a c-H-bonded conjugated pair. Let us point out that monomers μ directly connected to a charged group i are not included in the sum in

Equation 2.9 as this would lead to a chain overcharging due to their short distance. Definition provided in 2.9 makes the density ρ a step-like function of the inter-monomer distance, so that it can be used as a simple approach to indicate whether or not there is the possibility of a strong interaction between charged and neutral monomers. It is thus mandatory to chose a form of the potential mimicking such characteristic. The minimalist approach employed to do so uses a function $\tilde{e}$ that maximizes the number of c-H-bonds present by imposing that a neutral (charged) monomer can form a maximum of $n_{\mathrm{MB}}^{(\mathrm{n})}$ ($n_{\mathrm{MB}}^{(\mathrm{c})}$) at a time. Such a choice has some consequences: (i) it limits the number of coordinated monomers without the need of introducing specific orientation-dependent interactions; (ii) it allows to exploit the effect of conformational entropy in absence of any energetic cost associated with the exchange of c-H-bonds; (iii) the lack of orientation-dependent forces may overemphasize chains stabilization due to c-H-bonds compared to what one would expect if also geometrical terms were introduced. Nevertheless, we often limited only the number of charged monomers able to form c-H-bonds by setting $n_{\mathrm{MB}}^{(\mathrm{n})} = \infty$ (as done by Mella et al. in References [12, 37]), this in order to reduce the computational cost necessary to calculate MB interactions.

In our simulation, we usually set $r_{\mathrm{MB}} = 5$ Å and $\epsilon_{\mathrm{MB}} = -2$ kcal/mol; the parametrization has been done by Mollica in Reference [12] via atomistic MD simulations of the pair $(CH_3)_2N$–$(CH_3)_2NH^+$ in water.

2.1.1.6 Total potential

The system total potential U (or U_{tot}) results from the sum of all the (additive) terms discussed above, i.e.

$$U \equiv U_{\mathrm{tot}} = \sum U_{\mathrm{excV}} + \sum U_{\mathrm{bond}} + \sum U_{\mathrm{ang}} + \sum U_{\mathrm{Coul}} + U_{\mathrm{MB}} \,(+\dots), \quad (2.10)$$

where summations run over all the interacting particles. It follows that the system total internal energy results:

$$E_{\mathrm{tot}} = U_{\mathrm{tot}} + E_{\mathrm{kin}} = U_{\mathrm{tot}} + \frac{3}{2} N_{\mathrm{tot}} k_{\mathrm{B}} T, \quad (2.11)$$

where N_{tot} is the total number of particles in the system.

2.1.2 Cell model

Within the framework of the cell model [76], all particles are inside a (usually, but not necessarily, spherical) cell (i.e., no periodic conditions are applied), the latter being impermeable to all the species so that no particle can escape from it. Thus, for a spherical cell of radius R_{cell} we have

$$U_{\text{cell}}(r_i) = \begin{cases} 0 & \text{if } r_i < R_{\text{cell}} \\ +\infty & \text{if } r_i \geq R_{\text{cell}}, \end{cases} \tag{2.12}$$

where r_i is the distance of the i-th particle from the center of the cell. It immediately follows that R_{cell} implicitly defines the concentration of all species in solution. Usually, when polymeric species are simulated with such boundary model, R_{cell} value is set so that it is higher than the contour length of the chains (exception are simulations studying the effect of confinement on chains, such as in Reference [37]). Worth noticing, cell model simulations allow to directly compute the osmotic pressure π_{abs} (and, consequently, the osmotic coefficient $\Phi = \pi_{\text{abs}}/\pi_{\text{id}}$) of an electrolyte solution, because it is directly related to mobile ions concentration *at* the cell boundary [76].

2.1.3 Polymers and polyelectrolytes properties

2.1.3.1 Polymers conformational properties

End-to-end distance The "end-to-end distance" $r_{1\text{N}}$ is the distance between the first and the last monomer of a chain. For a linear polymer N-monomers long, the average root mean square end-to-end distance $\langle r_{1\text{N}} \rangle$ is defined as

$$\langle r_{1\text{N}} \rangle = \sqrt{\langle |\mathbf{r}_1 - \mathbf{r}_N|^2 \rangle}, \tag{2.13}$$

with the average taken over all the configurations sampled at equilibrium. In the formula, $\mathbf{r}_1$ and $\mathbf{r}_N$ are, respectively, the vector defining the position of the first and the last monomers of the chain. The concept of "end-to-end" distance can be easily extended also to chain tethered to a surface (as in polymer brushes or functionalized nanoparticles), to a common bead (as in star-shaped polymers or dendrimers), or to a common "backbone chain" (as in comb polymers); in such

cases, $\mathbf{r}_1$ would represent the position vector of the tethered monomer.

Radius of gyration The radius of gyration R_g is defined as the radial distance to a point which would have a moment of inertia the same as the body's actual distribution of mass, if the total mass of the body were concentrated. It is thus useful to describe the polymer size. Computationally, the average value of the squared radius of gyration of a polymer composed by N monomers can be computed as follows:

$$\langle R_\mathrm{g}^2 \rangle = \frac{1}{N} \left\langle \sum_i^N |\mathbf{r}_i - \mathbf{r}_\mathrm{CoM}|^2 \right\rangle; \tag{2.14}$$

here, $\mathbf{r}_i$ is the position vector of the i-th monomer, whereas $\mathbf{r}_\mathrm{CoM}$ is the position vector of the chain center of mass.

Hydrodynamic radius Another property which is useful to describe the size of a polymer chain is the hydrodynamic radius R_H, which is defined as the radius of an equivalent sphere diffusing in solution at the same rate as the polymer chain:

$$\left\langle \frac{1}{R_\mathrm{H}} \right\rangle = \frac{\langle \sum_{i \neq j}^N \frac{1}{r_{ij}} \rangle}{N^2}, \tag{2.15}$$

where r_{ij} is the distance between monomers i and j.

Persistence length The persistence length l_p is a property useful to quantify the rigidity (either intrinsic or induced by, e.g., the presence of Coulomb repulsion between charged monomers) of a polymer chain. l_p can be computed from the exponential decay of the orientation correlation of bond vectors along a polymer chain [77], resulting in

$$l_\mathrm{p} = \frac{\langle r_\mathrm{mm} \rangle}{\ln \langle \cos\theta \rangle}, \tag{2.16}$$

where $\langle r_\mathrm{mm} \rangle$ is the average bond length and $\langle \cos\theta \rangle$ is the average cosine of the angle θ between three adjacent monomers.

2.1.3.2 Weak acidity and basicity

When a chemical species (in our case a monomer) act as a weak (Brønsted) acid, it undergoes to the following simple chemical reaction:

$$\mathrm{HA} \rightleftarrows \mathrm{H^+} + \mathrm{A^-}, \tag{2.17}$$

where HA is the undissociated monomer, $\mathrm{A^-}$ is its dissociated form (i.e., the conjugated base) and $\mathrm{H^+}$ is the released proton. A similar equation can be written when monomers act as weak (Brønsted) bases:

$$\mathrm{B} + \mathrm{H^+} \rightleftarrows \mathrm{BH^+}, \tag{2.18}$$

with B and $\mathrm{BH^+}$ are, respectively, the unprotonated and protonated (i.e., the conjugated acid) forms of the basis. For sake of brevity, we shall take as an example and discuss the case of a polymer model whose monomers HA act as weak acids; almost identical derivations and conclusions can be easily obtained for weak bases simply by starting from Reaction 2.18 and retracing the same reasoning made for weak acids.

Like any other chemical reaction, also Reaction 2.17 is described by a thermodynamic equilibrium constant which in our case is

$$K_a = \frac{a_{\mathrm{A^-}} a_{\mathrm{H^+}}}{a_{\mathrm{HA}}}. \tag{2.19}$$

Thus, the thermodynamic acid dissociation constant K_a is a function of the activities a of involved species. We recall that $a_{\mathrm{X}} = \gamma_{\mathrm{X}}[\mathrm{X}]/c^{\ominus}$, where γ_X is the activity coefficient of species X, [X] is its molar concentration, and $c^{\ominus} = 1$ mol/l is the standard molar concentration (the latter ensures to have dimensionless a and γ). We also define $\mathrm{p}K_a$ as the negative decimal logarithm of K_a.

The ideal weak acidic behavior Within the simple picture in which no interactions between any weak acidic groups are present, the activity coefficient of all species results $\gamma = 1$, so that in Equation 2.19 activities a can be replaced by

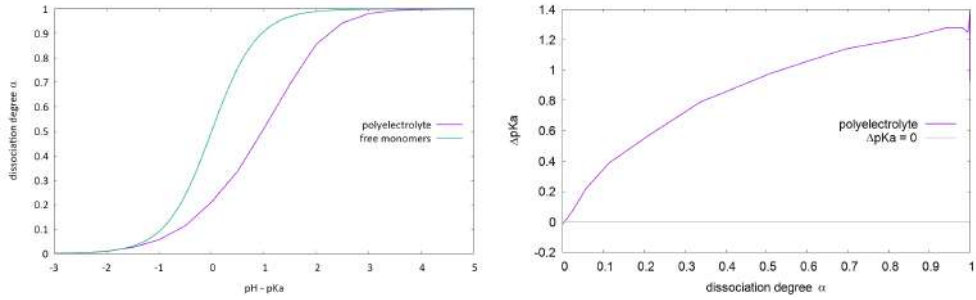

Figure 2.4: (a) simulated α as a function of pH - pK_a for a linear polyelectrolyte 120 monomers long (purple line) and free monomers ($\sim$ ideal case, teal line); (b) ΔpK_a as a function of α for the same polyelectrolyte.

molar concentrations obtaining

$$K_a^{\mathrm{id}} = \frac{[\mathrm{A}^-][\mathrm{H}^+]}{[\mathrm{HA}]c^{\ominus}}. \tag{2.20}$$

When interactions between the species are negligible, e.g. in conditions of high dilution, p$K_a \simeq$ pK_a^{id} and pH $= -\log_{10} a_{\mathrm{H}^+} = -\log[\mathrm{H}^+]$. We define the ionization degree (or degree of dissociation) α of HA as the number of dissociated acidic groups N_{A^-} divided by the total number of weak (hence, titratable) groups $N_0 = N_{\mathrm{HA}} + N_{\mathrm{A}^-}$

$$\alpha = \frac{N_{\mathrm{HA}}}{N_0} = \frac{[\mathrm{A}^-]}{[\mathrm{HA}] + [\mathrm{A}^-]} \tag{2.21}$$

Rearranging Equation 2.21 yields the Henderson-Hasselbalch equation

$$\alpha = \frac{1}{1 + 10^{\mathrm{pH}-\mathrm{p}K_a}}. \tag{2.22}$$

The latter equation may be a valid description in conditions that are approximable to the ideal case.

Weak acidity in polyelectrolytes When acidic monomers are connected forming a polyelectrolyte and all interactions (electrostatics, excluded volumes, bonds, etc.) are taken into account, the titration behavior strongly deviates from the ideal one described by the Henderson-Hasselbalch equation, as one can observe from Figure 2.4, the latter comparing the ideal case with the simulated average dissociation degree for a linear polyacid composed by 120 titratable beads. We define the average degree of dissociation $\langle\alpha\rangle$ as the dissociation degree α

averaged over all the monomers in solution and over all the sampled system configurations.

It is important to notice that, whereas in a solution of a free (non-bonded) weak acid all monomers HA show the same acidity, hence they have the same pK_a, when monomers are bonded to form a polyelectrolyte their acidity depends on their position along the chain, with monomers lying at the extremes of the polymer showing a lower acidity (hence, an higher pK_a) with respect to "inner" monomers, due to the fact that the latter have a greater monomer density around them, and hence they feel a greater density of charge (due to already ionized monomers) which partially inhibits their dissociation. The situation becomes even more complicate when non-linear polymer topologies are considered, with, e.g., star-shaped polyelectrolytes showing a decrease in monomer acidity the closer they lie to the central core (due to, once again, an increasing in ionizable monomer density). Having made this clear, for sake of simplicity we shall use the symbol "α" instead of $\langle\alpha\rangle$ also when discussing polyelectrolytes, assuming we are averaging not only on all sampled configurations but also on monomers that may have different pK_a's due to their position along the chain (and, if necessary, over all the chains in solution).

Therefore, summarizing, weak acid groups on polyelectrolytes tend to show a depressed acidity (hence a higher pK_a) if compared with same groups lying on molecules that are free to wander in solution. It follows that we can define $\Delta\mathrm{p}K_a$ as the shift in acidity between the polyelectrolyte and the ideal case

$$\begin{aligned} \Delta\mathrm{p}K_a(\alpha) &= \mathrm{p}K_a^{\mathrm{poly}}(\alpha) - \mathrm{p}K_a^{\mathrm{id}}, \\ \mathrm{p}K_a^{\mathrm{poly}}(\alpha) &= \mathrm{pH} - \log_{10}\left(\frac{\alpha}{1-\alpha}\right) \end{aligned} \tag{2.23}$$

Figure 2.4(b) shows how average monomer acidity varies as a function of the chain ionization degree. This representation allow not only to estimate the shift in pK_a due to the polymeric nature of the species by simply reading $\Delta\mathrm{p}K_a$ at $\alpha = 0.5$ (as generally done in literature), but also to effectively highlight the impact on the ionization behavior of additional factors such as chain rigidity, the possibility for monomers to interact via chemically specific interactions or the impact of salts in solution. Furthermore, from $\Delta\mathrm{p}K_a$, the impact on energetics of the dissociation process can be easily quantified via the relation

$\Delta[\Delta_{\text{disso}}A^{\circ}(\text{poly},\alpha)] = \Delta_{\text{disso}}A^{\circ}(\alpha) - \Delta_{\text{disso}}A^{\circ}(\text{ideal}) = 2.3025RT\Delta\text{p}K_a$, where R is the ideal gas constant, whereas $\Delta_{\text{disso}}A^{\circ}(\text{ideal})$ and $\Delta_{\text{dissoo}}A^{\circ}(\text{poly},\alpha)$ are the changes in standard Helmholtz energy due to, respectively, the dissociation of a monomer in the ideal case, and the dissociation of a monomer bonded in a polyelectrolyte having a ionization degree α.

2.2 Simulation methods

2.2.1 Canonical Monte Carlo simulations

Monte Carlo (MC) simulations are a broad class of computational methods that rely on rewriting deterministic problems into probabilistic form, so that appropriate random sampling may lead to obtain numerical results. They're very useful for simulating chemico-physical systems for which an analytical solution is too complex or even impossible to find, e.g. systems with a huge number of coupled degrees of freedom such as polymeric solutions.

Among MC methods, Markov chain MC approaches can be used in order to sample a probability distribution $\rho(x)$ of an observable $\mathcal{X}$. In the canonical ensemble, the average value of $\mathcal{X}$ is given by

$$\langle\mathcal{X}\rangle = \int \mathcal{X}(x)\rho_{\text{eq}}(x)\text{d}x = \frac{1}{Z}\int \mathcal{X}(x)e^{-\beta U(x)} \tag{2.24}$$

where $U(x)$ is the total energy of the system, Z is its partition function, $\beta = (k_{\text{B}}T)^{-1}$ and the integral is calculated over all the accessible configuration microstates. Since, in general, the integral in Equation 2.24 cannot be solved analytically, one can perform MC simulations in order to numerically compute it by generating a random sample of system configurations according to a certain distribution $\pi(x)$ (*vide infra*).

2.2.1.1 Markov Chain Monte Carlo simulations

We define as Markov chain a stochastic model describing a sequence of possible events in which the probability of each event depends only on the state attained before such event takes place. By constructing a Markov chain that has the desired stationary probability distribution $\rho_{\text{eq}}(x)$ as its equilibrium distribution, one can sample $\rho_{\text{eq}}(x)$ by recording states from the chain.

For a Markov process evolving in a discrete configuration space with a fictitious time step $\Delta t = 1$, namely a Monte Carlo step (MCS), the probability $P(j,t)$ to find the system in the state j at the time $t+1$ is given by the following "master equation"

$$P(j,t+1) = \sum_i \Big[w(j|i)P(i,t) - w(i|j)P(j,t) \Big]; \tag{2.25}$$

here, $w(j|i)$ denotes the *time independent* transition probability from the state i to the state j. Since i and j can be equal one to each other, and a transition $i \to j$ will certainly occur, we have that $\sum_i w(j|i) = 1$, so Equation 2.25 can be rewritten as the "stationarity condition".

$$P(j,t+1) = \sum_i w(j|i)P(i,t). \tag{2.26}$$

To simulate a chemico-physical system, $P(j,t)$ must converge to the stationary distribution $\rho_{\text{eq}}(x,t) \equiv \rho_{\text{eq}}(x) = \sum_j P_{\text{eq}}(j,t)$ (i.e., the canonical equilibrium distribution). The right-hand side of Equation 2.25 vanishes and we obtain the so called "detailed balance" condition:

$$w(j|i)\rho_{\text{eq}}(i) = w(i|j)\rho_{\text{eq}}(j). \tag{2.27}$$

The detailed balance is a sufficient but unnecessary condition to be satisfied in MC simulations. The stationarity condition (Equation 2.26), which is a less stringent condition, implies that $P(j) = P_{\text{eq}}(j)$ remains invariant during the Markov process, and it ensures to perform valid simulations if the MC sampling is ergodic.

2.2.1.2 Metropolis-Hastings scheme

The Metropolis–Hastings scheme is by far the most used method to perform MC coarse-grained simulations, and this is due to the fact that given any probability distribution $\rho_{\text{eq}}(x)$ and provided a function $\pi(x) \propto \rho_{\text{eq}}(x)$, it is possible to reconstruct $\rho_{\text{eq}}(x)$ simply by sampling $\pi(x)$. This allow to bypass the calculation of the normalization factor, which often results a very problematic step.

In order to sample a chemico-physical system satisfying the detailed balance

(Equation 2.27), the probability of transition between two state i and j can be defined as follows:

$$\frac{w(j|i)}{w(i|j)} = \frac{P_{\text{try}}(i \to j)P_{\text{acc}}(i \to j)}{P_{\text{try}}(j \to i)P_{\text{acc}}(j \to i)} = e^{-\beta[U(j)-U(i)]}. \tag{2.28}$$

$P_{\text{try}}(i \to j)$ and P_{acc} are, respectively, the probability to propose the change in state $i \to j$ and the probability to accept such change. One solution to Equation 2.28 has been proposed by Metropolis et al. [78], and it is know as the "Metropolis acceptance criterium":

$$P_{\text{acc}}(i \to j) = \min\left\{1, \frac{P_{\text{try}}(j \to i)}{P_{\text{try}}(i \to j)} e^{-\beta \Delta U}\right\}, \tag{2.29}$$

where $\Delta U = U(j) - U(i)$. When proposal probabilities are symmetric, i.e. $P_{\text{try}}(j \to i) = P_{\text{try}}(i \to j)$, we obtain the "Metropolis-Hastings acceptance criterium"

$$P_{\text{acc}}(i \to j) = \min\left\{1, e^{-\beta \Delta U}\right\}. \tag{2.30}$$

2.2.1.3 Monte Carlo simulations of polymers

In order to illustrate how Monte Carlo simulations work, we now analyze the algorithm used to sample configurations of a system (at the equilibrium) consisting in a single linear chain composed by L monomers, its counterions (CIs) and a background monovalent inert salt (e.g., NaCl). The algorithm can be schematized as follows:

1. the initial (state i) total potential $U(i)$ is computed;

2. a random particle k (either a polyelectrolyte's monomer or a mobile ion) with coordinates $\left(x_k^{(\text{i})}, y_k^{(\text{i})}, z_k^{(\text{i})}\right)$ is chosen to be displaced along the vector $\boldsymbol{\xi} = (\xi_x, \xi_y, \xi_z)$, where ξ_x, ξ_y, and ξ_z are three random real numbers uniformly generated in the interval $(-\Delta d_{\max}, +\Delta d_{\max})$, $\Delta d_{\max}$ being the maximum allowed displacement for the translation moves, the value of which is usually chosen so that $P_{\text{acc}} \approx 0.4 \div 0.5$;

3. the new (state j) total potential $U(j)$ is computed;

4. the probability of acceptance P_{acc} (Equation 2.30) is calculated:

a. if $P_{\text{acc}} \geq 1$, the new configuration j is retained;

b. if $P_{\text{acc}} < 1$, a random real number ξ is uniformly generated in the interval (0,1):

   b_1. if $\xi \leq P_{\text{acc}}$, the new configuration j is retained;

   b_2. if $\xi > P_{\text{acc}}$, the attempted move is rejected and the system is returned to its initial state j.

In order to reduce the computational cost of the simulations and to facilitate algorithm implementation, given a system composed by N particles, one may attempt the translation of each element (i.e., proceeding regularly from the 1$^{\text{st}}$ to the N^{th} particle) once per Monte Carlo step, instead of randomly choose a sequence of N random monomers. This sequential approach is still valid since each of the individual steps obeys (at least) stationarity condition (Equation 2.26).

In the proposed scheme, we stated that it is necessary to compute the *total* initial and final potentials, $U(i)$ and $U(j)$, for each attempted move. Actually, this is not true when contributions to the total potential are pairwise; in such a case, in fact, only contributions changing upon displacement of the k-th particle need to be taken into account. Such "tricks" allow to considerably reduce the computational cost of simulations. So, if all interactions are calculated pairwisely, the only contributions of the total potential that vary when a monomer k is displaced are the ones appearing in $U^{(k)} = \sum_{l\neq k}^{N} [U_{\text{LJ}}(r_{lk}) + U_{\text{Coul}}(r_{lk})] + \sum_{l=k-1\neq k}^{k+1} U_{\text{bond}}(r_{lk})$.*,†

2.2.1.4 Cluster moves

When simulating complex systems like polymers, a set of cluster moves can be also implemented both in order to speed up the convergence to the system equilibrium state and to better sample the potential energy surface. MC cluster moves are attempts to change the state (usually, the position) of a given group of particles, e.g the entire polymer chain or a segment of it. In polymer coarse-grained simulations, the most frequently implemented cluster moves are:

*The formula is valid for a monomer m which does not occupy the first or the last position along the chain and in absence of an angular contribution to the potential.

†This implies that all particles are listed in a correct way; e.g., all monomers (respecting their sequential position along the chain), then all CIs, then all salt ions.

1. **entire chain translation/rotation:** it consists in a rigid translation/rotation in space of a given chain with respect to the other chains and particles in the system;

2. **pivot move**: given two (randomly chosen) *adjacent* monomers i and $j = i + 1$, the move consists in an attempt to rotate all $k > i + 1$ monomers around the segment connecting i and j by an angle ϕ, $-\theta_{\text{pivot}} < \phi < \theta_{\text{pivot}}$, where θ_{pivot} is the maximum allowed angular displacement;

3. **crank-shaft move**: given two (randomly chosen) non-adjacent monomers i and $j > i$, the move consists in an attempt to rotate all the k monomers that lies between i and j (i.e., $i < k < j$) around the segment connecting i and j by an angle ϕ, $-\theta_{\text{c-shaft}} < \phi < \theta_{\text{c-shaft}}$;

3. **reptation move**: being i and j the first and last monomer of the chain (or *vice versa*), the reptation consists in moving i " beyond"j randomly choosing the former position so that it lies at a distance $r_0 \pm \Delta r_{\text{rept}}$, where r_0 is the equilibrium bond distance between monomers, and connecting the two with a bonding interaction.[‡]

As for "canonical" MC moves, also for cluster moves the parameters are set so to have an acceptance probability roughly equal to $40 \div 50\%$.

A smarter version of cluster moves, the so called "(partially) clothed cluster moves", has been proposed to improve polyelectrolyte sampling (see, e.g., Reference [79]). In fact, displacing long segments of a polyion without displacing accordingly its condensed counterions may carry a large energy expense and hence result in a decrease in the acceptance rate. Thus, (partially) clothed moves attempt to solve such issue by including, in cluster moves, (a portion of) the ion atmosphere surrounding the displaced segment. Our experience suggests that "naked " cluster moves are usually sufficient to obtain good sampling in presence of monovalent CIs. In case of multivalent counterions, we suspect that clothed moves can lead to a significant improvement in sampling the system potential energy surface; to date, however, simulatio results supporting this idea seems to be lacking in literature to the best of our knowledge.

[‡]Instead of a single monomer, an entire segment of the chain can be also translated; usually, the rate of acceptance decreases with the length of the segment

2.2.2 Simulating weak acidity/basicity with Monte Carlo: the "constant pH" method

The "constant-pH" method has been proposed by Reed and Reed [32] in order to simulate the titration of weak acidic or basic species such as weak polyelectrolytes.

As originally reported in Reference [32] and recently recalled in a review on simulations of weak polyelectrolytes and gels [42], the partition function of the constant-pH ensemble is

$$\mathcal{Z}_{\mathrm{cpH}} = \sum_{\bar{n}\in\mathcal{I}} \frac{N_0!}{[N_0(1-\bar{n})]!(N_0\bar{n})!}\left(10^{\mathrm{pH}-\mathrm{p}K_a}\right)^{N_0(1-\bar{n})} \int \Xi(U,\bar{n}) e^{[-\beta U(\mathbf{R},\bar{n})]}\mathrm{d}\mathbf{R}, \tag{2.31}$$

where N_0 is the number of titratable units, $\Xi(U,\bar{n})$ is the degeneracy of the total potential energy U given a specific degree of association $\bar{n} = 1-\alpha$, $\mathrm{p}K_a$ is the negative decimal logarithm of the dissociation constant K_a, $\mathcal{I}$ is the discrete set of allowed degrees of associations $\mathcal{I} = \{i\Delta\bar{n} \mid i \in 0, 1, \ldots, N_0\}$ in the simulation and $\Delta\bar{n} = 1/N_0$ is the smallest allowed change of $\bar{n}$ in the simulation. From Equation 2.31 it follows that the probability for a microstate i with a certain degree of association $\bar{n}$ is

$$P_i[\bar{n}, U(i)] = \frac{N_0!}{[N_0(1-\bar{n})]!(N_0\bar{n})!}\left(10^{\mathrm{pH}-\mathrm{p}K_a}\right)^{N_0(1-\bar{n})} e^{[-\beta U(i,\bar{n})]}. \tag{2.32}$$

The Metropolis acceptance probability (see Equation 2.29) for a deprotonation (dissociation) step $P_{\mathrm{asso}\,\rightarrow\,\mathrm{disso}}$, i.e. the transition from a protonated ("asso") to a deprotonated state ("disso"), can be expressed in terms of change in the association degree $\Delta\bar{n}$:

$$\begin{aligned}
P_{\mathrm{asso}\,\rightarrow\,\mathrm{disso}} &= \min\left\{1, \frac{P_{\mathrm{disso}}[\bar{n}-\Delta\bar{n}, U_{\mathrm{asso}}]}{P_{\mathrm{asso}}[\bar{n}, U_{\mathrm{disso}}]}\right\} \\
&= \min\left\{1, \frac{\left(\frac{N_0!}{[N_0(1-\bar{n}+\Delta\bar{n})]!(N_0\bar{n})!}\right)}{\left(\frac{N_0!}{[N_0(1-\bar{n})]!(N_0\bar{n}+N_0\Delta\bar{n})!}\right)}\left(10^{\mathrm{pH}-\mathrm{p}K_a}\right)^{N_0\Delta\bar{n}} e^{[-\beta\Delta_{\mathrm{asso}\,\rightarrow\,\mathrm{disso}}U]}\right\} \\
&= \min\left\{1, \frac{N_0\bar{n}}{N_0(1-\bar{n}+1)}\left(10^{\mathrm{pH}-\mathrm{p}K_a}\right)^{N_0\Delta\bar{n}} e^{[-\beta\Delta_{\mathrm{asso}\,\rightarrow\,\mathrm{disso}}U]}\right\} \\
&= \min\left\{1, \frac{N_{\mathrm{HA}}}{N_{\mathrm{A}^-}}\left(10^{\mathrm{pH}-\mathrm{p}K_a}\right)^{N_0\Delta\bar{n}} e^{[-\beta\Delta_{\mathrm{asso}\,\rightarrow\,\mathrm{disso}}U]}\right\}
\end{aligned} \tag{2.33}$$

In the last step we used the relation $\frac{N_0\bar{n}}{N_0(1-\bar{n}+1)} \simeq \frac{N_0\bar{n}}{N_0(1-\bar{n})} = \frac{N_{\mathrm{HA}}}{N_{\mathrm{A}^-}}$, which is valid for $N_0 \to \infty$. Setting $P_{\mathrm{asso}\,\to\,\mathrm{disso}} = \frac{N_{\mathrm{HA}}}{N_0} = 1-\alpha = \bar{n}$ and $P_{\mathrm{disso}\,\to\,\mathrm{asso}} = \frac{N_{\mathrm{A}^-}}{N_0} = \alpha$ results in the commonly used Metropolis-Hastings acceptance probability P_{cpH} for (de)protonation attempts, that is

$$P_{\mathrm{cpH}} = \min\left\{1, e^{-\beta\Delta U} 10^{\pm(\mathrm{pH}-\mathrm{p}K_a)}\right\} = \min\left\{1, e^{-\beta\Delta U \pm (\mathrm{pH}-\mathrm{p}K_a)\ln 10}\right\}, \quad (2.34)$$

where $\Delta U = \Delta_{\mathrm{asso}\,\to\,\mathrm{disso}} U$ or $\Delta_{\mathrm{disso}\,\to\,\mathrm{asso}} U$ is the change in energy due to the (de)protonation attempt. The "-" sign is used when a protonation is attempted, whereas the "+" sign is used when a dissociation is attempted.

In simple terms, the constant pH method assumes the system in equilibrium with an implicit infinite reservoir at a fixed chemical potential of H^+ ions, which is defined by the value assumed by the control parameter pH - pK_a. Thus, the state of a monomer m, e.g. charged (protonated, $q_m = 0$) or neutral (deprotonated, $q_m = -1$) in the case of a weak polyacid species, can be changed using the acceptance probability reported in Equation 2.34, which takes into account also the chemical potential of H^+ in solution. Every time a dissociation reaction is attempted, a CI (positive, in this case) is randomly inserted in the simulation cell in order to maintain the system electroneutral; conversely, a random CI is removed from the simulation box every time a dissociated monomer is protonated. Notice that constant-pH simulation scheme treats CIs as "dummy" particles whose role is only to maintain the system electroneutral, and their concentration does not coincide with the H^+ ones.[§] In fact, their actual number in the simulation cell may somewhat differ from the number of monovalent cations expected at a pH equal to the one imposed by the input pH - pK_a value if the simulation cell was coupled to a counterion reservoir. The implicit interpretation of the pH underestimates screening effects due to the absence of all explicit H^+ or OH^- ions, effect that may lead to inaccurate results at extremely high or low pH values, especially when the background ionic force is low or even absent [42,55].

Apart from the constant-pH ensemble, also the Reaction ensemble [80,81] (and the very recently developed Gran Reaction ensemble [82]) can be used in order to simulate weak polyelectrolytes. We refer the reader to References [42,55] for a

[§]At low pH values CI may represent H^+ in solution, whereas at high pH values they may represent OH^- counterions (e.g., Na^+); their chemical nature at intermediate pH values is somewhat unspecified.

detailed analysis of the differences between constant-pH and Reaction ensemble methods.

2.2.2.1 Helmholtz energy calculations

In the attempt of characterizing the equilibrium energetics of a polyelectrolyte as a function of pH, Reed and Reed [32] demonstrated under several simplifying assumptions that

$$A(\mathrm{pH}^*, R_{\mathrm{SC}}) = -k_{\mathrm{B}}T \ln(10) N_{\mathrm{mono}} \int_{\mathrm{pH} \ll \mathrm{p}K_a}^{\mathrm{pH}^*} \alpha(\mathrm{pH}, R_{\mathrm{SC}}) \mathrm{d}(\mathrm{pH} - \mathrm{p}K_a) \quad (2.35)$$

is the change in Helmholtz free energy of a weak polyacid linear chain composed by N_{mono} titratable monomers confined into a spherical cavity of radius R_{SC} upon increasing the pH from a value much lower than pK_a to a chosen pH*, and $\alpha(\mathrm{pH}, R_{\mathrm{SC}})$ is the average ionization degree of the species as a function of R, and the pH. Heuristically, Mella et al. employed such result to estimate the impact of chain ionization on the change in Helmholtz energy due to the confinement of linear polyelectrolytes inside slits, pores and spherical cavities at a specific pH [36, 37].

With respect to the validity of Equation 2.35, the knowledge of the partition function for the constant–pH ensemble [32, 42] allows us to prove that the integral of the ionization degree with respect to the pH correctly estimates the change in A for the *whole* system while increasing the proton chemical potential from a value sufficiently low to hamper ionization. In fact, as one can write the Helmholtz energy as $A = -k_{\mathrm{B}}T \ln(\mathcal{Z}_{\mathrm{cpH}})$, from Equation 2.31 it becomes possible to estimate the derivative of A with respect to pH (or, more conveniently, pH - pK_a). With the latter, one may exploit thermodynamic integration to compute ΔA associated to the ionization of polyelectrolytic systems due to a change in pH. Introducing $\mathcal{Z}_{\mathrm{conf}}(\bar{n}) = \int \Xi(U, \bar{n}) e^{(-\beta U(\mathbf{R}, \bar{n})} \mathrm{d}\mathbf{R}$ for convenience, and noticing that it does not

depend explicitly on the pH, one may write

$$\begin{aligned}\left(\frac{\partial A}{\partial(\mathrm{pH}-\mathrm{p}K_a)}\right) = &-\frac{k_\mathrm{B}T}{\mathcal{Z}_\mathrm{cpH}}\sum_{\bar{n}\in\mathcal{I}}\frac{N_0!}{[N_0(1-\bar{n})]![N_0\bar{n}]!}Z_\mathrm{conf}(\bar{n})[N_0(1-\bar{n})]\\ &(10^{\mathrm{pH}-\mathrm{p}K_a})^{N_0(1-\bar{n})-1}\ln(10)10^{\mathrm{pH}-\mathrm{p}K_a} =\\ =&-\ln(10)N_0\frac{k_\mathrm{B}T}{\mathcal{L}_\mathrm{pH}}\sum_{\bar{n}\in\mathcal{I}}\frac{N_0!}{[N_0(1-\bar{n})]![N_0\bar{n}]!}Z_\mathrm{conf}(\bar{n})[1-\bar{n}]\\ &(10^{\mathrm{pH}-\mathrm{p}K_a})^{N_0(1-\bar{n})} =\\ &=-\ln(10)N_0k_\mathrm{B}T\alpha \end{aligned} \tag{2.36}$$

where $\alpha \equiv \langle\alpha\rangle$ is an averaged value over $\mathcal{I}$. Integrating from an initial state for which $\mathrm{pH} \ll \mathrm{p}K_a$ (i.e., $\alpha = 0$) to the desired value of pH^*, one retrieves Equation 2.35.

2.2.3 Molecular Dynamics simulations

Molecular dynamics (MD) methods allow to simulate chemico-physical systems (either described by atomistic or coarse-grained models) by integrating the equation of motions for all the components over a certain lapse of time. In contrast with purely stochastic simulations (such as the Monte Carlo methods described in Section 2.2.1), they thus provide a picture of the dynamical evolution of the system. For a system conserving its energy (that is, in the microcanonical ensemble NVE), the trajectory of each interacting particle i can be numerically determined by solving equations of motion, the most common case being Newton's equations:

$$m_i\mathbf{a}_i = \mathbf{F}_i(\mathbf{r}^N) = -\nabla U_\mathrm{tot}(\mathbf{r}^N); \tag{2.37}$$

here, m_i is the i-th particle's mass, whereas $\mathbf{r}_i$, $\mathbf{a}_i$ and $\mathbf{F}_i$ are, respectively, the vectors defining its position, its acceleration, and the forces acting on it. U_tot is, instead, the total potential to which the particle i is subjected.

The integration scheme underlying our MD simulations is the "velocity Verlet"

integrator:

$$\mathbf{r}_i(t+\Delta t) = \mathbf{r}_i(t) + \mathbf{v}_i(t)\Delta t + \frac{1}{2}\mathbf{a}_i(t)(\Delta t)^2 \tag{2.38}$$

$$\mathbf{v}_i(t+\Delta t) = \mathbf{v}_i(t) + \frac{1}{2}[\mathbf{a}_i(t) + \mathbf{a}_i(t+\Delta t)]; \tag{2.39}$$

here, $\mathbf{v}_i(t)$ is the velocity of the i-th particle at the time t, and Δt is the integration time step.

For a system composed by N particles and obeying the ergodic hypothesis (which means that $\langle\mathcal{O}\rangle_{\text{ensemble}} = \langle\mathcal{O}\rangle_{\text{time}}$for any observable $\mathcal{O}$), it is possible to compute macroscopic thermodynamic properties from the evolution of a molecular dynamics simulation (i.e., from the trajectory generated in the $6N$ dimensional phase space):

$$\langle\mathcal{O}\rangle = \frac{1}{t_{\text{sim}}} \lim_{t_{\text{sim}}\to\infty} \int_0^{t_{\text{sim}}} \mathcal{O}\Big(\mathbf{r}^N(t), \mathbf{v}^N(t)\Big)\mathrm{d}t \tag{2.40}$$

$$\approx \frac{1}{M}\sum_{t=0}^{M} \mathcal{O}\Big(\mathbf{r}^N(t), \mathbf{v}^N(t)\Big). \tag{2.41}$$

.

In the canonical ensemble (NVT), the system energy "in excess" is exchanged with a thermostat in order to maintain T approximately constant. Several methods can be implemented to add and remove energy from the simulation cell, among which we mention the Langevin dynamics [83].

2.2.4 Langevin Dynamics

Langevin dynamics [83] introduces a Gaussian random force $\mathbf{R}_i$ and a friction coefficient γ in Newton's equation of motion, in order to convert such differential equations to stochastic differential equations:

$$m_i\mathbf{a}_i = \mathbf{F}_i(\mathbf{r}^N) + \mathbf{R}_i(\mathbf{r}^N) - \gamma m_i\mathbf{v}_i. \tag{2.42}$$

Importantly, the Gaussian force $\mathbf{R}$ must act on each particle independently and obey the fluctuation–dissipation theorem, hence it has to have a zero mean value

and a δ-distributed autocorrelation (δ being the Dirac's delta), that is:

$$\langle \mathbf{R}_i(t) \rangle = 0, \tag{2.43}$$

$$\langle \mathbf{R}_i(t) \cdot \mathbf{R}_j(t') \rangle = 6k_{\mathrm{B}}T\gamma\delta(t - t')\delta_{ij}. \tag{2.44}$$

This implies that it is assumed that the random force is completely uncorrelated at different simulation times $t \neq t'$.

Chapter 3

Absorbed Weak Polyelectrolytes: Impact of Confinement, Topology, and Chemically Specific Interactions on Ionization, Conformation Free Energy, Counterion Condensation and Absorption Equilibrium*

3.1 Introduction

The topic of polymers in general [84–112], and polyelectrolytes in particular [17, 113–121], absorbed into confining geometries has already attracted the attention of computational scientists [113, 120, 121] as a consequence of its relevance for several fields in science and technology. To name a few examples, we mention the interest in polymer partitioning (e.g. see [84, 89, 102]), RNA and DNA compaction inside capsids [120, 121] or neutral aggregates (e.g. vesicles) for gene delivery [17–19], as well as the induction of polyelectrolyte endocytosis due to electrostatic interactions. As to the first two topics, which have been in depth studied, a qualitative to semi–quantitative understanding of the rela-

*This chapter has been adapted from: Tagliabue, A., Izzo L., Mella M., Impact of Charge Correlation, Chain Rigidity, and Chemical Specific Interactions on the Behavior of Weak Polyelectrolytes in Solution, *Journal of Chemical Physics B*, 123, 42, 8872–8888 (2019).

tionship between parameters defining the systems (polymer stiffness, cavity size, polyelectrolyte and capsids charge densities, and counterions or background salt ions valence and concentration) with the spontaneity (or lack) of encapsulation/-confinement has now been reached [17,113–115,118,120,121]. In the specific case of strong polyelectrolytes, reaching the latter situation has led to unravel details such as the average size of the polyelectrolyte, its location and conformation inside the confining region, as well as the amount of ions condensed on the chain [18]. Compared to the case of neutral polymers or strong polyelectrolytes, the impact of confinement onto structural and energetic properties of weak polyelectrolytes has been, instead, much less investigated despite, for instance, their applicability as pH-responsive drug delivery systems. The limited amount of information available for this topic thus appears as a gap in need of fulfillment.

As far as we are aware, molecular theories have so far been applied to investigate or rationalize the impact of confinement and chain crowding on pH-responsiveness of ionic conduction inside nano-channels decorated with weak polyelectrolyte brushes [122–125]. More recently, Monte Carlo (MC) simulations have been used to explore how ionization, conformation and chain Helmholtz energy depend on the mode (1D, 2D, or 3D) and degree of confinement [37], and the presence of chemically specific interactions between charged and neutral ionizable groups [12]. The latter study suggested a marked impact on linear chain ionization of confinement inside spherical cavities (SC) due to, either, the smaller average distance between charged monomers compared to a free chain, and to a higher probability of forming neutral-charged monomer contacts when charged hydrogen bonds (c-H-bonds) were possible. These interactions, and the change in total ionization, translated into a lowering of the Helmholtz energy change associated to confining a chain inside a SC of radius R_{SC} at a given pH, $\Delta_{\mathrm{conf}} A(\mathrm{pH}, R_{\mathrm{SC}})$, compared to the case of fixed ionization degree (i.e., strong polyelectrolytes); it was thus possible to find a pH value at which the confinement was thermodynamically less disadvantageous than in the case of neutral chains.

Thanks to improved synthetic approaches, it has nowadays become possible to generate weak polyelectrolytes with structures differing from the standard linear one such as tree–like [26,27,48–51], star–like [52–54] or brushes. The change in geometrical disposition and, hence, in local density of ionizable monomers

compared to linear species should obviously impact on the electrolytic properties of macromolecules, so that the behavior with respect to global or local ionization [126], conformations in solution, thermodynamics of confinement, as well as the relative distribution of ions and ionized polymers may be markedly affected, as it neatly emerges titrating star–like poly(acrylic acid) (PAA) [52], poly(dimethylamino ethyl methacrylate) (PDMAEMA) [53], and poly(diethyl amino ethyl methacrylate) (PDEAEMA) [54]. For instance, the osmotic coefficient in the mentioned cases suggests that the amount of counterions acting as independent entities markedly decreases upon increasing the number of arms in the star–like polymer. If such dependency on the number of arms was correlated to the local density of ionized monomers, also confined species may show some dependency of the fraction of condensed counterions on the size of the confining cavity [18] if counterions escape is allowed (such as, for example, in capsids).

Following the widespread interest on the properties of confined neutral and ionized chains, this work extends our previous effort [37] in modeling confined polyelectrolytes to branched species. We do so with the intent of gauging the impact of confinement on the ionization behavior, especially with respect to the degree of branching, as well as the impact of the degree of ionization on the change in Helmholtz energy associated with polymer encapsulation. Improving on the modeling approach employed previously, we explicitly included the presence of counterions in our stochastic titration simulations to better mimic experiments [52,126]. Polyelectrolytes are therefore contained in a cavity permeable to explicitly treated pH-defining or neutralization deriving ions; this choice, more general than enclosing all particles inside the same cavity, allows us to seamlessly connect investigations dealing exclusively either with neutral chains or strong polyelectrolytes in capsids. As a byproduct of our modeling choice, the Donnan equilibrium of counterions is also monitored to highlight possible differences in counterion partitioning between the region occupied by the chain and the ones that are not as a function of polyelectrolytes characteristics. Thus, our effort adds new information to previous attempts of modeling star–like weak polyelectrolytes that include the application of SCF–type theories [127] to investigate conformational behavior as a function of the ionization degree, the testing of such theories against Monte Carlo titration data with explicit counterions, the use of free energy functional based molecular theories [128], and MC simulations

of hydrophobic star polyelectrolytes with [129] or without [130] explicit treatment of counterions. In latter studies, sequences of monomers with lower than average ionization are also seen at intermediate pH.

We also wish to investigate how the increase in local monomer density due to the star-like nature of the polyelectrolyte may impact on the ionization degree when c-H-bonds can form. In fact, the latter have been invoked, e.g., to rationalize the higher charge density found of plaques composed by water-insoluble copolymers [26, 27] (containing DMAEMA and methylmethacrylate, MMA, as co–monomers), and found to increase ionization of linear chains up to 2 orders of magnitude at pH$<$ pK_a [12]. As this consequence derives from a different behavior of monomers chemical potential with respect to the ionization degree compared to chains unable to form c-H-bonds, we shall compute the Helmholtz energy of absorbed chains as a function of pH$-$pK_a and exploit it to discuss how ionization impacts on the escape of a weak polyelectrolyte from a SC.

Of relevance for the latter issues, we mention the work by Szleifer and coworkers [131, 132], where the impact on conformations of nanoparticle carrying tethered poly-carboxylic acids due to Ca^{2+} ion coordination, as a function of both pH and nanoparticle curvature radius, was studied. The 1:2 Ca^{2+}–carboxylates coordination is, *de facto*, akin to the model discussed above involving formation of c-H-bonds, albeit it deviates from the latter in terms of the Gibbs energy change due to species association and for the monotonic increase in the number of coordination sites upon increasing pH.*

This chapter is organized as follows. Section 3.2 provides the details of our modeling approach, highlighting similarities and differences with Mella et al. previous works [12,37]. Section 3.3 presents results of our numerical simulations; to facilitate the description and the discussion of the results, the latter Section is divided in Subsections, each describing one of the aims stated previously. We draw our conclusion in Section 3.4; there, where we also widen our discussion to extend the relevance of our results. Finally, in Appendices 3.5 and 3.6 we present additional results.

*Ca^{2+} and –COO^- complexation releases roughly -3.8 kcal/mol, whereas c-H-bond formation frees roughly -2 kcal/mol. Also, one expects a monotonic increase in the number of Ca^{2+} coordination sites upon increasing the pH, whereas the number of possible c-H-bonds is instead a convex function of pH $-$ pK_a [12]

Abbreviation	Meaning
MC	Monte Carlo
SC	Spherical cavity
c-H-bond	Charged hydrogen bond
CI	Counterion
MB	Many-body

Table 3.1: List of abbreviations commonly used in this chapter

3.2 Methods and model

Our system consists of a spherical cavity (SC, or capsid) of radius R_{SC}, inside which a single weak polyelectrolyte chain is confined. The latter is composed of a neutral central monomer (or nucleus, C) and N_{arm} linear chains (or arms) tethered to it. Each arm is, in turn, composed by L weakly acidic monomers (beads). The number of total monomers, nucleus included, is thus $N_{\mathrm{mono}} = LN_{\mathrm{arm}} + 1$. Chain confinement inside the SC is simulated via hard walls, the confining potential given by

$$U_{\mathrm{caps}}(r_i) = \begin{cases} 0 & \text{if } r_i < R_{\mathrm{SC}} \\ +\infty & \text{if } r_i \geq R_{\mathrm{SC}}, \end{cases} \tag{3.1}$$

where r_i is the distance of the i-th monomer from the centre of the sphere.

Beads in each arm are connected via a harmonic stretching potential (see Equation 2.4), using the following parameters: $k_{\mathrm{bond}} = 200 k_{\mathrm{B}}T/\text{Å}$, where $k_{\mathrm{B}}T = 0.6616$ kcal/mol (that corresponds to $1.0544{\cdot}10^{-3}$ Hartree and $T \simeq 333$ K), and $\sigma = 3.85$ Å. The nucleus and the first monomer of each arm are connected with a similar interaction potential using, however, $\sigma_C = 2\sigma$ instead of σ, so that a larger excluded volume is attributed to the central core. A harmonic bending potential may also be added to confer rigidity to the polymer (see Equation 2.6), with an equilibrium angle $\theta_0 = 150°$ and an angular force constant $k_{\mathrm{ang}} \equiv k_{\mathrm{bend}} = 2 \cdot 10^{-3} k_{\mathrm{B}}T/\mathrm{deg}^2$. We refer to the latter species as "semi-rigid", whereas when no angular potential is present polyelectrolytes will be tagged as "(infinitely) flexible". No bending potential is applied to the monomers directly bonded to the nucleus, in order to allow them to find the better spatial arrangement as a function of N_{arm} and the other system parameters.

As mentioned, each monomer except the central one is treated as a weak acid; the latter property is simulated via the constant-pH method (see Section 2.2.2). A positive monovalent counterion (CI) is inserted (removed) each time a monomer dissociates (is neutralized). CIs may not be confined into the SC limiting the chain movement, i.e. $U_{\text{caps}}(r_i) = 0 \ \forall r_i$, i being a CI; this choice is made to mimic a SC inside which a polymer (and its CIs) may absorb from the surrounding space, as it happens in nature when DNA enters capsids.

However, in order to implicitly define monomer (and, consequently, CI and chain) concentration, all particles are enclosed in a spherical simulation cell with a radius $R_{\text{cell}} \equiv R_{\text{ext}}$ as in the standard cell model (see Section 2.1.2).

All charged particles in the system interact with each others via a pairwise Coulomb potential (see Equation 2.7); the solvent is treated as an unpolarizable dielectric continuum with a relative permittivity $\varepsilon_r = 78.3$ (i.e., roughly the one of water).

All N_{tot} particles in the system are treated as soft spheres; so, a WCA potential (see Equation 2.3) is implemented to simulate monomers' and CIs' excluded volume in order to avoid polymer entanglement and particles overlap. The "depth" of the WCA potential is $\epsilon = k_{\text{B}}T$. When the nucleus is involved, σ_C is used instead of σ.

Finally, in order to simulate the impact of c-H-bonds on polyelectrolyte behavior, we also employed a a many-body (MB) interaction potential previously introduced [12, 37] (see Section 2.1.1.5). Parameters defining these interactions are the cutoff radius ($r_{\text{MB}} = 5$ Å) below which charged and neutral monomers are considered to be interacting, the strength of the stabilizing interaction potential per interacting pair ($\xi = 2$ kcal/mol) and the maximum number of pair interactions that a neutral and a charged monomer can form ($n_{\text{MB}}^{(\text{n})}$ and $n_{\text{MB}}^{(\text{c})}$, respectively). In the present work, we have chosen $n_{\text{MB}}^{(\text{c})} = 2$, so to allow, e.g., the acceptance of two c-H-bonds by $-\text{COO}^-$, and either $n_{\text{MB}}^{(\text{n})} = \infty$, as previously employed, or 1, in order to investigate the impact of such parameter on the acid-base and energetic properties. Results obtained setting $n_{\text{MB}}^{(\text{n})} = 1$ are shown in the Appendix3.6.

Our simulations are performed via a classical MC approach, sampling the semi-grand canonical thermal density matrix of the system as function of the control variable pH - pK_a; the latter is a convenient proxy to control proton

chemical potential in solution (see Section 2.2.2). Monomers and counterions are displaced randomly along three orthogonal directions with a maximum attempted step, and the displacement is accepted using the classical Metropolis-Hastings rule (see Equation 2.30). In order to converge to thermal equilibrium more rapidly and to more efficiently explore the system potential energy surface, a series of cluster moves are also attempted (see Section 2.2.1.4); these are: (i) entire polyelectrolyte translations, and (ii) pivot moves. In the end, each Monte Carlo step consists of the attempted translation of each particle in the system, one attempt to change the charge state of a monomer, one rigid chain translation and one pivot move.

Changes in polyelectrolyte properties as a function of pH, R_{SC}, and chain stiffness ($k_{\mathrm{bend}} = 0$ or $2 \cdot 10^{-3} k_{\mathrm{B}}T/\mathrm{deg}^2 = 2.1088 \times 10^{-6}$ a.u. [133]) have been investigated employing a coarse grained polymer model containing, mainly, $LN_{\mathrm{arm}} = 120$ monovalent ionizable monomers and a centrally located neutral core. The SC radius R_{SC} spanned the range 21 Å $\leq R_{\mathrm{SC}} \leq$ 66 Å; as the repulsion between neutral monomers starts at an inter-monomer distance of 3.85 Å, the polymer volume fraction ϕ inside the SC spans the range $2.1 \times 10^{-4} \leq \phi \leq 6.2 \times 10^{-3}$. $R_{\mathrm{ext}} = 106$ Å unless otherwise specified. To investigate the impact of topology [52, 53], species with $N_{\mathrm{arm}} = 2$ and 8 were simulated. Also noteworthy, the species with $N_{\mathrm{arm}} = 8$ (henceforth "star–like", $L = 15$) fits within the widest SC ($R_{\mathrm{SC}} = 66$ Å) even when completely ionized.

3.2.1 Changes in Helmholtz energy due to confinement

As discussed in the past [37,84–87,91,104,105,118,119,134,135], a certain amount of reversible work is needed to confine a polymer inside a cavity due to the reduction of its configurational entropy. In case of a weak polyelectrolyte, such energetic penalty depends on both polymer structure itself and environment pH, as the latter influences its angular rigidity and the amount of condensed CIs. We previously characterized the effects due to ionization [37] via the quantity

$$I_{\xi^*}(\mathrm{pH}^*, R_{\mathrm{SC}}) = A_{\xi^*}(\mathrm{pH}^*, R_{\mathrm{SC}}) - A_{\xi^*}(\mathrm{pH}^*, \infty) \tag{3.2}$$

where A_{ξ^*} is the change in Helmholtz energy of a polyacidic chain with $\xi^* = \xi$ and confined inside a SC of radius R_{SC} upon increasing the pH from a value much lower than $\mathrm{p}K_a$ to pH*; the latter is computed exploiting Equation 2.35.

Whereas $I_{\xi^*}(\mathrm{pH}^*, R_{\mathrm{SC}})$ ($\equiv I$ in order to simplify the notation) was, unsurprisingly, always found positive when $\xi = 0$ and in the absence of CIs [37], it assumed negative values at low α when $\xi = 2$ kcal/mol thanks to the stabilization arising from c-H-bonds. As absence of CIs could have biased the estimated magnitude of the effect [37] even for $\xi = 0$, it seems worth recomputing I with a more realistic model and to explore it for also star-shaped polymers.

I is also of direct relevance if one wishes to discuss the statistical aspects of polymer escape from a narrow hole in the SC when such latter process is dominated by thermodynamics forces ensuing from a marked drop in Helmholtz energy during translocation [136]. In the latter case, the average escape time is proportional to $LN_{\mathrm{arm}}/\Delta\mu$, where $\Delta\mu$ is chemical potential gradient for monomers between absorbed and free states. This can be modified by ionizing the polymer in consequence of Coulomb repulsion, polymer stiffening, and formation of c-H-bonds [37]. As I gauges the excess Helmholtz energy due to chain ionization inside the SC compared to the free state taking as a reference a neutral chain with the same characteristics, it directly provides indications on how $\Delta\mu$ is modulated by the pH. Previous work by Mella and Izzo [37] suggested that, firstly, the drop in Helmholtz energy for a ionized chain upon escaping the confinement may be up to four times larger than for the neutral counterpart and, secondly, that c-H-bonds may, instead, reduce it.

With respect to the actual method for gauging I, we point out that estimating the term $A(\mathrm{pH}^*, \infty)$ in Equation 3.2 does not necessitate using SC with $R_{\mathrm{SC}} = \infty$; it would be adequate, in fact, that the SC is sufficiently wide to limit its influence on the titration curve. For this reason, and anticipating that increasing R_{SC} from 53 to 66 Å would only weakly impact on α even for the longer $N_{\mathrm{arm}} = 2$ species, we investigate the mentioned aspect approximating $I_{\xi^*}(\mathrm{pH}^*, R_{\mathrm{SC}})$ with $I_{\xi^*}(\mathrm{pH}^*, 66\ \text{Å}) \simeq A_{\xi^*}(\mathrm{pH}^*, R_{\mathrm{SC}}) - A_{\xi^*}(\mathrm{pH}^*, 66\ \text{Å})$. Notice that such approximation is expected to slightly underestimate the absolute value of I, as some residual interaction between monomers may still be present when $R_{\mathrm{SC}} = 66$ Å instead than $R_{\mathrm{SC}} = \infty$. It is also important to point out that we approximated the values of α in Equation 2.35 when $\mathrm{pH} - \mathrm{p}K_a < -3.5$ with an exponential function interpolating the two values computed at $\mathrm{pH} - \mathrm{p}K_a = -3.5$ and 3.0, a range of pH where the behavior of the ionization degree closely follow a straight line.

In this work, we also computed the energy difference

$$J(\mathrm{pH}^*, R_{\mathrm{SC}}) = A_{\xi=2}(\mathrm{pH}^*, R_{\mathrm{SC}}) - A_{\xi=0}(\mathrm{pH}^*, R_{\mathrm{SC}}), \tag{3.3}$$

which, at chosen pH^* and R_{SC}, differs from zero only due to the possible formation of c-H-bonds and thus contributes to define the ratio between the partition constants of polymers able or not to give rise to such interactions.

3.3 Results and discussion

Before starting the discussion, let us point out that the number of samples collected to estimate physical quantities for the systems investigated was sufficiently large to obtain a statistical accuracy of, at least, 1 part for thousands; we thus avoid to show statistical errors completely.

3.3.1 Titration curves

The behavior of $\Delta \mathrm{p}K_a = \mathrm{p}K_a^{\mathrm{poly}}(\alpha) - \mathrm{p}K_a^{\mathrm{id}}$, where $\alpha \equiv \langle\alpha\rangle$ for flexible and semi-rigid linear species (i.e., $N_{\mathrm{arm}} = 2$) is presented in Figure 3.1. When c-H-bonds cannot form ($\xi = 0$, upper panel of Figure 3.1), $\Delta \mathrm{p}K_a$ monotonically increases upon increasing α due to the increasingly higher electrostatic repulsion felt by a newly dissociated monomer. For the same reason, $\Delta \mathrm{p}K_a$ monotonically increases upon reducing R_{SC} due to a decrease in the average distance between monomers. Notice, however, that going from $R_{\mathrm{SC}} = 53$ Å to 66 Å impacts only weakly on α (see Figure 3.2) and, hence, on $\Delta \mathrm{p}K_a$; this evidence suggests that a cavity with $R_{\mathrm{SC}} = 66$ Å is already sufficiently wide so that it may be tentatively employed as if it represented the case with $R_{\mathrm{SC}} = \infty$ in Equation 3.2.

Comparing flexible and semi-rigid cases at a chosen SC width, one notices that the latter always present a lower value of $\Delta \mathrm{p}K_a$ than the former, a finding due to the larger average distance between monomers in stiffer chains [37] imposed by the angular potential.[†] Apart from increasing the average arm extension $\langle r_{1\mathrm{N}}\rangle$, the bending potential reduces the entropy associated with the intra-chain

[†]As an example, we report that a neutral (i.e., when $\mathrm{pH} \ll \mathrm{p}K_a$) linear semi-rigid chain composed by $L = 15$ monomers increases its average "end-to-end" (or arm average extension, $\langle r_{1N}\rangle$, see Equation 2.13) distance from 22.7 to 31.5 Å upon increasing k_{ang} from 0 to $2 \cdot 10^{-3} k_{\mathrm{B}}T/\mathrm{deg}^2$.

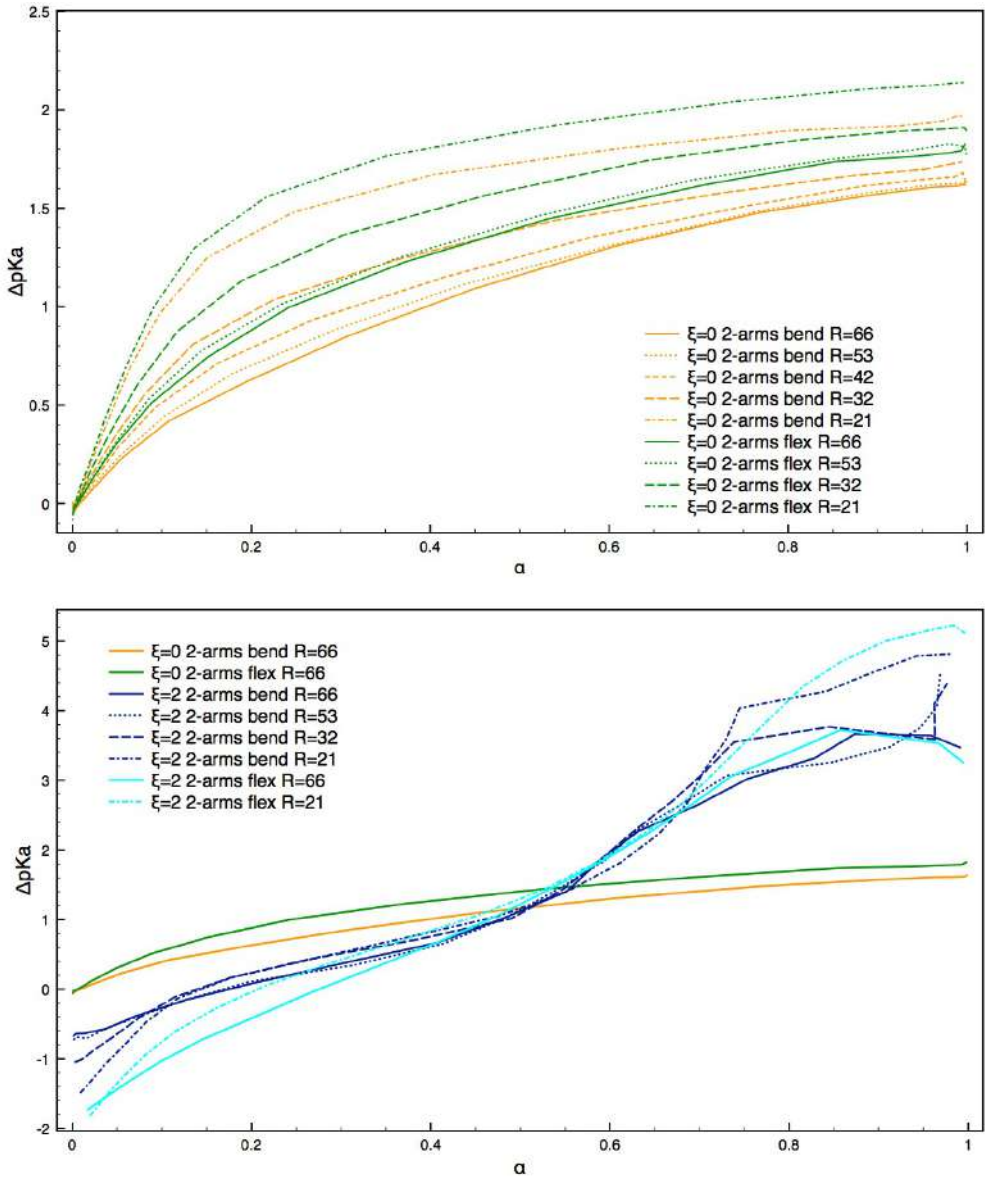

Figure 3.1: $\Delta \mathrm{p}K_a$ versus ionization degree α for semi-rigid ("bend") and flexible weak polyelectrolytes with $N_{\mathrm{arm}} = 2$ for various values of $R = R_{\mathrm{SC}}/\text{Å} \in \{21, 32, 42, 53, 66\}$; $\xi = 0$ (upper panel) or 2 kcal/mol (lower panel).

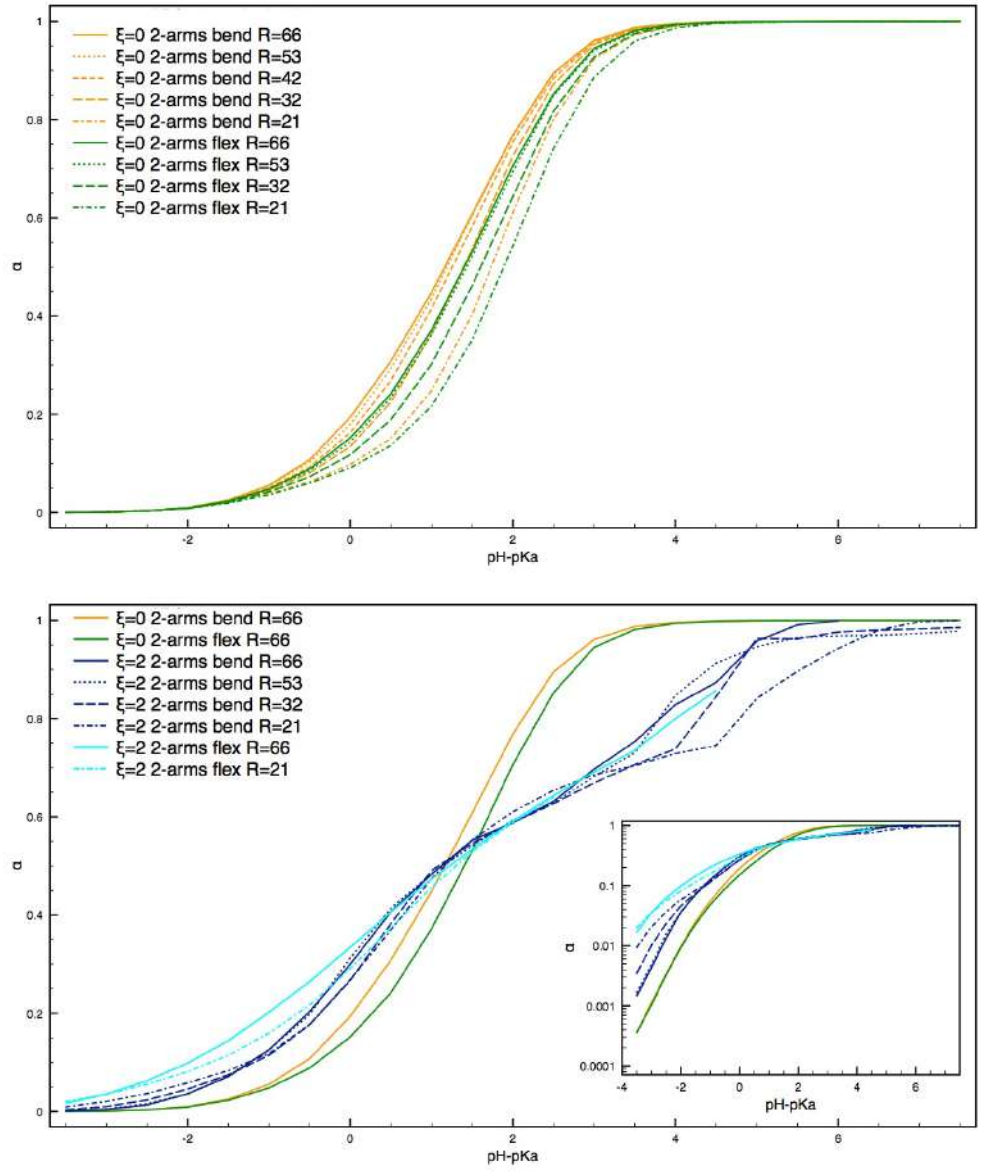

Figure 3.2: α as a function of pH - pK_a for semi-rigid ("bend") and flexible weak polyelectrolytes with $N_{\mathrm{arm}} = 2$ ("2-arms") for various values of $R = R_{\mathrm{SC}}/\text{Å} \in \{21, 32, 42, 53, 66\}$; $\xi = 0$ (upper panel) or 2 kcal/mol (lower panel).

distribution of monomers, so that the entropic penalty to be paid due to the "Coulomb-induced linearization" upon further ionization is lowered. As for a direct comparison with available experiments, we notice that results reported in Figure 3.1 underestimate the shift in pK_a seen in the titration of PMAA [137] ($\Delta pK_a = 2$) and PDMAEMA [53, 138] ($\Delta pK_a = 2.19$). Given both the coarse-grained nature of our model and the continuum dielectric representation of water (see, e.g., References [139, 140]), such underestimation ought to be expected.

Turning to the case of linear chains able to form c-H-bonds ($\xi = 2$ kcal/mol, $n_{\mathrm{MB}}^{(\mathrm{n})} = \infty$; see lower panel of Figure 3.1, and see Figure 3.2), the impact of the latter on α and ΔpK_a is clearly apparent. In general, c-H-bonds increase chain ionization by decreasing pK_a^{poly} over the lower ionization range ($\alpha \lesssim 0.45$) compared to the $\xi = 0$ case, whereas pK_a^{poly} increases in the remaining range of α values. Notice that this behavior is quite general and independent of the SC radius. Moreover, the *negative* ΔpK_a values obtained when $\alpha \lesssim 0.15$ indicate that the polyelectrolyte ionizes more than in the ideal case; clearly, the decrease of ΔpK_a by up to 2 pK_a units contradicts general expectations with respect to charge regulation. This deviation becomes even starker if one considers the low α behavior shown by ΔpK_a as a function of R_{SC}: in this case, we notice an increase in monomer acidity upon decreasing R_{SC}, a phenomenon once again attributable to an increase in the probability of contact between ionized and neutral monomers [37]. Finally, we mention that the somewhat erratic behavior of ΔpK_a values for $\alpha > 0.7$ can be due to a rougher energy landscape induced by c-H-bonds themselves.

The behavior of ΔpK_a versus α for a polyelectrolyte with $N_{\mathrm{arm}} = 8$ is presented in Figure 3.3 (see also Figure 3.4, which presents the behavior of α as a function of pH - pK_a). Overall, it follows what previously discussed for linear species upon reducing R_{SC} or increasing rigidity, even though one notices a slower increase in ionization for the 8-arms species with $\xi = 0$ kcal/mol species previously indicated in the literature by both computational [127, 130] and experimental [52, 53] studies. Our models predict a $\Delta pK_a(\alpha = 0.5)$ between $\mathrm{N_{arm}} = 2$ and 8 of 0.09 and 0.12 for, respectively, flexible and semi-rigid species, whereas the experimental titration suggest a change in the same property of roughly 0.3 for PAA [52] and 0.2 for PDMAEMA [53]. Thus, while our model correctly predict the qualitative change in pK_a, it slightly underestimates the measured quanti-

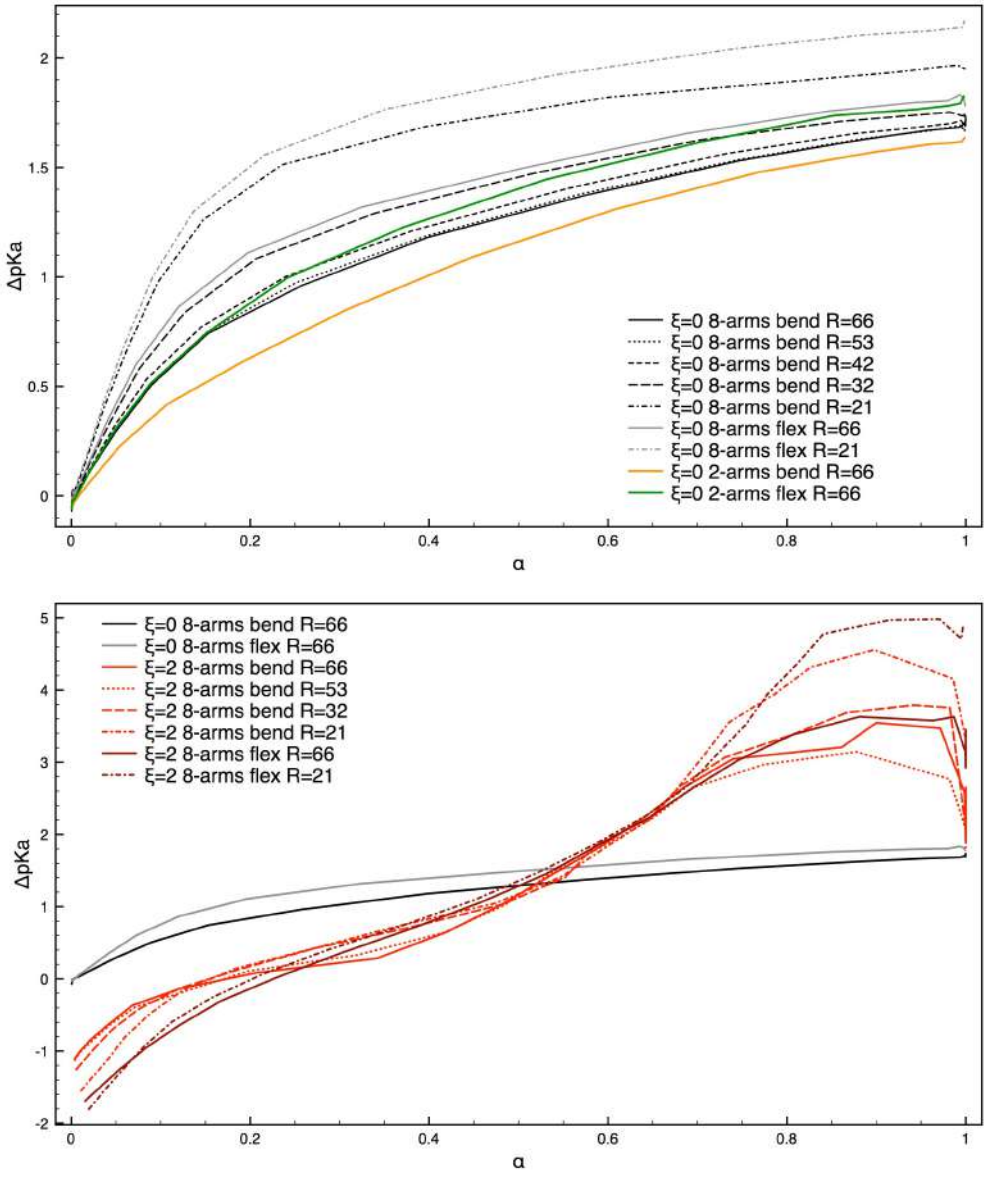

Figure 3.3: $\Delta \mathrm{p}K_a$ versus ionization degree α for semi-rigid ("bend") and flexible weak polyelectrolytes with $N_{\mathrm{arm}} = 2$ for various values of $R = R_{\mathrm{SC}}/\text{Å} \in \{21, 32, 42, 53, 66\}$; $\xi = 0$ (upper panel) or 2 kcal/mol (lower panel).

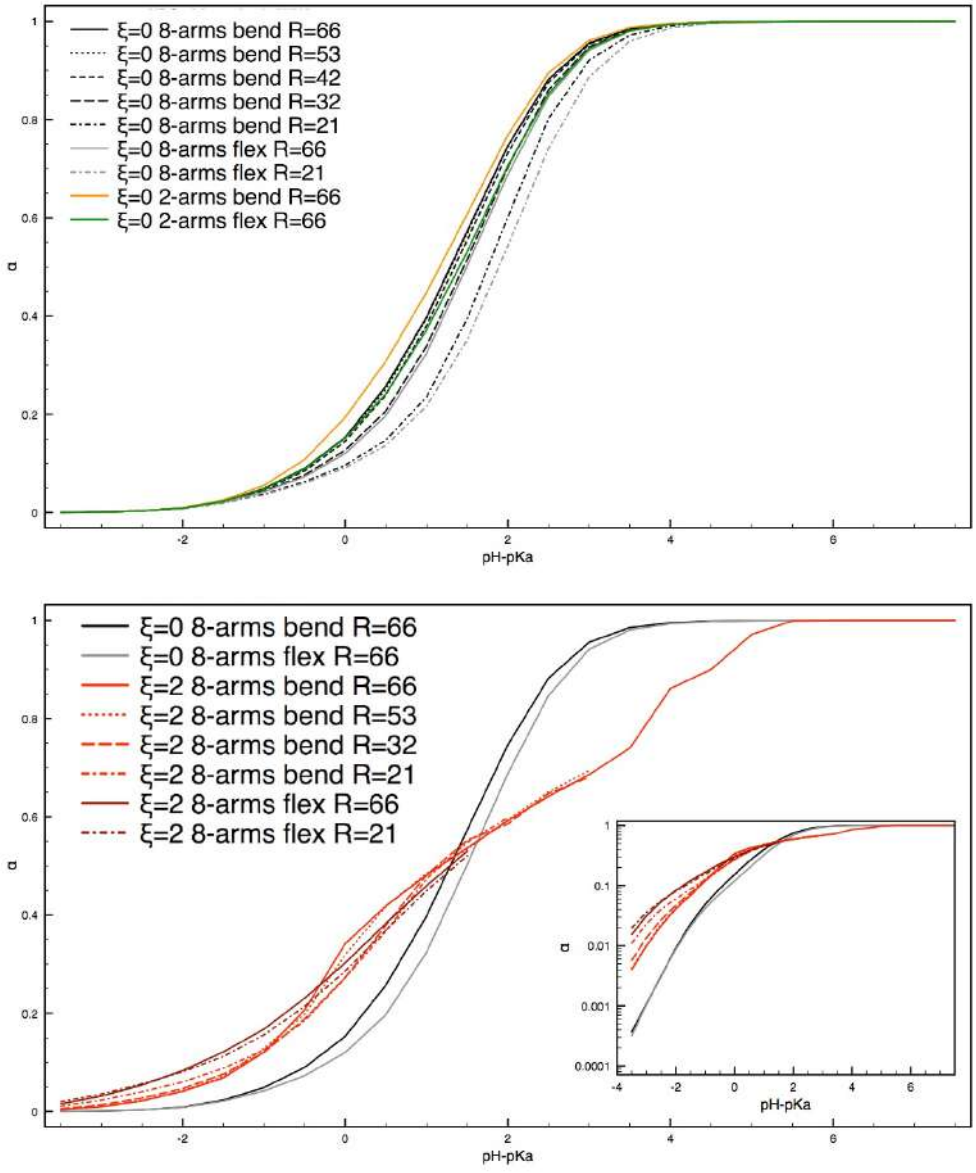

Figure 3.4: α as a function of pH - p$K_a$for semi-rigid ("bend") and flexible weak polyelectrolytes with $N_{\rm arm} = 8$ for various values of $R = R_{\rm SC}/\text{Å} \in \{21, 32, 42, 53, 66\}$; $\xi = 0$ (upper panel) or 2 kcal/mol (lower panel).

ties. Obviously, the model could be brought into better agreement by properly tuning parameters defining the chain potential such as the equilibrium distance of connected monomers or their radii. Considering, however, that a discrepancy of 0.1 units of pK_a is equivalent to an error of only $\sim 0.2RT$ in terms of the Helmholtz energy, such refinement appears unwarranted to us at this moment. Also noteworthy, it is the fact that ΔpK_a at low α is slightly more negative than for 2-arms species when $\xi = 2$ kcal/mol, an effect most likely due to the higher density of monomers around the core and that extends the range of negative ΔpK_a by 0.05 units, at least.

3.3.2 Ionization along the chain contour

ΔpK_a values (Figures 3.1 and 3.3) neatly demonstrated the influence of vicinal charges on the ionization when $\xi = 0$, even though these are quantities averaged over the whole polyelectrolyte. Single monomers may, instead, behave somewhat differently depending on their location along arms/chains due to the difference in local electrostatic potential [141–143]. That this is the case, it has already been shown by previous SCF [127] and MC [130] investigations on both linear and star-like species; these have suggested that chain ends are more ionized than monomers located around chain midpoint (or attached to the central branching point in star–like polyelectrolytes). Here, we investigate the impact of confinement and c-H-bonds on such behavior by analyzing ionization profiles along arms.

Figure 3.5 shows the average charge $\langle q(i) \rangle$ carried by monomers as a function of their location i along an arm ($i = 1$ identify monomers directly tethered to the nucleus) for 2-arms polyelectrolytes. The $\xi = 0$ case (upper panel) conforms with expectations, with monomers close to chain extremes (or bound to the nucleus, as this is assumed to have $\epsilon_r = 78.3$ due to a limit of our model description) being more dissociated. Interestingly, arm midpoint monomers may not necessarily be the least ionized (see, e.g., the $R_{\mathrm{SC}} = 21$ Å case), a finding probably due to the local (conformational-dependent) nature of the electrostatic potential felt by each monomer, which modulates the chemical potential of charged beads. Our narrowest SC is *de facto* fairly crowded and it may induce the "locking" of a specific conformation as soon as the stiffness of the polyelectrolyte is sufficiently high due to intra-chain repulsion. This observation notwithstanding, one may apply

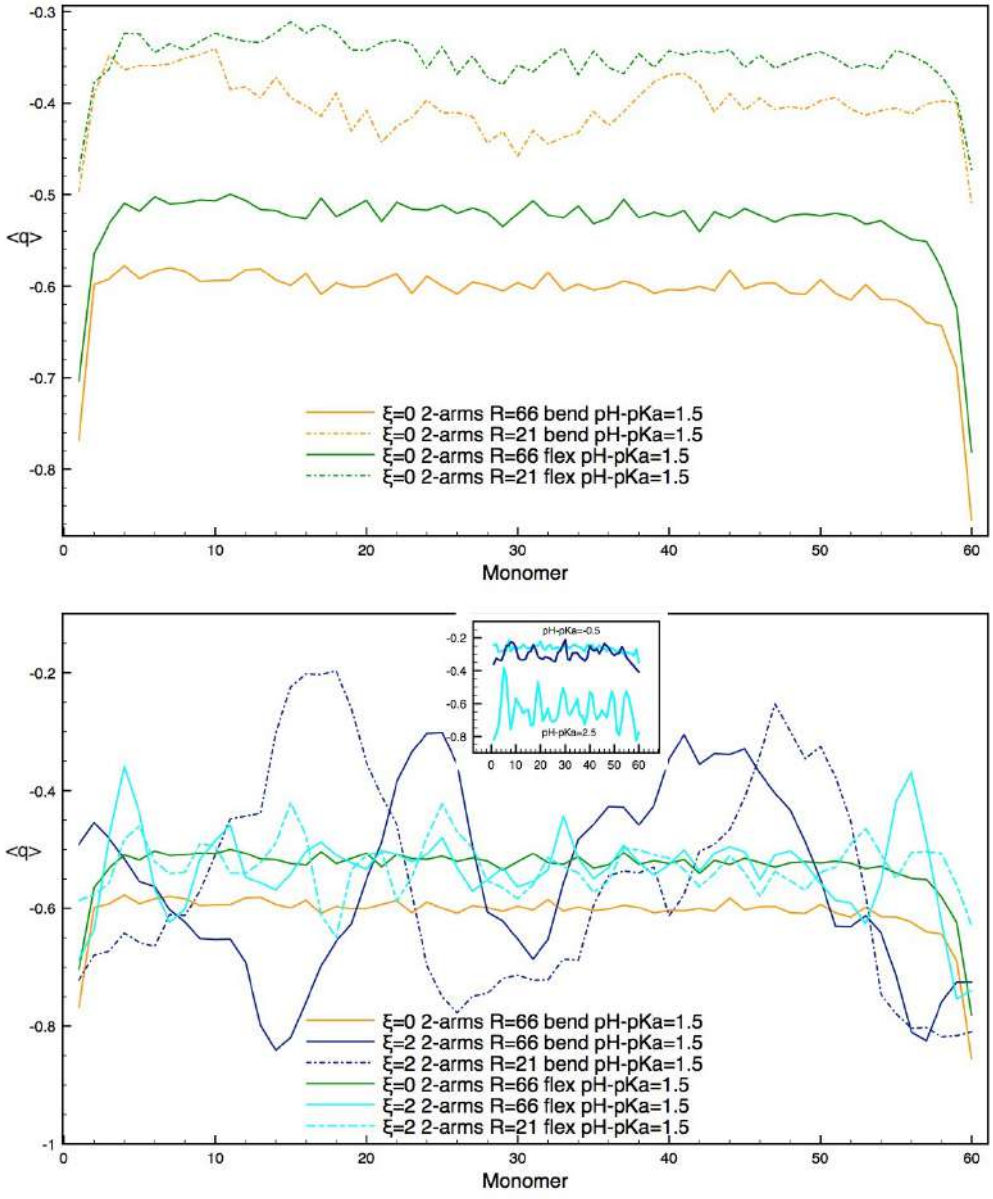

Figure 3.5: Average charge $\langle q(i) \rangle$ as a function of the monomer position i along the arms ($i = 1$ indicates the monomer tethered to the nucleus) for semi-rigid ("bend") and flexible 2-arms weak polyelectrolytes. $R = R_{\mathrm{SC}}/\text{Å} \in \{21, 66\}$; $\xi = 0$ (upper panel) or 2 kcal/mol (lower panel).

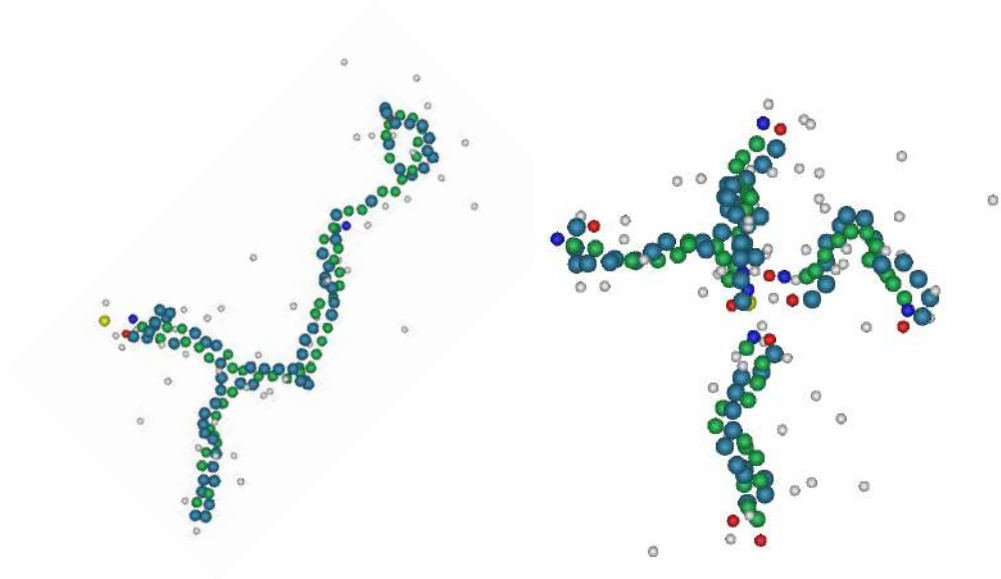

Figure 3.6: Conformations of a 2-arms (left) and 8-arms (right) semi-rigid polyelectrolyte with $\xi = 2$ kcal/mol confined inside a SC of radius $R_{\mathrm{SC}} = 66$ Å at pH $-$ p$K_a = 1.5$ ($\alpha \simeq 0.55$). Notice the "hairpin" formed by one of the arms with a loop composed of only three monomers in the 2-arms polyelectrolyte, as well as the 3/5 ratio between neutral/ionized peripheral monomers in the 8-arms species. Color scheme: neutral monomers in cyan (in blue if terminal or tethered), ionized monomers in green (in red if terminal or tethered), nucleus in yellow, CIs in light gray.

the Henderson–Hasselbalch equation (Equation 2.22) to the results reported in Figure 3.5 estimating the difference in $\mathrm{p}K_a^{\mathrm{poly}}(i)$ between the terminal and medial monomers, which turns out to be roughly 0.6 and 0.5 units, respectively, for the semi-rigid and flexible species confined into a SC with $R_{\mathrm{SC}} = 66$ Å; it is, instead, somewhat lower inside the smaller SC.

The behavior followed by $\langle q(i) \rangle$ (Figure 3.5, lower panel) becomes much less regular upon switching on MB interactions ($n_{\mathrm{MB}}^{(\mathrm{n})} = \infty$ and $n_{\mathrm{MB}}^{(\mathrm{c})} = 2$). In fact, we observe marked oscillations as a function of the monomer location and whose magnitude increases upon decreasing R_{SC}. This is particularly evident for the semi-rigid species at pH-p$K_a = 1.5$, but it becomes marked also for the flexible counterpart at a slightly higher pH (e.g., at pH - p$K_a = 2.5$; see inset in the lower panel of Figure 3.5). In fact, the oscillations of $\langle q(i) \rangle$ values become so wide that their minimum values are well below the ionization for the $\xi = 0$ case, suggesting that c-H-bonds may "depress" the ionization of specific monomers so to maximize their energetic effect; this requires neutral and ionized monomers to be close neighbors.

This conclusion is well supported by snapshots extracted from a simulation of a semi-rigid 2-arms polymer inside a SC with $R_{SC} = 66$ Å (Figure 3.6). There, the presence of short trains of undissociated monomers adjacent to streaks of ionized ones is evident and, together with the mathematical details of the model, makes clear that it may be difficult to neutralize a charged monomer surrounded by neutral ones, or to ionize a neutral monomer when this is forming a c-H-bond with an ionized one. Apart from the peculiar local ionization behavior, the impact of c-H-bonds extends also on the set of conformations assumed during the simulations, with Figure 3.6 evidencing the formation of a duplex structure formed by the two arms and interrupted by a hairpin with a loop composed of only three monomers. Such behavior is instead totally absent when $\xi = 0$ (*vide infra* Figure 3.8).

The upper panel Figure 3.7 provides $\langle q(i) \rangle$ trends for simulations involving 8-arms species with $\xi = 0$ kcal/mol; as expected, $\langle q(i) \rangle$ decreases upon reducing i, the only exception being seen for the tightly confined ($R_{SC} = 21$ Å) semi-rigid species (the latter presenting a minimum in ionization at $i = 7$). Comparing the local ionization trend for 8-arms species, which shows a continuously decreasing $\langle q(i) \rangle$ upon moving from the periphery to the star center when $R_{SC} = 66$ Å and a sudden increase in ionization of the distal monomer, with the much flatter behavior of $\langle q(i) \rangle$ for linear chains suggests that both inter- and intra-arms repulsion are at play in defining the local ionization state in star polyelectrolytes. This finding is somewhat at variance with what previously suggested, where the results were interpreted on the basis of a prevalence of inter-arms repulsion close to the core and intra-arms repulsion at the periphery of the star.

When $\xi = 2$ kcal/mol (lower panel of Figure 3.7), acidity of monomers closer to the nucleus increases; this is likely to be connected to a higher monomer density in the core vicinity, which increases the likelihood of forming c-H-bonds. Besides, the presence of such interactions induces fluctuations similar to what seen in Figure 3.5 also for semi-rigid star-like polyelectrolytes.

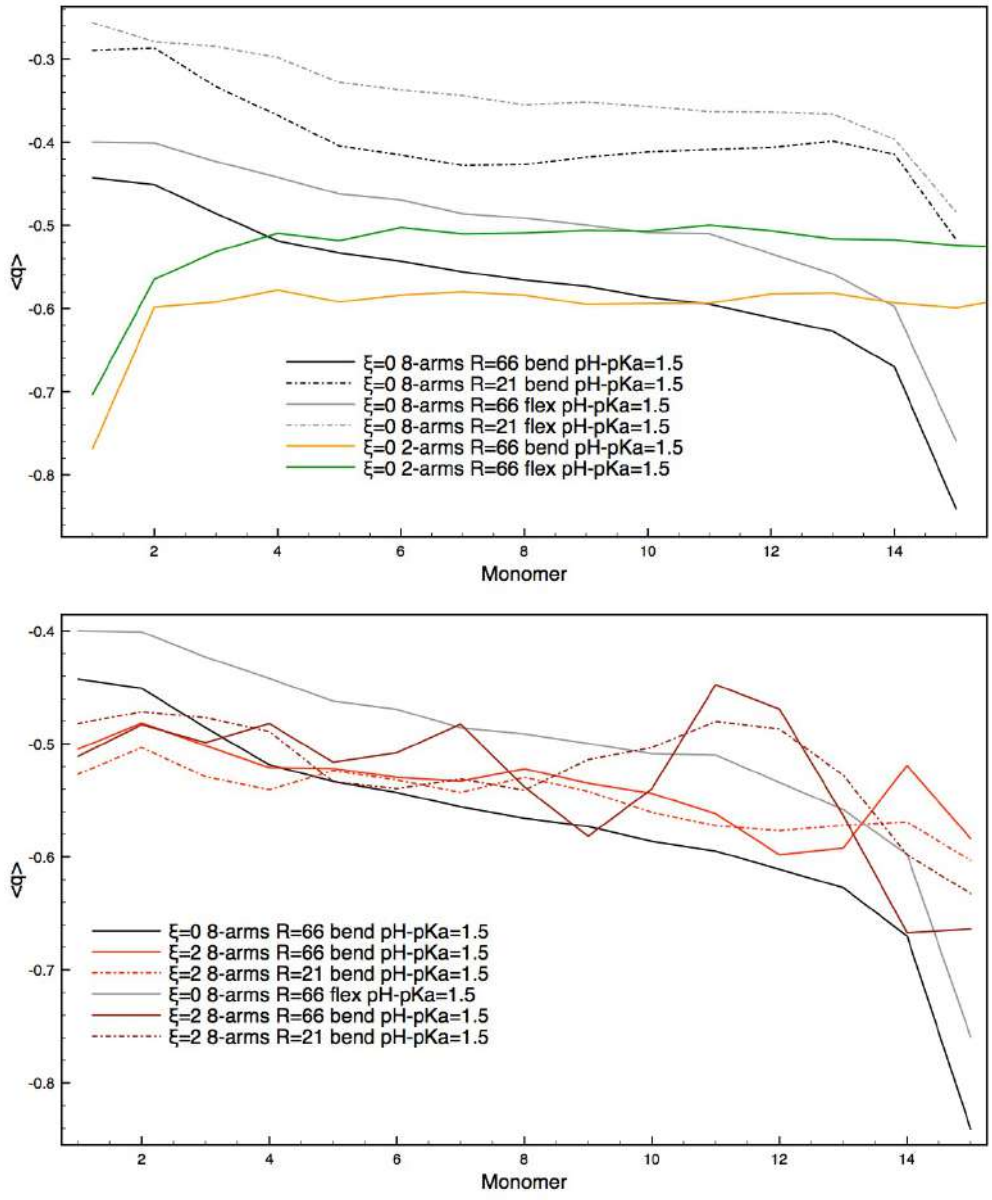

Figure 3.7: Average charge $\langle q(i) \rangle$ as a function of the monomer position i along the arms ($i = 1$ indicates the monomer tethered to the nucleus) for semi-rigid ("bend") and flexible 8-arms weak polyelectrolytes. $R = R_{SC}/\text{Å} \in \{21, 66\}$; $\xi = 0$ (upper panel) or 2 kcal/mol (lower panel).

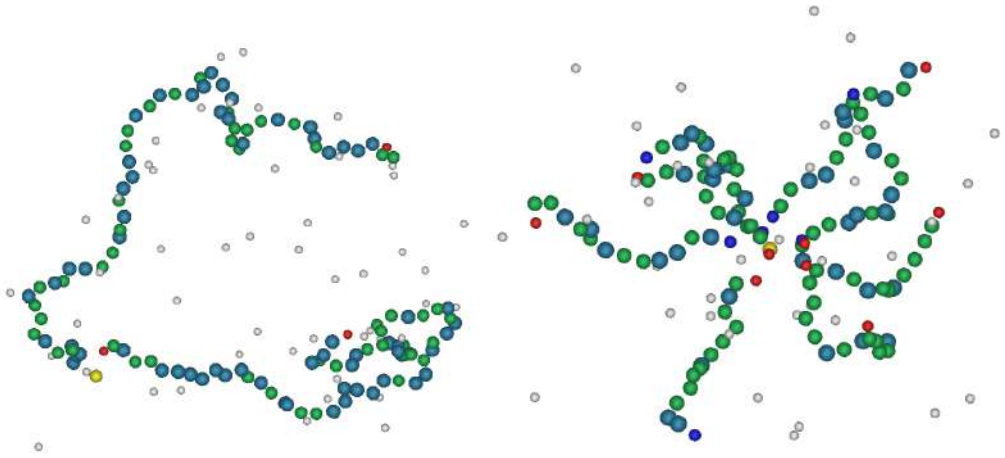

Figure 3.8: Conformations of a 2-arms (left) and 8-arms (right) semi-rigid polyelectrolyte with $\xi = 0$ kcal/mol confined inside a SC of radius $R_{\rm SC} = 66$ Å at pH $-$ p$K_a = 1.5$ ($\alpha \simeq 0.55$). The color scheme is the same as in Figure 3.6.

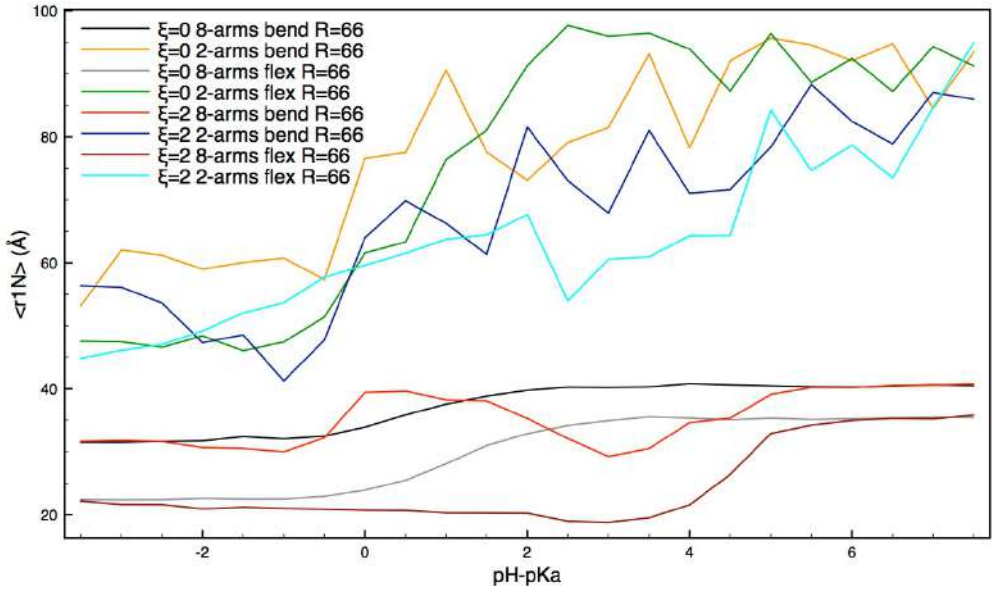

Figure 3.9: $\langle r_{1\rm N}\rangle$ distance as a function of pH $-$ pK_a for 2-arms and 8-arms species. Shown are data for semi-rigid ("bend") and flexible polymers contained into SC with $R = R_{\rm SC}/\text{Å} = 66$; $\xi = 0$ (upper panel) or 2 kcal/mol (lower panel).

3.3.3 Conformations, radial density profiles and counterions condensation

A comparison between the simulations snapshots shown in Figures 3.6 and 3.8 for both 2- and 8-arms polyelectrolytes suggests that the conformations sampled by the polymeric species depends not only on pH but also on the value attributed to ξ. With $\xi > 0$, *de facto*, the pH value controls both the ionization degree and the probability of forming c-H-bonds, their likelihood being a positive concave function of the pH itself, with the limiting value of zero when $\text{pH} \ll \text{p}K_a$ or $\text{pH} \gg \text{p}K_a$. In other terms, c-H-bond formation may induce deviations from, for instance, the commonly discussed monotonic polyelectrolyte swelling for both linear and star-shaped species [127, 131] as evidenced by Szleifer and co–workers [131, 132] as consequence of Ca^{2+}–mediated bridging between carboxylate groups, or in presence of hydrophobic forces [129, 130].

A non-monotonic behavior for the average arms extension[‡] $\langle r_{1N} \rangle$ for species with $\xi = 2$ kcal/mol is clearly seen in Figure 3.9, and it is particularly apparent for flexible species around $\text{pH} - \text{p}K_a = 3.0$. Albeit $\langle r_{1N} \rangle$ is a conformation–dependent quantity more difficult to converge compared to, e.g., the gyration radius (Equation 2.14), we discuss the former because it is less prone to be biased by the confinement into SC at low pH than the latter. In fact, we commonly found the core monomer located close to the cavity wall at low pH even for semi-rigid species; the net effect of such an arrangement is, obviously, to artificially shift the geometrical center of the polymer away from the star center so that species appears, in average, more compact than it would be if unconfined.

Similar results are also found for smaller SC, albeit the differences in behavior of $\langle r_{1N} \rangle$ versus pH are somewhat reduced by the tighter confinement. We also notice that the mechanism of shortening $\langle r_{1N} \rangle$ when $\xi = 2$ kcal/mol differs between flexible and semi-rigid species, as made apparent by Figure 3.10. Thus, each arm in a flexible species (left panel, Figure 3.10) coils up onto itself forming small clusters; couples of inter-wound arms are, instead, present in the case of semi-rigid species, with one arm in each couple (usually the one with the highest ionization) being back-bended (hence, shortened) on the other (less ionized).

[‡]The average arms extension for a star-shaped polymer is analogous to the end-to-end distance for a linear chain (see Equation 2.13); it represents the average distance between terminal monomers and monomer directly tethered to the central bead.

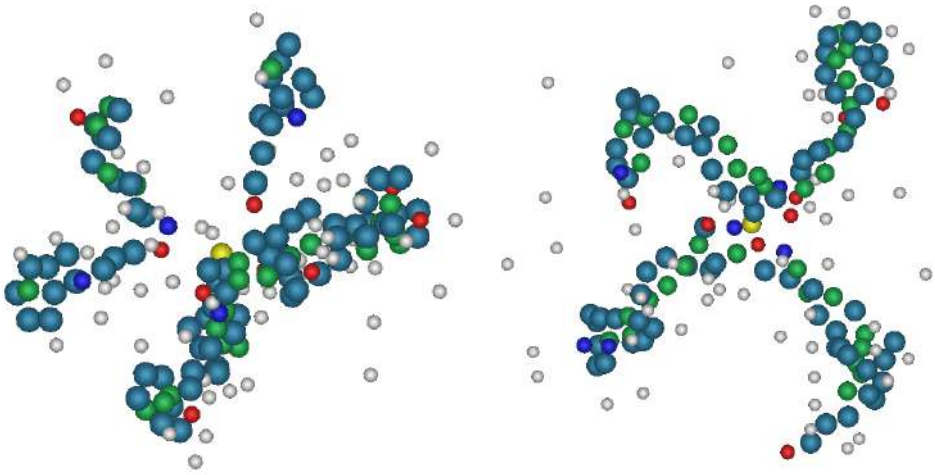

Figure 3.10: Simulation snapshots for flexible (left) and semi-rigid (right) 8-arms species able to form c-H-bonds at pH $-$ pK_a $= 3.0$ inside a SC with $R_{\mathrm{SC}} = 66$ Å. The color scheme is the same as in Figure 3.6.

Such structure maximizes the number of c-H-bonds formed.

The more compact conformations afforded by chains with $\xi = 2$ kcal/mol (compare Figures 3.6, 3.10, and 3.8), may *de facto* impact on the charge distribution inside the SC and, consequently, also on the quantity of counterions that may remain inside the SC to partially compensate for polyelectrolyte's charges. To gauge this behavior, we computed the average fraction of CIs present at a specific pH that are contained inside the SC despite its permeability. Such quantity is defined as

$$\psi(\mathrm{pH}, R_{\mathrm{SC}}) = \frac{\int_0^{R_{\mathrm{SC}}} r^2 \rho_{\mathrm{CI}}(r, \mathrm{pH}) dr}{\int_0^{R_{\mathrm{ext}}} r^2 \rho_{\mathrm{CI}}(r, \mathrm{pH}) dr}, \tag{3.4}$$

where $\rho_{\mathrm{CI}}(r, \mathrm{pH})$ is the CIs radial density. The behavior of $\psi(\mathrm{pH}, R_{\mathrm{SC}})$ is shown in Figure 3.11. Notice that analyzing the fraction of available counterions located inside the SC instead of the absolute number allows one to focus more easily on correlation effects due to polymer shape and size, which define the electrostatic potential around a chain, rather than leaving them convoluted with the ionization ability of the polyelectrolyte. From the results, we notice that, first, the fraction of CIs maintained inside the SC at low pH - p$K_a$values agrees very well with the $(R_{\mathrm{SC}}/R_{\mathrm{ext}})^3$ ratio, thus indicating that proper configurational sampling is obtained, and, second, that differences between flexible and semi-rigid chains disappear at high pH due to the increase in Coulomb-induced stiffness of the

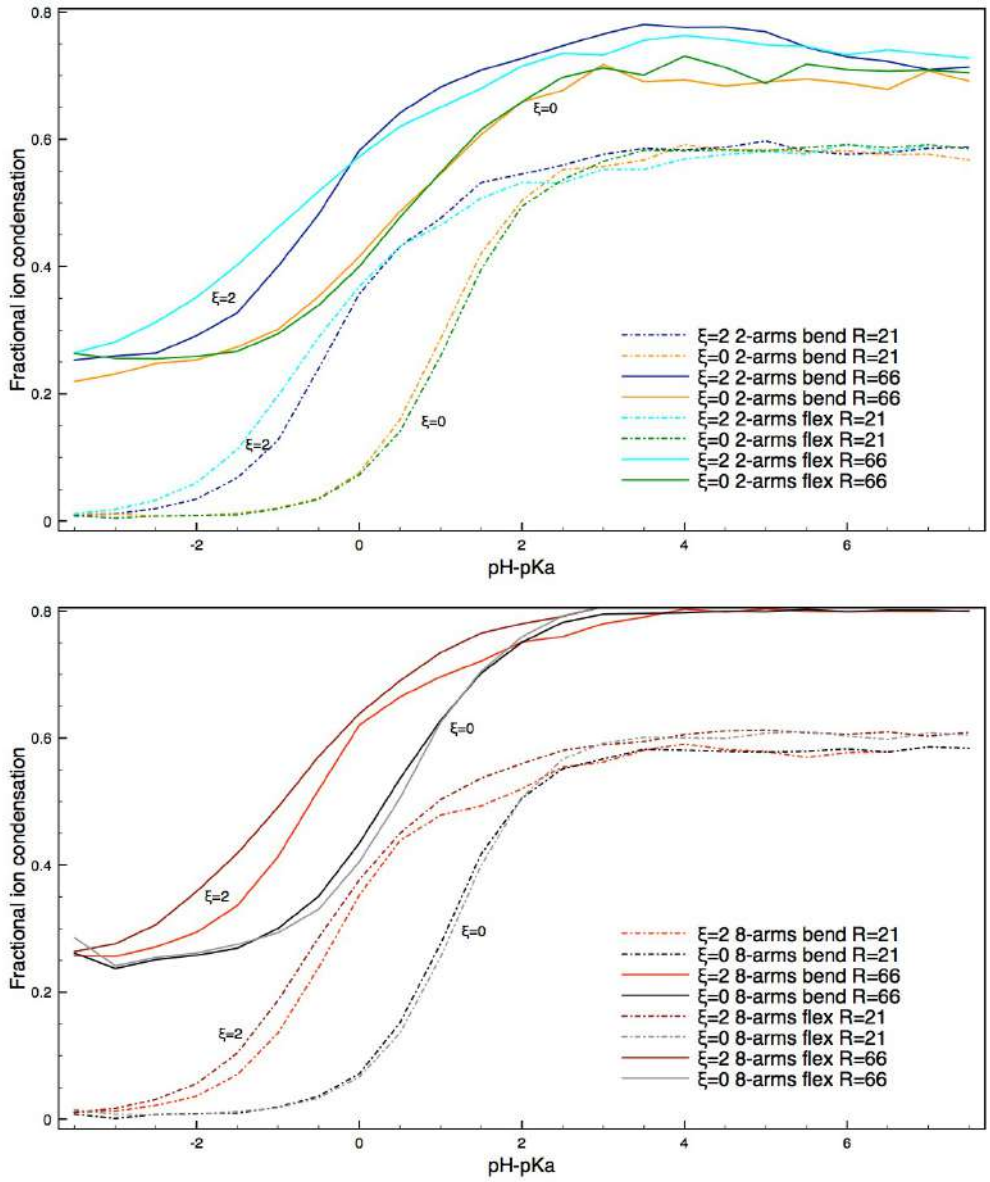

Figure 3.11: Fractional CI condensation $\psi(\mathrm{pH}, R_{\mathrm{SC}})$ as a function of pH for 2-arms (upper panel) and 8-arms (lower panel) species. Shown are data for semi-rigid ("bend") and flexible polymers confined inside a SC with $R = R_{\mathrm{SC}}/\text{Å} \in \{21, 66\}$.

former. At intermediate pH values, instead, we notice that chains with $\xi = 2$ kcal/mol maintain markedly more CIs inside the SC than ones with $\xi = 0$; in the latter case, the amount of CIs absorbed is nearly identical for flexible and semi-rigid species, whereas the former attract more CIs inside the SC than semi-rigid ones where able to form c-H-bonds. This is likely to be due to the more compact conformations (resulting in an higher charge density) assumed by the flexible chains (see Figure 3.9). For the same reason, star-shaped polyelectrolytes always attract more CIs inside the SC than linear ones, such evidence being magnified at high pH values in the largest cavity studied. A similar effect was previously evidenced for strong polyelectrolytes in terms of the number of condensed CIs [144] or larger deviation from the ideal osmotic pressure.

The "charge density" argument may also justify the maximum in $\psi(\mathrm{pH}, R_{\mathrm{SC}})$ evident around $\mathrm{pH} - \mathrm{p}K_a = 3.0$ for linear species with $\xi = 2$ kcal/mol in the widest SC. Such an effect disappears at high pH values due to the reduction of the number of neutral monomers, and the resulting chain swelling, which, eventually, spreads on the SC inner surface due to electrostatic repulsion. As 2-arms chains confined inside a SC with $R_{\mathrm{SC}} = 21$ Å do not show any indication for a maximum in ψ, it seems that aggregation due to c-H-bond formation no longer plays a role when ψ is too high. To investigate which monomer density is sufficiently high to hinder the appearance of such an effect, Figure 3.12 provides ψ at various R_{SC} for the semi-rigid chain with $\xi = 2$ kcal/mol. From the latter, one notices that the relative height of the maximum with respect to the value at high pH is a non-monotonic function of R_{SC}, the $R_{\mathrm{SC}} = 53$ Å case showing the highest relative value. Thus, whereas a slight decrease in R_{SC} facilitates polyelectrolyte compaction upon ionization and, hence, an increase in polymer charge density, such an advantage is lost when the monomer density inside a SC is already sufficiently high so that the formation of c-H-bonds only marginally increases the latter.

To understand whether or not the degree of CIs condensation on charged chains is influenced as well as ψ, we define the "condensation index" as

$$\gamma(R_l, \mathrm{pH}) = \frac{\int_0^{R_l} r^2 \rho(r, \mathrm{pH}) dr}{\int_0^{\infty} r^2 \rho(r, \mathrm{pH}) dr}; \tag{3.5}$$

here, $\rho(r, \mathrm{pH})$ is the distribution of distances r between charged monomers and

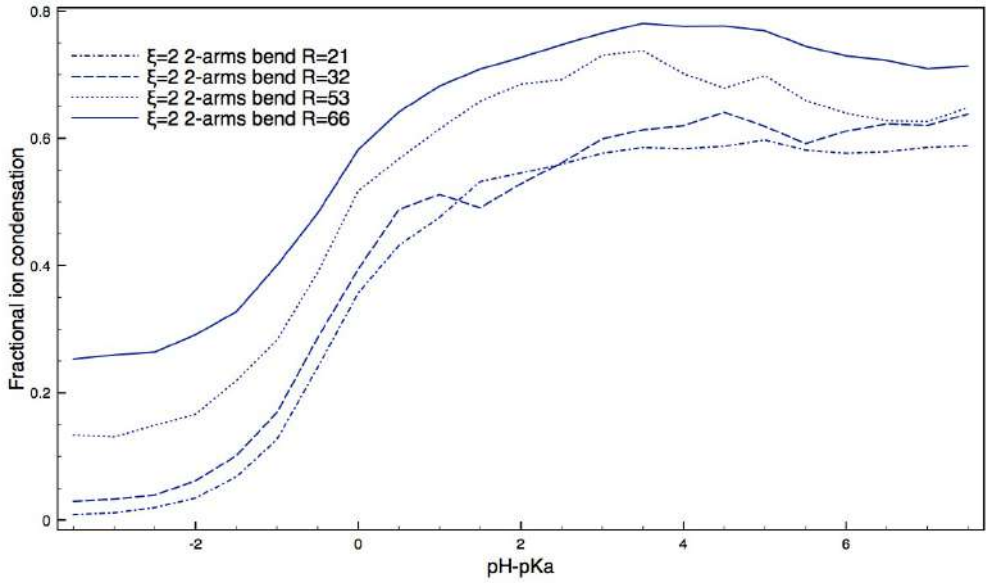

Figure 3.12: Fractional ion condensation as a function of pH for 2-arms semi-rigid polymers with $\xi = 2$ kcal/mol contained inside a SC with $R = R_{SC}/\text{Å} \in \{21, 32, 53, 66\}$.

CIs, whereas $R_l = 2\sigma = 7.7$ Å is the threshold distance at which the pair of such particles are considered no longer bound.[§,¶]

Figure 3.13 shows the behavior of $\gamma(\text{pH}, R_l) \equiv \gamma$ for semi-rigid polyelectrolytes; flexible species showed similar trends. One notices the presence of a marked maximum in γ in the range $3 \lesssim \text{pH} - \text{p}K_a \lesssim 4$ for c-H-bond forming species, whereas $\xi = 0$ curves monotonically converge to a limiting value upon increasing the pH. Worth noticing, there is a positive correlation between pH values at which the maximum in γ is located for species able to form c-H-bonds and around which compacted arms start to stretch; this suggests, once again, that both the charge and the volume over which is distributed play a role in defining the amount of CIs closely surrounding a polyelectrolyte.

[§]In water, the chosen R_l is close to the Bjerrum distance, at which the thermal energy allows two monovalent ions of opposite charges to easily escape their mutual attraction.

[¶]Albeit alternative definitions for a condensation index are indeed possible, (e.g., the probability of finding a counterion inside cylinders of radius R_l and whose axis coincides with the straight line joining two bonded monomers) our definition for $\gamma(R_l)$ has the advantage of being directly related to one of the pair distributions commonly sampled during our simulations. Besides, we aim mainly to compare "condensation tendencies" as a function of chain topology and conformations (the latter very dependent to the pH values) rather that provide absolute values (which are markedly influenced by the model details), so that any definition that monotonically follows the change in CIs local density around a chain should suffice.

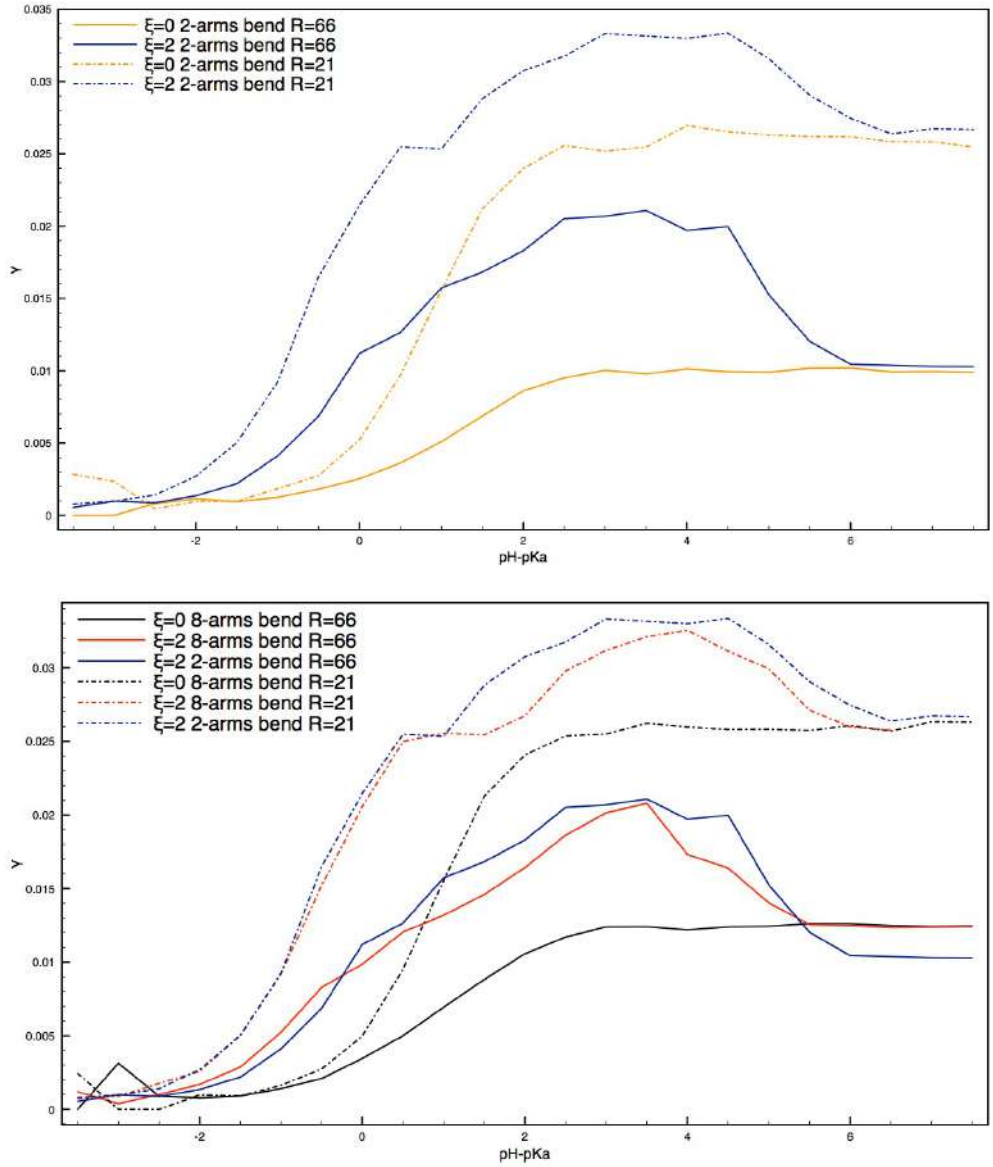

Figure 3.13: CIs condensation probability $\gamma(R_l)$ as a function of pH for 2-arms (upper panel) and 8-arms (lower panel) polyelectrolytes. Shown are data for semi-rigid ("bend") species, $\xi = 0$ and 2 kcal/mol, contained inside SC with $R = R_{\rm SC}/\text{Å} \in \{21, 66\}$.

3.3.4 Dependency of polyelectrolyte Helmholtz energy on confinement and charged hydrogen bonds

Figure 3.14 presents the behavior of I for chains confined in a SC with R_{21} Å (see Equation 3.2)[‖]. For all species with $\xi = 0$, I is positive definite and monotonically increasing over the whole range of pH explored. Notice, also, that I assumes larger values for the 2-arms species, a finding that is mainly due to its ability to better maximize the distance between charged monomers when confined in the widest SC; this results in a lower Helmholtz energy A for such species with respect to 8-arms ones. Additionally, we point out that I is lower for flexible species than for semi-rigid ones; in this case, the difference is due to the steeper relative decrease in α upon decreasing R_{SC} from 66 to 21 Å witnessed for stiff species (see Figures 3.2 and 3.4).

As for polyelectrolytes able to interact via c-H-bonds, we notice the presence of, at least, one interval of low pH - pK_a values where $I < 0$, the clear indication that the additional stabilization provided by the c-H-bonds formation may become stronger upon reducing R_{SC} in a way that markedly depends on chain stiffness; thus, I assumes values around -2 kcal/mol for flexible species, whereas it can reach roughly -8 kcal/mol for semi-rigid ones. Moreover, the absolute value of I when $\xi = 2$ kcal/mol remains quite low until $\mathrm{pH} - \mathrm{p}K_a \simeq 3$, then it begins to rapidly increase in parallel with the increase of $\langle r_{1N} \rangle$ (see Equation 3.9) due to the cluster dissolution or unfolding. In case of semi-rigid polymers, we also notice the presence of a relative minimum around $\mathrm{pH} - \mathrm{p}K_a \simeq 3$; this is due to a recrossing (i.e. $\alpha_{\xi=2}(\mathrm{pH}^*, 21) > \alpha_{\xi=2}(\mathrm{pH}^*, 66)$ when $1.5 < \mathrm{pH}^* < 2.5$) of titration curves obtained for $R_{\mathrm{SC}} = 21$ and 66 Å.

In order to investigate the impact that c-H-bonds have on the energetics of confined weak polyelectrolytes, Figure 3.15 presents the behavior of $J(\mathrm{pH}) \equiv J$ (see Equation 3.3) for flexible and semi-rigid polymers. Before commenting it, let us stress that J should be equal to zero when $\mathrm{pH} \ll \mathrm{p}K_a$ and $\mathrm{pH} \gg \mathrm{p}K_a$, as chains (both with and without MB interactions enabled) should behave similarly in those condition and thus should have the same Helmholtz energy, a fact related to the vanishingly small probability of forming a c-H-bond when $\alpha \to 0$ or 1. From our results, one immediately notices that flexible species generally conform to such

[‖] We recall that we approximate $R_{\mathrm{SC}} = \infty$ with $R_{\mathrm{SC}} = 66$ Å

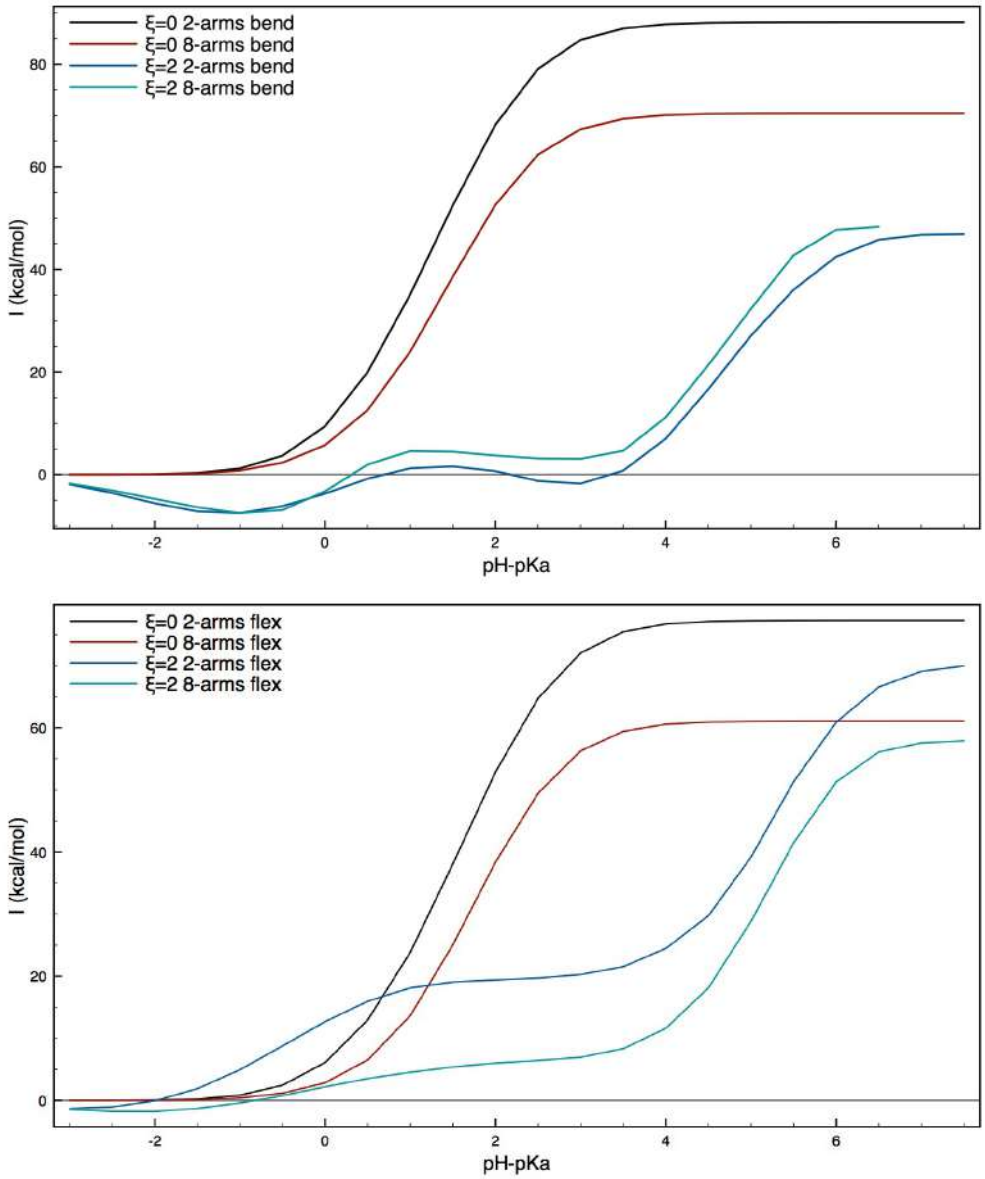

Figure 3.14: I (in kcal/mol) as a function of pH - pK_a for 2-arms and 8-arms species. Shown are data for semi-rigid ("bend", upper panel) and flexible chains (lower panel) with $\xi = 0$ and 2 kcal/mol.

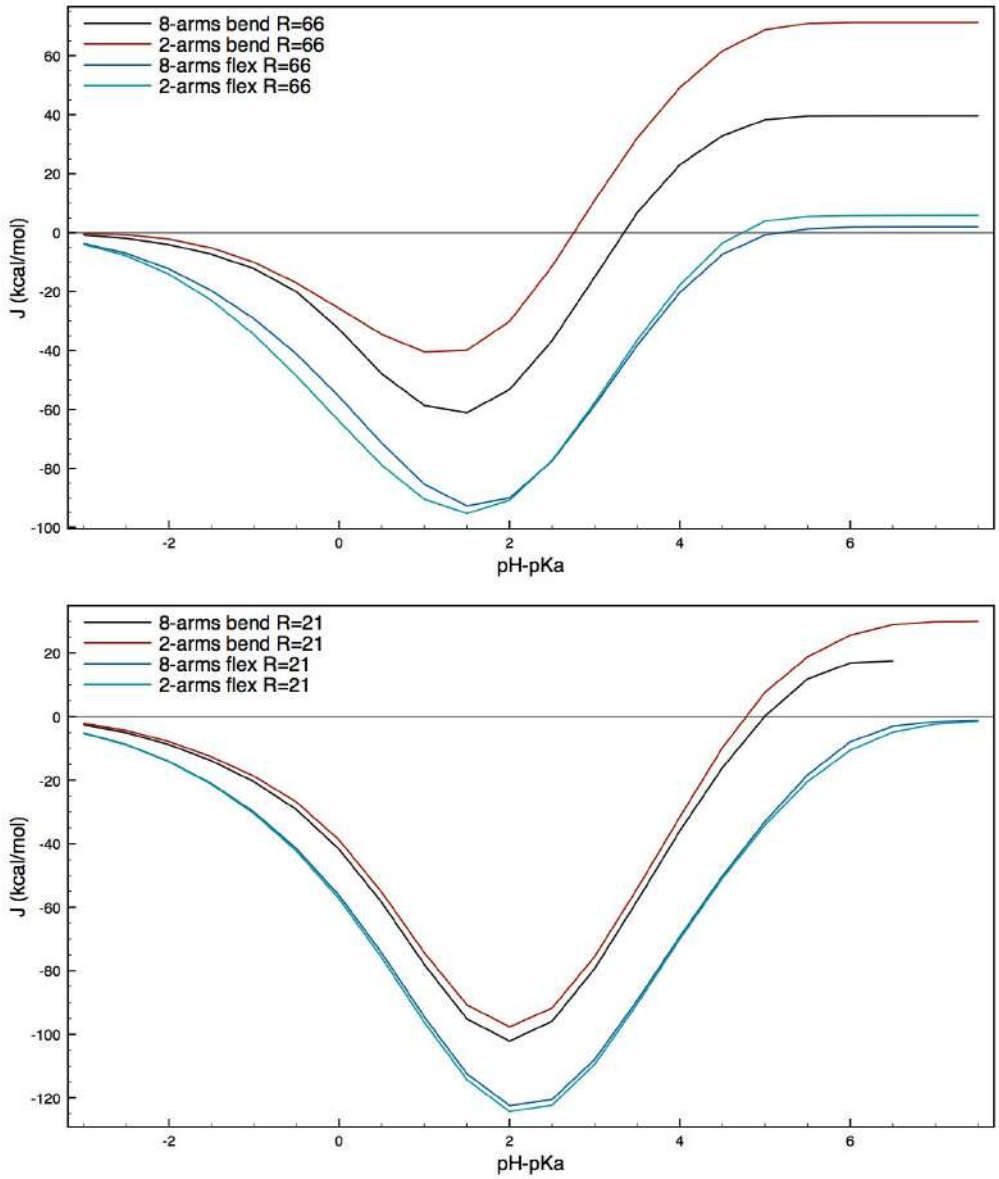

Figure 3.15: J (kcal/mol) as a function of pH for 2-arms and 8-arms species. Shown are data for semi-rigid ("bend") and flexible chains confined inside a SC with $R = R_{\rm SC}/\text{Å} = 66$ (upper panel) and 21 (lower panel).

expectation, the weak deviation from zero seen when $R_{SC} = 66$ Å at high pH being likely due to a mild inaccuracy in the integration that provides the values of A employed. Apart from this minor shortcoming, $J < 0$ over the vast majority of pH range explored for flexible species. From the quantitative point of view, 2-arms and 8-arms flexible species differ only slightly in terms of the values of J, the lowest value computed in both SC shown indicating a lowering of the Helmholtz energy due to the c-H-bonds by $\sim$ 100–120 kcal/mol. The largest stabilization is found when $R_{SC} = 21$ Å due to a higher probability of charged–neutral monomer interactions as a consequence of the reduced volume available to the chain. Also semi-rigid polymers present wide ranges of pH over which $J < 0$, due, again, to the presence of c-H-bond interactions. Such stabilization is, however, less marked than for flexible species, a finding probably due to a lower neutral–charged monomers contact probability (see Figures 3.1 and 3.3 for the impact on $\Delta \mathrm{p}K_a$, and Figures 3.2 and 3.4 for the difference in α). The same argument helps also to rationalize the lower minimum value of J for 8-arms species, as the latter present always a slightly higher ionization when $\mathrm{pH} - \mathrm{p}K_a < 1$.

At variance with the behavior seen for flexible species, however, in case of stiffer chains J does not converge to 0^- for $\mathrm{pH} \to \infty$ as one would expect. We believe such discrepancy to be a consequence of the mildly non-ergodic nature of MC sampling when $\mathrm{pH} - \mathrm{p}K_a \gtrsim 2$ and both MB and angular terms of the potential are present. In other words, the substantial energy barrier that ought be surmounted to unfold/"de–cluster" the chain when many c-H-bonds are present makes such event not as frequently sampled during a simulation as it should basing simply on statistical thermodynamic grounds. The effect of this biased sampling is to keep artificially lower the value of A until the polyelectrolyte reaches a "supercharged state" (akin to the supersaturated state needed to coalesce molecules into droplets) at which the c-H-bonds present are no longer capable of preventing the expansion, which happens over a limited range of pH. When this behavior is juxtaposed with the intrinsically limited accuracy of the thermodynamic integration scheme, it introduces a systematic error in our calculations.

3.4 General discussion and conclusions

In this work, we have explored ionization behavior ,as well as conformational and energetic properties of weak polyelectrolytes as a function of pH, chain structure and rigidity, its degree of confinement inside a spherical cavity (SC), and the possibility for monomers to interact via charged hydrogen bonds (c-H-bonds). To do so, we performed MC simulations implementing a coarse-grained primitive model of polyelectrolytes and the cell model. As to the confinement imposed to the polyelectrolyte, we have opted for a capsid-like cavity that limits polyelectrolyte diffusion but is permeable to counterions (CIs). [18,120,121] Albeit in the limit of no capsid internal surface charge, the results shown in this work substantially extend previous works on the strong polyelectrolytes confined inside the cell model system, as we explored ranges of "annealed" ionization never investigated before.

With respect to the dissociation behavior, we found that, as usually, species unable to interact via c-H-bonds decrease their ionization upon tightening confinement or increasing the number of arms at fixed number of total monomers. Also local ionization degree along arms follows the commonly expected "edge effect" in 2-arms species, and a monotonic increase while moving toward the periphery in star–like polyelectrolytes. At variance with this behavior, low pH ionization increases upon decreasing R_{SC} when c-H-bonds can form (even for $n^{\mathrm{n}}_{\mathrm{MB}} = 1$, see Appendix 3.6). Parallel to this results, we found a marked tendency of the latter species toward arm clustering (flexible chains) or inter-winding (semi-rigid chains), the net consequence of which is a much rougher behavior of the local arm ionization compared with $\xi = 0$ cases. Opposite to this, when $\xi = 2$ kcal/mol the ionization degree at intermediate pH values ($1 \lesssim \mathrm{pH} - \mathrm{p}K_a \lesssim 4$) results always substantially lower than its $\xi = 0$ counterpart.

Arms clustering and inter-winding also reduced average size of polyelectrolytes able to form c-H-bonds (see, e.g., Figures 3.6, 3.9 and 3.10), and thus increased the spatial density of charges generated by ionization. As a direct consequence, we observe a higher concentration of CIs inside the SC. Such finding is clearly interpreted as a charge–charge correlation effect on the basis of the non-monotonic behavior of the CIs condensation probability γ (see Figure 3.13). Similar behaviors have been evidenced by the calculation of the Fourier transform of the monomer-CI correlation function [145], and were connected to an increase in the

ionization degree of strong polyelectrolyte star's arms.

With specific relevance to chains absorption in cavities [37,84–87,91,104,105,118,119,134,135], we point out that the possibility to form c-H-bonds may impact positively on the polyelectrolyte partition constant not only compared to species unable to do that, but also with respect to the case of a fully undissociated weak polyelectrolyte (i.e., when $\mathrm{pH} \ll \mathrm{p}K_a$), at least over a range of pH values. The implication of these findings is clear: the expected increase in stiffness induced by chain dissociation, which should lower the entropy of a confined chain raising its Helmholtz energy, is overcompensated by the attractive c-H-bonds, at least in a range of pH values. Whereas the former observation just mentioned is related to the generally lower values of I when c-H-bonds can form (see Figure 3.14), which in turn relates with generally lower J values (see Figure 3.15), the second evidence spans from the fact that I may assume *negative* values. This is more evident for semi-rigid species than for flexible ones, as the former benefit more when it comes to form c-H-bonds by being more tightly confined into a cavity. In any case, the fact that I may be as low as ~ 7.5 kcal/mol for $R_{\mathrm{SC}} = 21$ Å implies that the partition constant of a semi-rigid chain with $\xi = 2$ kcal/mol at $\mathrm{pH} - \mathrm{p}K_a = 1$ may be roughly $8.5 \cdot 10^4$ times higher than its limiting $\mathrm{pH} \ll \mathrm{p}K_a$ value.

We finally discuss the implications emerging from the results on I with respect to the rate of escape of a chain at a given pH from a small hole in the SC, as introduced at the end of Section 3.2. If thermodynamics dominates the phenomenon, results in Figure 3.14 suggest that the relative escape rates of ionizable chains compared to the neutral counterparts qualitatively depends on both ξ and pH values. Thus, the escape rate of the ionized species would always be higher for species unable to form c-H-bonds. There are, instead, intervals of (low) pH values inside which $I < 0$, and a neutral chain should escape more rapidly when $\xi = 2$ kcal/mol. Another qualitative difference in behavior is made evident by comparing flexible and semi-rigid chains. In fact, the escape rate of semi-rigid species able to form c-H-bonds is predicted to always be lower than for $\xi = 0$ counterparts. This is instead true only when $\mathrm{pH} - \mathrm{p}K_a \geq 1$ for flexible 2-arm chains. Albeit we expect the relative behaviors just discussed to be qualitatively correct, the thermodynamic framework originally proposed by Muthukumar [136] may miss a few interesting statistical and dynamical effects. For instance, it is

not useful to discuss the crossover in dynamics emerging upon increasing the polymer stiffness [146], which may be made more complicate for our systems as the average distance between charged monomers belonging to the escaped polymer head is higher than for their absorbed counterparts. This should lower both the Coulomb energy and the rigidity of the escaped part, thus modulating the intensity of the thermodynamic force [147]. Besides, the Helmholtz energy profile for the translocation of star polymers through a pore may be different from the one for linear species [148], and it may also be modulated by how the ionization of monomers inside the pore responds to the additional entropic constraint.

3.5 Appendix: additional titration results to explore the impact of changing R_{ext}

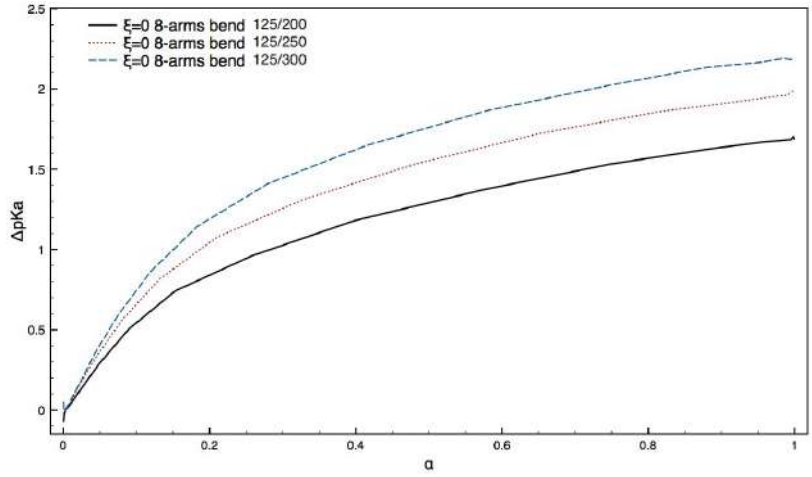

Figure 3.16: $\Delta \text{p}K_a$ as a function of α for semi-rigid ("bend") 8-arms species with $\xi = 0$ computed varying the radius of the external cell ($R_{\text{ext}} = \{104\,\text{Å}, 130\,\text{Å}, 156\,\text{Å}\} = \{200\,\text{bohr}, 250\,\text{bohr}, 300\,\text{bohr}\}$). $R_{\text{SC}} = 66$ Å$= 125$ bohr in all cases.

Figure 3.16 presents the impact of varying R_{ext} on the titration behavior of 8-arms polyelectrolytes with $\xi = 0$ confined into a SC with $R_{\text{SC}} = 66$ Å. As it is easily noticed, CI concentration implicitly defined by the formula $C_{\text{CI}} = \alpha L N_{\text{arm}}/(\frac{4}{3}\pi R_{\text{ext}}^3)$ plays a role as important as the size of the confining cavity in defining α. The mechanism by means of which such effect is produced is, again, ascribable to a decrease in screening between polymer charges due to a lower, in average, ionic force exerted by CIs. As a consequence, at a certain α values, the

more R_{ext} is larger, the more the system energy is higher. Such enthalpic effect overcompensates the gain in entropy that the system may obtain dissociating more thanks to the wider volume available to counterions. A similar trend for $\Delta \text{p}K_a$ versus R_{ext} is found also for linear chains or species with $\xi = 2$ kcal/mol (not shown).

We conclude this analysis noticing that also the extreme limit generated by increasing $R_{\text{ext}} \to \infty$, namely $C_{\text{CI}} \to 0$, is worth considering given previous published works [12, 13, 29, 31, 37, 149]. In this limiting situation, one would expect a decrease of α due to the absence of screening; this is confirmed by the simulation results shown in Figure 3.17, which indicate a reduction by, at least, 50% of α when $\text{pH} = \text{p}K_a$.

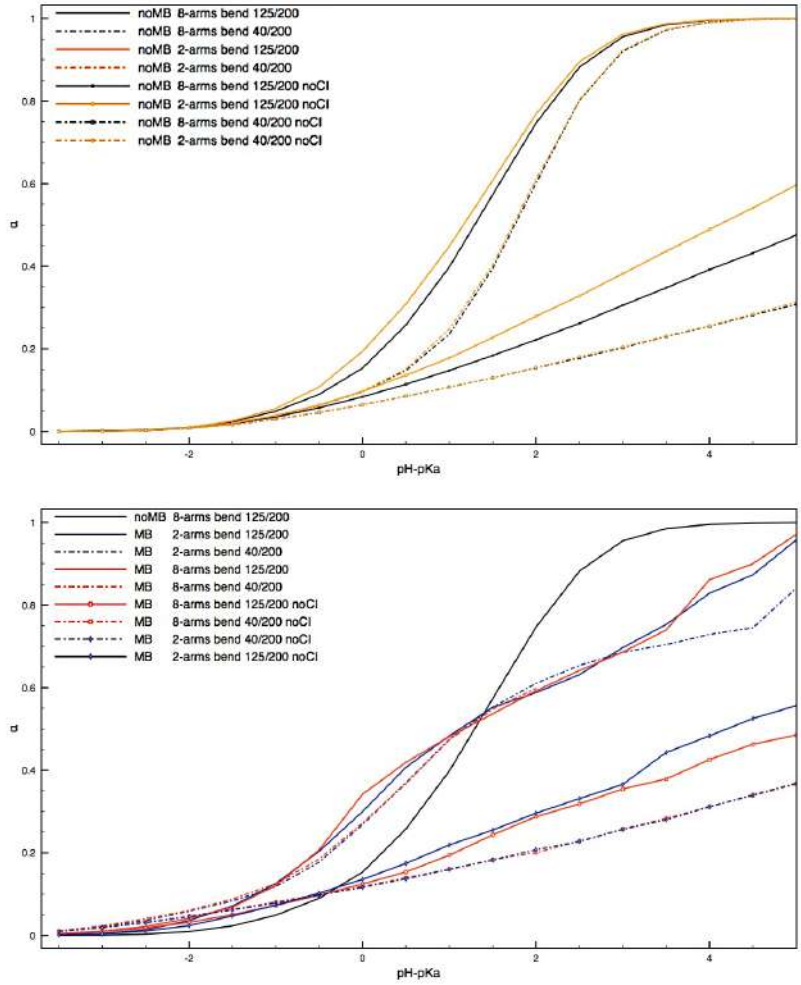

Figure 3.17: α as a function of pH - pK_a for semi-rigid ("bend") polyelectrolytes and two values of $R_{\text{SC}}/R_{\text{ext}}$, both with ($\xi = 2$ kcal/mol, labeled with "MB ") and without ($\xi = 0$, labeled with "noMB ") c-H-bonds. In a few simulations (tagged with the label "no CI") CIs were not introduced during the titration process.

3.6 Appendix: simulation results for polyelectrolytes able to form c-H-bonds with $n_{\mathrm{MB}}^{(\mathrm{n})} = 1$.

In this Appendix we show the results obtained from simulations for system capable to form c-H-bonds but with $n_{\mathrm{MB}}^{(\mathrm{n})} = 1$ instead of $n_{\mathrm{MB}}^{(\mathrm{n})} = \infty$ (other parameters: $n_{\mathrm{MB}}^{(\mathrm{c})} = 2$, $\xi = 2$ kcal/mol). $n_{\mathrm{MB}}^{(\mathrm{n})} = 1$ cases are tagged with the label "monoN" in the Figures.

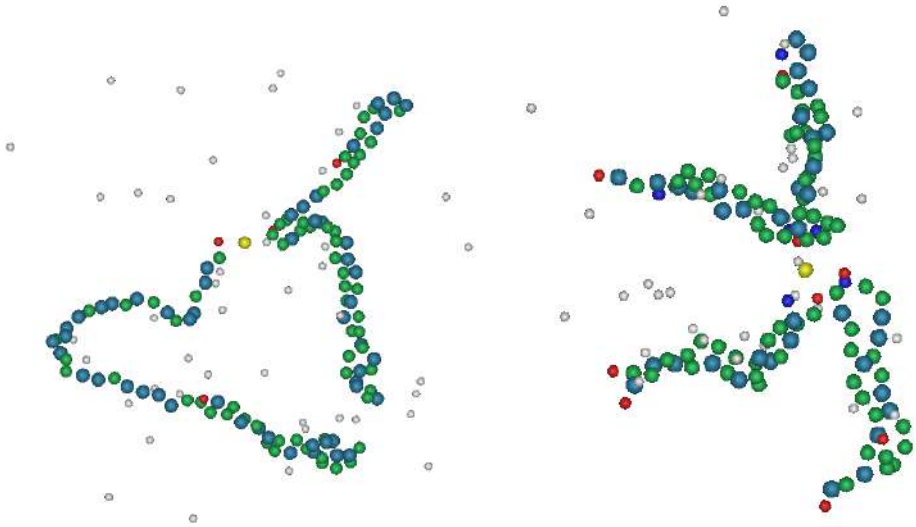

Figure 3.18: Conformation of a 2-arms (left) and 8-arms (right) semi-rigid polyelectrolyte, with $\xi = 2$ kcal/mol, $n_{\mathrm{MB}}^{(\mathrm{c})} = 2$ and $n_{\mathrm{MB}}^{(\mathrm{n})} = 1$, confined inside a SC with $R_{\mathrm{SC}} = 66$ Å ($R_{\mathrm{ext}} = 106$ Å) at $\mathrm{pH} - \mathrm{p}K_a = 1.5$. The color scheme is the same as in Figure 3.6.

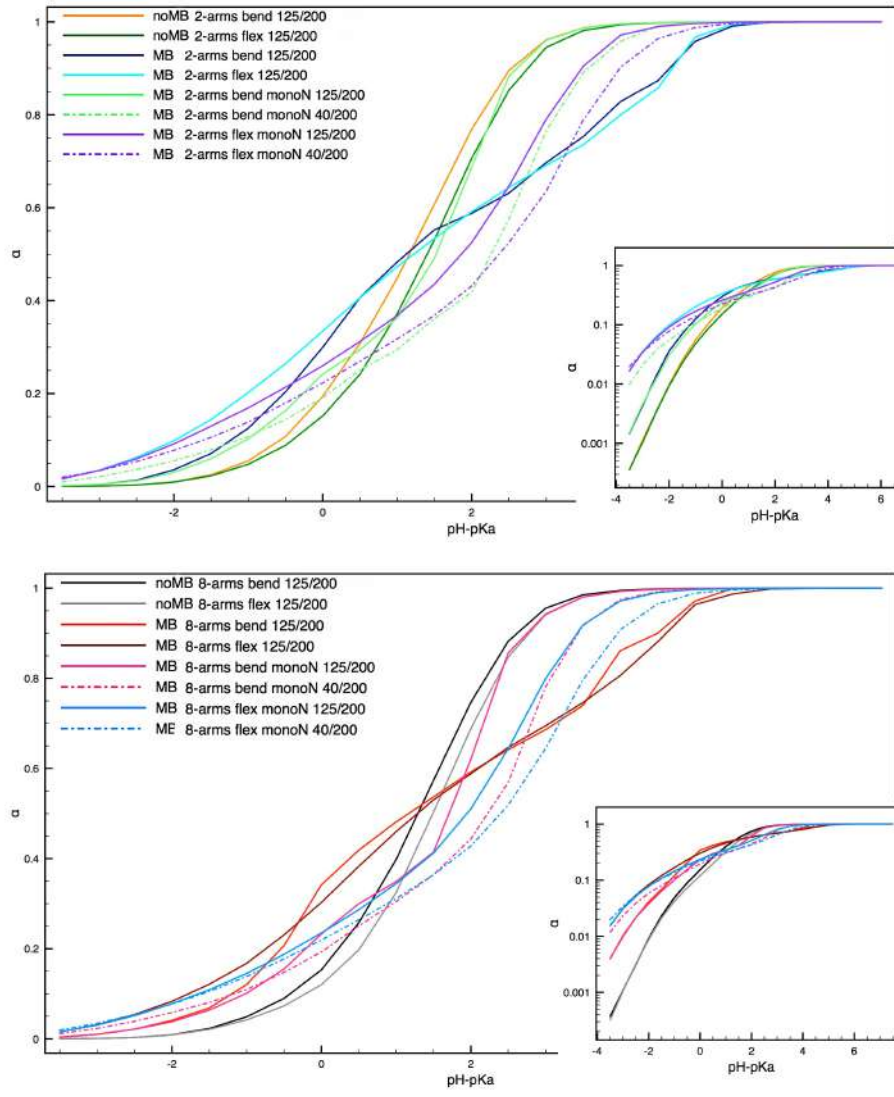

Figure 3.19: α as a function of $\mathrm{pH} - \mathrm{p}K_a$ for 2-arms (upper panel) and 8-arms (lower panel) polyelectrolytes. A few cases with $\xi = 0$ or $n_{\mathrm{MB}}^{(\mathrm{n})} = \infty$ are reported as a comparison.

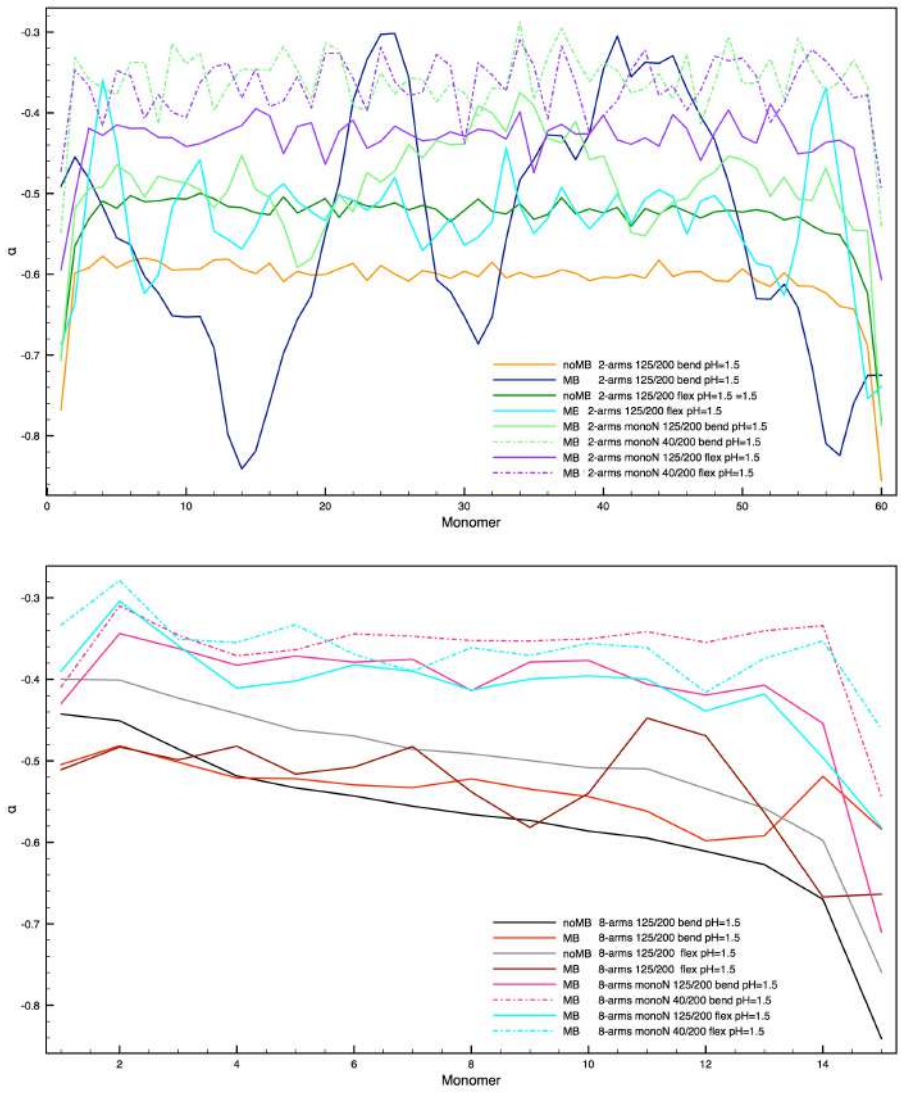

Figure 3.20: Local average charge along the chain for 2-arms (upper panel) and 8-arms (lower panel) polyelectrolytes. A few cases with $\xi = 0$ or $n_{\mathrm{MB}}^{(\mathrm{n})} = \infty$ are reported as a comparison.

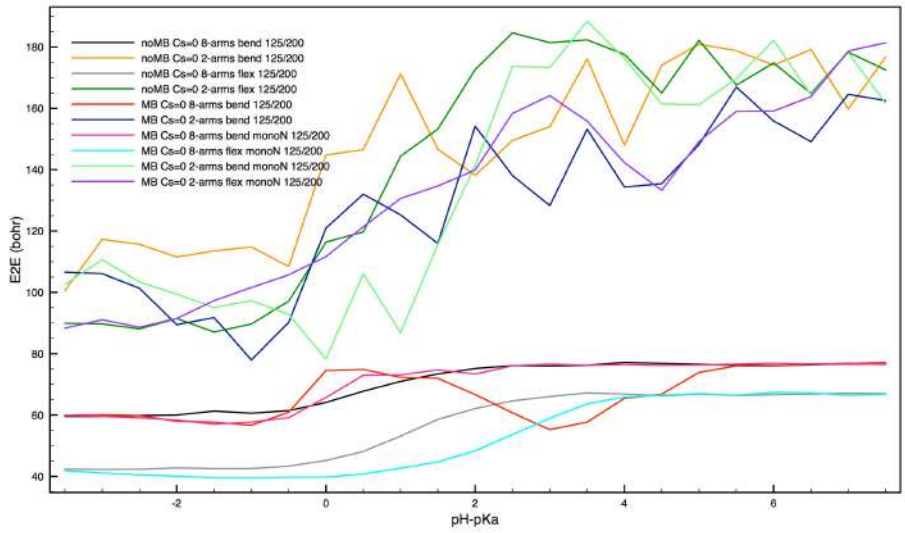

Figure 3.21: Average arm extension $\langle r_{1N} \rangle$ as a function of $\mathrm{pH} - \mathrm{p}K_a$. A few cases with $\xi = 0$ or $n_{\mathrm{MB}}^{(\mathrm{n})} = \infty$ are reported as a comparison.

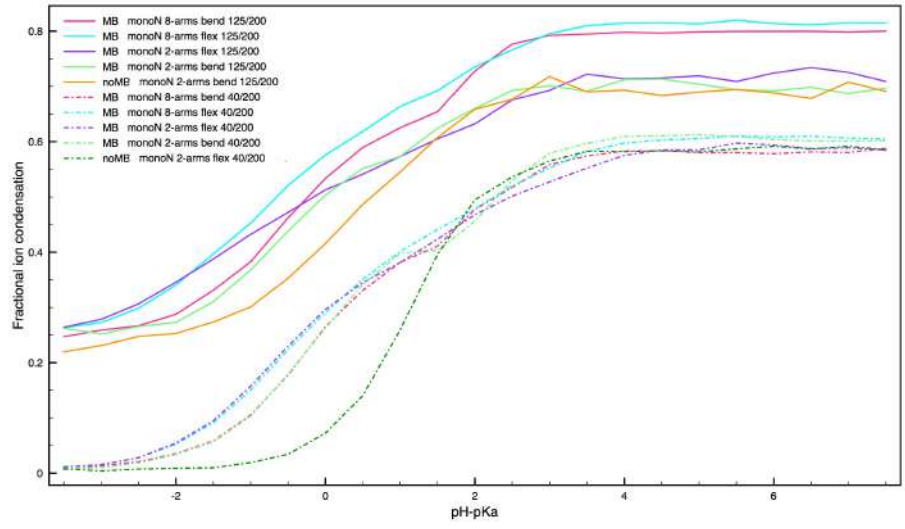

Figure 3.22: Fractional ion condensation ψ as a function of $\mathrm{pH} - \mathrm{p}K_a$. A few cases with $\xi = 0$ or $n_{\mathrm{MB}}^{(\mathrm{n})} = \infty$ are reported as a comparison.

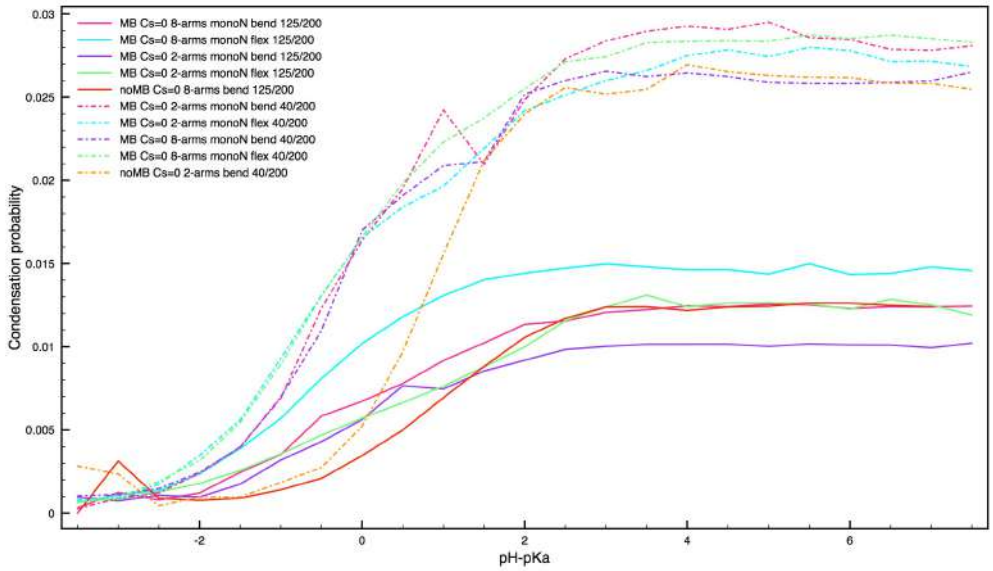

Figure 3.23: γ as a function of pH. A few cases with $\xi = 0$ or $n_{\mathrm{MB}}^{(\mathrm{n})} = \infty$ are reported as a comparison.

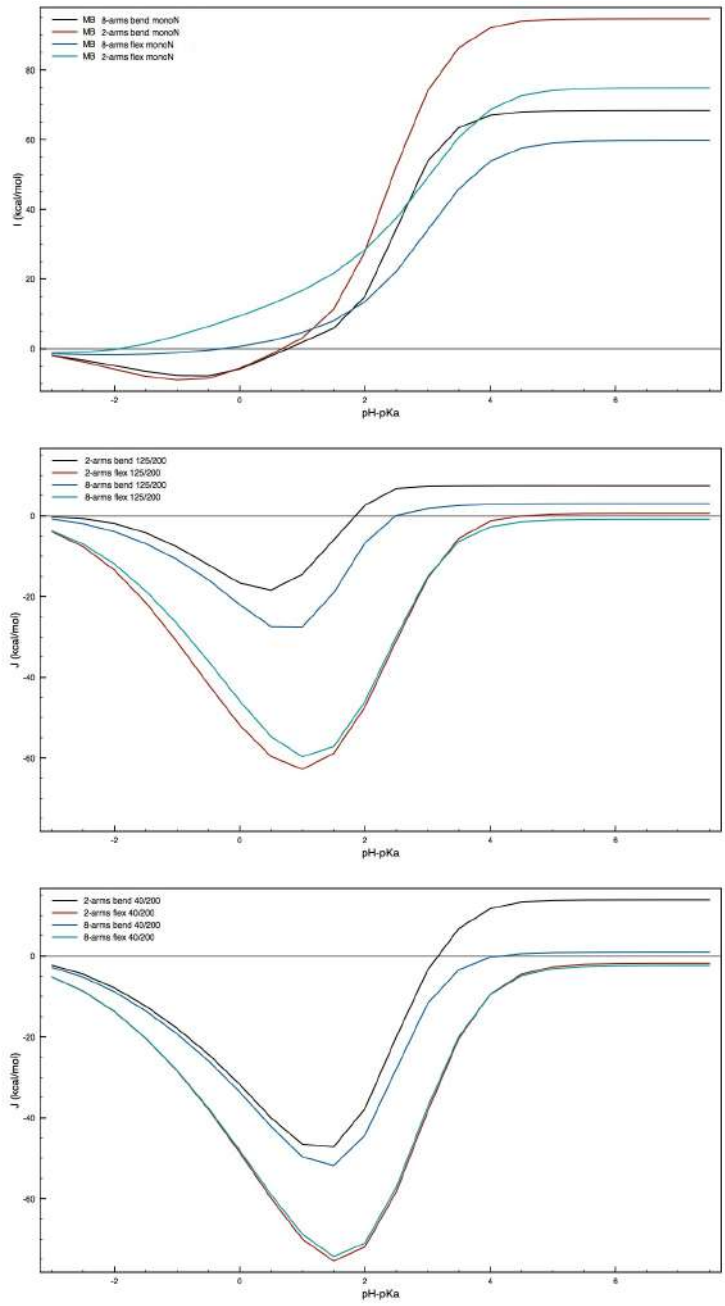

Figure 3.24: I (upper panel) and J (middle panel: $R_{\mathrm{SC}} = 66$ Å; lower panel: $R_{\mathrm{SC}} = 21$ Å) as a function of $\mathrm{pH} - \mathrm{p}K_a$.

Chapter 4

Impact of Charge Correlation, Chain Rigidity and Chemical Specific Interactions on the Behavior of Weak Polyelectrolytes in Solution*

4.1 Introduction

Polymers composed of monomers acting as weak electrolytes (either acids or bases) present ionization properties that depend markedly on their environment (e.g, see References [37, 122–125, 150–157]). As chain conformations in such species are controlled by the ionization degree α via the electrostatic interaction of ionized groups [12, 29–35, 37–42], the polyelectrolyte environment also indirectly impacts on structural details at a chosen pH.

Additional factors that may play a role in defining the properties of a polyelectrolytic system are the concentration of the ionizable groups (depending on both the concentration of chains bearing ionizable monomers [38,158,159] and the amount of the latter on each chain [158]), and structural details such as the number of branches or vicinally-tethered chains [35,53,54,127–130,137,138,141,160], or chain stiffness [7, 33, 37, 161]. Notice that increasing the number of arms in star–like polyelectrolytes or the density of chains on surface-tethered species is

*This chapter has been adapted from: Tagliabue, A., Izzo L., Mella M., Impact of Charge Correlation, Chain Rigidity, and Chemical Specific Interactions on the Behavior of Weak Polyelectrolytes in Solution, *Journal of Physical Chemistry B*, 123, 42, 8872–8888, 2019.

somewhat akin to increasing the local concentration of monomers, with the predictable impact of decreasing the ionization degree at a chosen pH compared to isolated species due to electrostatic repulsion [38, 162].

Somewhat more recently, researchers have also begun to explore the interplay between the factors mentioned above, which control ionization or conformations, and the presence of physical or chemically-specific interactions between chain monomers; this effort has been spurred by the interest toward smarter stimuli-responsive materials. Thus, useful pieces of information on how the presence of hydrophobic interactions [34, 38, 39, 129, 149, 155, 160, 163–169], and ion electrostatic [6, 33, 143, 170] or chemical coordination [12, 37, 131, 132] impact on conformations and ionization capability have become available. In particular, our group focused on the possibility for the polyelectrolyte to form charged hydrogen bonds (c-H-bonds); the latter are attractive interactions that can develop between conjugated acid-base pairs (e.g. carboxylic acid–carboxylate or ammonium–amine interactions). This interest stemmed from the observation that NH_4^+ and NH_3 dimerize in H_2O due to the stronger basic properties of NH_3 compared with solvent molecules [74]. Such tendency may, however, be somewhat reduced (or even enhanced) by excluded volume or confinement effects, topology and rigidity of the polymer (for example a poly–amine), and entropic requirements such as the need for an appropriate relative orientation between interacting groups or polymer segments. For example, in our previous works we demonstrated that c-H-bonds between neutral and protonated amino groups effectively increases polymer basicity due to the fact that these interactions stabilize the positive charge on the ionic group. These evidences have been found to increase ionization of linear polymers up to two orders of magnitude when $\mathrm{pH} < \mathrm{p}K_a$ [12], helping to rationalize the higher charge density found on the surface of plaques of water-insoluble methyl methacrylate and (dimethylamino)ethyl methacrylate copolymers. Moreover, we observed a competition between charged and neutral group clustering and Coulomb repulsion developing upon increasing the total charge, an effect that is different from what happens in presence of solvophobic interactions, which are usually considered invariant with respect to the total polymer charge.

In this work, we aim to extend the present knowledge on the cooperation between monomer (or chain) concentration, chain rigidity and chemically–specific interactions in defining the ionization and conformational properties of linear

polyelectrolytes. We tackle the mentioned task by means of computer simulations to unravel non–trivial features of such interplay exploiting a "primitive model" for the description of the ionizable species and the constant-pH method to simulate titration processes (see Section 2.2.2). For the sake of simplicity, we avoided to include ions deriving from background salts; thus, our simulations describe solutions with zero background ionic force. To obtain a deeper characterization of the polyelectrolytic system behavior as a function of the pH, we also computed relevant thermodynamics quantities such as the variation of the system Helmholtz energy, as well as the variance of the interaction potential. The latter allows us to discuss possible cooperative behaviors, e.g. CIs distribution, controlled by the proton chemical potential. Moreover, we investigate how the distance between two chains, the average value of which is controlled by the total concentration of chains C_p, modulates ionization and conformations employing a "Window Simulations" (WS) sampling approach [171–173].

As for our interest in chemically-specific interactions, we investigate the possible formation of charged hydrogen bonds between neutral and ionized monomers, which, in the current case, behave as weak (e.g. carboxylic) acids. Given the chemical nature of the ionizable groups, c-H-bond interactions are markedly many-body (MB) in nature (i.e., a group can only afford a maximum number of contacts well below its geometrical coordination capability); we describe such characteristic via a MB model developed in our group [12, 37] (see also Section 2.1.1.5). In practice, the model describes possible double coordination of a proton to two basic groups, in a way similar to coordination of calcium cation described in References [131, 132].

The Chapter is organized as follows. In Section 4.2, the models and methodologies employed in our work are described somewhat in detail. Section 4.3, instead, presents and discuss the numerical results obtained simulating polyelectrolytes with different stiffness and chemical behavior (i.e., with or without the possibility to interact via c-H-bonds) at different concentrations. The analysis of how properties depend on the distance between chains is provided in Section 4.4. Section 4.5 gives additional discussions and the general conclusions of our work. Finally, in Appendix 4.6 we provide trajectory snapshots for all the simulated systems.

Abbreviation	Meaning
c-H-bond	Charged hydrogen bond
MB	Many-body
CI	Counterion
WS	Window sampling
CoM	Center of mass
PMF	Potential of mean force
PDF	Pair distribution function

Table 4.1: List of abbreviations commonly used in this chapter

4.2 Methods and Model

Our system consists of a spherical cavity (cell model, see Equation 2.12) with radius $R_{\text{cell}} = 66.125$ Å, into which n short linear polyelectrolyte chains and their counterions (CIs) are confined. Each chain is composed of $L = 15$ monomers, so that the total number of monomers in the cell is $N_{\text{mono,tot}} = Ln = 15n$. Monomers in each chain are connected via a harmonic stretching potential (see Equation 2.4), with $k_{\text{bond}} = 200 k_{\text{B}}T/\text{Å}^2$, $l_0 \equiv \sigma = 3.85$ Å [133], and $k_{\text{B}}T = 9.4371 \cdot 10^{-4}$ Hartree $= 0.5922$ kcal/mol (which corresponds to a temperature $T \simeq 298$ K). In some simulations, a bending potential (see Equation 2.6) is also added to make the polyelectrolyte stiffer, with a bending force constant $k_{\text{ang}} = 2 \cdot 10^{-3} k_{\text{B}}T/\text{deg}^2$ and an equilibrium angle $\theta_0 = 150°$ [133]. We will refer to this type of chains as "semi-rigid"; otherwise (i.e., $U_{\text{ang}} = 0$) we will talk about "(infinitely) flexible" chains*.

Each monomer is treated as a weak acid and can therefore exist in two different state: neutral ($q_{\text{mono}} = 0$) or negatively charged ($q_{\text{mono}} = -1$). As will be explained later in this section, the state of each monomer can vary during the simulation, while the total number of monomer must remain constant, so that $N_{\text{mono,tot}} = N_{\text{mono,charged}} + N_{\text{mono,neutral}} = nL$. In order to maintain the electroneutrality of the system, there must be a positive monovalent CI in the cell ($q_{\text{CI}} = +1$) for each negative charged monomer, so that $N_{\text{CI}} = N_{\text{mono,charged}}$

*l_0 and θ_0 implemented parameters are taken from Reference [133] by Ziebarth et al. in which the authors perform coarse-grained simulations of poly ethylimine; these parameter were already used in References [12, 37] by Mella et al. in order to investigate the impact of intra-chain c-H-bonds on weak polyelectrolytes. For sake of comparability, we decided to maintain the same parameters value even if we are simulating polyacids. In order to obtain the "correct" titration behavior, one can simply invert the titration curves.

and the total number of charged particle is $N_{\text{charged}} = N_{\text{mono,charged}} + N_{\text{CI}}$. The total number of particles in the system is then given by $N_{\text{tot}} = N_{\text{mono,tot}} + N_{\text{CI}}$. The solvent is treated as a dielectric continuum, and charged particles interact with each others via a pairwise Coulomb potential (see Equation 2.7; the relative dielectric permittivity, $\varepsilon_r = 78.3$, corresponds to the one of water at $T = 298$ K is the dielectric constant of water.

All N_{tot} particles are treated as soft spheres, and a WCA potential (see Equation 2.3) with $\epsilon = k_{\text{B}}T$ and $\sigma = l_0$ is applied to simulate their excluded volumes in order to avoid polymer entanglements and particles overlaps.

Finally, in order to simulate the impact of chemically specific interactions on the polyelectrolyte behavior, we also employed a (MB) interaction potential U_{MB} previously introduced by our group [12,37]. Details are reported in Section 2.1.1.5; here, we use a cutoff radius $r_{\text{MB}} = 5$ Å, $n_{\text{MB}}^{(\text{n})} = \infty$, $n_{\text{MB}}^{(\text{c})} = 2$, and $\xi_{\text{MB}} = 2.0$ kcal/mol. For sake of simplicity, we introduce the parameter $\zeta = \xi_{\text{MB}}/(\text{kcal/mol})$ to specify when a MB interaction can be formed or not ($\zeta = 2$ or $\zeta = 0$, respectively).

Simulations are performed via a classical Monte Carlo approach, sampling the semi-grand-canonical thermal density matrix of the system as function of the control variable pH - pK_a, which is a convenient proxy to control the chemical potential of H^+ in solution. All particles are displaced using the classical Metropolis-Hastings acceptance rule (Equation 2.30) [78], whereas the constant-pH method has been implemented in order to simulate the weak acidic behavior of the polyelectrolytes (see Section 2.2.2). In order to speed up the convergence to the equilibrium state and to better sample the ensemble of system configurations, the following cluster moves have been also implemented (see Section 2.2.1.4 for details): (i) entire chain translations; (ii) pivot moves. Therefore, we define a Monte Carlo step (MCS) as composed by a translation attempt for each particle, plus one attempt to titrate (i.e. associate or dissociate) a randomly chosen monomer, plus one entire chain translation move and one pivot move.

4.2.1 Titration simulations

In this section we describe how simulations have been performed. n uncharged chains, each one composed by $L = 15$ monomers, are randomly positioned inside

the cell, and the system is thermalized for 10^5 MCS using a value of the control parameter pH - pK_a that ensure chain neutrality (usually pH - p$K_a \leq -4.0$); system properties are subsequently collected during a run $1.8 \cdot 10^5$ MCS long. The entire process is then repeated starting from the last system configuration obtained and increasing the value of pH - pK_a by Δ(pH - pK_a)= 0.5 until $\alpha \simeq 1$. The sets of parameters whose impact is explored by means of titration simulations are: (i) the number of chains in the cell, $n = \{1, 2, 8\}$; (ii) the rigidity of the chain, i.e. $k_{\text{ang}} = \{0, 2 \cdot 10^{-3} k_{\text{B}}T/\text{deg}^2\}$; (iii) the possibility ($\zeta = 2$) or not ($\zeta = 0$) for monomers to form c-H-bonds. For each set of parameters, 100 independent complete titrations were performed in the attempt to improve the sampling of configurations that may be kept separated by high energy barriers due to, e.g., the presence of several c-H-bonds; we therefore present averaged results accompanied by their standard errors.

4.2.2 Window potential simulations

With the aim of precisely investigating how inter-chain distance influence polyelectrolytes acidity and conformations, especially when c–H–bonds are possible, we performed window sampling simulations (WS). This methodology is often used to overcome the tendency of the Metropolis method to sample preferentially low energy regions.

In our WS simulations, the system is composed of $n = 2$ chains confined in the spherical cell (we recall that $R_{\text{cell}} = 66.125$ Å) but subjected to the following potential:

$$U_{\text{WS}}(d_{\text{CoMs}}) = \begin{cases} 0 & \text{if } a < d_{\text{CoMs}} < b \\ \infty & \text{otherwise,} \end{cases} \tag{4.1}$$

where d_{CoMs} is the distance between the centers of mass (CoMs) of the two interacting chains and $0 < a < b \leq R_{\text{cell}}$. No such restriction is instead placed on CIs, and each WS simulation has been performed in the same way as the titration simulations previously described to gauge the impact of varying the parameters n, ζ and k_{ang}. Given the large number of d_{CoMs} intervals employed, however, a maximum of 15 independent simulations per interval have been performed.

An interesting byproduct of WS simulation is the potential of mean force (PMF, or free energy curve) as a function of d_{CoMs}, $w(r) = w(d_{\text{CoMs}})$. To obtain

it, one could sample the pair distribution function $g(r) = e^{-\beta w(r)}$ of the CoMs of the two chains freely moving inside the entire cell ($\beta = (k_B T)^{-1}$); here $w(r)$ is the interaction potential acting on the two CoMs, i.e. the quantity we would like to obtain. The direct sampling (and inversion) of $g(r)$ is, however, hampered by the low probability (hence high statistical errors) of sampling configuration with low r due to entropic or energetic reasons, while long distance regions are visited with a frequency sufficiently high to precisely estimate relative probabilities.

To improve on such situation, we initially sampled $g^{(0)}(r)$ over an interval $a = a^{(0)}$ and $b = R_{\text{cell}}$ with $a^{(0)}$ sufficiently high to provide a large overlap with the distribution of d_{CoMs} obtained by sampling $e^{-\beta w(r)}$ without restraints. Subsequently, one chooses a second interval $(a^{(1)}, b^{(1)})$, with $a^{(1)} < a^{(0)} < b^{(1)} < R_{\text{cell}}$ and $b^{(1)} - a^{(0)}$ sufficiently large to provide a good overlap between the two ranges of d_{CoMs}, and samples $g^{(1)}(r)$ inside it. The latter is then scaled by a constant $c^{(1)}$ chosen to minimize the least square difference between $g^{(1)}(r)$ and $g^{(0)}(r)$ over the interval $(a^{(0)}, b^{(1)})$. The same procedure is reiterated on a new interval, e.g. $(a^{(2)}, b^{(2)})$ with $a^{(2)} < a^{(1)} < b^{(2)} < b^{(1)}$, to obtain the scaling constant $(c^{(2)})$ that "fits" $g^{(2)}(r)$ to $g^{(1)}(r)$ over $(a^{(1)}, b^{(2)})$, and so on. In conclusion, one can rebuild the global $g(r)$ inside a specific interval $(a^{(j)}, b^{(j)})$ by $g^{(j)}(r) \prod_{i=1,j} c^{(i)}$. From this, $w(r)$ is easily obtained by inversion, apart from its asymptotic value that we arbitrarily set to zero. For a list of the simulated (a, b) intervals, *vide infra* Table 4.2 in Section 4.4.

4.2.3 Helmholtz energies

In this work, we exploit 2.35 in order to collect information on how a change in polyelectrolyte concentration C_p (from a state "1" to a state "2"; i.e. from $C_p, 1$ to $C_p, 2$) impacts on the variation of A per chain upon ionization. Thus, we computed the quantity

$$I'_{\zeta^*}(\text{pH}^*, C_{p,1}, C_{p,2}) = \frac{A_{\zeta^*}(\text{pH}^*, C_{p,2})}{n_2} - \frac{A_{\zeta^*}(\text{pH}^*, C_{p,1})}{n_1}, \tag{4.2}$$

where $A_{\zeta^*}(\text{pH}^*, C_p)$ is the change in Helmholtz free energy due to the ionization process when the polyelectrolyte solution has a concentration $C_p = n/V_{\text{cell}}$, with $V_{\text{cell}} = \frac{4}{3}\pi {R_{\text{cell}}}^3$ being the volume of the simulation cell. ζ^* can be either equal to 0 or 2.

We define

$$J'(\mathrm{pH}^*, R) = A_{\zeta=2}(\mathrm{pH}^*, R) - A_{\zeta=0}(\mathrm{pH}^*, R) \tag{4.3}$$

as the energy difference between the $\zeta = 0$ and $\zeta = 2$ cases at certain values of pH^* and R; thus, J' differs from zero only due to the possible formation of c-H-bonds and contributes to define the ratio between the partition constants of polyelectrolytes with and without MB interactions. As we found $J' < 0$ over the majority of the pH range explored for all the simulated species (linear [37], and star-shaped (see Chapter 3) flexible and semi-rigid polyelectrolytes), which indicates the stabilizing effect of the c–H–bonds, we now analogously compute

$$J'(\mathrm{pH}^*, n) = \frac{A_{\zeta=2}(\mathrm{pH}^*, n)}{n} - \frac{A_{\zeta=0}(\mathrm{pH}^*, n)}{n}, \tag{4.4}$$

which represents the contribution to the Helmholtz energy of the system arising from c–H–bonds at given values of pH and number of chain in the cell n.

4.3 Results and discussion: titration simulations

4.3.1 Impact of polyelectrolyte concentration, rigidity and chemically specific interactions on ionization behavior

We start the presentation of our results discussing how $\Delta \mathrm{p}K_a$ depends on the dissociation degree α (see Equations 2.21 and 2.23) for different numbers ($n = 1, 2, 8$) of pentadecameric flexible chains in the cell (Figure 4.1, green and black curves; see also Figure 4.2, in which the behavior of α as a function of pH - $\mathrm{p}K_a$ is shown). In absence of MB interactions, we observe the expected monotone increase of $\Delta \mathrm{p}K_a$ as α increases, due to the progressively higher concentration of charges on the chains. At variance with these results, we observe a different trend when c-H-bonds can be formed. At low ionization degrees ($\alpha \lesssim 0.33$ for $n = 1$, 2; $\alpha \lesssim 0.42$ for $n = 8$) the shift in $\mathrm{p}K_a$ is not only lower than the $\zeta = 0$ case, but it assumes *negative* values; this means that acidic groups on chains ionize more than corresponding free ideal monomers in solution. As demonstrated previously [12,37], this happens because the formation of c-H-bonds results in a decrease of the total free energy of the system and, thus, stabilizes the polyelectrolytes. As α increases, it becomes more and more difficult to ionize

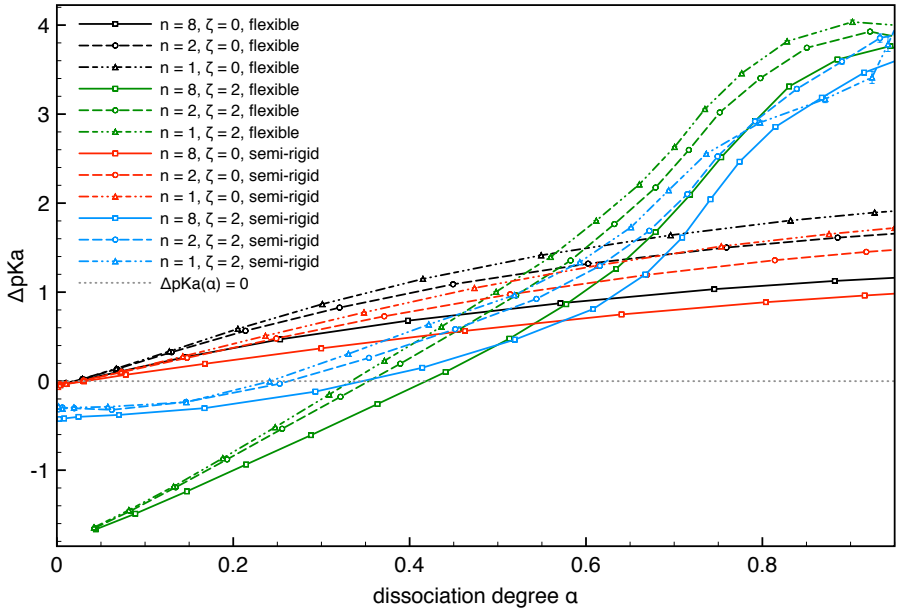

Figure 4.1: ΔpK_a as function of α for all the combinations of n, ζ and K_{ang}. $n = 1, 2, 8$ correspond, respectively, to chains concentration $C_p \simeq 1.37 \cdot 10^{-3}$ M, $2.74 \cdot 10^{-3}$ M, $1.10 \cdot 10^{-2}$ M, and monomers concentration equal to $C_m \simeq 2.06 \cdot 10^{-2}$ M, $4.11 \cdot 10^{-2}$ M, and $1.65 \cdot 10^{-1}$ M. The dotted gray line is a guide for the eye in order to discern positive and negative values of ΔpK_a. Standard error bars are smaller than plot symbols.

monomers due to the fact that further dissociation would not only increase the total charge density on the chains, but would also result in a decrease of the number of c-H-bonds.

The impact of introducing a bending potential (red and light blue curves in Figures 4.1 and 4.2) in addition with the possibility for monomers to interact via intra-molecular c-H-bonds has been already discussed in References [37]. Summarizing, flexible chains ionize more than rigid ones at low pH - pK_a values as the former can form charged-neutral contacts more easily; at intermediate pH - pK_a values, instead, the former are less ionized due to their ability to maintain clusters composed by a large amount of both neutral and charged monomers. The latter findings must be contrasted with the case $\zeta = 0$, for which increasing the stiffness slightly increases the dissociation over the whole range of pH - pK_a, due to the fact that the introduction of an angular potential term increases the polymer size and linearizes it; this results in a higher average distance between charged monomers.

When n is incremented from 1 to 8 at a fixed value of pH - pK_a (i.e., con-

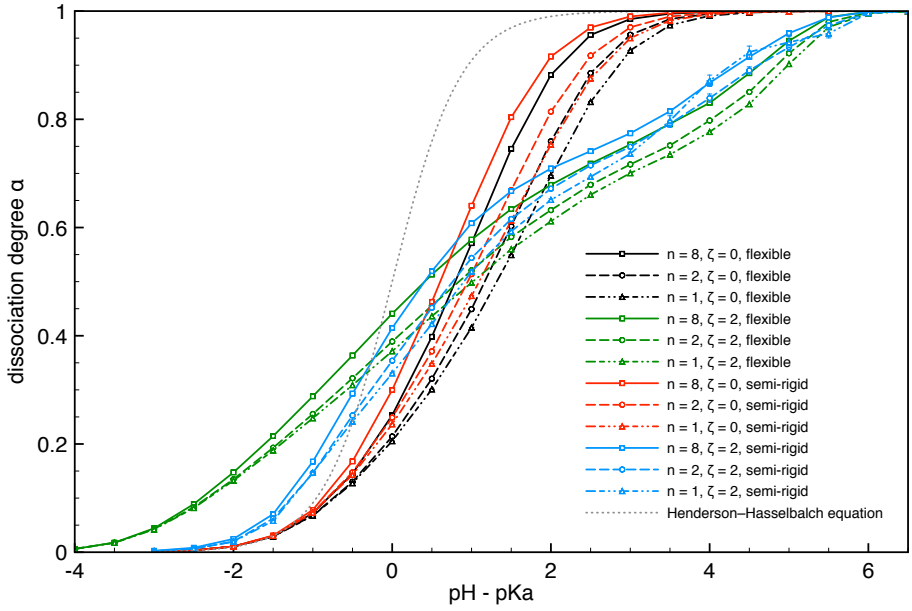

Figure 4.2: Dissociation degree α as function of the control parameter $\mathrm{pH} - \mathrm{p}K_a$ for all the combinations of n, ζ and K_{ang}. The dotted gray line indicates the ideal behavior predicted by the Henderson-Hasselbalch equation. Standard error bars are smaller than plot symbols when not visible.

centration of titratable monomers increases from $2.06 \cdot 10^{-2}$ M to $1.65 \cdot 10^{-1}$ M) we observe that the ionization degree increases. This behavior has been already pointed out in References [158] and [159], where it is shown that the dilution of a polyelectrolyte solution results in a more pronounced deviation from the ideal behavior described by the Henderson–Hasselbalch equation (see Figure 4.2). Nová et al. [159] ascribed this behavior to the fact that, when the polyelectrolyte solution is diluted, CIs are distributed over a wider volume and their lower concentration results in a weaker screening effect, and hence to a stronger repulsion of the bare charges on the chain that lead to a suppression of the acidity.

In addition to what just discussed, our simulations allowed us to investigate the role of the polymer concentration C_p when species have an intrinsic stiffness and when monomers are able to interact via c-H-bonds. In order to investigate such impact as function of C_p, we computed the differences in $\Delta\mathrm{p}K_a$ between $n = 1$ and the $n = 8$ cases, that is $\Delta_{C_p}(\Delta\mathrm{p}K_a) = \Delta(\Delta\mathrm{p}K_a) = \Delta\mathrm{p}K_a(n = 8) - \Delta\mathrm{p}K_a(n = 1)$. Results are reported in Figure 4.3. Overall, when species do not form c-H-bonds, $\Delta(\Delta\mathrm{p}K_a)$ monotonically decreases as chains ionize; this

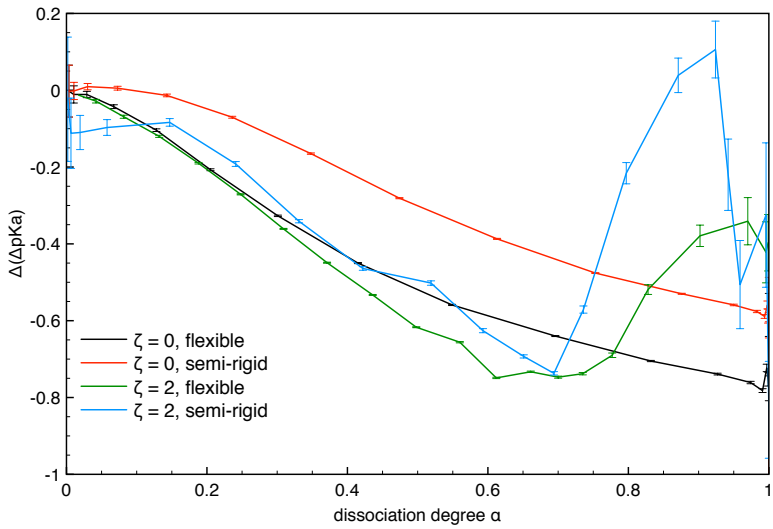

Figure 4.3: Differences in ΔpK_a versus α arising from different polyelectrolyte concentrations C_p (i.e., $n = 1$ and $n = 8$) for the four combinations of stiffness and ζ simulated.

is in agreement with the argument that polyelectrolytes acidity increases with the number of CIs in solution. Concentration has a more marked impact on the acidity of flexible chains (for which $\Delta(\Delta pK_a) \simeq -0.5$ at $\alpha = 0.5$) with respect to semi-rigid one ($\Delta(\Delta pK_a) \simeq -0.3$ at the same dissociation degree); this is ascribable to the fact that, at a given dissociation degree, flexible chains presents a higher charge density with respect to semi-rigid ones due to their smaller size (*vide infra* Figures 4.6 and 4.7) and, thus, they are able to attract more CIs.

Comparing $\zeta = 0$ and $\zeta = 2$ cases for flexible polyelectrolytes, we do not observe any specific impact of concentration at low ionization degree ($\alpha \lesssim 0.25$). At intermediate–high α values, instead, we notice an increase in acidity species able to form c-H-bonds. We suggest that this is due to the synergy between the generally more compact conformations afforded by chains able to form MB contacts (see Chapter 3 and Figures 4.6 and 4.7), which, in turn, generates a higher charge density, and the higher concentration of CIs around the polymer. This effect clearly emerges from the analysis of the pair distribution functions (PDFs) calculated between CIs and monomers reported in Figure 4.4. For semi-rigid chains, this effect is even more marked. Moreover, for stiffer species we also observe a negative $\Delta(\Delta pK_a)$ at low degree of dissociation ($\alpha \lesssim 0.2$); since CIs concentration at those dissociation degree values is very low, we ascribe such evidences mainly to the fact that chain linearization, hence the wider volume

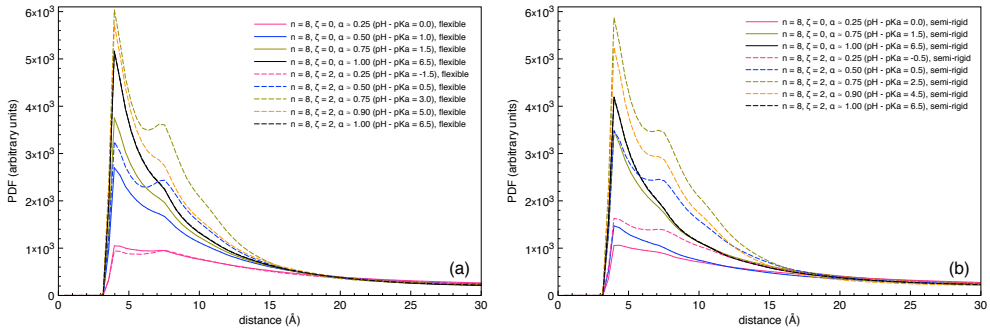

Figure 4.4: Pair distribution functions calculated between monomers (both neutral and charged) and CIs, with (dashed lines) and without (solid lines) MB interactions. Shown are data for various α values: $\alpha \simeq 0.25$ (pink), $\alpha \simeq 0.50$ (blue), $\alpha \simeq 0.75$ (olive green), $\alpha \simeq 0.90$ (orange), $\alpha \simeq 1.00$ (black). (a) flexible chains; (b) semi-rigid chains. Each distribution value has been divided by the correspondent volume element.

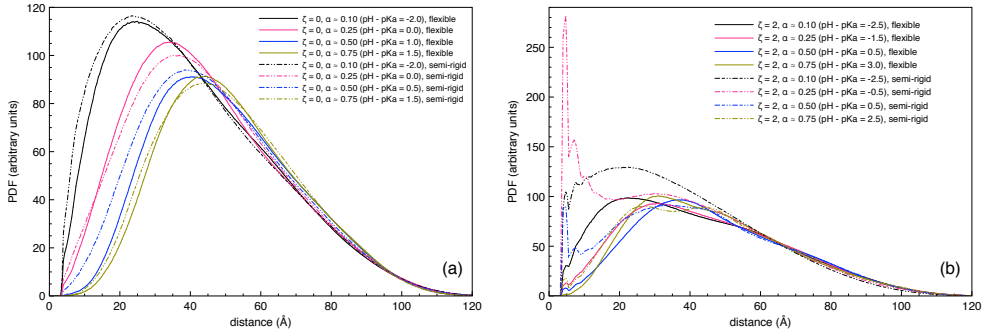

Figure 4.5: Inter–chain monomer–monomer PDFs for $n = 8$, different chain stiffness (flexible: solid lines; semi-rigid: dotted-dashed lines), and various ionization degrees. (a) $\zeta = 0$; (b) $\zeta = 2$.

swept arising from the presence of an angular term of the potential, leads to an increased probability for semi-rigid chains to form inter-chain c-H-bonds (see Figure 4.5). Finally, increasing the concentration when $\alpha \gtrsim 0.75$ results in a depression of acidity for both flexible and semi-rigid species able to form c-H-bonds, and this is due to the fact that the higher CI concentration stabilizes clusters formed by interacting ionized and neutral monomers. This prevents their dissociation, limits the increase in ionization upon increasing the pH and shifts to higher α values the dissolution of these structures.

As suggested above, inter-chain c–H–bonds may be key to rationalize ionization properties as a function of C_p; thus, Figure 4.5 reports PDFs calculated only on monomers (both neutral and charged) belonging to different chains in order to gauge their effect. Despite the fact that the control parameter of our simula-

tions is pH - pK_a, we decided to compare PDFs at the same value of α; this is due to the fact that contact probabilities and morphological properties presented directly depend on the ionization degree of the system, which, only in turn, depends on the pH. The disadvantage of this approach lies in the fact that α is not a parameter that is directly under our control, so its value for each extrapolated distribution can approximately vary by $\pm 5\%$. With this caveat in mind, it is evident that, for weak polyelectrolytes unable to form c-H-bonds (Figure 4.5 (a)), distribution peaks shift to higher values as α increases; this is attributable to an incremented repulsion between chains due to their higher charge. In spite of this, the contact probability between monomers is sizable for $\alpha \lesssim 0.5$. Moreover, one can notice that semi-rigid polymers distributions are shifted slightly further to the left with respect to flexible ones, indicating that the rigidity induced by the presence of the angular term of the potential allows monomers in different chains to come closer (i.e., it softens the effective potential of mean force between the chains).

When monomers can form c-H-bonds ($\zeta = 2$, Figure 4.5 (b)), one can instead notice more evident differences between flexible and semi-rigid species. Thus, we observe a small peak located at a distance approximately equal to l_0 when $k_{\text{ang}} = 0$, a structure denoting that monomers belonging to different chains may be in contact. The fact that this peak is not present when $\zeta = 0$ is a clear evidence of the presence of inter-chain MB interactions. For stiffer chains we notice that the peak centered in l_0 is much more pronounced and increases in intensity moving from pH - p$K_a = -2.5$ ($\alpha \simeq 0.10$, dotted-dashed black curve) to pH - p$K_a = -1.5$ ($\alpha \simeq 0.25$, dotted-dashed pink curve). Because the folding process necessary to give rise to intra-chain charged-neutral contacts in semi-rigid chains is energetically expensive, c-H-bonds can be maximized if different chains interact with each other. Conversely, a flexible chain can easily rearrange to give rise to structures that saturate the number of allowed c-H-bonds even without interacting with other chains. Said this, and bearing in mind that the maximum number of charged-neutral contacts that a charged monomer can form is $n_{\text{MB}}^{(\text{c})} = 2$, it follows that for flexible chains is entropically and energetically more favorable to form *intra*-chain c-H-bonds, whereas for semi-rigid ones can be more favorable to form *inter*-chain c-H-bonds if, during their diffusive motion, they come close together. Indications supporting these evidences may be found

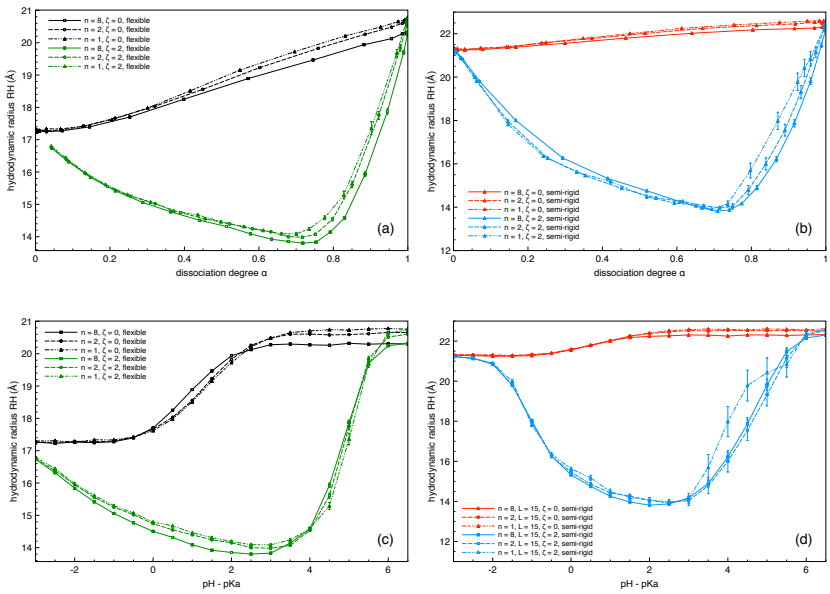

Figure 4.6: Hydrodynamic radius R_{H} as function of α (upper panels) or pH - pK_a (lower panels) for the four combination of rigidity and ζ.

also comparing snapshots extrapolated from MC trajectories shown in Figures 4.21 (a) and 4.22 (a).

4.3.2 Impact of polyelectrolyte concentration, rigidity and chemically specific interactions on chains morphology

Figures 4.6 (a) and (c) show the average hydrodynamic radius $\langle R_{\mathrm{H}} \rangle \equiv R_{\mathrm{H}}$ (see Equation 2.15) versus α for flexible chains at different concentrations with (green curves) and without (black curves) the possibility to form c-H-bonds.

For a "canonical" (i.e., $\zeta = 0$) weak polyelectrolyte, R_{H} remains nearly constant for $\alpha < 0.2$, because the charge density on the chain is not sufficiently high to induce an expansion; above that value, it increases linearly with α until the chain is fully ionized. The impact of concentration on chain size is once again in agreement with what observed by Panagiotopoulos [158] and Nová et al. [159]: the more the system is diluted, the lesser chains are screened by CIs, a situation resulting in a more marked chain swelling. When flexible polyelectrolytes are able to form c-H-bonds, the behavior of R_{H} as function of α is, instead, non-monotonic and not trivial. In fact, R_{H} decreases as chain ionization increases until $\alpha \simeq 0.7$; this is due to the fact that chains tend to form clusters in order to

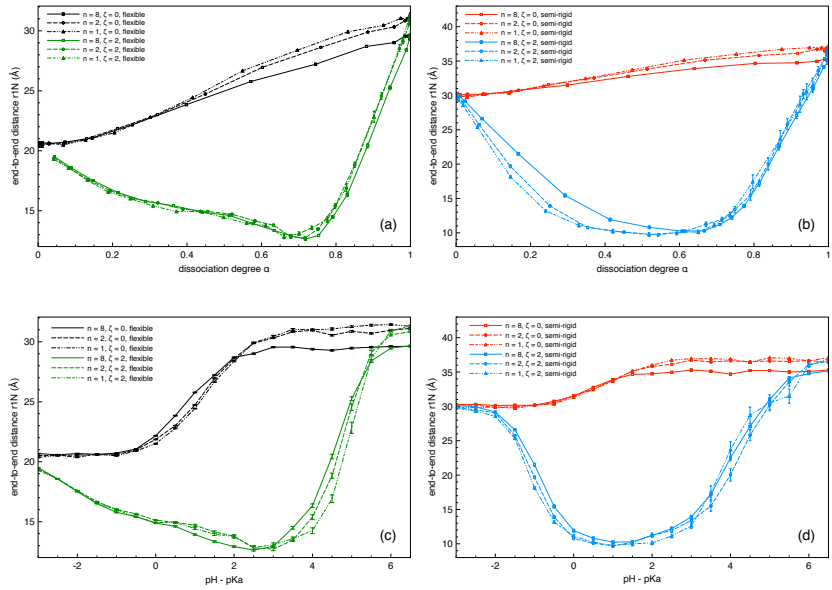

Figure 4.7: End-to-end distance r_{1N} as function of α (upper panels) or pH - pK_a (lower panels) for the four combination of rigidity and ζ.

maximize charged-neutral monomer-monomer contacts as they dissociate. A further ionization above $\alpha \simeq 0.7$ involves the breaking of MB interactions, so chains start to unfold increasing their size. Nevertheless, the effect of polyelectrolyte concentration is the same as the one observed for the $\zeta = 0$ case.

Semi-rigid chains present trends for R_{H} similar to the ones discussed for flexible species (see Figures 4.6 (b) and (d)), albeit with a noticeable difference: diluted systems composed of semi-rigid chains with $\zeta = 2$ show a slightly smaller R_{H} than more concentrated ones when $\alpha \lesssim 0.7$. Such difference can arise from the fact that is more favorable for semi-rigid chains to generate inter-chain MB interactions rather than intra-chain ones due to the bending potential; this results in less compact geometries as the repulsive Coulomb force increases upon dimerization.

The behavior of the average end-to-end distance $\langle r_{1\mathrm{N}} \rangle \equiv r_{1\mathrm{N}}$ (see Equation 2.13) appears very similar to the one observed for R_H (see Figure 4.7), and it would seem to require no additional comments. In spite of this, probability distributions for $r_{1\mathrm{N}}$ (Figure 4.8) indicate that the behavior of polyelectrolytes with $\zeta = 2$ is far more complicate and interesting than the simpler average values suggested. Thus, while we observe smooth, albeit asymmetric, distributions that

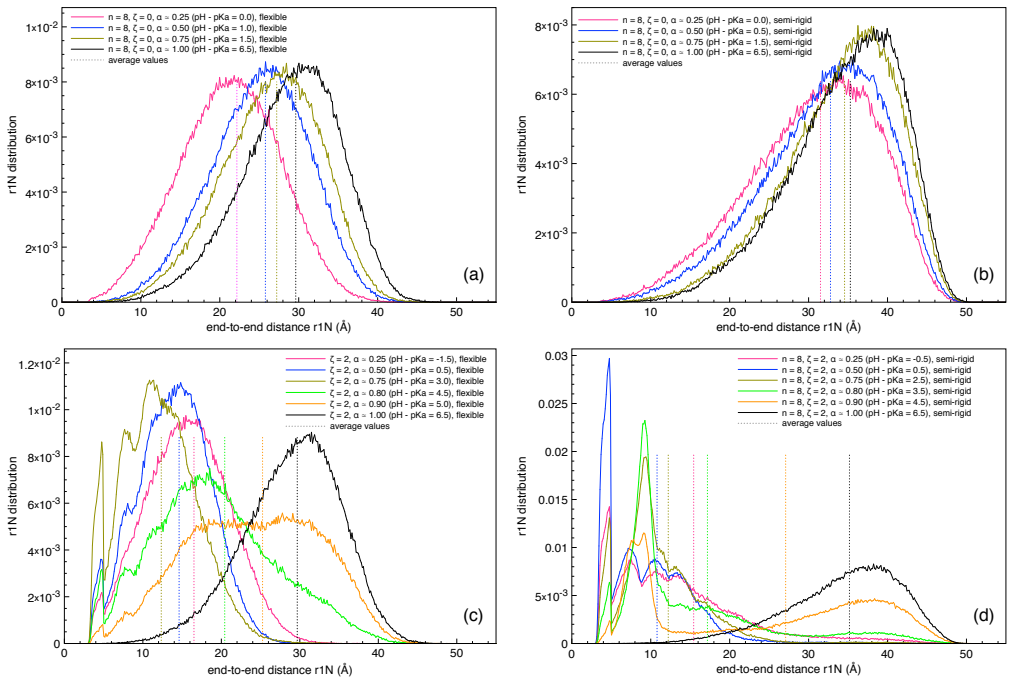

Figure 4.8: End-to-end r_{1N} distributions for the four systems: (a) $k_{\text{bend}} = 0$, $\zeta = 0$; (b) $k_{\text{bend}} = 2 \cdot 10^{-3} k_B T/\text{deg}^2$, $\zeta = 0$; (c) $k_{\text{bend}} = 0$, $\zeta = 2$; (d) $k_{\text{bend}} = 2 \cdot 10^{-3} k_B T/\text{deg}^2$, $\zeta = 2$. Shown are distributions for various values of the dissociation degree: $\alpha \simeq 0.25$ (pink), $\alpha \simeq 0.50$ (blue), $\alpha \simeq 0.75$ (olive green), $\alpha \simeq 0.80$ (bright green), $\alpha \simeq 0.90$ (orange), $\alpha \simeq 1.00$ (black). Dotted vertical lines identify average values (from Figure 4.7). These distributions are obtained from simulations with $n = 8$ in order to maximize the number of statistical samples.

shift toward longer distances as α increases when $\zeta = 0$ ((a) and (b) panels), $\zeta = 2$ distributions are more intricate. Considering flexible species first (Figure 4.8 (c)), we observe that distributions shift toward shorter r_{1N} as α increases from 0.25 to 0.75, with chains assuming globular conformations due to the tendency to form intra-chain c-H-bonds. More interestingly, we observe the growth of peaks centered at values that are multiple of l_0, which indicate that polyelectrolytes can fold onto themselves placing their extremes at relative positions commensurate with their monomer spacing, a behavior that may also appear if ion coordination is allowed [131, 132]. As ionization further increases, distributions shift toward longer r_{1N} due to the increases Coulomb repulsion; it is, however, apparent that polyelectrolytes exist in two states (see, e.g., distribution at $\alpha = 0.90$, orange curve), a globular (or clustered) one and a coiled (or unfolded) one, depending on the number intra-chain c-H-bonds they form (see also Figure 4.21).

The behavior discussed becomes even more extreme for semi-rigid chains (panel (d) of Figure 4.8, and Figure 4.22), with the very sharp and tall peaks at low r_{1N} values indicating chains tendency to maximize MB interactions by forming one (or sometimes two) hairpins. Interestingly, we notice that Coulomb repulsion becomes too strong making the symmetrical hairpins energetically less favorable than asymmetrical ones when $\alpha \simeq 0.75$–0.80, inducing the enhancement of a peak centered at $\sim 2.5 l_0$ at the expense of other peaks. Finally, chains start to unfold when the ionization increases further ($\alpha \simeq 0.90$), and the distribution becomes clearly bimodal.

In principle, behaviors evidenced for r_{1N} distributions when $\zeta = 2$ could indicate the presence of a phase transition. In order to verify such hypothesis, we computed

$$\Omega = \frac{\langle U_{\text{tot}}^2 \rangle - \langle U_{\text{tot}} \rangle^2}{\langle N_{\text{tot}} \rangle k_{\text{B}} T^2}; \tag{4.5}$$

here, U_{tot} is the total potential of the system (see Equation 2.10), $\langle N_{\text{tot}} \rangle$ is the average number of particles in the cell and $\langle U_{\text{tot}}^2 \rangle - \langle U_{\text{tot}} \rangle^2$ is the variance of U_{tot}. For our systems, which are simulated in the constant-pH ensemble, Ω represents a component of the thermal capacity at constant volume C_V, a property that is usually used to detect first- and second-order phase transition in grand-canonical simulations. Results are illustrated in Figure 4.9. When species are not able to form c-H-bonds, Ω grows monotonically with α. The fact that, at low ionization

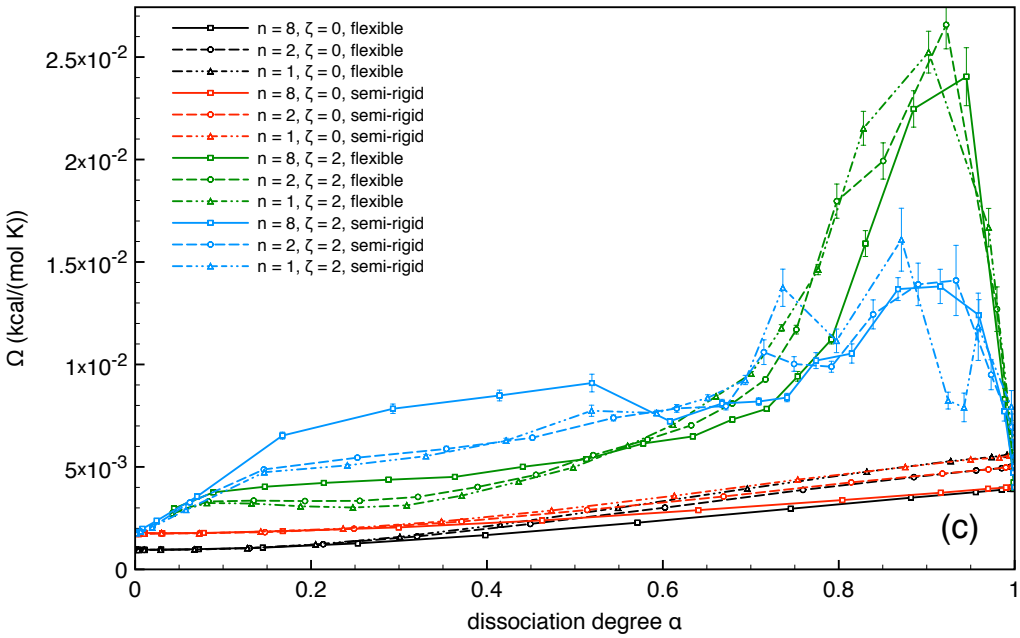

Figure 4.9: Ω in kcal/(mol K) as a function of α.

degrees, Ω assumes higher values when chains are semi-rigid simply depends on the presence of the angular term in the total potential U_{tot}: when α increases, Ω converges to the same value for both flexible and stiffer cases because the lack of an angular potential in the flexible case is partially compensated by the stiffening deriving from charges accumulation on the polyelectrolyte, and also because Ω is averaged on the total number of particles $\langle N_{\text{tot}} \rangle$, which increases as monomers dissociate (so that the impact of U_{bend} on Ω becomes lower).

When c-H-bonds can form, instead, Ω shows a non–monotonic behavior as function of α. At low–intermediate dissociation degrees, we thus observe that Ω increases both for flexible chains and semi-rigid chains due to the formation of MB interactions; in the latter case the increment is more marked due to presence of the angular term in the potential. Upon increasing α above 0.5, for stiffer chain we observe also a moderate decrease in Ω due to a loss of MB contacts (this probably correspond to the transition from a symmetric to an asymmetric bending discussed previously) before the polyelectrolyte starts to unfold. This feature is not present in the case of flexible chains, which, at most, show the presence of an inflection point around $\alpha = 0.6$.

Finally, both flexible and semi-rigid chains present a peak centered at $\alpha \simeq$

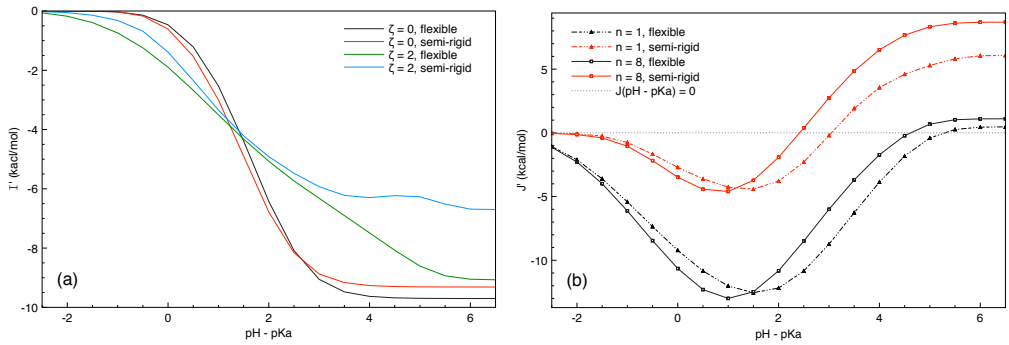

Figure 4.10: (a) I' (in kcal/mol) as function of pH - pK_a for the four combinations of ζ and chain rigidity investigated for $n = 8$; (b) J' (in kcal/mol) for $n = 1, 8$ and for different chain stiffness.

0.9, which we interpret as a sign of a first order phase transition from a folded geometry to an unfolded one. The difference in peak height ($1.4 \cdot 10^{-2}$ kcal/(mol K) for semi-rigid chains and $2.4 \cdot 10^{-2}$ kcal/(mol K) for flexible ones) arises from the presence of the angular potential in semi–rigid chains potential, for which unfolding is energetically less demanding. Worth noticing, the fact that the unfolding process takes place at such high α values probably derives from our choice of parameters defining MB interactions (in particular $n_{\mathrm{MB}}^{(\mathrm{n})} = \infty$, a choice made to reduce the computational cost of evaluating MB interactions knowing that it does not modifies the qualitative behavior of titration curves and of the system overall – see Chapter 3).

4.3.3 Impact of polyelectrolyte concentration, rigidity and chemically specific interactions on Helmholtz energy

In order to investigate the impact of polyelectrolyte concentration on system Helmholtz energy A, we computed $I'(\mathrm{pH}^*, C_{p,1}, C_{p,2})$ (see Equation 4.2) for the four combinations of stiffness and ζ. In practice, since the volume of our system is fixed, we compared simulations with $n = 1$ and $n = 8$ chains inside the cell. Results are reported in Figure 4.10 (a). I' assumes negative values in the whole range of pH explored and for all the investigated species, and it is a monotonic decreasing function of pH - pK_a (and, consequently, of α) for all the cases analyzed, exception made for stiffer chains with MB interactions at pH - p$K_a > 4$. This general trend descends from the fact that the ability of screening polyelectrolyte charges by the CIs increases more rapidly when 8 chains are present compared

to the single chain case upon increasing the pH and (hence) ionization.

At a finer level of details, our data indicate that I' is lower for the c–H–bonding chains when pH - p$K_a \leq 1.5$, the flexible species being the one that gain the most by the increase in concentration probably due to their higher ionization at low pH. The latter idea also justifies the finding that chains with $\zeta = 0$ present a more negative I' when pH - p$K_a \geq 1.5$ (see Figure 4.2), whereas the crossing of I' curves for semi–rigid and flexible species around pH - p$K_a \geq 2.5$ is likely to be due to the higher difference in α as a function of n seen for the latter polymers.

To investigate with precision the impact of MB interactions on A, we also computed the quantity J' (Equation 4.4); results are shown in panel (b) of Figure 4.10. Here, we notice that $J' < 0$ over the vast majority of the pH range explored and the stabilization due to c-H-bonds is less marked in the semi-rigid case than for flexible species. As in the rationalization provided for the relative value of α, we attribute this finding to a lower neutral–charged monomers contact probability.

4.4 Results and discussion: window sampling simulations

The results discussed in Section 4.3, together with the data presented in References [158] and [159], indicate the macroscopic impact of C_p on the behavior of linear polyelectrolytes. They, however, shed only limited light on the microscopic changes that relate with such macroscopic aspects. Thus, to improve our understanding of these systems, especially when c-H-bond can be formed, we performed window sampling (WS) simulations (see Section 4.4) in order to investigate the behavior of two chains and their CIs as function of chain centers of mass (CoMs) distance, d_{CoMs}. The intervals of d_{CoMs} considered in our WS simulations are summarized in Table 4.2.

As a general comment on the quality of our WS simulations, let us mention that distributions in overlapping windows were invariably found to run parallel to each other, a finding indicating that they differed only by a multiplicative constant. This, in turn, suggested the lack of need for more complicate simulation schemes such as replica exchange, a finding probably due to the length of our simulations, the "softness" of the restrained coordinate d_{CoMs}, the implementation

of cluster moves (pivot moves and rigid translations) in our simulation algorithm, and, obviously, the fact that we are simulating short chains.

Table 4.2: List of the intervals of CoMs distances, $d_{\mathrm{CoMs}} \in (a, b]$, sampled in our WS simulations. The "TOT." tag refers to the case in which the two chains are free to move in the cavity without any additional constraint (as in titration simulations described in Section 4.3). Intervals recurring in subsequent Figures are highlighted in bold.

	a (Å)	b (Å)
INT. 01	**0.0**	**2.6**
INT. 02	0.0	5.3
INT. 03	**2.6**	**7.9**
INT. 04	5.3	13.2
INT. 05	**7.9**	**18.5**
INT. 06	13.2	23.8
INT. 07	**18.5**	**29.1**
INT. 08	21.2	34.4
INT. 09	29.1	42.3
INT. 10	37.0	50.3
INT. 11	45.0	58.2
INT. 12	**52.9**	**66.1**
TOT.	**0.0**	**66.1**

4.4.1 Impact of inter-chain interactions on ionization behavior, counterion distribution and polymer conformations

Figure 4.11 shows $\Delta \mathrm{p}K_a$ as function of α when the CoMs of two chains are restrained to lie within a specific interval of distances, that is $d_{\mathrm{CoMs}} \in$ (a,b] (see Table 4.2). When $\zeta = 0$ $\Delta \mathrm{p}K_a$ always increases as d_{CoMs} diminishes. This effect arises from the fact that the closer are polymers, the stronger is repulsion between charges. The highest difference between well separated chains (INT. 12) and chains in contact (INT. 01) is observed in the range of ionization $\alpha = 0.25 \div 0.50$, with a maximum distance-depending variation of $\Delta \mathrm{p}K_a$ of roughly 0.4 pK_a units for flexible polymers and 0.3 pK_a units for semi-rigid ones.

When c-H-bonds can form, instead, we observe a trend reversal at low α values ($\alpha \lesssim 0.07$ in the flexible case, see also the inset in Figure 4.11 (a); $\alpha \lesssim 0.20$ in the semi-rigid one). In the latter case, nearby chains ionize more easily with respect to separated ones thanks to the formation of inter-chain c-H-bonds, an effect

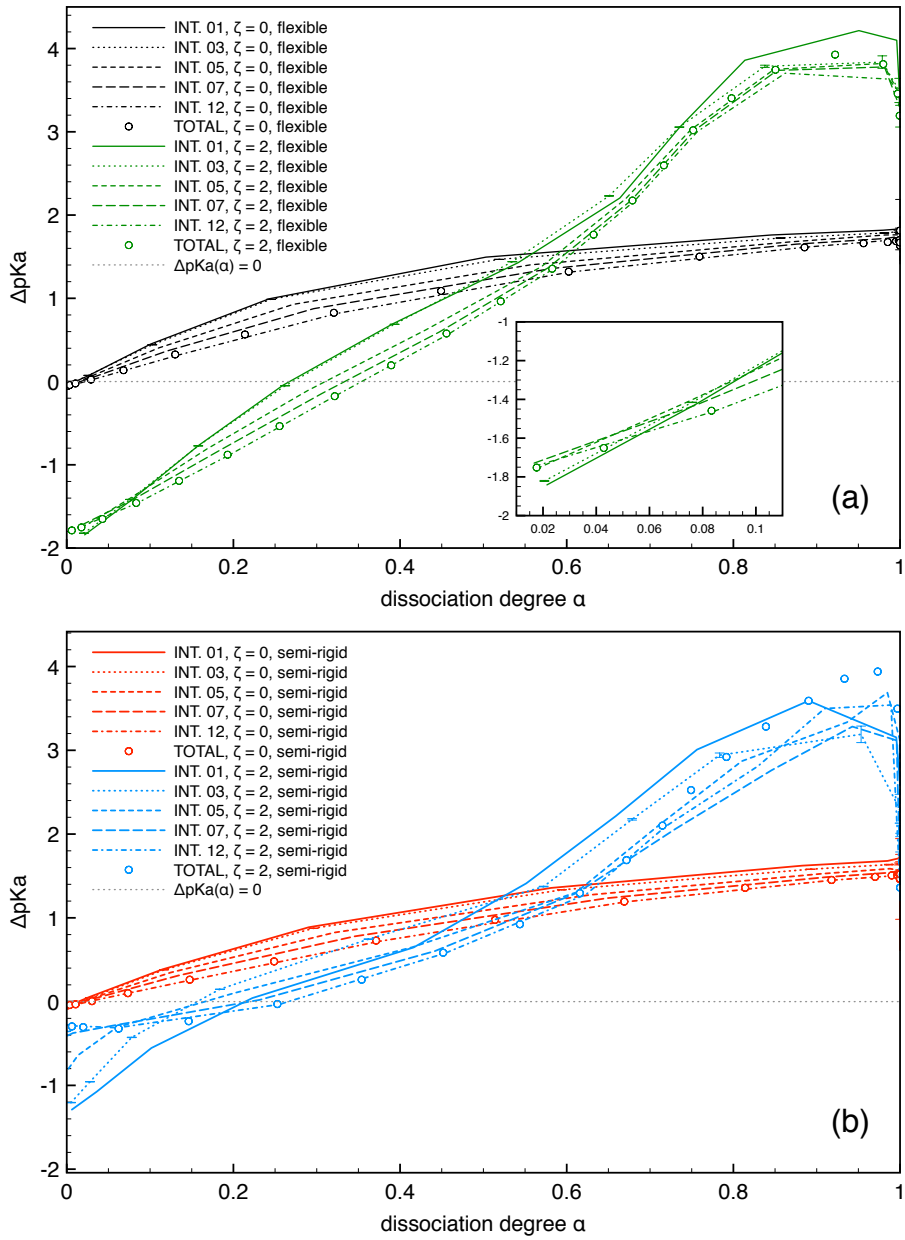

Figure 4.11: $\Delta \mathrm{p}K_a$ as function of α for various d_{CoMs} intervals: (a) flexible, and (b) semi-rigid chains. The dashed gray line is only a guide to the eye in order to discern positive and negative values of $\Delta \mathrm{p}K_a$. The inset in panel (a) shows the behavior of $\Delta \mathrm{p}K_a$ for flexible chains when $\alpha < 0.2$. With the hope to improve chart readability, standard error bars has been plotted only for the "INT 03" case

intensified and extended to longer d_{CoMs} when semi-rigid species are involved, probably due to their larger span. Finally, we mention that oscillations in $\Delta \mathrm{p}K_a$ observed for the latter species when $\alpha \gtrsim 0.8$ arise from the fact that simulations may become less ergodic in presence of many c-H-bonds.

Given the results in Figure 4.11, one may wonder if the effects on α mentioned have a local counter part, as it is a well know effect in linear weak polyelectrolytes that monomers lying at the extremes of a chain tend be more likely to ionize than ones located in polymer inner regions. Thus, Figure 4.12 shows the ionization degree α as a function of their position along the polymer, the pH and d_{CoMs}. The value is averaged over the two chains, and all the four combinations of stiffness and ζ are shown.

When $\zeta = 0$ (Figures 4.12 (a) and (b)), we observe the expected behavior for both flexible and semi-rigid species kept at long distances. Decreasing the distance between interacting chains results in a magnification of the differences in ionization, so that $\Delta(\Delta \mathrm{p}K_a) \simeq 0.71$ for flexible species and $\Delta(\Delta \mathrm{p}K_a) \simeq 0.75$ for semi-rigid ones when $d_{\mathrm{CoMs}} < 2.5$ Å and pH - pK_a = 1.50. Looking at trajectory snapshots (Figures 4.23 and 4.24), we observe that the more marked decrease in acidity of central beads depends on the "χ-shaped" geometry assumed by two nearby chains.

When polyelectrolytes are able to form c-H-bonds, the behavior becomes once again more complicated. Analyzing the case of flexible chains first, we notice that charges are uniformly distributed over all the polymer when pH - pK_a is low ($\alpha \lesssim 0.4$), exception made for second-last monomers, which are slightly less acidic than the others. This depends on the fact that end monomers can back-bend, dissociate and form a c–H–bond with third-last beads, resulting in a depressed acidity of the penultimate beads. At intermediate pH - pK_a values, the behavior followed by α becomes much less regular, showing marked oscillations as a function of the monomer location. As d_{CoMs} decreases, oscillations appears less marked, suggesting that the closeness between the two chains may induce their partial elongation and linearization. Finally, the dissociation of internal monomers at high α and low CoMs distances results partially inhibited as a consequence of their reciprocal position and orientation of the two chains.

Local ionization behavior tends to become even more intricate for semi-rigid chains. For instance, we notice at the onset that many curves are not symmetric

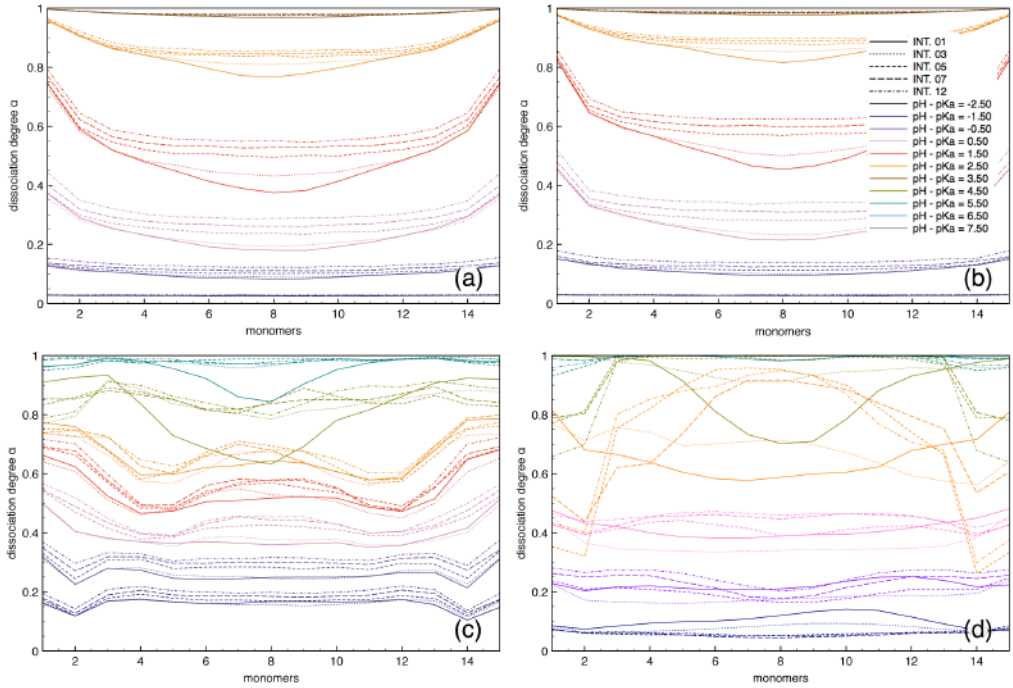

Figure 4.12: Average α as function of the monomer position along the chains for different pH - pK_a and d_{CoMs} values: (a) $\zeta = 0$, flexible; (b) $\zeta = 0$, semi-rigid; (c) $\zeta = 2$, flexible; (d) $\zeta = 2$, semi-rigid.

probably due to a partial failure of Monte Carlo sampling to obtain ergodicity. At low values of pH - pK_a, we do not observe the depression of α seen for the penultimate monomer of flexible species, since this effect is hampered by the local rigidity. At intermediate pH (e.g., pH - pK_a = 2.50, orange curves), instead, well separated chains (INT. 07–12) show the tendency to being dissociated preferably around midpoint; this is probably due to the fact that chains are too far to interact with each other but they tend to bend on themselves forming a folded conformation in which central monomers give rise to a central neutral core that stabilize the surroundings dissociated monomers (see, e.g., Figure S4.26 (n)). When the two chains are close together (INT 01, 03), they instead tend to arrange parallel to each other in order to maximize MB contacts. From trajectory snapshots (Figure S4.26 (b), (c), (f), (g)) we observe that this parallel disposition maximize the number of c-H-bonds inter-chain c-H-bonds, with portion of neutral and charged segments that alternate on both polyelectrolytes.

An alternative viewpoint useful to characterize the restrained systems is represented by the behavior of the total potential U_{tot} versus d_{CoMs}. Analyzing this for the $\zeta = 0$ case at several α or pH - pK_a values (data shown in Figures 4.13 and 4.14, respectively), we observe that U_{tot} monotonically increases with α for both flexible and semi-rigid species, as it would be expected by the fact that electrostatic repulsion between monomers cannot be fully screened by the presence of CIs, which only partially distribute on the chains. In spite of this, it emerges also that bringing two chains close together does not always involves an increment in the total potential U_{tot}. Thus, when species are infinitely flexible (Figure 4.13 (a)), we note that U_{tot} increases as d_{CoMs} decreases only if $\alpha < 0.5$; the trend results instead reversed for $\alpha > 0.5$. This behavior takes place because the more the two polyelectrolytes are ionized and close to each other, the higher is the charge density due to the "complex" they form; this fosters CIs accumulation, which in turn screens electrostatic repulsion between the two polyelectrolytes lowering U_{tot}. A similar behavior can be observed also for semi–rigid species (see Figure S4.13 (b)).

Supports for this rationalization come from Figure 4.15 (a), which shows PDFs calculated between monomers (both neutral and charged) and CIs for fully ionized (pH - pK_a = 6.5) interacting polyelectrolytes at different d_{CoMs}. When the two chains are well separated (INT.12), we notice the presence of two separated

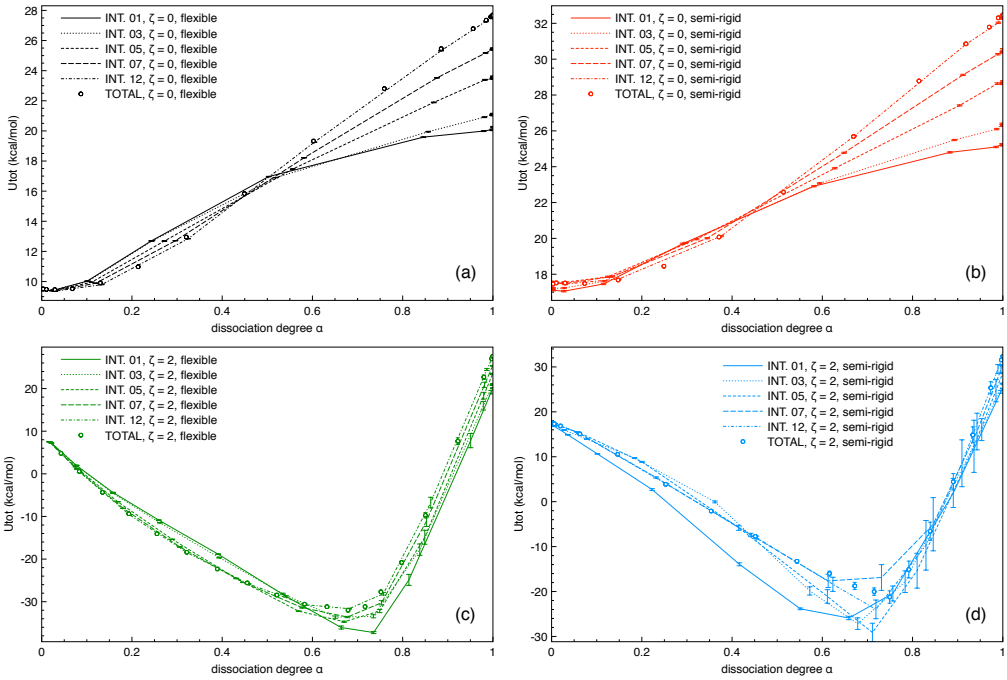

Figure 4.13: Total potential $U_{\rm tot}$ (in kcal/mol) as a function of α for different intervals of $d_{\rm CoMs}$: (a) flexible, $\zeta = 0$; (b) semi-rigid, $\zeta = 0$; (c) flexible, $\zeta = 2$; (d) semi-rigid, $\zeta = 2$.

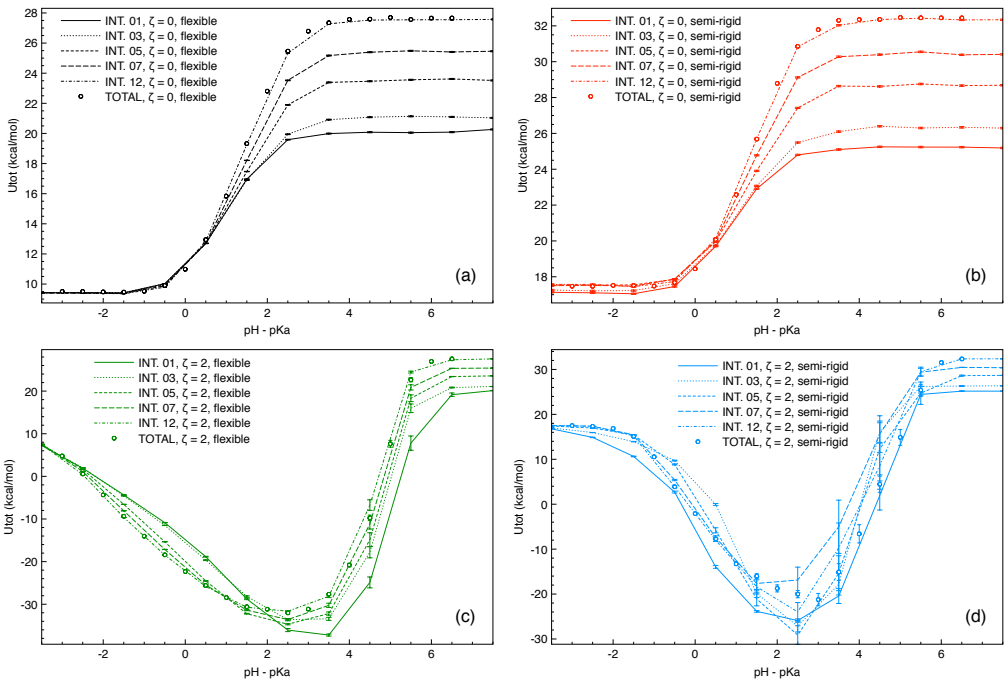

Figure 4.14: Total potential energy $U_{\rm tot}$ as a function of pH - pK_a: (a) $\zeta = 0$, flexible; (b) $\zeta = 0$, semi-rigid; (c) $\zeta = 2$, flexible; (d) $\zeta = 2$, semi-rigid.

peaks indicating that each macromolecule possesses its own cloud of CIs. As the polyelectrolytes approach each other (intermediate distances, INT. 07), CIs surrounding one chain start to feel the partially screened electrostatic attraction coming from the other one, so they move in the region of space between the two polyelectrolytes. Finally, when chains are close together (INT 01, 03) we observe only a marked peak, followed by a shoulder representing those CIs not in between the polyelectrolytes. Notice that, whatever is the interval of d_{CoMs} values simulated, flexible chains appear able to attract more CIs on themselves, due to the slightly more compact conformations they are able to assume.

As for chains with $\zeta = 2$, we notice that U_{tot} decreases upon increasing α up to 0.7 due to the formation of c-H-bonds. As polyelectrolytes further dissociate, the potential increases as a consequence of the decrease in the number of neutral monomers, which are needed for those stabilizing interactions. From Figures 4.13 and 4.14 (panels (c) and (d)), it is also evident that the finer details of U_{tot} behavior are once again made more complicated by the presence of c-H-bonds, which make them markedly dependent on the relative distance between chains, the conformations that these are forced to assume, as well as the propensity to attract CIs. In case of semi-rigid chains, the possibility of a limited ergodicity of the Monte Carlo sampling when $\alpha > 0.6$ may also impact on the precision of our results.

With the aim of shedding some light on the intricate behavior of U_{tot} in presence of c-H-bonds, we now look at monomer–CIs pair distribution functions sampled at pH - pK_a = 3.0 (which corresponds $\alpha \simeq 0.6$–0.7, depending on the polymer stiffness) and for several intervals of d_{CoMs} (Figure 4.15 (b)), together with a few conformations extracted during our simulations (Figures 4.25 and 4.26). As for CI distributions, albeit the general trend is similar to the one shown in panel (a) of Figure 4.15 for $\zeta = 0$, we can evidence a few differences. First of all, the distribution peaks at short distances appear more structured than when $\zeta = 0$, evidencing that the presence of c-H-bonds makes the polymer fold on itself and generate closely packed clusters. Moreover, peaks at short distances increase as the flexible chains approach each other, thus indicating that CIs tend to move in the region between polymers, whereas the main distribution peak for semi–rigid species decreases in intensity in passing $d_{\mathrm{CoMs}} \in (7.9\ \text{Å}, 18.5\ \text{Å})$ to $d_{\mathrm{CoMs}} \in (0.0\ \text{Å}, 2.6\ \text{Å})$. The origin of such difference becomes evident looking at the

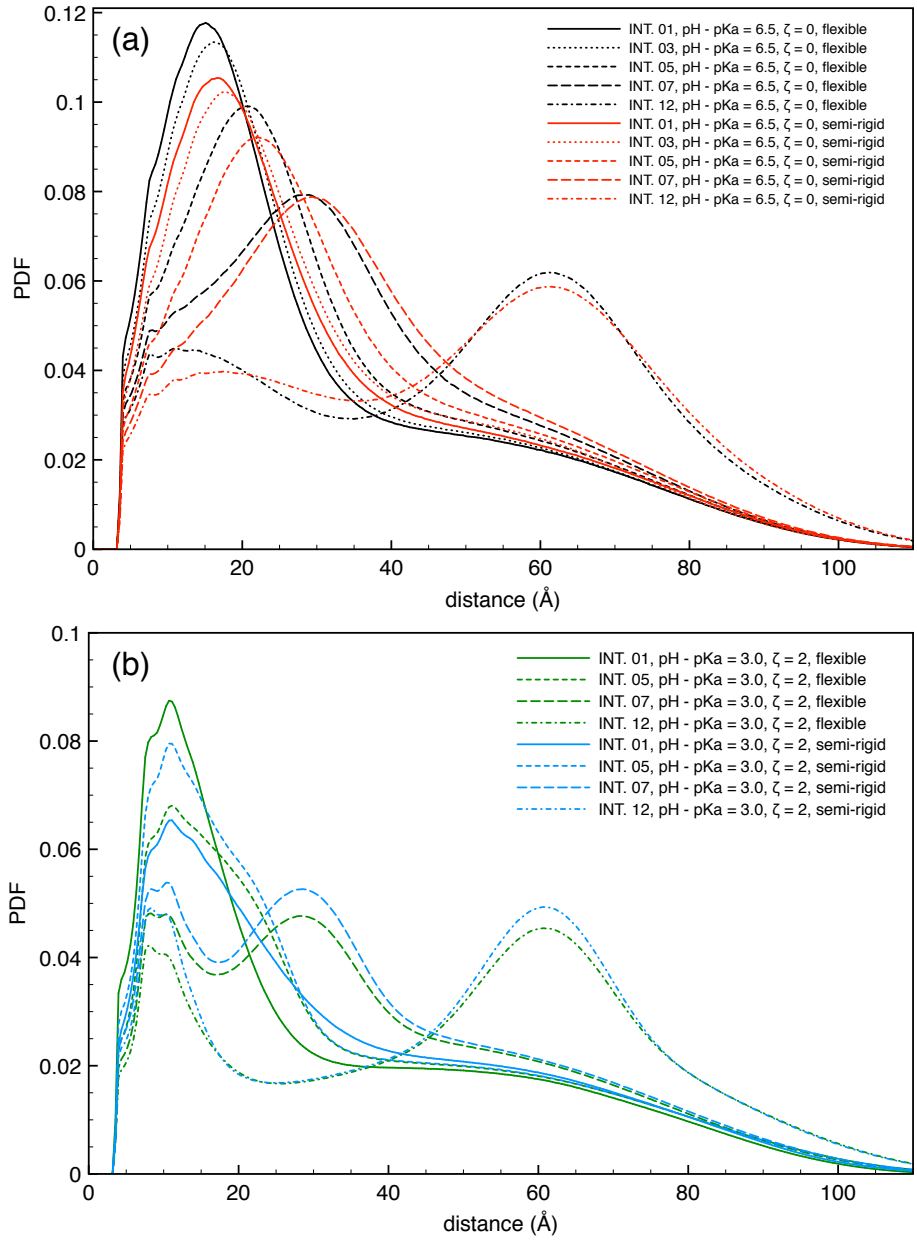

Figure 4.15: Monomers-CIs pair distribution functions for different d_{CoMs} intervals: (a) $\zeta = 0$, pH - pK_a = 6.5 (notice that the same distributions for species with $\zeta = 2$ should converge to the plotted curves as pH - p$K_a \to \infty$); (b) $\zeta = 2$, pH - pK_a = 3.0.

corresponding trajectory snapshots (panels (c) and (k) in Figures 4.25 and 4.26), where it is shown that flexible chains conserve CIs between themselves thanks to the irregular form of their coils, whereas two semi–rigid chains arrange parallel to each other so as to maximize lateral contacts and leave no enough space for CIs between them. Conformations help also to rationalize the difference in behavior between flexible and semi–rigid chains at low ionization ($\alpha \leq 0.65$), where the former present an increasing value of U_{tot} for decreasing d_{CoMs}, whereas the trend is more erratic for semi–rigid chains. *De facto*, flexible polymers forming c–H–bonds behave akin to similar species with $\zeta = 0$, showing an increase in Coulomb repulsion upon decreasing their distance despite the CIs screening due to their cluster–like form. Conversely, the juxtaposition between a rod–like conformation and chain vicinity when $d_{\text{CoMs}} \in (0.0\ \text{Å}, 2.6\ \text{Å})$ allows semi–rigid chains to align and form many more MB contacts than when restrained at longer d_{CoMs}.

To conclude the presentation of results obtained with WS simulations, we provide a more quantitative gauge of the conformational behaviors pictorially shown in Figures 4.25 and 4.26. Thus, Figure 4.16 shows the average $r_{1\text{N}}$ as function of α at different d_{CoMs} values. In absence of MB forces, for a chosen degree of ionization chains elongation tends to increase as they approach one to each other (or at a certain pH value). Deviations from such behavior are however observed when polyelectrolytes are highly ionized. Thus, we notice that chains restrained to have $d_{\text{CoMs}} \in (7.9\ \text{Å}, 18.5\ \text{Å})$ show an higher $r_{1\text{N}}$ than when $d_{\text{CoMs}} \in (0.0\ \text{Å}, 2.6\ \text{Å})$, an unexpected result that can be understood looking at the conformation assumed by the system in the latter case and shown in Figure 4.17 for semi-rigid fully ionized polyelectrolytes. Thus, while panel (a) shows th previously discussed "χ-shaped" conformation, the rotate perspective in panel (b) evidences that chains are bent (i.e. they reduce their $r_{1\text{N}}$) in order to attract more CIs.

As for the $\zeta = 2$ cases, we observe that flexible polymers closely follow the non-monotonically behavior already described for unrestrained chains (see Figure 4.6), extending upon reducing inter-chain distance. At variance with such regular behavior, semi–rigid polymers present a local maximum in the value of $r_{1\text{N}}$ when $\alpha \simeq 0.55$ and $d_{\text{CoMs}} \in (0.0\ \text{Å}, 2.6\ \text{Å})$. This feature is rationalized by the energetic advantage gained upon extension by the chains, as this conformation would allow them to orient in parallel and form many c-H-bonds simultaneously (see Figures

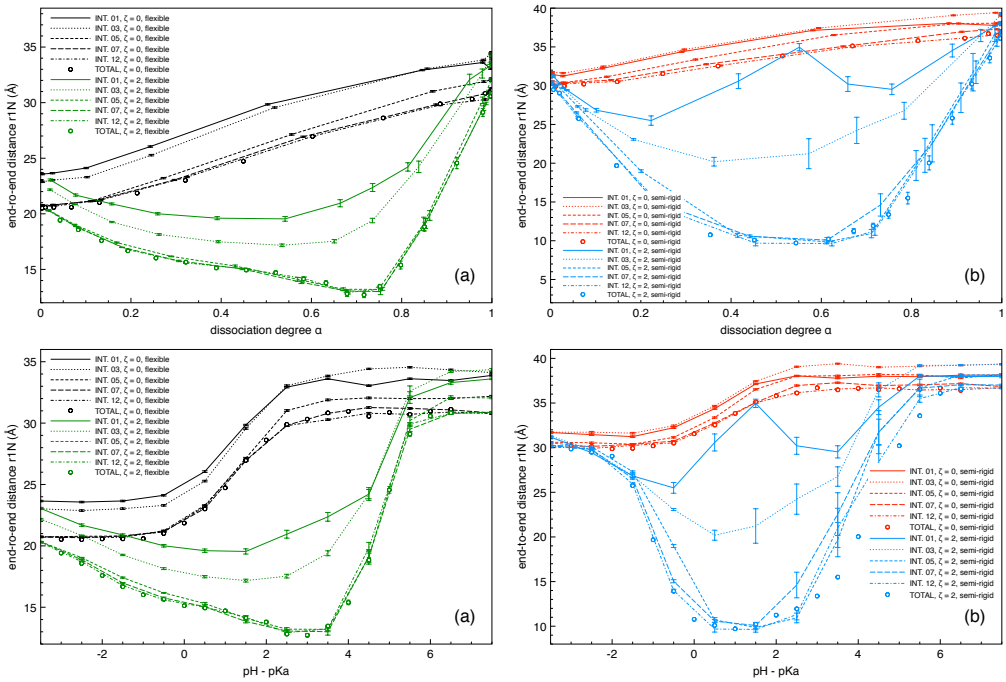

Figure 4.16: End-to-end distance r_{1N} as a function of α (upper panels) and pH - pK_a(lower panels) for different intervals of d_{CoMs}: panels (a) and (c) flexible chains; (b) and (d) semi-rigid ones.

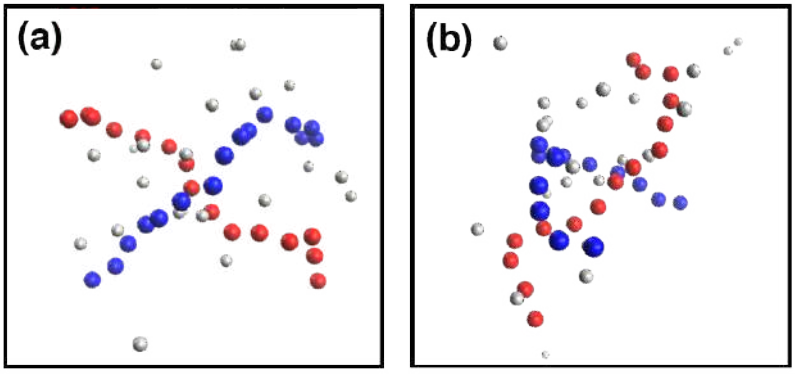

Figure 4.17: Trajectory snapshots showing two fully ionized (pH - p$K_a = 4.5$) interacting flexible chains (INT. 01). The two chains are drawn in red and blue, CIs in white. Panels (a) and (b) represent the same identical snapshot but seen from two different perspectives.

4.26 (b) and (c)).

4.4.2 Potential of mean force calculations

The chains properties as a function of both the distance between their centers of mass d_{CoMs} and their ionization degree α presented in Section 4.4 evidenced interesting differences in behavior for the systems investigated; however, their impact depends on the relative probability of finding two chains within a specific range of distances. Obviously, this probability can be "manipulated" experimentally by appropriately choosing the system concentration. This notwithstanding, there is still a (at least entropic) cost to be paid for two chains to closely approach each other, and it seems useful to provide quantitative indications on how such cost depends on polyelectrolytes peculiarities. Thus, we computed $\Delta w(d_{\mathrm{CoMs}}) = w(d_{\mathrm{CoMs}}) - w(\infty)$, which is the amount of reversible work required to bring two chains at the distance d_{CoMs} if, initially, their CoMs lay at infinite separation. We arbitrary set $w(\infty) = 0$, as our interest is on the relative change in Helmholtz energy along the process. Results for the four combinations of ζ and stiffness are shown in Figure 4.18.

When $\zeta = 0$, Figure 4.18 (a), $\Delta w(d_{\mathrm{CoMs}})$ monotonically increases as $d_{\mathrm{CoMs}} \to 0$; moreover, $\Delta w(d_{\mathrm{CoMs}})$ increases with pH (and, hence, α). These evidences can be explained by the progressive increment of the repulsive electrostatic forces acting between the two polyelectrolytes, plus additionally contributions of excluded volume effects when chains are close together. For two flexible chains, thus, $w(10\ \text{Å}) \simeq 2.5$ kcal/mol $\simeq 3.8 k_{\mathrm{B}}T$ at pH - p$K_a = -1.5$, whereas $w(10\ \text{Å}) \simeq 11.5$ kcal/mol $\simeq 17 k_{\mathrm{B}}T$ at pH - p$K_a = 7.5$. PMF curves calculated for semi-rigid chains lies always below flexible ones for distances $d_{\mathrm{CoMs}} < 15$ Å, indicating that rod–like conformations lower the work required to bring together two semi-rigid chains.

Turning to flexible polyelectrolytes able to form c-H-bonds (Figure 4.18 (b)), our results highlight that $\Delta w(d_{\mathrm{CoMs}})$ does not monotonically increase as the pH rises when chains are close together ($d_{\mathrm{CoMs}} \lesssim 10$ Å). Worth noticing, the decrease of Δw upon increasing pH at short d_{CoMs} ought to be taken as an evidence of the possibility for them to stabilize each other via the formation of inter-chain c-H-bonds (see upper panels of Figures 4.25). Moreover, we observe that there is

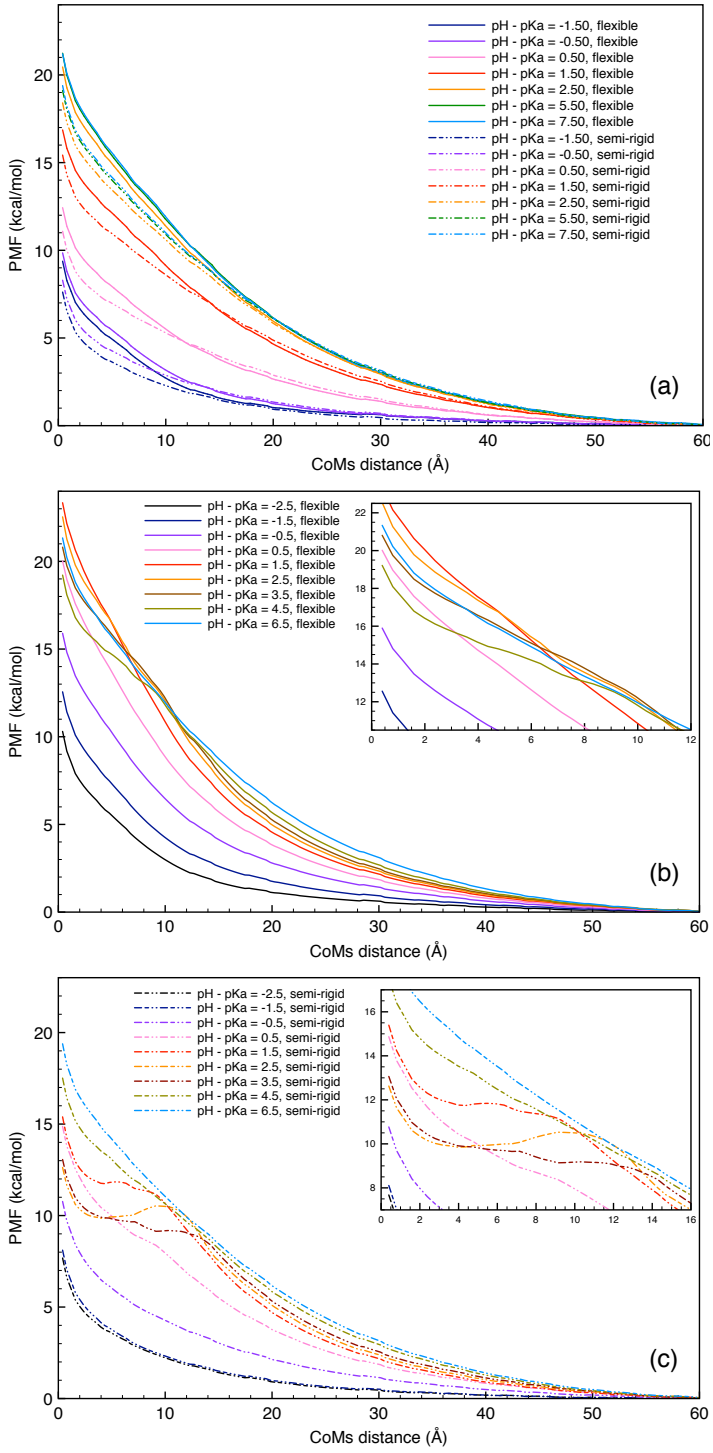

Figure 4.18: Potentials of mean force as function of pH - pK_a for flexible (solid lines) and semi-rigid (dotted–dashed lines) chains: (a) $\zeta = 0$;(b) and (c) $\zeta = 2$.

a range of short distances in which the PMF curve for fully ionized chains (pH - pK_a = 6.5) lies below the curve calculated at pH - pK_a = 1.5; we attribute this behavior to the fact that fully ionized chain can attract more CIs, which screen repulsive electrostatic interactions between the two macromolecules.

Charged H-bonds impact is even more pronounced for semi-rigid species (Figure 4.18 (c)); thanks to the fact that the two chains can arrange parallel to each other (Figure 4.26 (c)), we observe the presence of a minimum located at $d_{\mathrm{CoMs}} \simeq 2.5$ Å, $\Delta w(2.5\ \text{Å}) \simeq 10$ kcal/mol (roughly $15 k_{\mathrm{B}}T$ units above the energy at infinite separation) when pH - pK_a = 2.5. At that centers of mass distance, the curve lies roughly 5 kcal/mol below the one calculated for the $\zeta = 0$ case.

Finally, it is important to note that, while for semi-rigid species the possibility to form c-H-bonds lowers the PMF curve at short distances with respect to the $\zeta = 0$ case (e.g. compare curves at $d_{\mathrm{CoMs}} = 5$ Å and pH - p$K_a = -2.5$), the presence of MB interactions increase the reversible work needed to bring the two chains close together when the polyelectrolyte is infinitely flexible. This evidence can be explained by recalling that flexible chains tend to fold maximizing intra-chain contacts; this, coupled with a lower concentration of CIs in solution (with respect to the $\zeta = 0$ case), slightly increases the work required to bring the centers of mass of the two chains close together.

4.5 General discussion and conclusions

In this work we performed coarse-grained simulations of weak polyelectrolytes via a Monte Carlo approach, accounting for the ionization equilibrium of monomers by means of the constant pH ensemble and explicit counterions. Our aim was to investigate how polyelectrolyte concentration, chain rigidity and the possibility to form inter- and intra-chain charged hydrogen bonds (c-H-bonds, $\zeta = 2$) could synergistically contribute to modify titration behaviors and conformations of poly-acidic species, counterions (CIs) distribution or impact on the Helmholtz energy of the system.

We found that increasing polyelectrolyte concentration results in an enhanced acidity for all the combinations of stiffness and ζ analyzed (Figure 4.1). For species unable to form c-H-bonds, this is attributable to an increase in screening due to CIs and it is more pronounced for flexible species due to their higher

charge density. In the $\zeta = 2$ case, the effect just discussed is supplemented by the formation of inter-chain c-H-bonds, which leads to a markedly lower monomer pK_a at low ionization (Figure 4.5).

A bimodal behavior in the end-to-end distributions at intermediate–high ionization degrees (Figure 4.8) was evidenced only when formation of c-H-bonds was allowed, a trait indicating the coexistence of two conformations, one folded (or clustered) and one unfolded, the transition between the two appearing first-order like (Figure 4.9).

As for the impact of concentration on system Helmholtz energy A (Figure 4.10), we found that the increased CIs screening of polyelectrolyte charges present at higher C_p resulted in a lower Helmholtz energy per chain in all the cases analyzed. The effect due to c-H-bonds formation modified the general trend described lowering further the Helmholtz energy of systems with $\zeta = 2$ when pH - p$K_a < 1.5$.

The evidence that two or more solvated polyelectrolytes may come sufficiently close to interact, e.g., via c-H-bonds, so that their titration behavior and conformations are affected, prompted us to perform window sampling (WS) simulations restraining their centers of mass distance. For species unable to form c-H-bonds, we found that pK_a always increases as d_{CoMs} diminishes (Figure 4.11 (a)). Conversely, we observed a trend reversal at low α values when $\zeta = 2$ (Figure 4.11 (b)), especially in presence of semi-rigid chains; thus, the formation of inter-chain c-H-bonds increases monomer acidity, modulates the local ionization behavior of monomers (Figure 4.12), qualitatively changes the behavior of the total potential of the system versus α (Figures 4.13), and impacts on CIs distribution and chains conformations (Figures 4.15 and 4.16, respectively).

Finally, potentials of mean force (PMF) extracted from window sampling simulations shed light on how chain rigidity and c-H-bonds modify the amount of reversible work $\Delta w(d_{\mathrm{CoMs}})$ required to bring two chains at a distance d_{CoMs}. In detail, we found that increasing chain stiffness slightly lowers Δw when $\zeta = 0$. Δw, instead, does not monotone increase as the pH rises when chains can form c-H-bonds and are close together (Figure 4.18 (b) and (c)), the chemically specific interactions giving rise to minima in PMF curves when chains are semi-rigid.

In concluding, we mention that it may be interesting to extend the work presented here to investigate the role of an explicit treatment of solvent molecules, as

well as of the background ionic strength (especially in the case of multi-valent ions, which could favor chains aggregation) in modifying polyelectrolytes properties in the near future. Studying polyelectrolytes with more complicate topologies (e.g. star– or comb–like) may prove also useful in shedding light on their self-assembly mediated by chemically specific or ionic interactions.

4.6 Appendix: trajectory snapshots

Here we report snapshots for all the simulated systems and for both titration simulations ($n = 8$ case) and window sampling simulations. The color scheme is the following: neutral monomers in gray, charged monomer in pink, CIs in white; the first and the last monomer of each chain are depicted in blue and red, respectively, regardless their ionization state.

4.6.1 Titration simulations

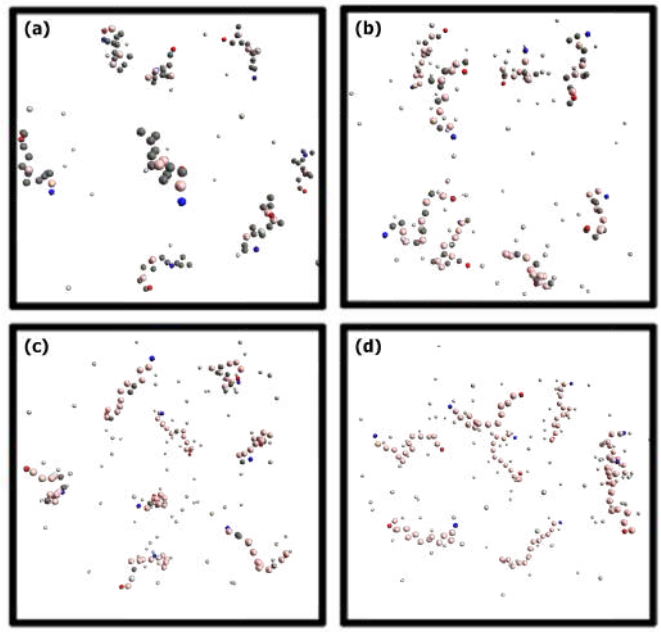

Figure 4.19: Trajectory snapshots for $n = 8$ flexible chains with $\zeta = 0$ at various α: (a) $\alpha = 0.25$, (b) $\alpha = 0.50$, (c) $\alpha = 0.75$, (d) $\alpha = 1.00$

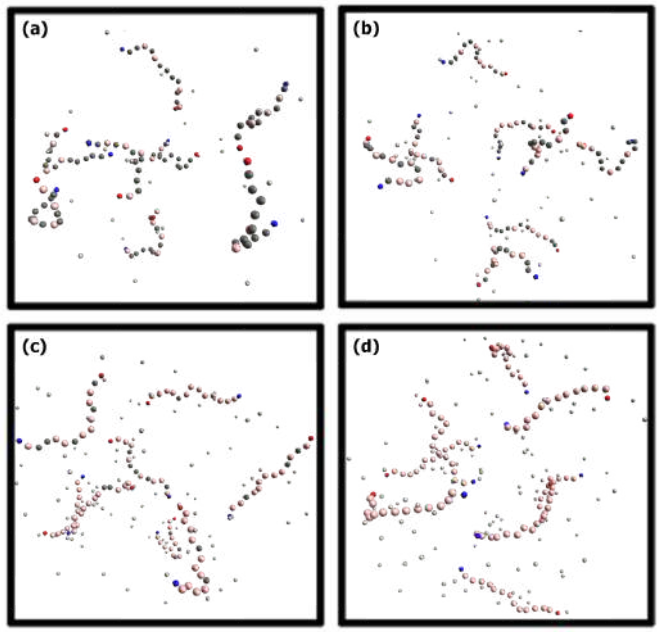

Figure 4.20: Trajectory snapshots for $n = 8$ semi-rigid chains with $\zeta = 0$ at various α: (a) $\alpha = 0.25$, (b) $\alpha = 0.50$, (c) $\alpha = 0.75$, (d) $\alpha = 1.00$.

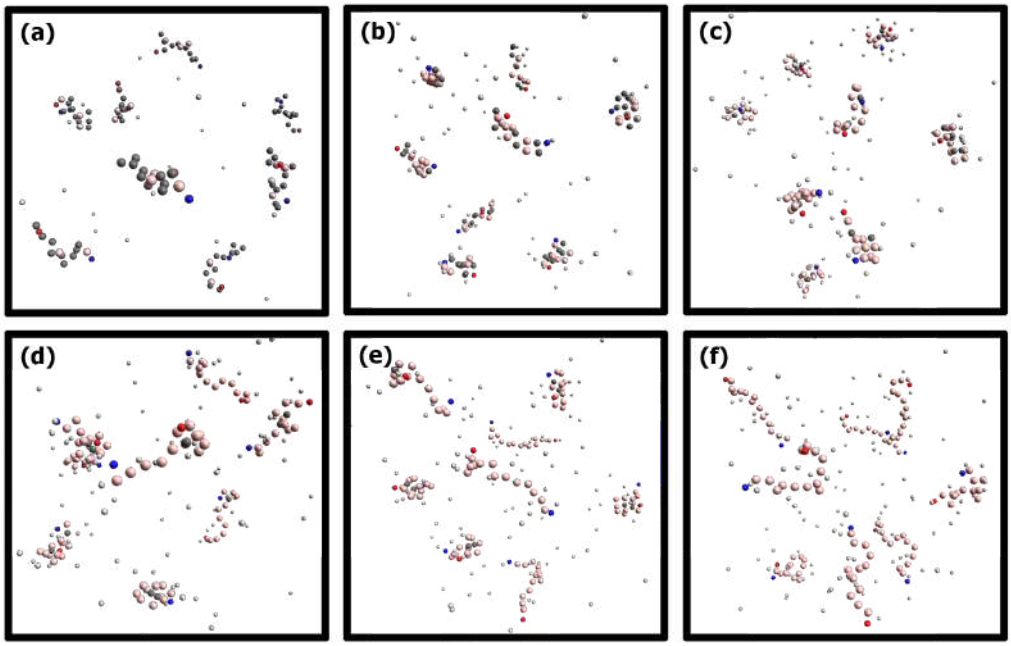

Figure 4.21: Trajectory snapshots for $n = 8$ flexible chains with $\zeta = 2$ at various α: (a) $\alpha = 0.25$, (b) $\alpha = 0.50$, (c) $\alpha = 0.75$, (d) $\alpha = 0.80$, (e) $\alpha = 0.90$, (f) $\alpha = 1.00$.

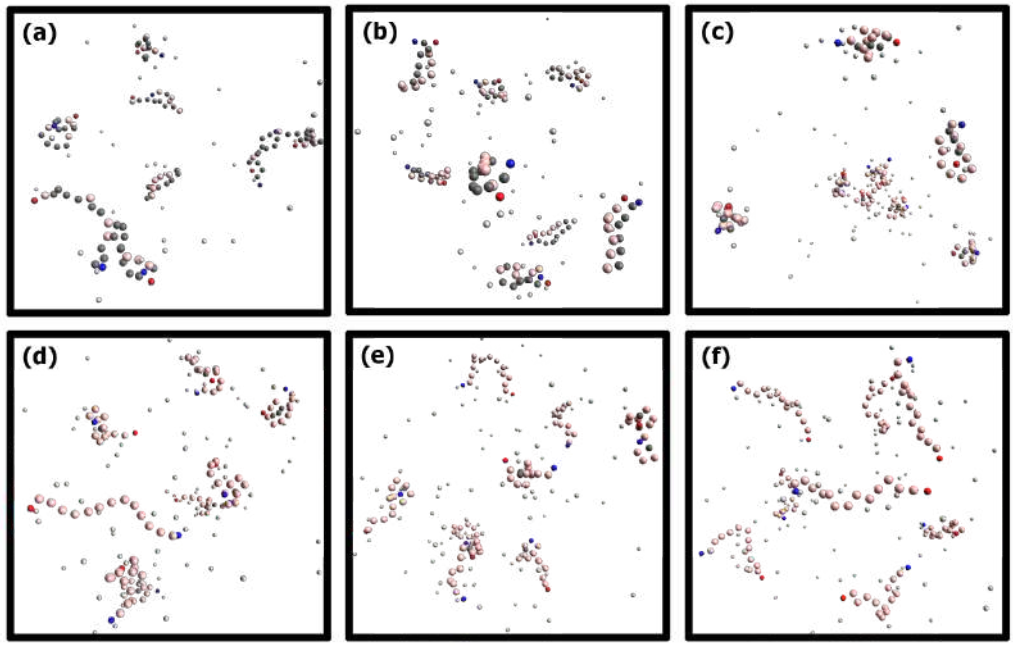

Figure 4.22: Trajectory snapshots for $n = 8$ semi-rigid chains with $\zeta = 2$ at various α: (a) $\alpha = 0.25$, (b) $\alpha = 0.50$, (c) $\alpha = 0.75$, (d) $\alpha = 0.80$, (e) $\alpha = 0.90$, (f) $\alpha = 1.00$.

4.6.2 Window sampling simulations

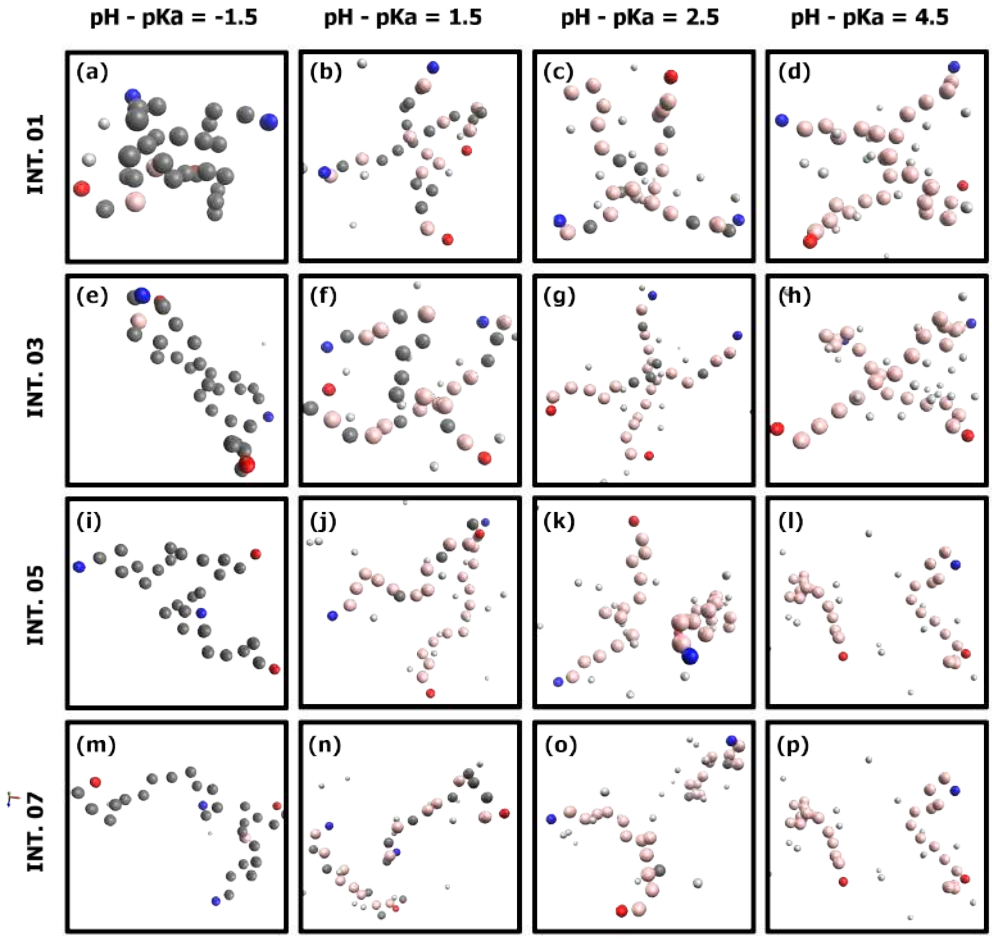

Figure 4.23: Trajectory snapshots for 2 flexible chains with $\zeta = 0$ at various pH - pK_a values and d_{CoMs} intervals.

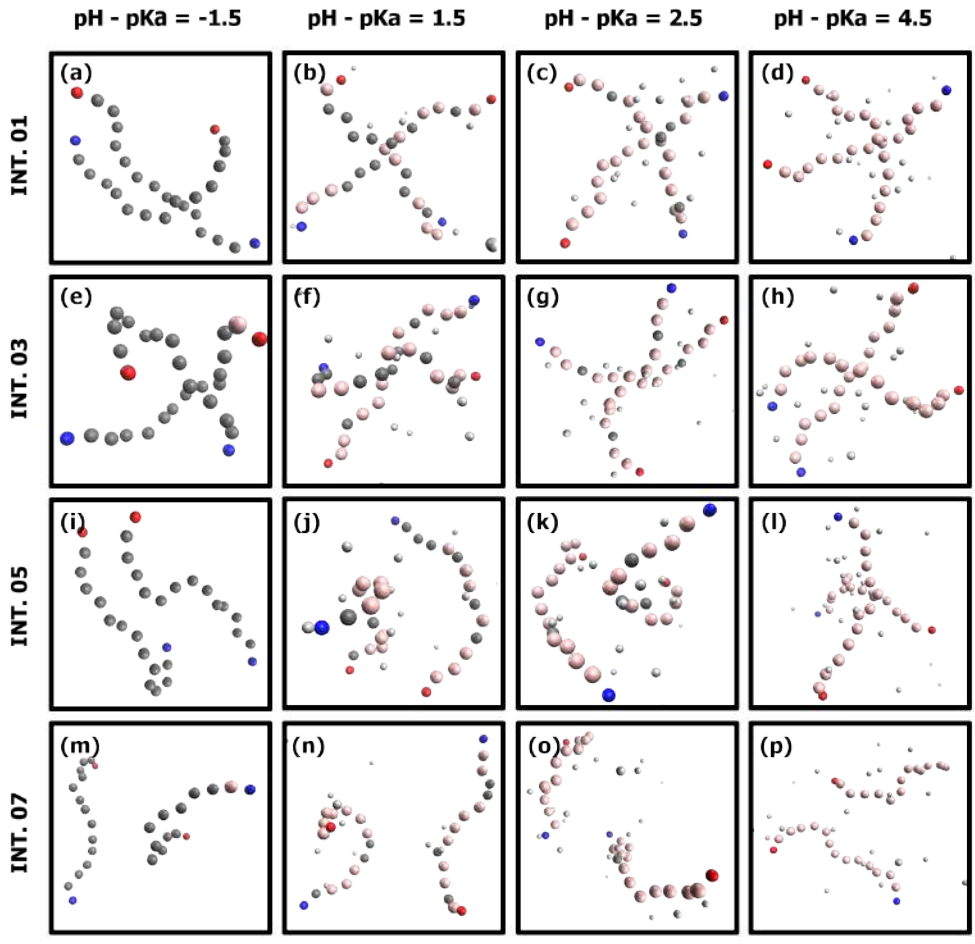

Figure 4.24: Trajectory snapshots for 2 semi-rigid chains with $\zeta = 0$ at various pH - pK_a values and d_{CoMs} intervals.

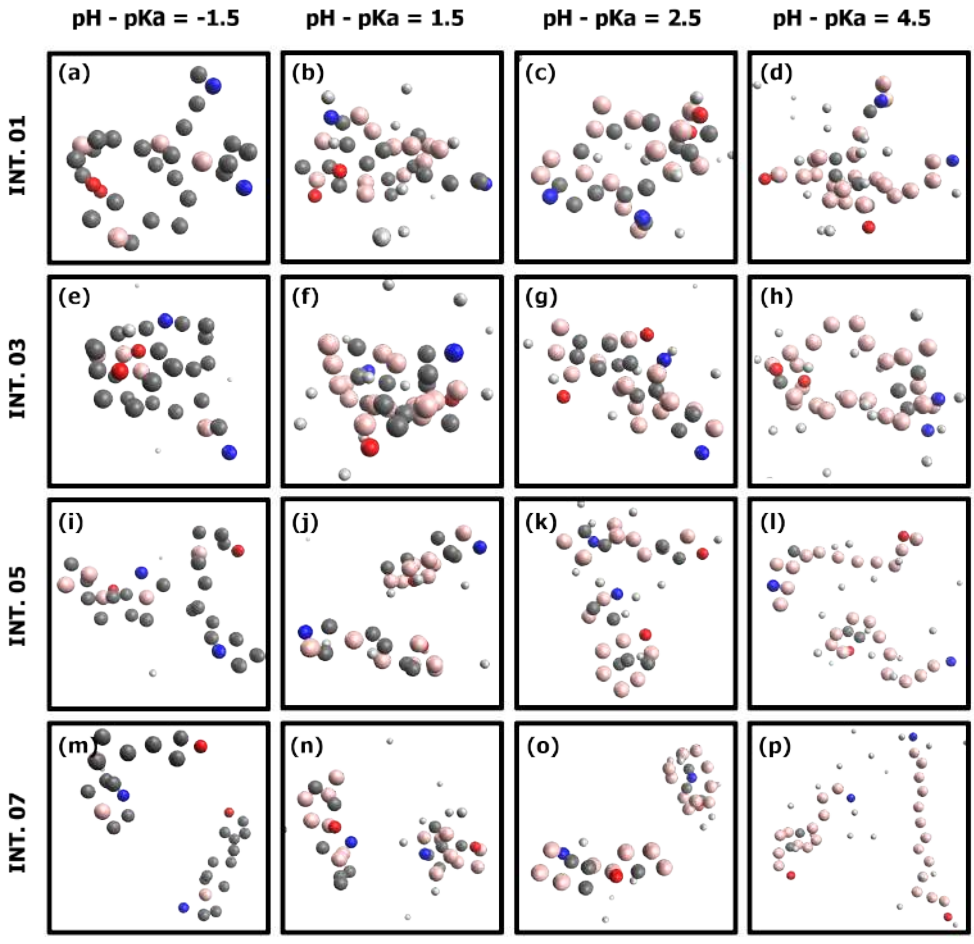

Figure 4.25: Trajectory snapshots for 2 flexible chains with $\zeta = 2$ at various pH - pK_a values and d_{CoMs} intervals.

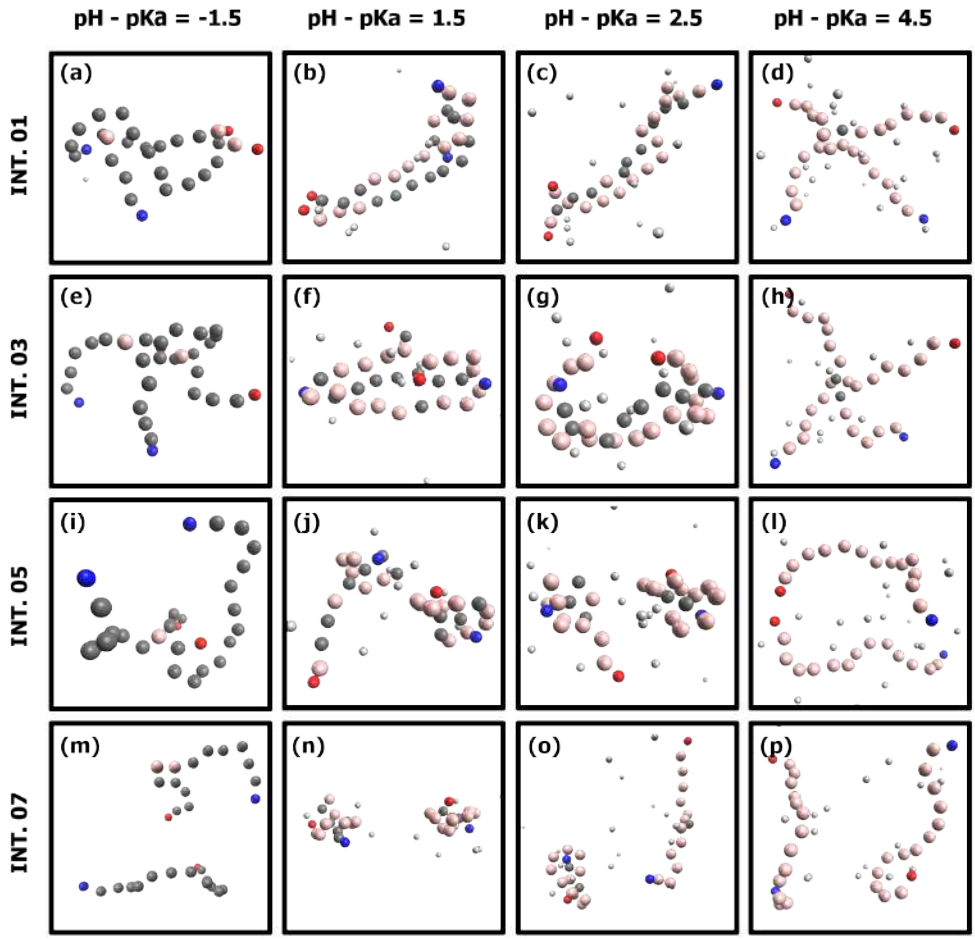

Figure 4.26: Trajectory snapshots for 2 flexible chains with $\zeta = 2$ at various pH - pK_a values and d_{CoMs} intervals.

Chapter 5

Monte Carlo Study of the Effects of Macroion Charge Distribution on the Ionization and Adsorption of Weak Polyelectrolytes and Concurrent Counterion Release*

5.1 Introduction

The topic of nanoparticles (NPs), macroions or colloids complexation with polymeric electrolytes mediated by Coulomb interaction has spurred a large amount of research over the last twenty years [6–15, 39, 113, 143, 174–196]. Motivations behind such effort are various in nature, going from the necessity of a deeper understanding of interactions between multiply charged species in solution [6–15], to the quantitative characterization of surface charge density [187, 189], to a better understanding of thermodynamics of such complex mixtures [194, 196], and finally to an accurate description of possible charge polarization on fluid membrane surfaces [190–192].

Form a theoretical point of view, what makes so interesting the family of systems just mentioned is the long range nature of their interactions, which invari-

*This chapter has been adapted from: Mella M., Tagliabue A., Mollica L., Izzo L., Monte Carlo Study of the Effects of Macroion Charge Distribution on the Ionization and Adsorption of Weak Polyelectrolytes and Concurrent Counterion Release, *Journal of Colloid and Interface Science*, 560, 667-680, (2020)

ably leads to a strong correlation between the motion of charge bearing entities. The scenario becomes even more complicated when polyelectrolytes behave as weak acids or bases; in these cases, solution pH represents an additional variable that may influence properties of formed complexes, and that can hence be used to tune electrostatic interactions between weak poly-acids/bases and NPs, the latter supposed to bear a constant surface charge.

In this work, we have focused on studying formation of complexes between weak polyacid species and positively charged spheres representing compact NPs, macroions or colloids. Such systems have been investigated by theoretical means in several previous works. Thus, Monte Carlo titration simulations have been used to determine the impact of pH, NP size, ionic force, and chain stiffness on the structural details of the formed complex [7, 13, 179]. A comparison between adsorption of short and long weak polyacids has recently been carried out, and it showed how long chains tend to more strongly modulate (up to a marked sign inversion) the colloid charge while protruding tails than an equivalent amount of monomers distributed over several shorter chains [14]. The latter partition between NP surface and solution, the adsorbed ones usually being more ionized than the desorbed counterparts. In all the cases, oppositely charged NP modifies titration curves, shifting the inflection point toward lower pH values, as well as the charge distributions along chains. Such effect is even more marked when many-body (MB) forces such as charged hydrogen bonds (c-H-bonds) are allowed between ionized and neutral monomers [12]. When more than one NP is involved, complexation is facilitated by an increase in chain flexibility [16], whereas overcharging due to NPs complexation on the polyacid was more marked when stiffer chains were used. A more recent study evidenced that, due to charge mobility, weak polyacids are better at bridging charged NPs than strong polyanions when their overall ionization is low [15].

We extend the mentioned research efforts in several ways. First, we expand the set of structures of weak polyacid systems by including star–like species (henceforth indicated as $\mathcal{S}$) together with linear ($\mathcal{L}$) polymers. Second, both $\mathcal{L}$ and $\mathcal{S}$ species, which were also allowed to form inter and intra-chain c-H-bonds, are brought into interaction with colloids that differ in the representation of their surface charge. In one case, this is modeled as a (commonly employed) NP-centered positive charge; the charge of the second macroion type is

instead represented by monovalent mobile cations radially tethered to the NP surface. With these choices, we aim to understand the impact of charge polarization on polymer–NP complexes, as it has already been shown that mobility of charge-bearing surface groups impacts on the distribution of charges surrounding macroions [197–200]. Third, divalent ions are employed to neutralize the colloids charge, and results are compared with a few simulations performed with monovalent counterparts, as we wish to better comprehend the impact of more strongly bound counterions on the complexation process, which necessarily involves their "evaporation" or, at least, the decrease of their local surface concentration. In doing this, we take the first step of a research effort aiming at generating an improved description of the interaction between ionizable species (even surfaces, in the future) and bacteria [26,27,201], whose wall is made structurally stable by the presence of calcium and magnesium cations. Fourth, we investigate the evolution of the osmotic pressure (or, rather, the osmotic coefficient) versus pH in order to gauge possible differences in ions correlation as a function of polyelectrolytes and colloids charge and structural details. Finally, we study the dependency of the Helmholtz energy of our systems on the pH exploiting the statistical mechanics relationship between $(\partial A/\partial \mathrm{pH})$ and α. We do so in order to characterize possible exchange processes in solution containing different macroions and/or polyelectrolytes.

5.2 Models and Methods

The properties of the systems under investigation are obtained within the theoretical framework determined by the cell model (see Section 2.1.2), in which the center of mass of monomers and their counterions (p-CIs) are confined inside a spherical cell with radius $R_{\mathrm{cell}} \equiv R_{\mathrm{ext}}$ and centered at the origin of Cartesian axes.

Our system consists of a centrally located impenetrable spherical nanoparticle (NP, or macroion, or colloid) of radius $R_{\mathrm{NP}} < R_{\mathrm{ext}}$, and bearing a positive total charge $\mathcal{Z}_{\mathrm{NP}}$, and of weak polyelectrolytic species. The NP total charge is neutralized by N_{anion} anions (m-CIs) of valency $q(\mathrm{A})$, so that $\mathcal{Z}_{\mathrm{NP}} = q(\mathrm{A})N_{\mathrm{anion}}$, and it is represented either as a "centrally located charge" ("CCTC" macroion) or as $\mathcal{Z}_{\mathrm{NP}}$ monovalent cations tethered to the NP surface by a harmonic poten-

tial restraining them to lie externally with an equilibrium distance $\sigma = 3.85$ Å from the surface itself (surface-tethered mobile monovalent spherical charges, or "SMMSC" macroion).

Weak polyelectrolytes are such that N_{arm} flexible linear arms depart from a neutral central monomer (nucleus, C) (star-like polyelectrolytes, $\mathcal{S}$), or contain N_{chain} free linear chains ($\mathcal{L}$). Chains or arms contains L spherical weakly acidic monomers (beads) each; thus, the number of ionizable monomers is $N_{\text{mono}} = LN_{\text{arm}}$ or LN_{chain}. For convenience of discussion, we indicate the species with a nucleus, N_{arm} arms and L monomers per arm as as star–like or with $\mathcal{S}(N_{\text{arm}}, L, X)$, where $X =$ CCTC or SMMSC represents the macroion they are exposed to. Similarly, systems composed of N_{chain} free chains are indicated as $\mathcal{L}(N_{\text{chain}}, L, X)$.

Beads in each arm or chain are connected via an harmonic potential (see Equation 2.4) with a force constant $k_{\text{bond}} = 200 k_{\text{B}}T/\text{Å}^2$, and an equilibrium distance $\sigma = 3.85$ Å (the thermal energy is $k_{\text{B}}T = 0.6616$ kcal/mol). If present, the nucleus has $\sigma_C = 2\sigma$, similarly to the weak polyelectrolytes inside neutral capsids previously studied by us [36] and discussed in Chapter 3.

Each monomer is a weak acid and can assume two different charge states: neutral ($q(\text{mono}) = 0$) and negatively charged ($q(\text{mono}) = -1$). Weak acidity is simulated by means of the constant-pH method (see Section 2.2.2); hence, system electroneutrality is conserved by randomly introducing or deleting a positive monovalent counterion (p-CI, $q(\text{CI}) = +1$) Thus, the total number of particles in the system varies and is then given by $N_{\text{tot}} = N_{\text{mono}} + N_{\text{CI}} + \mathcal{Z}_{\text{NP}}(1 + 1/\text{q(A)})$ when SMMSC colloid is present, or by $N_{\text{tot}} = N_{\text{mono}} + N_{\text{CI}} + \mathcal{Z}_{\text{NP}}/\text{q(A)}$ in the case of CCTC macroion*. Charged particles interact with each others via a pairwise Coulomb potential (see Equation 2.7) screened by an uniform dielectric with a relative permittivity $\epsilon_r = 78.3$ identical to the one of water at room temperature.

All N_{tot} particles are treated as soft spheres by implementing a WCA potential (see Equation 2.3), with $\sigma = 3.85$ Å and $\epsilon = k_{\text{B}}T$. In the case star's nuclei are involved, σ_C is used instead of σ.

Finally, c-H-bonds are introduced with by means of our many-body interaction potential (MB)† (see References [12,36,37] and Section 2.1.1.5), with $r_{\text{MB}} = 5$

*+1 (in both SMMSC and CCTC cases) when $\mathcal{S}$–type systems are simulated, due to the fact that we have to take into account also for the star nucleus.

†In the present work, we have chosen $n_{\text{MB}}^{(\text{c})} = 2$, so to allow, e.g., the acceptance of two

Å, $\xi = 2$ kcal/mol, $n_{\mathrm{MB}}^{(\mathrm{n})} = 1$, and $n_{\mathrm{MB}}^{(\mathrm{c})} = 2$.

System configurations are sampled by means of Monte Carlo (MC) simulations, and random displacements are accepted using the classical Metropolis-Hastings rule (Equation 2.30). Apart from single particle displacements, a series of cluster moves (see Section 2.2.1.4) are also attempted; these are: (i) entire species translation; and (ii) pivot move. In the end, each MC step (MCs) consists of the attempted translation of each particle in the system, one attempt to change the charge state of a titratable monomer, one rigid chain translation and one pivot move.

The changes in system properties as a function of pH have been investigated employing coarse grained polymer models containing, mainly, $N_{\mathrm{mono}} = 60$ or 120 monovalent ionizable monomers distributed in equal number either in the arms of star polyelectrolytes or in free linear chains. $\mathcal{Z}_{\mathrm{NP}}$ and R_{NP} are chosen be 58 electronic charges and 40 Å, respectively, so that the macroion surface charge density has a similar value to the one employed in previous works on charge-induced polymer adsorption [6, 13, 184, 188]. As the repulsion between neutral monomers starts at a distance of 3.85 Å, the polymer volume fraction ϕ inside the cell spans the range $2.9\times10^{-3} \leq \phi \leq 5.8\times10^{-3}$ or $3.1\times10^{-3} \leq \phi \leq 6.2\times10^{-3}$ depending, respectively, if one considers the volume of the whole cell or subtracts the volume occupied by the NP. An useful quantity to characterize the studied systems is the mixing ratio $\mathcal{R} = LN_{\mathrm{arm}}/\mathcal{Z}_{\mathrm{NP}} = LN_{\mathrm{chain}}/\mathcal{Z}_{\mathrm{NP}}$, which defines the sign and modulus of the charge that the NP may assume if *all* the polyelectrolytes are adsorbed on the latter. In term of colloidal species, CCTC and SMMCS model macroions may be taken as representative, respectively, of an inorganic NP with an uniform surface charge density or of micelles formed by at least two surfactants, only one of which is ionic in nature. For the sake of simplicity, in this seminal study we have chosen take into account for the viscosity of the micellar core by allowing frictionless tangential mobility to the SMMCS surface charges; as far as the migration of the ionic surfactants is concerned, our results are thus representative of an ideal thermodynamic equilibrium state.

As the formation of polyelectrolyte/macroion complexes ought to induce the

c-H-bonds by $-\mathrm{COO}^-$, and $n_{\mathrm{MB}}^{(\mathrm{n})} = 1$ as the neutral carboxylic group can donate a single H–bond. Notice that this minimalist approach does not take into account of H-bonds that can form between uncharged carboxylic groups.

release of counterions from both species, we investigated the impact on the osmotic pressure that such process has by computing the osmotic coefficient ($\Phi = \pi_{\text{abs}}/\pi_{\text{id}}$) as a function of pH. Within the framework of the cell model, the osmotic pressure π_{abs} of the composed systems is directly related to the species concentration *at* the cell boundary [76]; this is an extremely local quantity requiring quite extensive MC sampling to obtain reasonably precise values for an insightful discussion. As a consequence, all our simulations have been run until a relative standard error of 5% compared to the associate average value π_{abs} was obtained. As a positive byproduct, all other physical quantities for the systems investigated have reached a statistical accuracy of, at least, 1 part for thousands; we thus avoided to show statistical errors completely.

5.2.1 Helmholtz energy calculation

Despite equation 2.36 was originally derived employing various assumptions and simplifications [32], we demonstrated that the result is of general validity (see Chapter 4); thus, it can be exploited to estimate the change in Helmholtz energy of an electrolytic system induced by a variation of the pH and the consequent association/dissociation of ionizable groups as $[\partial A/\partial(\text{pH} - \text{p}K_a)] = -\ln(10) N_{\text{mono}} k_{\text{B}} T \alpha$ even if other charge-bearing species are present inside the simulation cell.

In this work, we shall exploit Equation 2.36 to investigate how the details of polyelectrolyte structure impact on its energy as a function of pH - pK_a by computing $\Delta(\Delta A)$ between, for instance, star-shaped species with various number of arms, as well as between polyelectrolytes that have the same geometrical structure but differ for the possibility or not to for c-H-bonds. Notice that the values of α(pH) in Equation 2.36 when $\text{pH} - \text{p}K_a < -6$ were represented with an exponential function interpolating the last two computed values.

5.3 Results and discussion

5.3.1 Titration curves

Figure 5.1 present results $\Delta\text{p}K_a$ (see Equation 2.23) for systems with $N_{\text{mono}} = 60$, whereas titration curves are shown in Figure 5.2. These have been obtained employing divalent colloid counterions and for a mixing ratio $\mathcal{R} \simeq 1$. Also shown,

Abbreviation	Meaning
MC	Mont Carlo
c-H-bond	Charged hydrogen bond
MB	Many-body
NP	Nanoparticle
CI	Counterion
p-CI	Polyelectrolyte counterion (cation)
m-CI	Macroion counterion (anion)
CCTC	Macroion-centered located charge
SMMSC	surface-tethered mobile monovalent spherical charges

Table 5.1: List of abbreviations commonly used in this chapter

there are results for similar species titrated in presence of an uncharged colloid.

For species unable to form c-H-bonds (upper panels of Figures 5.1 and 5.2), it neatly emerges the ionization inducing action of macroion on weak polyelectrolytes, a stark indication of which is provided by the negative values of $\Delta \mathrm{p}K_a$ at low pH. There are, however, clear differences related to both the macroion charge representation and the structure of titrated species. In fact, linear species result more easily ionizable than star-shaped ones, and shorter chains are, in the average, more easily ionizable than longer ones [12, 36, 37]. Moreover, CCTC species has a lower impact on ionization than SMMSC colloid especially for $\mathcal{S}(2, 30)$ and $\mathcal{S}(6, 10)$. This effect is somewhat reduced in the $\mathcal{L}(6, 10)$ case, but it still remains fairly evident especially at high ionization.

Similar comments can be made when species are able to form c-H-bonds (lower panels of Figures 5.1 and 5.2), even though systems are more ionized than the $\xi = 0$ counterparts when $\mathrm{pH} - \mathrm{p}K_a$ [12,36,37], a finding that reflects itself on the presence of wide range of pH over which $\Delta \mathrm{p}K_a < 0$ for the species with $\xi = 2$ kcal/mol. The latter behavior is also found when *monovalent* m-CIs are used (see Figure 5.3). This may be due to either a weaker screening of the positive macroion charge by monovalent m-CIs, or to the effect of a stronger electrostatic repulsion between the divalent m-CIs and the ionized monomers.

We also simulated a few systems with $N_{\mathrm{mono}} = 120$ (for which $\mathcal{R} \simeq 2$) in order to investigate the impact of increasing polyelectrolyte size, the results being shown in Figure 5.4. For these, one may expect a reduced impact of the macroion on the polyelectrolyte ionization, at least when $\alpha N_{\mathrm{mono}} > \mathcal{Z}_{\mathrm{NP}}$. For the SMMSC colloid,

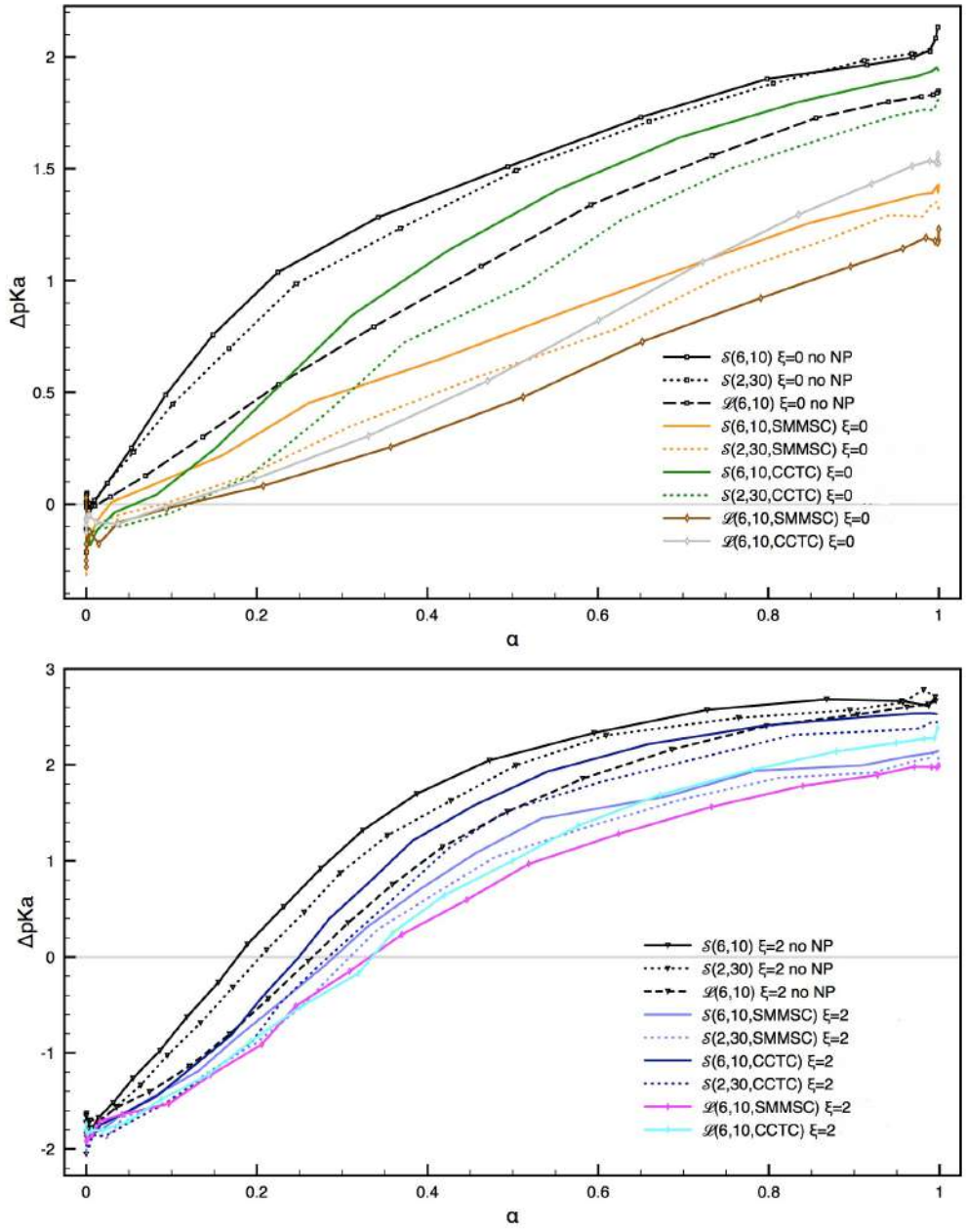

Figure 5.1: $\Delta \mathrm{p}K_a$ versus α for the case $N_{\mathrm{mono}} = 60$ and $\xi = 0$ (upper panel) and $\xi = 2$ kcal/mol (lower panel). The label "no NP" indicates the absence of a surface charge (and, consequently, associated counterions) for the nanoparticle.

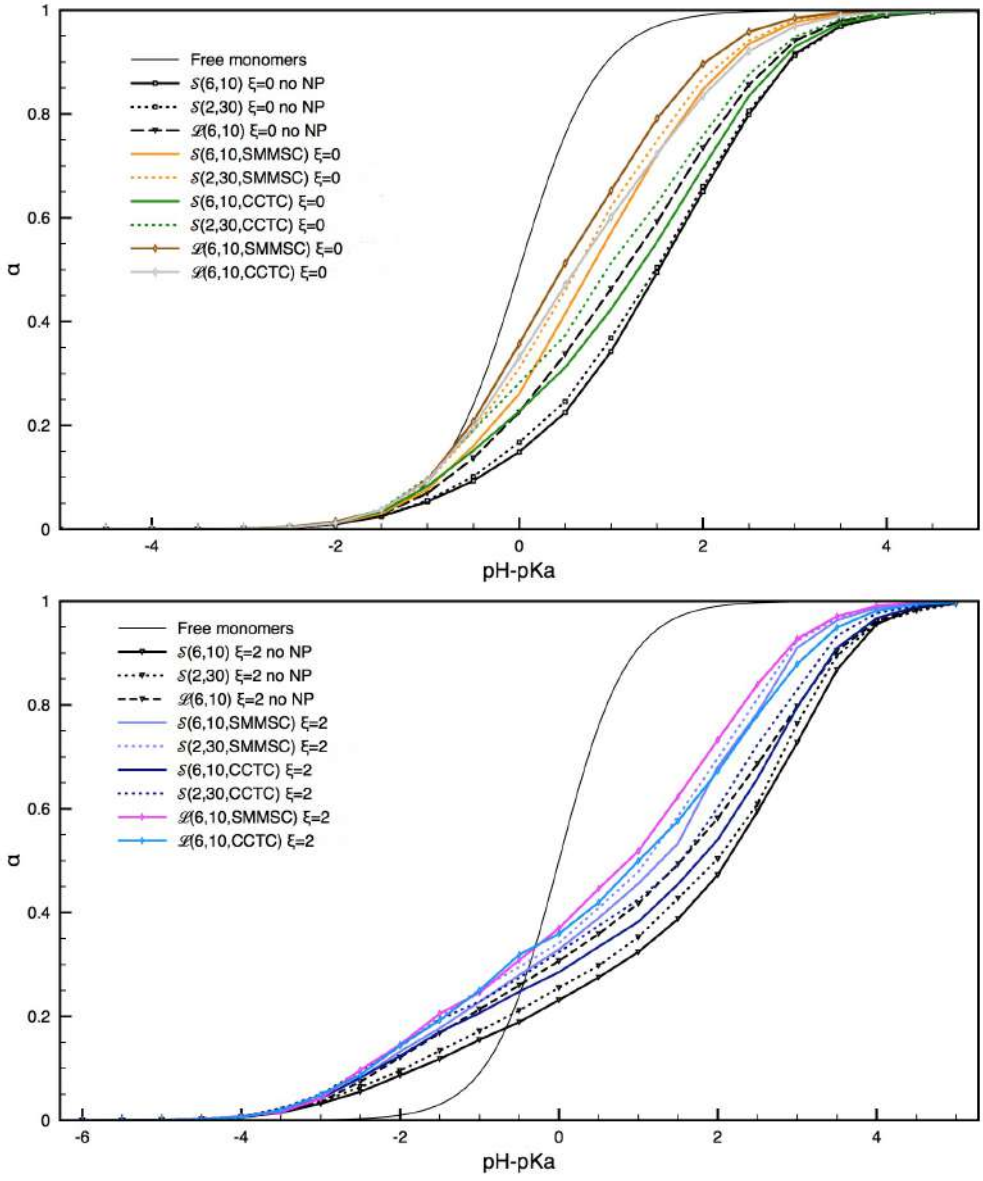

Figure 5.2: α as a function of $\mathrm{pH} - \mathrm{p}K_a$ for the case $N_{\mathrm{mono}} = 60$; $\xi = 0$ (upper panel) and $\xi = 2$ kcal/mol (lower panel). The label "no NP" indicates the absence of a surface charge (and, consequently, associated counterions) for the nanoparticle.

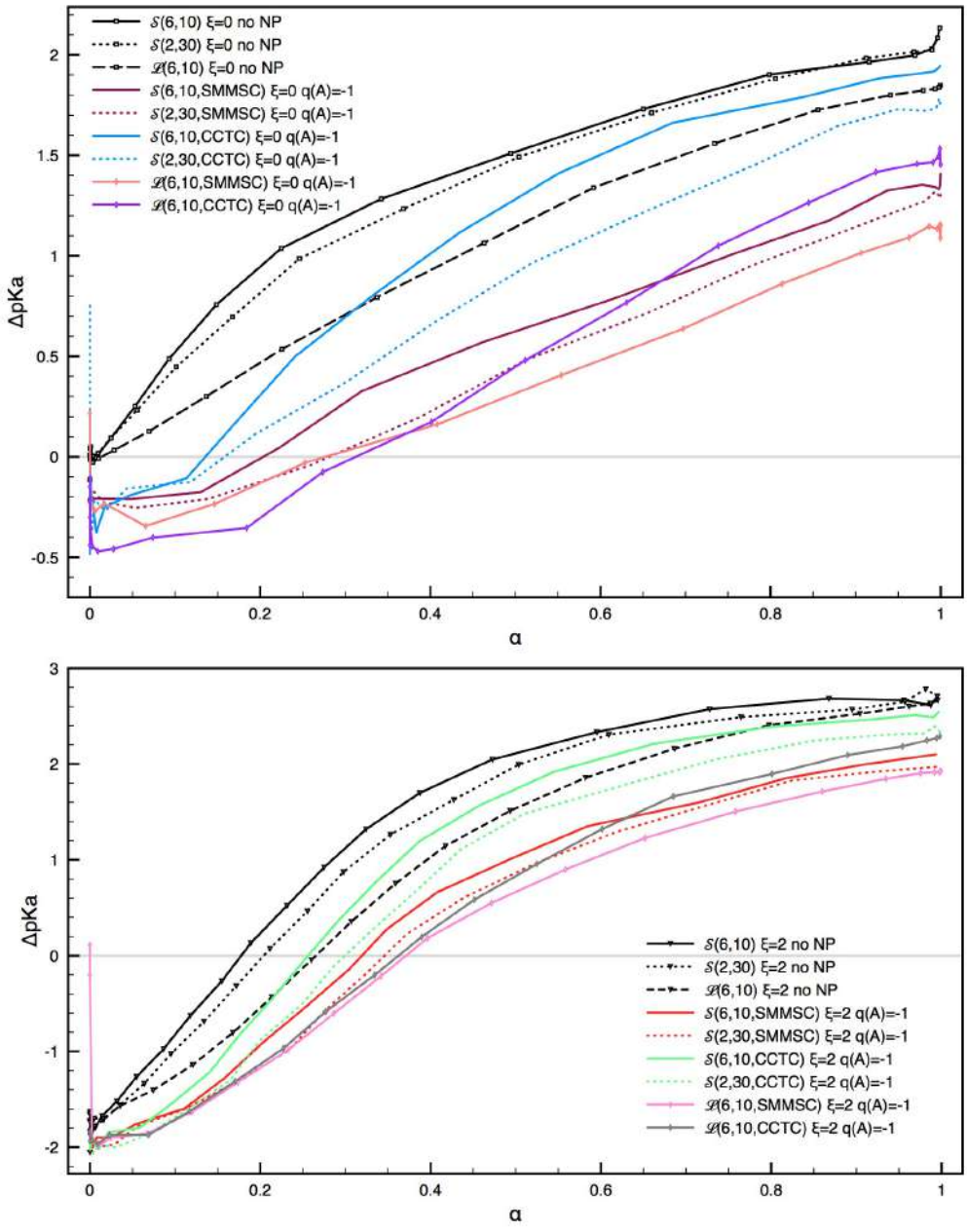

Figure 5.3: ΔpK_a as a function of α in case of *monovalent* m-CIs (i.e., $q(A) = -1$), for $N_{mono} = 60$, and $\xi = 0$ (upper panel) or 2 kcal/mol (lower panel).

such an expectation is fulfilled, $\mathcal{S}(6,20)$ showing a higher $\Delta \mathrm{p}K_a$ than the $\mathcal{S}(6,10)$ counterpart when $\alpha > 0.4$. The increase in $\Delta \mathrm{p}K_a$ is even more marked, and it extends to the whole pH range investigated, for species with 12 arms. We suggest that such differences may be connected to the shorter average distances between monomers in the latter type of polyelectrolytes, which makes energetically more demanding ionizing additional monomers due to an increased Coulomb repulsion.

At variance with what just discussed, increasing the number of monomers per arm (or the number of arms) to reach $N_{\mathrm{mono}} = 120$ has a different impact when the CCTC macroion is present. In fact, while $\Delta \mathrm{p}K_a$ for $\mathcal{S}(12,10)$ is always higher than for the $N_{\mathrm{mono}} = 60$ case, the same quantity is lower for $\mathcal{S}(6,20)$. Such difference may be due to the juxtaposition between the spatially uniform electric field on the CCTC surface and the higher concentration of p-CIs introduced during the titration of the $N_{\mathrm{mono}} = 120$ polymers. *De facto*, the higher ionic force present close to the end of the titration of species with $N_{\mathrm{mono}} = 120$ may also explain the slower increase in $\Delta \mathrm{p}K_a$ when $\alpha > 0.4$ for $\mathcal{S}(12,10)$ compared to $\mathcal{S}(6,10)$.

Summarizing, results show that increasing polyelectrolyte size more markedly evidences differences in behavior between SMMSC and CCTC systems, the latter favoring more ionization of star–like species with a higher N_{arm} despite the identical number of total monomers.

As the macroion is the source of a non-uniform electric field, distinct polymer arms may present differences in ionization behavior, even in the average. In order to investigate this possibility, Figure 5.5 shows the average arm ionization degree for $\mathcal{S}(6,10)$ for $\xi = 0$ (upper panel) and $\xi = 2$ (lower panel). As references, also, the $\mathcal{L}(6,10)$ case is included. From these results, we notice that the macroion presence induces both arms and free chains to assume relative ionization degrees that may substantially differ from the system average ionization much more than when the macroion is absent. This effect seems more marked for the star-like species than for the independent chains (see, e.g., at $\mathrm{pH} - \mathrm{p}K_a \simeq 1$), suggesting that the degree of correlation between the ionization behavior of different chains is increased by being tethered to a central core.

Differences between arm ionization degree and average ionization for multi-arm species increases upon increasing N_{mono} to 120 (see Figure 5.6), and it appears particularly marked for $\mathcal{S}(12,10)$ probably due to a higher monomer density

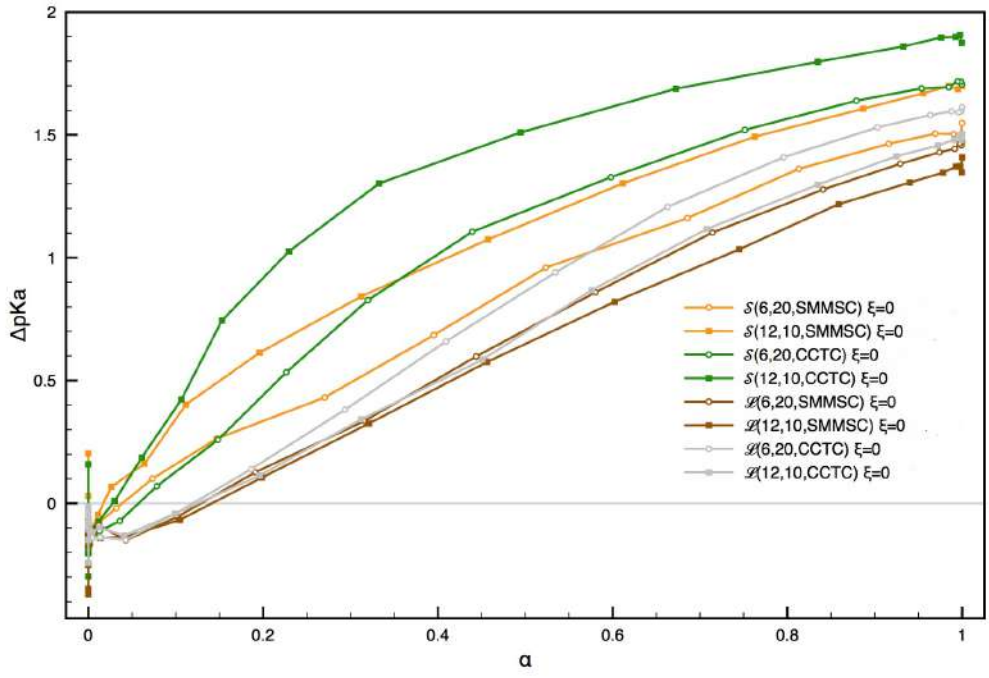

Figure 5.4: $\Delta \mathrm{p}K_a$ as a function of α for $N_{\mathrm{mono}} = 120$ and $\xi = 0$.

that hamper the spatial re-arrangement of arms. This idea is supported by the reduced scatter for the arm ionization degree obtained by titrating an equivalent amount of free chains (lower panel of Figure 5.6).

5.3.2 Adsorption on the Macroion

As discussed in Section 5.1, the onset of a negative charge on the polyelectrolyte due to the neutralization of acidic groups may lead to chain adsorption on the positively charged macroion. The average number of chains adsorbed on both the CCTC and SMMSC colloids, $\langle N \rangle$, as a function of $\mathrm{pH} - \mathrm{p}K_a$ is shown in Figure 5.7 for $\mathcal{S}(2, 30)$ and $\mathcal{S}(6, 10)$, as well as for $\mathcal{L}(6, 10)$. For sake of simplicity, we considered that a chain or arm is adsorbed when at least one of its monomers is adsorbed; a monomer is considered adsorbed when lies at a distance shorter than 7 Å (roughly the Bjerrum length in water at room temperature) from either the CCTC surface or one of the SMMSC–tethered charged particle.

Our results suggest an abrupt increase in the number of adsorbed chains over a limited range of pH values (roughly 2 pH units) located well before the titration midpoint in all the case shown. As for the $\mathcal{L}(6, 10)$ and $\mathcal{S}(2, 30)$ cases, polymers

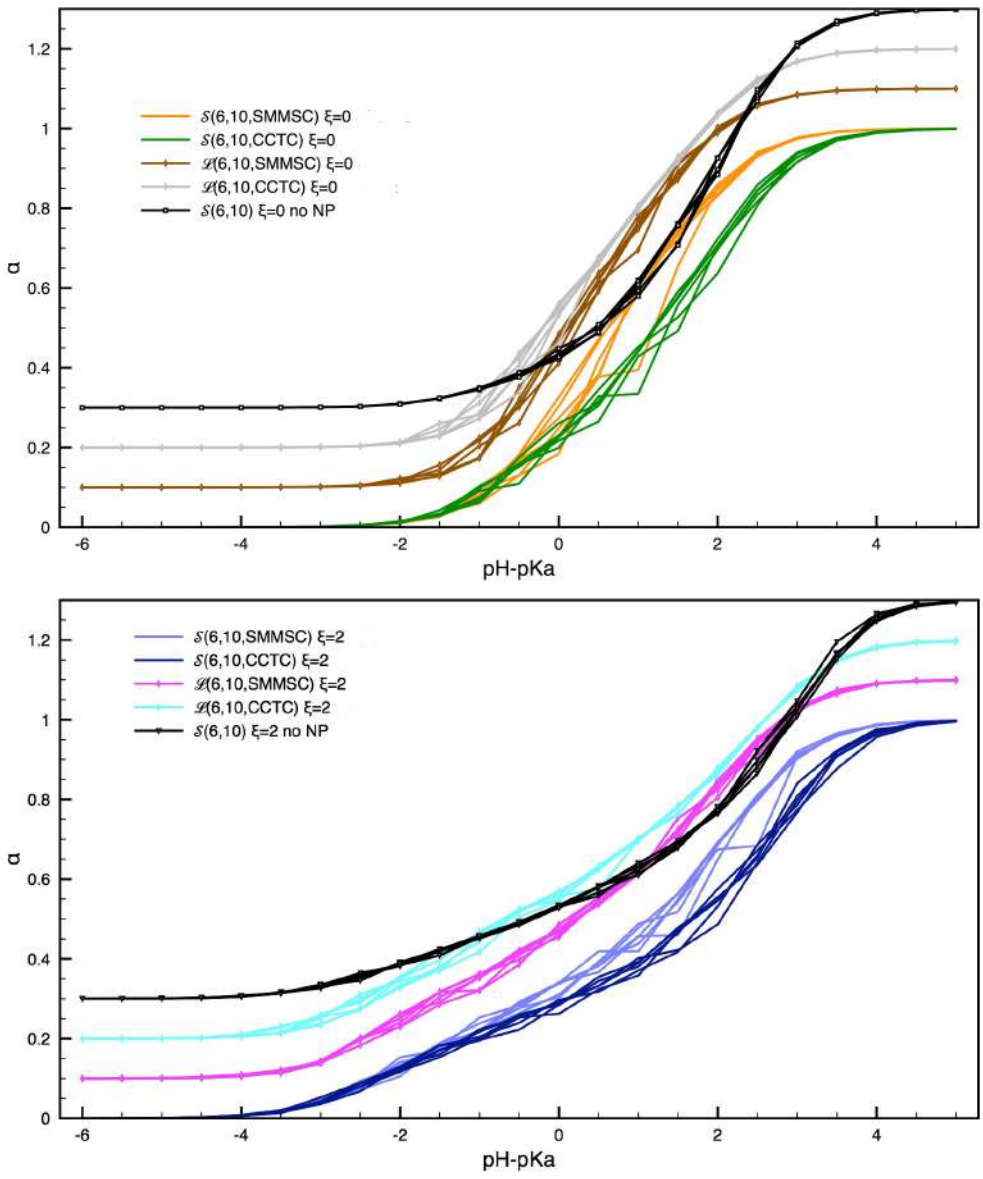

Figure 5.5: α as a function of $\mathrm{pH} - \mathrm{p}K_a$ for each arm/chain for $N_{\mathrm{mono}} = 60$ and $\xi = 0$ (upper panel) or $\xi = 0$ (lower panel). The different sets of lines have been shifted upward in the graph in order to provide a clearer view of their different behaviors. The label "no NP" indicates the absence of a surface charge (and, consequently, associated counterions) for the nanoparticle.

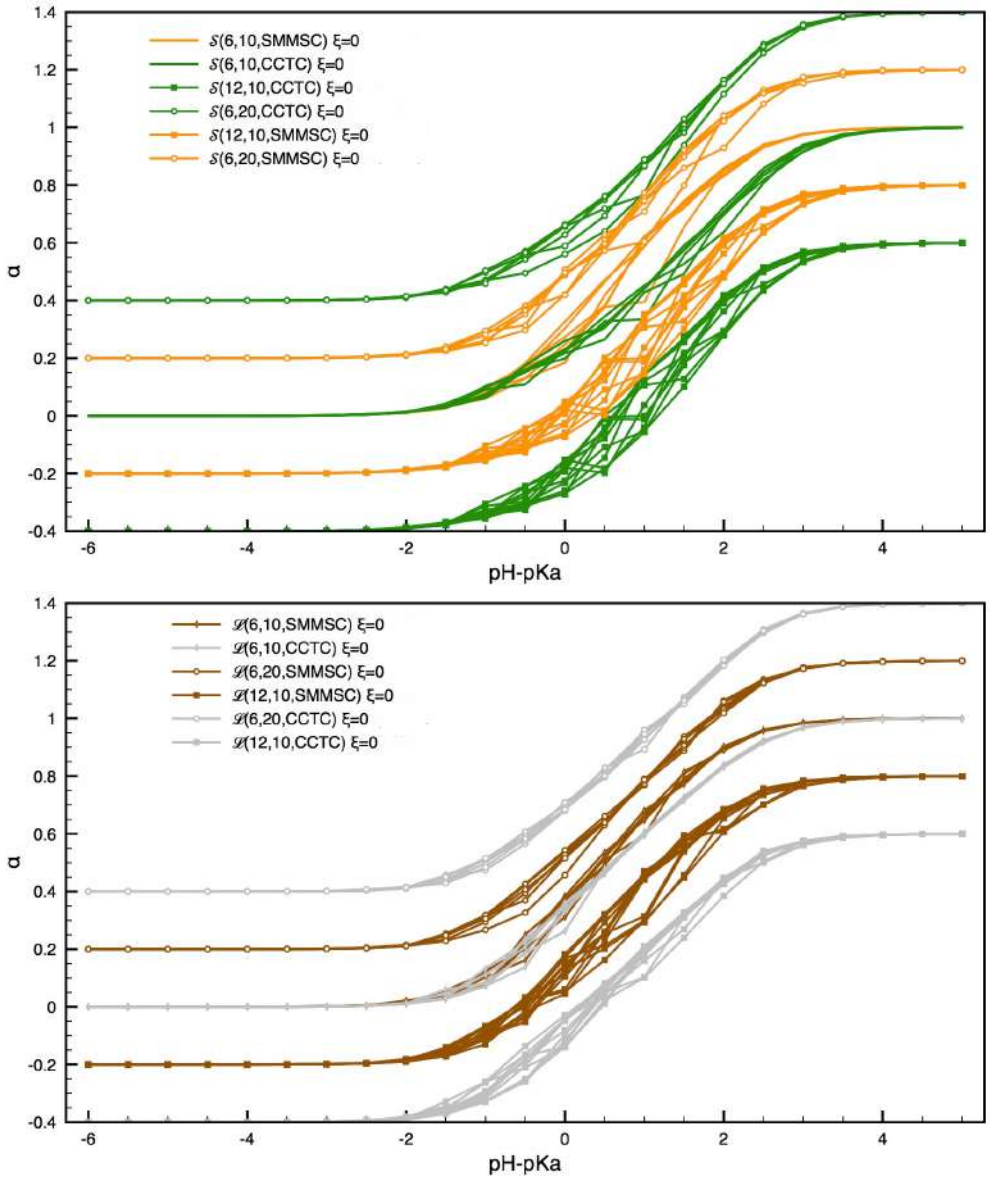

Figure 5.6: α as a function pH - pK_a for different polyelectrolyte arms (upper panel) or free chains (lower panel); $N_{\text{mono}} = 60$ or 120, and $\xi = 0$. The different sets of lines have been shifted upward in the graph in order to provide a clearer view of their different behaviors.

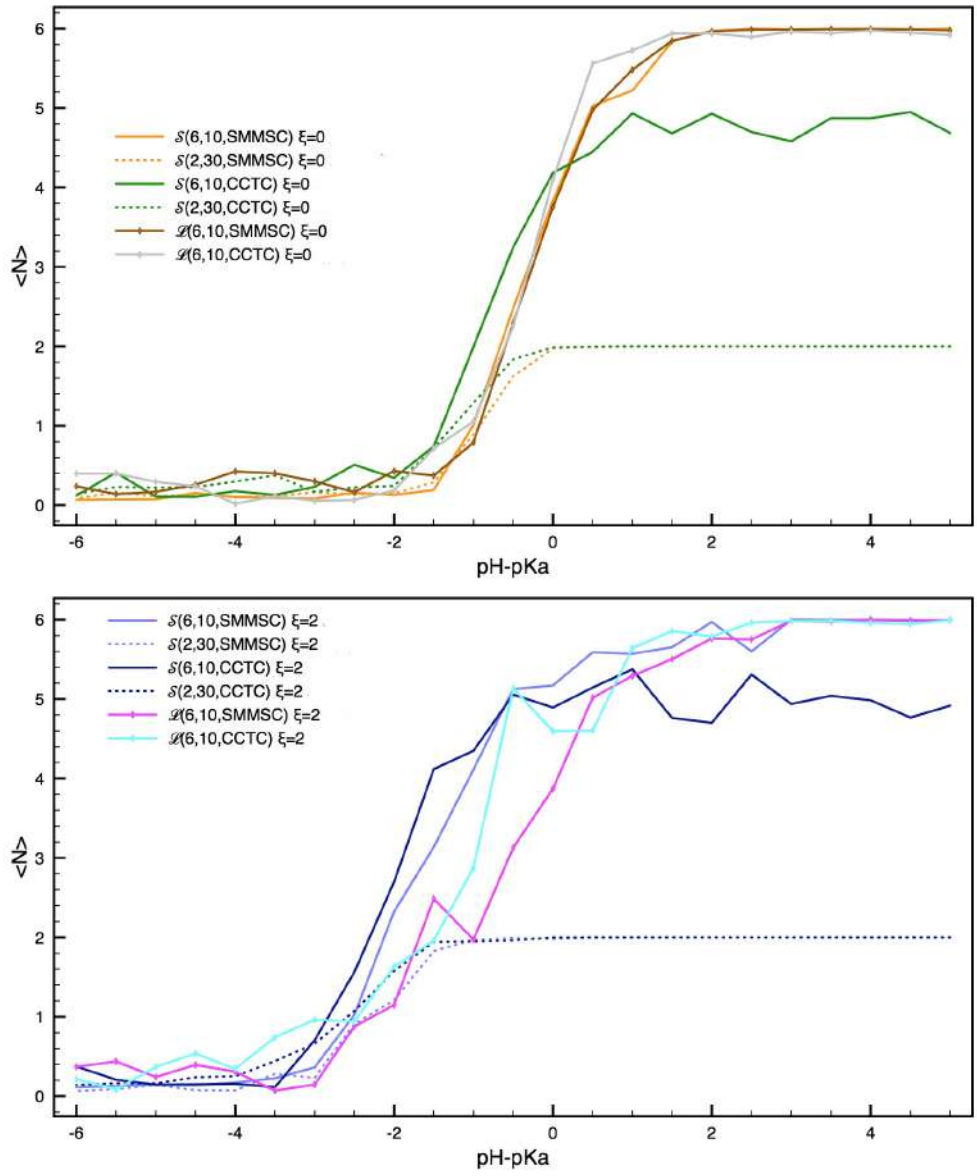

Figure 5.7: Average number of adsorbed chains $\langle N \rangle$ as a function of pH - pK_a for $N_{\text{mono}} = 60$ and $\xi = 0$ (upper panel) or $\xi = 2$ kcal/mol (lower panel).

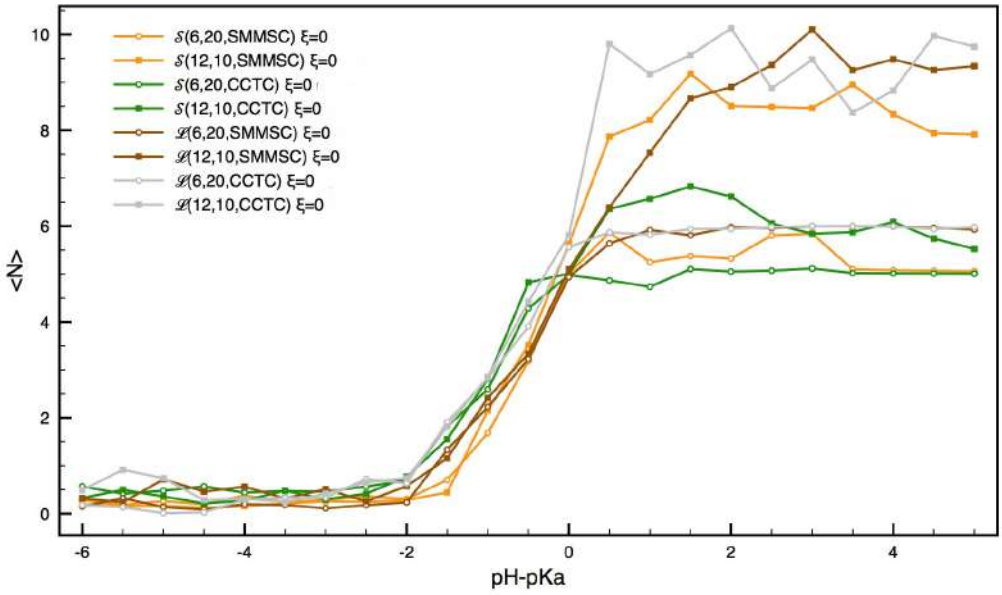

Figure 5.8: Average number of adsorbed chains $\langle N \rangle$ as a function of pH - pK_a of $N_{\text{mono}} = 120$ and $\xi = 2$ kcal/mol.

are completely adsorbed on both types of macroion at high pH similarly to what previously evidenced in [14] when $\mathcal{R} = 1$. Conversely, CCTC and SMMSC colloids differ with respect to the number of arms of star-like specie adsorbed at high pH, the value for CCTC suggesting that one arm (i.e., 20% of the total number) remains non-adsorbed on the colloid surface. The trends just discussed are present even when c-H-bonds are allowed, and are even more marked for star-like systems with $N_{\text{mono}} = 120$ (hence, $\mathcal{R} = 2$), as shown in Figure 5.8. For the latter systems, we only mention here that the highest number of adsorbed arms is found in a range of pH values such that the polyelectrolyte is not completely ionized, suggesting that inter-arm repulsion plays an important role in defining such property.

The findings and the conclusions just discussed find support also in the graphical representation of the systems structures shown in Figure 5.9, and, at a finer level of detail, from the data on the fraction of adsorbed monomers and their radial distributions.

As to Figure 5.8, we notice that the SMMSC macroion tends to adsorb 67% of the total number of arms in $\mathcal{S}(12, 10)$, which is 2 or 3 arms more than what happens with the CCTC colloid (with 45% adsorbed); despite this, the SMMSC

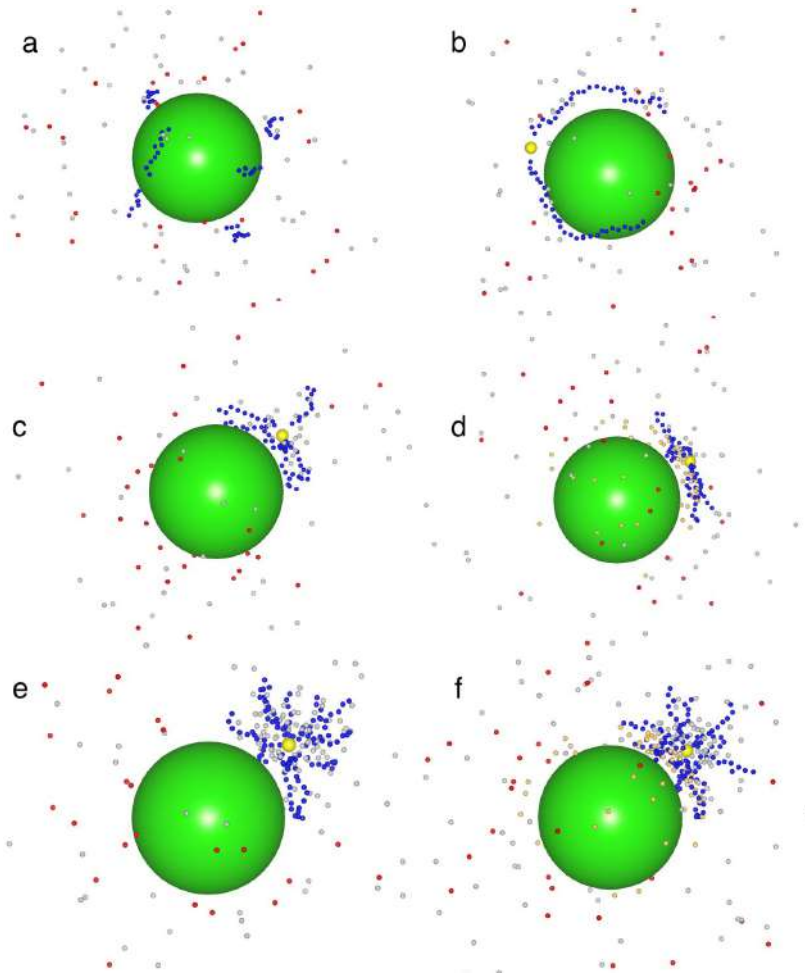

Figure 5.9: Configurations sampled at full ionization ($\mathrm{pH} - \mathrm{p}K_a = 5$) for the following systems: (a), $\mathcal{L}(6, 10, \mathrm{CCTC})$; (b), $\mathcal{S}(2, 30, \mathrm{CCTC})$; (c), $\mathcal{S}(6, 10, \mathrm{CCTC})$; (d), $\mathcal{S}(6, 10, \mathrm{SMMSC})$; (e), $\mathcal{S}(12, 10, \mathrm{CCTC})$; (f), $\mathcal{S}(12, 10, \mathrm{SMMSC})$. Color coding: neutral nucleus in yellow; charged monomers in blue; p-CIs in light gray; m-CIs in red; macroion charges in light orange; the impenetrable NP is depicted in green.

colloid is no longer able to adsorb all branches of the star as in the $N_{\text{mono}} = 60$ case. At a finer level of detail, we also notice that the maximum number of adsorbed arms is no longer found when $\alpha = 1$; rather, a lower ionization ($0.5 \leq \alpha \leq 0.6$) is needed to maximize arm coordination, suggesting that inter–arm repulsion plays some role in defining the number of polymer branches in contact with the NP's. A similar idea would also rationalize the fact that $\mathcal{S}(6, 20)$ adsorbs only five branches at high pH on the SMMSC macroion rather than six as its smaller counterparts.

In the case of free chains systems, instead, the CCTC colloid tends to adsorb more chains than SMMSC macroion, albeit this happens only in the range $-2 \leq \text{pH} - \text{p}K_a \leq 1$. At higher pH, both NP's adsorb the same number of chains (all chains in the $\mathcal{L}(6, 10)$ case, and 9–10 when $\mathcal{L}(12, 10)$ is present). With this in mind, we notice that moving from $\mathcal{S}$ to $\mathcal{L}$ (i.e., untethering star's arms so that they act as free linear chains) fosters a slightly higher coordination to the macroions compared to the corresponding star-like species, a finding probably due to the ability for a better spatial organization that maximizes attraction between NP and chains and minimizes the repulsion between charged monomers.

A complementary view of the polyelectrolytes–macroion complexes is provided by the fraction of adsorbed monomers $\langle M \rangle$ shown in Figure 5.10. In the N_{mono} case, it is worth noting that the systems composed of six free chains somewhat deviate from the expectation of a large fraction ($> 5/6$) of adsorbed monomers at high pH in spite of adsorbing all arms ($\langle N \rangle = 6$), suggesting that the polymers ought to present desorbed sections (either tails or loops, depending if these involve terminal or mid-chain monomers). Also noteworthy, it is the fact that $\mathcal{L}(6, 10)$ coordinated to the CCTC macroion, *de facto* adsorb a number of monomers that would be compatible with the adsorption of only four of the six arms even though it reaches $\langle N \rangle = 5$.

When we increase the number of ionizable monomers to 120, we notice that $\mathcal{L}(6, 20)$ and $\mathcal{S}(6, 20)$ tend to adsorb more monomers on both macroions compared to the $\mathcal{L}(12, 10)$ and $\mathcal{S}(12, 10)$ cases indicating the effect of reducing the system overall entropy by lengthening arms or chains; this notwithstanding, the fraction of adsorbed monomers remains quite low compared to the number of adsorbed chains (or the fraction of adsorbed monomers when $N_{\text{mono}} = 60$), and it is due to the stronger electrostatic repulsion between ionized beads.

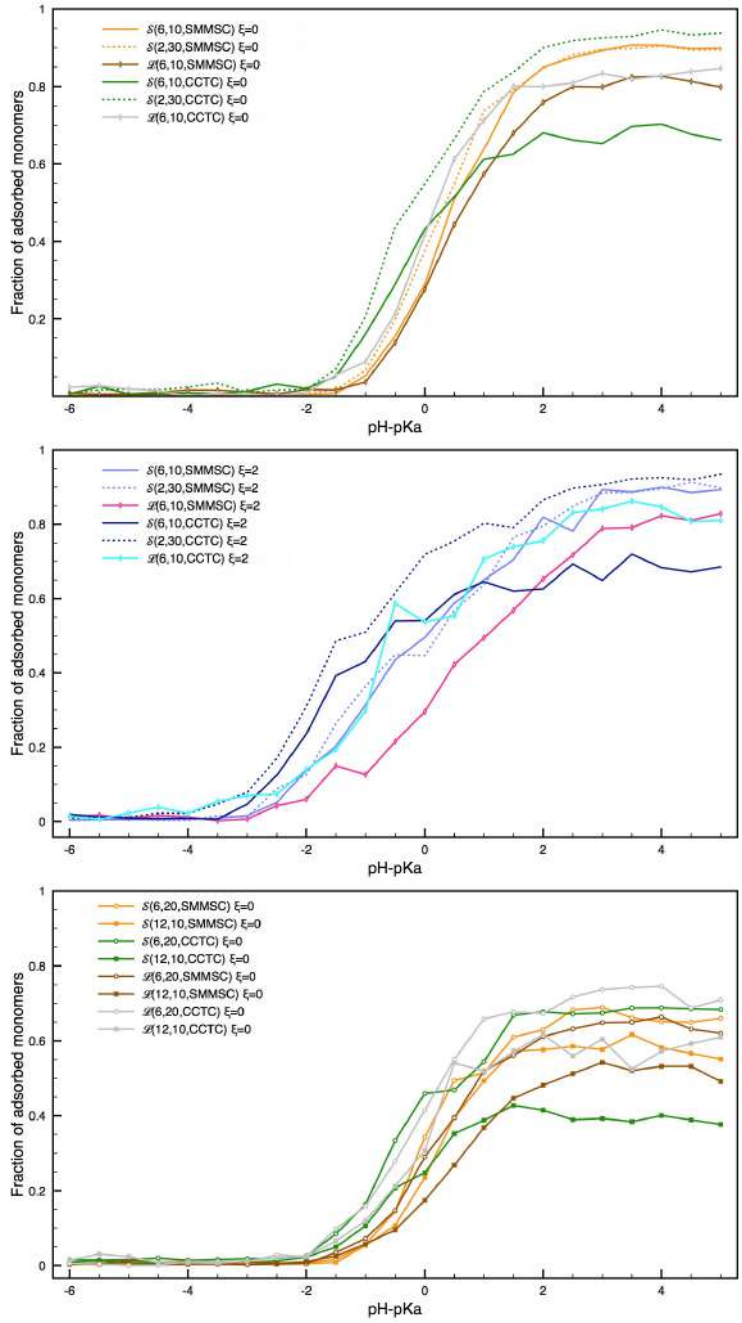

Figure 5.10: Average fraction of adsorbed monomers $\langle M \rangle$. Upper panel: $N_{\text{mono}} = 60$, $\xi = 0$; middle panel: $N_{\text{mono}} = 60$, $\xi = 2$; lower panel: $N_{\text{mono}} = 120$, $\xi = 0$.

The spatial disposition of the polyelectrolyte monomers can be more precisely described by the probability distribution function $p(R)$ of finding a monomer at a distance R from the macroion geometrical center (*vide* Figures 5.11 and 5.12). Let us begin by presenting the results for the systems composed of $N_{\text{mono}} = 60$ and with $\xi = 0$ (left panels of Figure 5.11). At very high pH (i.e., at almost full ionization), all systems tend to accumulate the ionized monomer as close as possible to the macroion surface, albeit a few interesting differences are clearly present. First, the maximum in $p(R)$ for the polyelectrolyte adsorbed onto the SMMSC macroion is lower and positioned further away from the surface than in the CCTC case due to the fact that the monovalent macroion charge–bearing species are located externally to the surface. Second, the distribution for $\mathcal{S}(6, 10)$ adsorbed onto the CCTC colloid markedly displays a tail extending up to 80 Å from the colloid center, which is not present in all the other systems and is evocative of the presence of a desorbed arm (Figure 5.7).

As soon as the pH lowers and the global ionization decreases (e.g., see the middle–left panel of Figure 5.11, $\text{pH} - \text{p}K_a = 1$ and $0.4 \lesssim \alpha \lesssim 0.5$), distributions broaden toward larger R values, with $\mathcal{L}(6, 10)$ and $\mathcal{S}(6, 10)$ giving clear indications of the desorption of at least one arm/chain. Such distribution broadening is markedly augmented by lowering further the pH (see, e.g., the lower–left panel of 5.11, where $\text{pH} - \text{p}K_a = -1$ and $\alpha \simeq 0.1$), with all $p(R)$ extending up to R_{ext}. Clearly evident, there is also the multimodal nature of the distribution obtained from $\mathcal{L}(6, 10)$, which indicates the complete desorption of a few chains.

Turning to the $N_{\text{mono}} = 120$ cases (hence, $\mathcal{R} = 2$), one notices that all systems present a much wider $p(R)$ at high $\text{pH} - \text{p}K_a$ values (right panels of Figure 5.11) than $N_{\text{mono}} = 60$ cases. There are, however, qualitative differences in the distribution as a function of the number of arms (hence their length) or the polymer architecture. Thus, the cases of $\mathcal{L}(6, 20)$ and $\mathcal{S}(6, 20)$ interacting with the SMMSC macroion are more compact suggesting their complete adsorption. At variance with these, the $\mathcal{S}(6, 20)$ interacting with the CCTC colloid presents a weak but wide shoulder evocative of the desorbed arm suggested by the value of $\langle N \rangle$, while $\mathcal{S}(6, 20)$ cases show well defined secondary maxima supporting the idea of multiple desorbed arms. Finally, the $p(R)$ of $\mathcal{L}(12, 10)$ has a very wide shoulder extending to the limit of the simulation cell, in agreement with the low fraction of adsorbed chains. Upon lowering the pH to $\text{pH} - \text{p}K_a = 1$ (mid–right

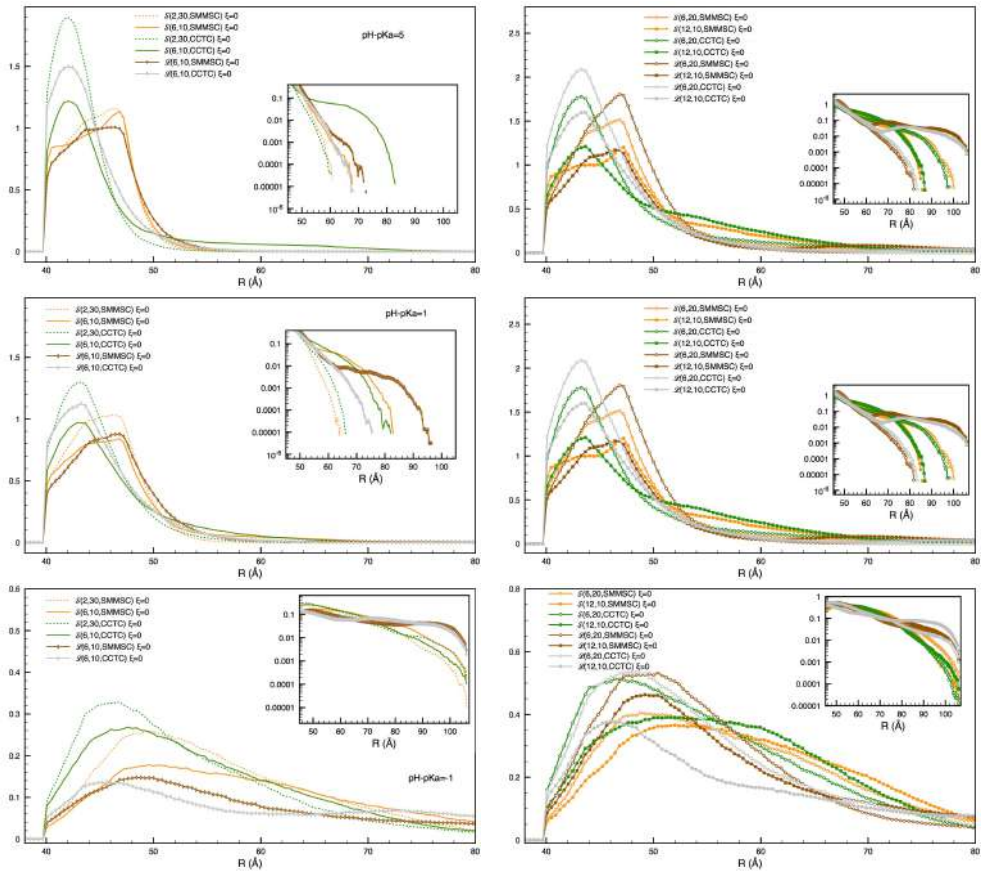

Figure 5.11: Monomers radial distribution function $p(R)$ (arbitrary units) for $N_{\mathrm{mono}} = 60$, $\xi = 0$, and three different pH values. Upper panels: $\mathrm{pH} - \mathrm{p}K_a = 5.0$; middle panels: $\mathrm{pH} - \mathrm{p}K_a = 1.0$, lower panels: $\mathrm{pH} - \mathrm{p}K_a = -1.0$. Left panels refer to the N_{mono} cases, whereas right panel refer to the $N_{\mathrm{mono}} = 120$ cases.

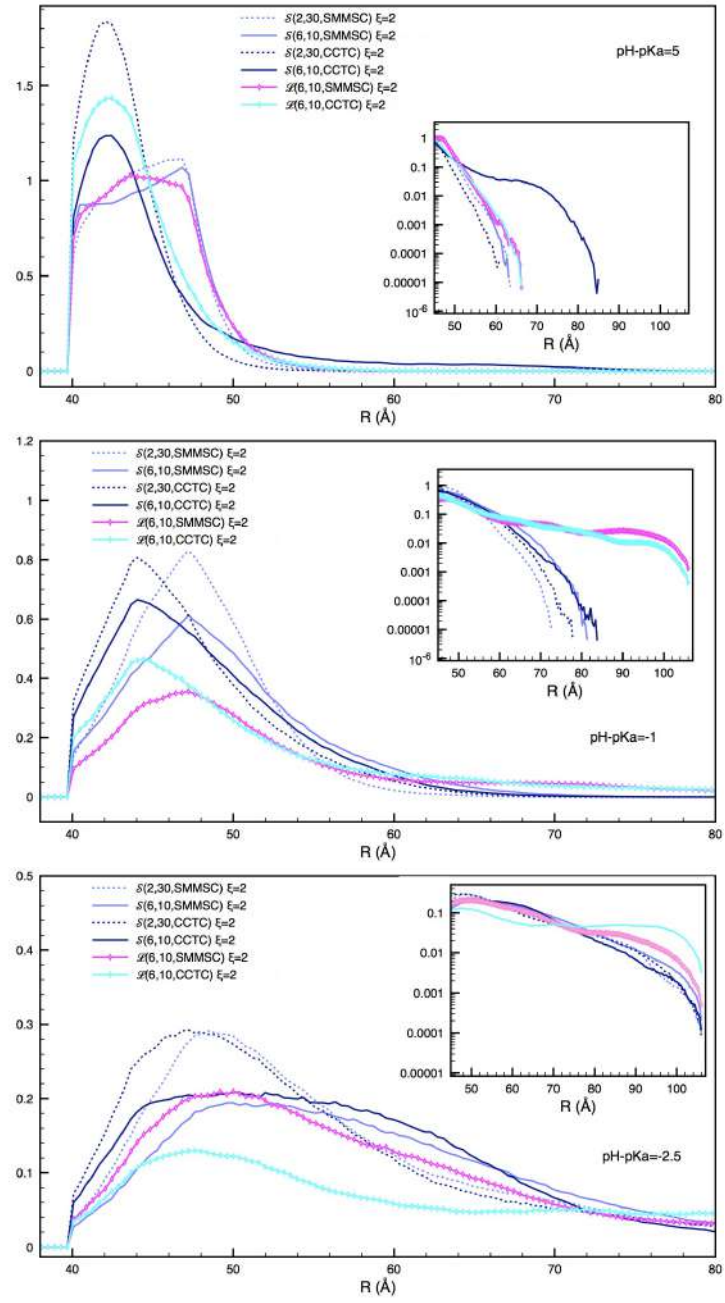

Figure 5.12: Monomers radial distribution function $p(R)$ (arbitrary units) for $N_{\text{mono}} = 60$, $\xi = 2$ kcal/mol, and three different pH values. Upper panel: $\text{pH} - \text{p}K_a = 5.0$; middle panel: $\text{pH} - \text{p}K_a = -1.0$, lower panel: $\text{pH} - \text{p}K_a = -2.5$.

panel of Figure 5.11) and, successively, to pH $-$ p$K_a = -1$ (lower–right panel of Figure 5.11), the distributions further widen and intensify their long R components. This is particularly evident for the systems composed of free chains that can completely detach from the macroions.

A similar behavior is observed also for the systems composed of $N_{\text{mono}} = 60$ and with $\xi = 2$ kcal/mol (see Figure 5.12), albeit with an interesting difference emerging for $\mathcal{S}(2, 30)$ and $\mathcal{S}(6, 10)$ cases: the broadening of distributions starts at lower pH than in the $\xi = 0$ case; thus, one must reach pH $-$ p$K_a - 1$ (mid panel of Figure 5.12, $\alpha \simeq 0.2$) to obtain a $p(R)$ of comparable width to the one at pH $-$ p$K_a = 1$ for the $\xi = 0$ case. At variance with this finding, distributions for $\mathcal{L}(6, 10)$ with $\xi = 2$ kcal/mol show the same multimodal behavior found in the case in which c-H-bonds cannot form at the same pH, albeit with somewhat less intense long R maxima. In turn, this suggests that the latter interactions may only quantitatively modulate adsorption as a side effect of the increased ionization rather than as a consequence of inter-chain c-H-bonds.

In principle, the data just presented allow us to discuss the possibility of macroion neutralization or even overcharging due to the adsorption of (partially, or fully) dissociated polyacids. Thus, the finding that all six free chains can be adsorbed at high pH on both colloid models when $N_{\text{mono}} = 60$ (see Figure 5.7) indicates that the difference in surface charge distributions has a limited impact when $\mathcal{R} \simeq 1$ and, hence, neutralization can be easily obtained. Despite the fact that only five branches of $\mathcal{S}(6, 10, \text{CCTC})$ are adsorbed, the same conclusion is reached for the remaining cases in Figure 5.7 as even the non-adsorbed arm contributes to the overall charge of the star-like polyelectrolyte–macroion complex. In turn, the observation just presented indicates that the global charge of the latter species can be easily estimated via the relation $\mathcal{Z}_{\text{NP}} - \alpha N_{\text{mono}}$ as soon as a single monomer can be considered adsorbed. Obviously, the polymer charge is concentrated over a smaller portion of the macroion surface when star-like species are present than in the case of an equivalent N_{mono} distributed over free chains, thus possibly producing strongly dipolar species.

A similar analysis can be carried out when $N_{\text{mono}} = 120$ (or $\mathcal{R} = 2$). In such case, the far from complete adsorption of free polyacid chains ($\langle N \rangle / N_{\text{chain}} \simeq 0.8$) for $\mathcal{L}(12, 10)$ suggests that, at maximum, $(\mathcal{Z}_{\text{NP}} - \langle N \rangle \alpha N_{\text{arm}})/\mathcal{Z}_{\text{NP}} \simeq -0.63$ can be reached. Conversely, there is no difference due to macroion charge distribution

or number of arms in the maximum possible overcharging at very high pH (i.e. $(\mathcal{Z}_{\mathrm{NP}} - \alpha N_{\mathrm{mono}})/\mathcal{Z}_{\mathrm{NP}} \simeq -1$) when star-like species are involved, and this is due to the fact that non-adsorbed arms are still part of the polymer-colloid complex.

5.3.3 Partitioning of Macroion's and Polyelectrolyte's Counterions

As indicated in Section 5.1, the progressive adsorption of the ionized polyelectrolytes onto the macroions is expected to foster the desorption of (divalent) m-CIs, as well as the "evaporation" of p-CIs introduced during titration simulations. To gauge the first of these phenomena, we estimate the fraction of "condensed" m-CIs (*de facto*, the fraction of m-CIs lying within b Å from the NP) as

$$\Psi(b) = \frac{\int_0^b R^2 \rho_c(R) dr}{\int_0^{R_{\mathrm{ext}}} R^2 \rho_c(R) dr} \tag{5.1}$$

where $\rho_c(R)$ is the radial density for m-CIs. Figure 5.13 shows $\Psi(b)$ for divalent m-CIs as a function of pH when $b = 53$ Å, a radius inside which the majority of the adsorbed charged monomers are contained when polyelectrolytes are fully ionized (see Figures S5.11 and 5.12).

At low pH ($\alpha \simeq 0$), one notices that a large fraction (> 0.6) of the divalent m-CIs are condensed on the macroion despite the width of the simulation sphere, the CCTC colloid condensing slightly more than the SMMSC macroion due to the higher electrid field present on its surface. The amount of m-CIs adsorbed on the macroion decreases upon increasing the pH (hence, α). Also to be noticed, there are a less steep lowering of $\Psi(b)$ upon increasing the pH and a substantially higher degree of condensation when $\alpha = 0$ in the case of the CCTC colloid, with both the slope $\left(\frac{\mathrm{d}\Psi(b)}{\mathrm{dpH}}\right)$ and the high pH value of $\Psi(b)$ for the latter markedly depending on polyelectrolyte structure. Thus, $\mathcal{L}(6, 10)$ impacts, roughly, 1.4 times more on $\Psi(b)$ than $\mathcal{S}(2, 30)$, which lowers $\Psi(b)$ 1.3 times more than $\mathcal{S}(6, 10)$.

Upon increasing N_{mono} (see lower panel of Figure 5.13), the amount of m-CIs released is always increased compared to the systems shown in the $N_{\mathrm{mono}} = 60$ case, due to the polyelectrolytes higher total charge, even though it seems to correlate positively with the macroion surface coverage that bigger polymeric species can provide. Interestingly, the tendency shown by the CCTC macroion

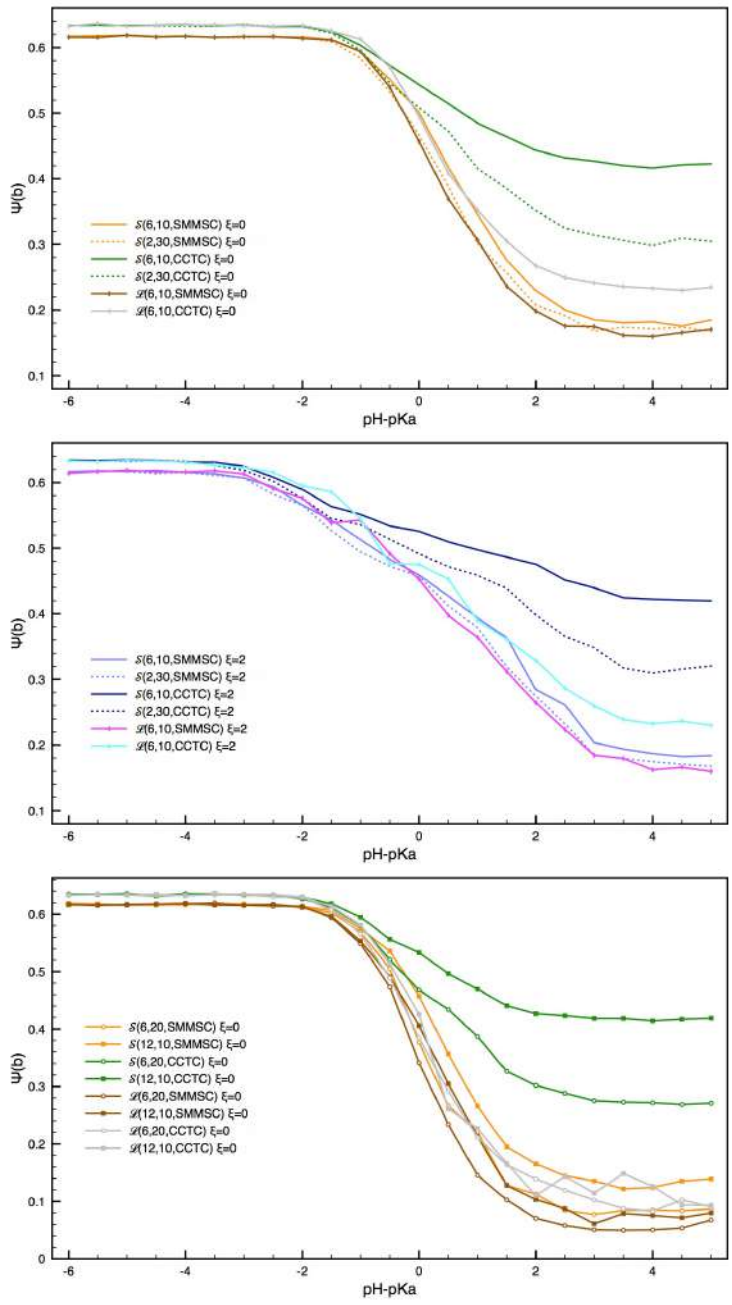

Figure 5.13: Fraction of condensed m-CIs Ψ on macroion for various systems. Upper panel: $N_{\text{mono}} = 60$ and $\xi = 0$; mid panel: $N_{\text{mono}} = 60$ and $\xi = 2$ kcal/mol; lower panel: $N_{\text{mono}} = 120$ and $\xi = 0$.

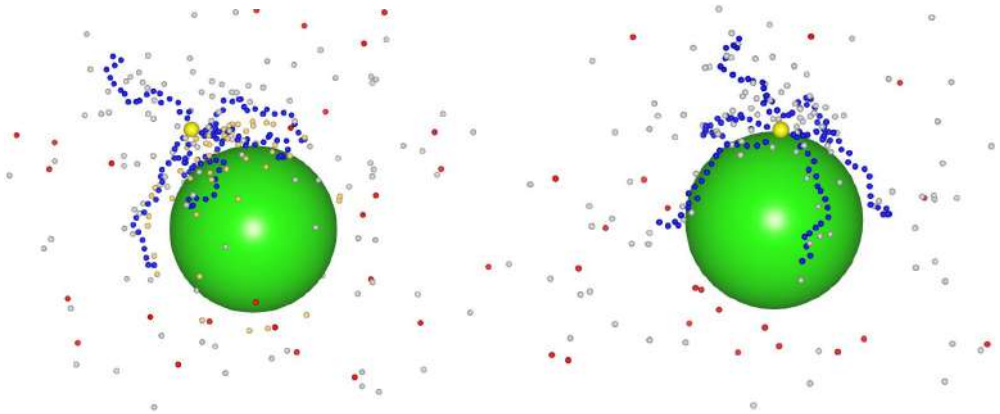

Figure 5.14: Configurations sampled at $\mathrm{pH} - \mathrm{p}K_a = 5$ ($\alpha \simeq 1$) for a six-arms star-like polyelectrolyte with $N_{\mathrm{mono}} = 120$ interacting with a SMMSC macroion (left) or a CCTC macroion (right). The color scheme is the same as Figure 5.9.

of releasing less m-CIs than the SMMSC colloid upon adsorbing star-like species seen when $N_{\mathrm{mono}} = 60$ is conserved also when $\mathcal{R} = 2$. To investigate the origin of such differences, Figure 5.14 shows the high pH configurations sampled at high pH values for the $\mathcal{S}(6, 20)$ polyelectrolyte adsorbed on both type of colloid.

From Figure 5.14, one can notice a more marked asymmetry in the angular distribution of the CCTC m-CIs with respect to the centroid of the ionized polyelectrolyte, the former being preferentially positioned in the hemispace opposite to the one where the polymer is complexed, and lying, in the average, closer to the CCTC macroion surface than in the case of the SMMSC colloid. Given the strong polarization of the SMMSC surface charge induced by the polymer adsorption, which leaves the SMMSC nanoparticle without "attractive patches" for m-CIs, these phenomena ought to be connected to the presence of a much stronger electric field on the unoccupied portion of the surface of the CCTC colloid, where the effect of an almost unscreened central charge can be felt. This has already been evidenced during the formation of complexes between charged colloids and star strong polyelectrolytes [176].

The differences in polyelectrolyte conformations and macroion charge distributions shown in Figure 5.14 suggest also that the degree of condensation for p-CIs on the polyelectrolyte itself may be a function of the system structural details; thus, the natural repulsion between p-CIs and the colloids may lead to a stronger condensation the more the free arms remain desorbed. To investigate

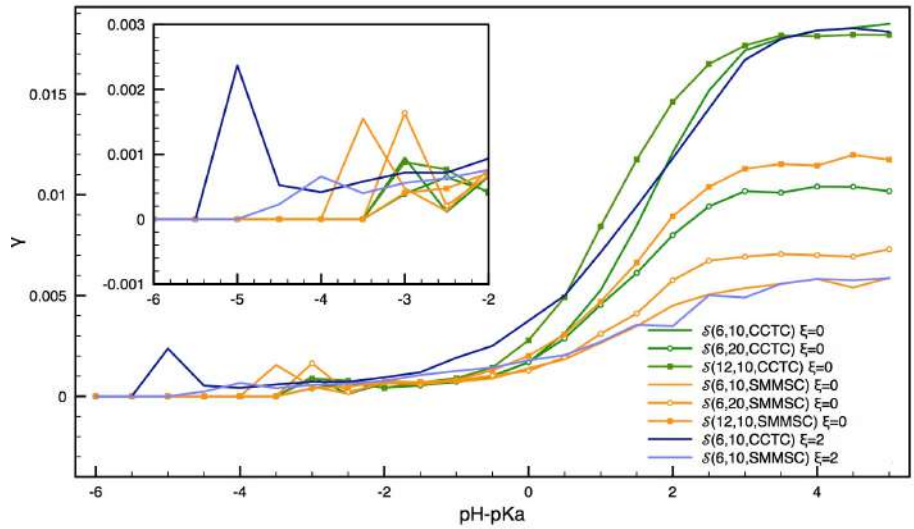

Figure 5.15: $\gamma(R_l = 7\,\text{Å}, \text{pH})$ as a function of $\text{pH} - \text{pK}_\text{a}$ for star-like systems. The inset is an expanded view of the behavior of γ at low pH.

this possibility, Figure 5.15 shows the behavior of $\gamma(R_l, \text{pH}) = \frac{\int_0^{R_l} r^2 \lambda(r,\text{pH}) dr}{\int_0^{\infty} r^2 \lambda(r,\text{pH}) dr}$, previously used as the p-CIs "condensation index" on a polymer, versus the solution pH for all the star–like species simulated (see Chapter 3). In the definition, $\lambda(r)$ is the radial distribution function between the monomers of a polyelectrolyte and p-CIs, while $R_l = 7$ Å is the distance that, somewhat arbitrarily, defines whether a ion is condensed or not on a chain.

Apart from the expected increase in γ upon increasing the pH, data shown in Figure 5.15 clearly indicate that the CCTC macroion disfavor less the condensation of p-CIs of a chosen star polyelectrolyte on the latter than the SMMSC colloid. This is due to, at least, two causes: first, the mobility of the SMMSC charges allows them to surround the adsorbed polyelectrolyte arms partially shielding their charge; and, second, the larger number of non-adsorbed arms present in complexes with the CCTC macroion with respect to the SMMSC colloid produces a higher charge density with a centroid that is located away from the repelling NP surface and that more strongly attracts p-CIs. The latter argument is also able to rationalize the differences in γ between $\mathcal{S}(6, 20)$ and $\mathcal{S}(12, 10)$, the latter locating a larger fraction of its total charge (roughly 30–50% versus 16%) away from the surface. Finally, we notice the presence of local maxima or shoulders at low pH values for many of the cases shown. These suggest that the few ionization

events present at low pH necessitate of inserting the neutralizing counterion close to the dissociating monomer. Upon increasing the pH, such requirement weakens substantially due to the analytical form of the Metropolis-Hastings ionization acceptance step.

As a macroscopic consequence of the different ion distributions, dissimilarities may be present in the behavior of the absolute osmotic pressure π_{abs}, or rather the osmotic coefficient $\Phi = \pi_{\text{abs}}/\pi_{\text{id}}$, versus $\text{pH} - \text{p}K_a$ for the studied systems. Here, π_{id} is the osmotic pressure computed via Nerst law assuming that all species behave ideally (i.e., they are non-interacting). Thus, Φ is a direct measure of the impact that ion condensation or spatial correlation between species with opposite charges have on the value of π_{abs}, and it can be semi-quantitatively estimated exploiting the cell model used in our simulations [202]. π_{abs} was found to increase upon increasing the pH due to the release of m-CIs following polyelectrolytes adsorption and the introduction of p-CIs. However, we previously observed how the activity of mobile ions markedly depended on the characteristics of each system. Thus, Figure 5.16 presents Φ for both monovalent and divalent anions cases.

At low pH, a situation in which the osmotic pressure is only due to the divalent macroion counterions, we notice that the osmotic coefficient is quite small ($\Phi \simeq 0.25$) in all cases, indicating that a large amount of anions is indeed osmotically inactive as it is either condensed on or maintained very close to the colloid (see Figures 5.13 and 5.14). The value of Φ is somewhat higher when monovalent m-CIs are present (Figure S5.16), even though it still suggests that these have a strongly non homogeneous distribution.

Upon increasing the pH, we notice a rapid increase of Φ over an interval of $\text{pH} - \text{pK}_\text{a}$ values (roughly $-2 < \text{pH} - \text{pK}_\text{a} < 0.5$) that closely correspond with the ranges over which both the ionization of the polyelectrolytes and the average number of adsorbed monomers increases. The increase in Φ may thus be due to the simultaneous release of both macroion (see Figure 5.14) and polyelectrolyte CIs, the latter mutually compensating each other as a consequence of the adsorption.

Interestingly, differences in the behavior of Φ appear upon increasing $\text{pH} - \text{p}K_a$ above 0.5 for all studied systems. Thus, whereas $\mathcal{S}(2, 30)$ and $\mathcal{S}(6, 10)$ adsorbed on the SMMSC macroion and $\mathcal{L}(6, 10)$ interacting with both colloids reach a limit

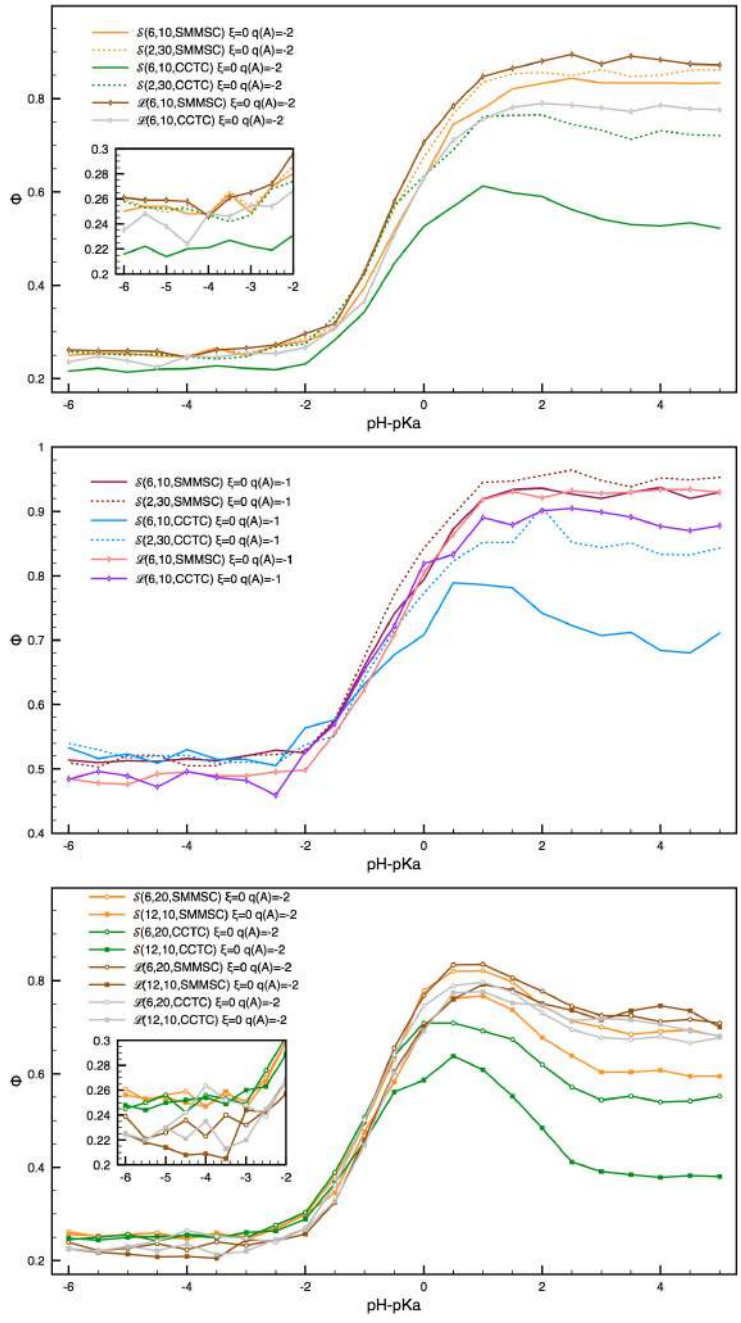

Figure 5.16: Osmotic coefficient Φ as a function of pH $-$ pK_a for various systems. Upper panel: $N_{\text{mono}} = 60$, $\xi = 0$, divalent m-CIs ($q(\text{A}) = -2$); mid panel: $N_{\text{mono}} = 60$, $\xi = 0$, monovalent m-CIs ($q(\text{A}) = -1$); $N_{\text{mono}} = 120$, $\xi = 0$, divalent m-CIs ($q(\text{A}) = -2$).

value for Φ, the remaining systems presented a substantial (20%, at least) decrease in the osmotic coefficient value. The mentioned decrease is made more marked by increasing N_{mono}, increasing the number of arms in star-like species, or by adsorbing polyelectrolytes on the CCTC macroion. In the latter respects, the magnitude of decrease in Φ seems to negatively correlate well with the capability of a polyelectrolyte to foster desorption from a specific macroion thanks to longer arms or to a more homogeneous surface coverage, whereas it positively correlates with the tendency to condense its own CIs (see Figure 5.15) on a larger number of non-adsorbed arms (Figures 5.7 and 5.8). The latter observation is reminiscent of the experimental results presented in Reference [137], where a decrease in Φ is seen upon increasing the number of arms, and in Reference [203], where recapture of p-CIs by polystyrene sulfonate adsorbed onto lysozyme has been evidenced for $\mathcal{R} > 1$.

5.3.4 Impact of the Polyelectrolyte Structure and Interactions on its Helmholtz energy as function of the pH

As presented in Section 3.3.1, polymer structure and interaction forces impact on α at a chosen $\text{pH} - \text{p}K_a$ value and, as a consequence of Equation 2.35, also on the value of the Helmholtz energy for the whole system. *Di per se*, knowing A (or rather ΔA, see Equation 2.35) may appear of little interest; the latter value, however, may be used to estimate changes in Helmholtz energy in processes of general interest, among which we mention:

i. the exchange of a "canonical" polyelectrolyte (i.e., $\xi = 0$) adsorbed onto a specific macroion at a chosen pH with one with identical structure and composition but able to form c-H-bonds ($\xi = 2$ kcal/mol);

ii. the exchange of a polyelectrolyte adsorbed onto a specific macroion at a chosen pH with another composed of the same number of monomers but presenting a different geometrical structure;

iii. the exchange of a chosen polyelectrolyte between two different macroions.

The former two processes provide indications on the dependence on polyelectrolytes structure or chemical nature on thermodynamical stabilization of the macroion–polyelectrolyte complexes and, when polyelectrolytes are adsorbed, on

the critical aggregation concentration of the species forming colloids if these are considered a model for micelle or vesicle–like species [9]. The third process, instead, suggests which type of macroion may win the competition for a specific polyelectrolyte. Results obtained for systems with $N_{\text{mono}} = 60$ are shown in Figure 5.17.

As for the exchange between polyelectrolyte with and without c-H-bonds, data in Figure 5.17 (upper panel) indicate that there is a range of pH values in which the presence of MB interactions makes the polyelectrolyte–macroion complex energetically more stable than in the $\xi = 0$ case, regardless of polyelectrolyte structure and macroion charge distribution. This is due to the superposition of two effects, namely the higher ionization at low pH and the more compact nature maintained up to medium pH afforded by c-H-bonding species. Importantly, no differences are present between the two species at high α values, as expected basing on the absence of c-H-bonds near complete ionization.

Turning to the exchange between polymers with a different structure (mid panel of Figure 5.17), our data suggest that the Helmholtz energy of the complexes increases upon increasing the structuring of polyelectrolytes: thus, the $\mathcal{L}(6, 10)$ complex is more stable by, at least, 10 kcal/mol compared to the $\mathcal{S}(2, 30)$ one, whereas the exchange $\Delta(\Delta A)$ of the latter with the $\mathcal{S}(6, 10)$ (resulting in increasing the number of arms while maintaining constant the total number of monomers) is positive by, at least, 10 kcal/mol. These differences can be easily rationalized recalling the dependency of ionization on the species structure (Section 3.3.1), the one with the highest α showing the more negative ΔA. The same idea can also be used to rationalize the larger ΔA seen for the exchange process involving the CCTC macroion than for the SMMSC colloid.

Finally, $\Delta(\Delta A)$ for the exchange between CCTC and SMMSC macroions suggests that complexes with the latter are substantially more stable than with the former when $\alpha > 0.1$, as it would have been expected basing on the relative values for the ionization degrees. We notice, however, that complexes between $\mathcal{S}(2, 30)$ and $\mathcal{S}(6, 10)$ and the CCTC macroion are slightly more stable than their counterparts with the SMMCS colloid at very low pH, a finding in agreement with the marginally higher ionization in the former cases. Identical conclusions are reached when species forming c-H-bonds or with $N_{\text{mono}} = 120$ are involved in the exchange (not shown).

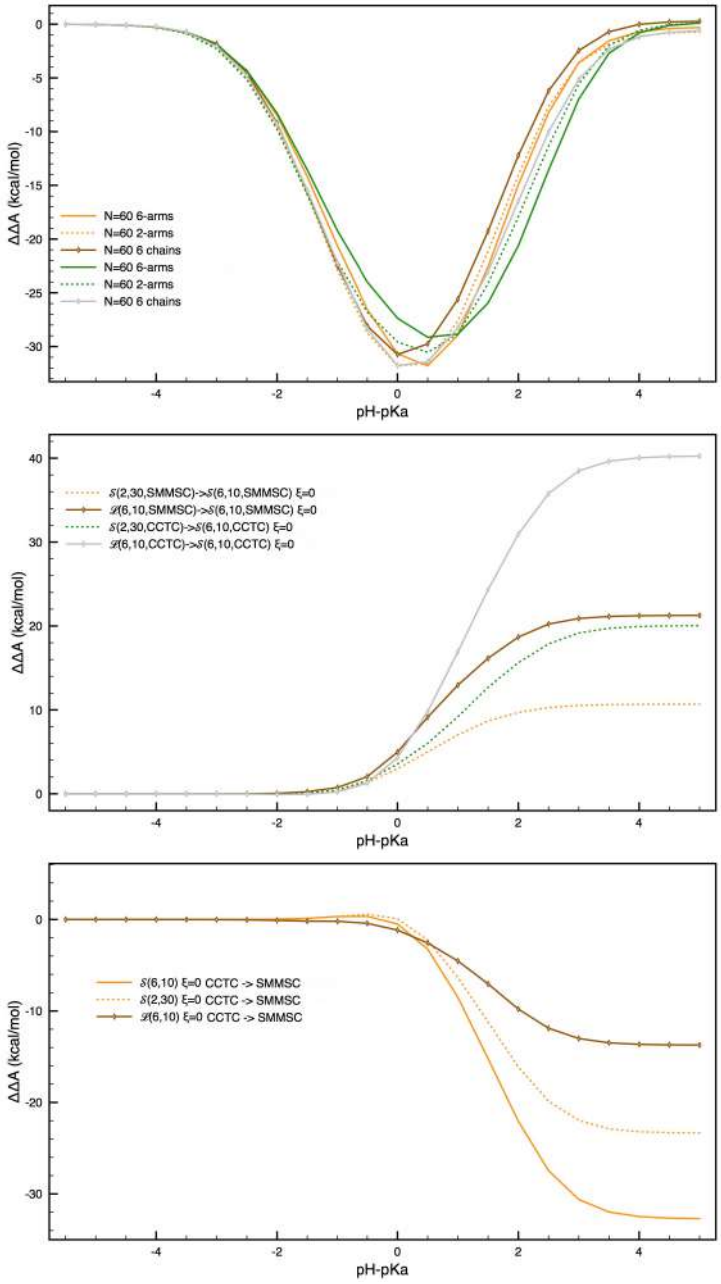

Figure 5.17: Differences in ΔA, i.e. $\Delta(\Delta A)$, due to an increase of pH for a few exchange processes related to adsorption of polyelectrolytes with $N_{\text{mono}} = 60$. Upper panel: exchange between polyelectrolytes able and unable to form c-H-bonds (i.e., $\xi = 0$ versus $\xi = 2$ kcal/mol); mid panel: changes in polyelectrolytes structures; lower panel: change in macroion's charge distribution (i.e., CCTC versus SMMSC).

5.4 Conclusions

In this work we have theoretically studied the ionization of weak polyacids interacting with oppositely charged macroions as a function of pH, which invariably leads to the formation of electrostatically–stabilized complexes between the two species when pH $\geq$ pK_a. The situations explored by us correspond to the strong associative charging limit (SACL, when $-1 <$ pH $-$ p$K_a < 1$) and the strong charging limit (SCL, pH $-$ p$K_a > 3$) previously analyzed by Whitmer and co-workers [204]. Compared to such work, however, we have extended substantially the families of investigated systems with respect to CIs' valence, polyelectrolytes structure (and number of chains/arms), as well as the nature and features of the constantly charged species in order to further shed light on facets previously not illuminated. Thus, comparing the impact of macroion counterions (m-CIs) valence, it emerges that adsorption-increased ionization in the SACL is lower when m-CIs are divalent. The same happens for the value of the osmotic coefficient Φ, which gauges the ionic correlation between the m-CIs and the formed complex and that was previously left unexplored. Interestingly, our results on Φ indicate markedly non-monotonic trends upon increasing the pH (hence, polyelectrolyte ionization) for both star-like species and short linear chains when $\mathcal{R} > 1$, which contrast with the commonly observed decrease in Φ upon increasing polyelectrolyte ionization [202, 205]. As far as we know, this behavior for Φ versus polyelectrolyte ionization has not been discussed earlier, and its due to the counteracting trends of initially releasing m-CIs and p-CIs upon polyelectrolyte adsorption, followed by p-CIs capture on the increasingly ionized polymer chains (especially when $\mathcal{R} > 1$) as seen by Cousing and co-workers [203].

The findings on α and Φ suggest that adsorption in the SACL is even more dominated by internal energy aspects of the process [204] when m-CIs are divalent, as less entropy is gained due to m-CIs release while ionization of the weak acid takes place. Focusing on differences induced by the possibility of spatially rearranging macroion charge as it happens when two oppositely charged chains interact, the increase in α upon adsorption is markedly higher when surface charges can adapt their spatial location, so that even Φ is increased. A similar trend is seen also for the number of adsorbed arms or monomers. Turning to the consequences related to a change in polyacid structure and length when

$\mathcal{R} \simeq 1$, we notice that α, Φ, and polyacids adsorption are impacted negatively by weak polyelectrolyte ramifications in both SACL and SCL.

From a more quantitative viewpoint, exploiting 2.35 has helped to clarify possible advantages or disadvantages that should be expected with respect to the complexation ability of weak polyelectrolytes as a function of chains structure with limited computing costs. Thus, complexes stability when $\mathcal{R} = 1$ ought to decrease on going from short free chains, to a single long chain, to star-like species. This finding would appear counter-intuitive if one considers only the change in polyelectrolyte entropy upon complexation. Juxtaposing this correlation with the realization that the formation of polyelectrolyte complexes [206] and polyelectrolyte-charged NP composites [207] could be highly correlated [208], one may find ways to gain a better control over the kinetics of composites formation, as well as their rheological properties.

Apart from these aspects, results described in this chapter bear importance also for the formation of advanced materials [209] and meta–materials [210]. In particular, our results gauge the extent of modification obtainable for the coordination mode between polyelectrolytes and macroions (e.g. number of non-adsorbed arms, Figures 5.9, 5.14 and 5.7) adjusting both pH and chains structure, so that changing the mentioned parameters may allow one to precisely set the average distance between charged planar or spherical colloids in composite polyelectrolyte-NP materials [211]. In turn, one may improve the regulation of conduction via electron tunneling from between NPs [212], or the construction of dense arrays of fluorescent [207] or magnetic [213] NPs.

Focusing only on the formation of stoichiometric 1:1 complexes between star polyacids and macroions, one quickly realizes that these represent a possible type of Janus NP, which may be nearly spherical (see, e.g., $\mathcal{S}(6, 10, \mathrm{SMMSC})$ or, possibly, $\mathcal{S}(5, 10, \mathrm{CCTC})$), or dumbbell-like [214] (e.g., $\mathcal{S}$(12,10,CCTC), and $\mathcal{S}$(12,10,SMMSC)), or protruding one (or even more) "antenna–like" arm [178] (e.g., $\mathcal{S}$(6,10,CCTC), $\mathcal{S}$(6,20,CCTC), and $\mathcal{S}$(6,20,SMMSC)). In all cases, the generated systems are representative of "monovalent" patchy NPs with strongly asymmetric (dipolar) interactions [176, 177]. Moreover, our results suggest that a strong polarization of surface charges may be induced upon adsorption of the star polyelectrolyte in the specific case involving colloids formed by a mixture of ionic and non-ionic surfactants provided the micelle core is fluid. This would seg-

regate the non-ionic surfactants into a surface domain, probably generating the J-NP2 type of systems whose solvent evaporation-driven aggregation has been studied previously [215]. The dissymmetric complex may, eventually, undergo useful chemical transformations (e.g. a reticulation) "freezing" the distorted distribution, and/or modifying the liophilicity of non-ionic surfactants [216]. This may foster novel aggregation modalities by, for instance, tuning of the ratio of liophilic and liophobic surface areas compared to polymeric three-components micelles [217], a result simply obtained by choosing the proper relative amount of surfactants in the micelles.

The polarization of ionic surfactants may also foster inhomogeneity in the micellar core if the liophobic tails of the two surfactants markedly differ in composition and/or properties [218]. In the case micelles are employed as drug delivery systems, the asymmetric core may, for instance, facilitate loading if one of its portion is less viscous or a better solvent for the pahrmacologically active substances [218]. An intriguing possibility that may also emerge is the compartmentalization of two active molecules inside the micellar core exploiting a difference in their partition ratio, a strategy that may also pay dividends when applied to drug transport via pH-sensitive polymersomes [219, 220].

Finally, we highlight the relevance that a few of the results discussed in this work may have on the bactericidal activity of insoluble weak polyelectrolytes [26, 27, 201], considering that the electrostatic interaction between the negatively charged bacterial wall with its double layer containing divalent ions and ionizable weak polybases closely resembles our models apart from charge inversion. We begin by noticing that even short polybases appear able to release calcium ions from the wall double layer permeabilizing the wall [221], and that resistance to polycationic antibacterial substances may be imparted by adding limited amount of Ca(II) ions [222]. What our results indicate is that our model of polyacids foster the release of a sizable fraction of divalent anions even at pH values where a very limited ionization would be expected for free polymers. In turn, this suggest that properly selecting the dissociation constant of the weak electrolytic groups to "just about" conserve chain neutrality in the operational conditions may, first, facilitate the penetration of the latter through the m-CIs layer and, second, foster the dispersion of the latter due to adsorption–induced chain ionization. Notice, also, that the effectiveness of this mechanism appears to be increased when c-H-

bonds can be formed. This finding provides support to the two step mechanism of action discussed in Reference [223] for the insoluble PEG–b–(PMMA–ran–DAAEMA) terpolymers [26, 27, 201].

Chapter 6

On the Distribution of Hydrophilic Polyelectrolytes and their Counterions around Zwitterionic Micelles: the Possible Impact on the Charge Density in Solution*

6.1 Introduction

Micelles composed of surfactants with zwitterionic headgroups such as phosphorylcholines or sulfobetaines are employed when the absence of strong electrostatic forces may be advantageous for any intended application (for example, in generation of bio-compatible, non-immunogenic species that resist protein fouling [224,225], enhanced delivery of drugs [226–228], or in skin care products [229]), or as a model for biological membranes to investigate the interaction between the latter and the surrounding aqueous environment [230–232]. Zwitterionic micelles, however, show properties profoundly different from the ones of non-ionic aggregates despite their formal charge neutrality. For instance, they are believed to acquire an overall negative charge via anions accumulation close to their inter-

*This chapter has been adapted from: Mella M., Tagliabue A., Izzo L., On the Distribution of Hydrophilic Polyelectrolytes and their Counterions around Zwitterionic Micelles: the Possible Impact on the Charge Density in Solution *Soft Matter*, Advanced article (doi.org/10.1039/D0SM01541E),

Abbreviation	Meaning
SBS	Sulphobetaine–like surfactant
PBS	Phosphorylcholine–like surfactant
C_{SBS}	Cationic moiety of SBS, lying close to the micellar core
A_{SBS}	Anionic moiety of SBS, pendant tethered to C_{SBS}
A_{PBS}	Anionic moiety of PBS, lying close to the micellar core
C_{PBS}	Cationic moiety of PBS, pendant tethered to A_{PBS}
P	Polyanion
p-CI	Polyanion counterion
M	Micelle
M/P	System composed of M and P in the same simulation cell
cmc	Critical micellar concentration
cac	Critical aggregation concentration

Table 6.1: List of abbreviations commonly used in this chapter

facial region, if sulfobetaine headgroups are involved [233–235]. The so acquired negative charge impacts on ion distribution by attracting a diffuse layer of positive ions that partially masks the acquired negative charge producing the so called "chameleon effect".

The mechanism involved in negative charging of zwitterionic micelles just mentioned has been subject of many studies, both experimental [235] and theoretical [236–239]. When the zwitterionic headgroup has the positive moiety directly bound to the hydrophobic surfactant tail, as in the case of sulfobetaine based surfactants (SBS), the selective anion partitioning appears related to the double layer-like spatial disposition of the positive (C_{SBS}) and negative (A_{SBS}) headgroup moieties, with A_{SBS} lying further away from the core surface than C_{SBS} in the micellar corona [236, 238, 239]. In principle, polyanion accumulation at the micelle/solution interface may also happen via the same mechanism.

Accumulation of anions appears possible even though the relative positioning between positive and negative moieties in the zwitterionic headgroup is inverted [235] as it happens in phosphorylcholine based surfactants (PBS); this phenomenon, however, seems to require the presence of small or doubly charged cations. The latter may be involved in coordination equilibria with phosphate groups, a chemical phenomenon that would lead the micellar corona to acquire a global positive charge. As the thrust for coordination ought to be, mainly, due to electrostatic forces (both Ca^{2+} or Mg^{2+} induce anion accumulation in PBS mi-

celles despite the lack of empty d orbitals [235]), anion accumulation may appear also in presence of polycations thanks to their high charge density.

Assuming for the sake of speculation that anion accumulation just mentioned may also be induced substituting simple anions or cations with polyanions or polycations due to charge density effects, one may wonder whether or not the impact of such substitution could be more profound due to marked (and unbalanced) reduction in the entropy of ionic components. In particular, it may be interesting to investigate which (if any) role is played by polyanion counterions (p-CIs) localized at the polyelectrolyte/solution interface. These, for instance, may reduce the polyion effective charge compared to the formal one and potentially lower the interaction strength with micelles. Alternatively, polyelectrolyte capability to act as vector for the p-CIs may be much increased compared to the "separated ions" case. Apart from the effects just mentioned, p-CIs localization on polyelectrolytes seems to influence chain flexibility, its persistence length and, hence, its conformations [30, 240]; the latter are aspects that may impact on the adsorption of the chain on a micelle [6,8,9,16,185]. This may be particularly relevant in our case as the external moiety of headgroups can also hamper adsorption, at least, due to their occupied volume.

In this work, we have thus focused on studying the interaction between zwitterionic micelles and strong polyelectrolytes to understand if preferential adsorption may also appear when polyions (specifically polyanions) are present. To evidentiate if any effect is induced by connecting charged species together, we compare such systems with similar ones containing monovalent ions. The latter cases have been previously studied by theoretically means. Thus, a Gouy-Chapman like simple spherical model for the micelles with an impenetrable core and a concentric disposition of charged moieties akin to the one expected for sulfobetaines [236] justified the increase in anion concentration in the vicinity of the hydrophobic core on the basis of the presence of a capacitor-like dipolar region. With the addition of the possibility for an increase of the radial distance between the micelle core surface and charged pendants upon increasing the concentration of a background salt [241] and of differences in anion chemical potential between the latter region and the solution bulk, a similar model was demonstrated able of interpreting anion elution volumes over zwitterionic stationary phases [237]. Support for the dipolar disposition of positive and negative charged parts in zwitterionic

headgroups was obtained via coarse grained [238] and atomistic [239] molecular dynamics simulations of micelles composed of sulfobetaines. While the former study evidenced a preferential accumulation of chloride anions inside the micellar corona, an atomistic model was needed to correctly predict the relative partitioning of perchlorate, iodide, bromide and chloride anions.

For the sake of clarity, let us specifically mention how the understanding of the interaction between zwitterionic micelles and electrolytic solutions is extended by the research effort we undertook. First, we provide indications on the impact that increasing the charge density of the mobile ionic species (i.e., anions) by connecting them in polyions has on the charging of the dipolar layer due to selective adsorption. We do so employing polyelectrolytic species with both a linear (henceforth indicated as $\mathcal{L}$) and a star-like ($\mathcal{S}$) structure, as the latter possesses an even higher charge density for equal number of monomers. Second, we explore the possibility that forming micelle/polyions (M/P) complexes may favor the co-adsorption of species bearing a charge of identical sign to the innermost headgroup moiety one (e.g., p-CIs if the micelle is composed by SBS) inside the micellar corona. Third, we estimate the impact of the interaction between zwitterionic surfactants and polyelectrolytes on the concentration needed to observe micelle formation, an issue that has been experimentally investigated previously [242–246] highlighting that even neutral polymers may substantially reduce it. In this respect, it appears puzzling that hydrophilic polyanions, instead, did not lower the critical concentration at which zwitterionic surfactants aggregate (cac) forming M/P complexes as they do when charged surfactants are involved [9]. In order to explore this aspect, we compute the change in Helmholtz energy due to mixing separate solutions ($\Delta_{\mathrm{mix}}\mathrm{A}$) containing either micelles or charged polymers as originally suggested by Wallin and Linse when charged micelles were investigated [9]. To accomodate the differences in behavior between the latter and our systems, we needed, however, to develop an alternative thermodynamics path to describe the mixing process. This involves the recently derived statistical mechanics relationship between ($\partial A/\partial \mathrm{pH}$) and the average dissociation degree $\langle\alpha\rangle \equiv \alpha$ (see Equations 2.35 and Reference [240]). Fourth, we exchanged the positions of negative and positive zwitterionic moieties with respect to the micellar core to investigate if the alternative double layer structure (as it happens in phosphorylcholine-based surfactants, PBS) may modify the structure and en-

ergetics of the composite M/P system. Finally, we explored how the presence of zwitterionic micelles impacts on osmotic properties of polyelectrolytes computing the system osmotic coefficient.

To highlight our findings, we mention that the results evidenced a mild impact of zwitterionic micelles on the conformation properties of polyelectrolytes. In spite of this, stark changes in charge distributions around the micelles were found upon linking anions into a polyanion compared with the cases of "independent" (or "free") anions. Thus, the maximum of the negative charge density in the micelle vicinity increased either 30 or 40–folds compared to the free ions when the micelle was composed of PBS or SBS, respectively. For both micelle types, also the concentration of p-CIs at the micelle surface is vastly increased compared to the free ions case, a finding indicating that polyanions may act as vector for species that would be electrostatically repelled in their absence. Besides, the difference in the radial distribution of polyanions due to a change in headgroups finds a counterpart in the anionic chain adsorption probabilities, which is halved by substituting SBS with PBS. Finally, our prediction of changes induced by polyelectrolytes on the surfactant critical concentration (or critical aggregation concentration, "cac") needed to form micelles with respect to the critical micelle concentration ("cmc", i.e. in absence of polyanions) agrees well with experiments involving water soluble polyelectrolytes [244], indicating that only minor changes ought to be expected. This evidence is rationalized by our computational results as due to weak electrostatic interactions (mainly due to the lack of enthalpic effects) between micelles and polyanions.

6.2 Models and Methods

The properties of systems under investigation are obtained with a coarse-grained primitive model of electrolytes within the theoretical framework determined by the cell model (see Section 2.1.2), where system constituents are enclosed inside a sphere of radius $R_{\text{cell}} \equiv R_{\text{ext}}$. Importantly, this modeling choice allowed us to compute the osmotic pressure π_{abs} due to the polyelectrolyte, which is directly related to the species concentration *at* the cell boundary [76]. From π_{abs}, the osmotic coefficient $\Phi = \pi_{\text{abs}}/\pi_{\text{id}}$ was obtained, with π_{id} being the osmotic pressure exerted by the polyelectrolyte if all constituents acted ideally.

More in detail, our system is composed of a zwitterionic micelle and a strong polyelectrolyte with its counterions. The core of the former is represented as a centrally located impenetrable spherical nanoparticle of radius $R_{\mathrm{M}} < R_{\mathrm{ext}}$ and bearing $\mathcal{Z}_{\mathrm{M}} = 59$ zwitterionic headgroups (hence, it is overall neutral). Here, $R_{\mathrm{ext}} = 159$ Å and $R_{\mathrm{M}} = 20$ Å. In the cases akin to SBS, $\mathcal{Z}_{\mathrm{M}}$ monovalent cations ($\mathrm{C_{SBS}}$, to recall the headgroup structure) are tethered to the micelle surface by a harmonic potential (see Equation 2.4) restraining them to lie externally with an equilibrium distance $\sigma_{\mathrm{C}} = 1.0$ Å from the micelle surface itself (the force constant is $k_{\mathrm{bond}} = 200 k_{\mathrm{B}}T/\mathrm{Å}^2$, with $k_{\mathrm{B}}T = 0.5922$ kcal/mol and, hence, $T = 299$ K), and are allowed to move freely parallel to it. One charge-compensating monovalent anion ($\mathrm{A_{SBS}}$) is bonded to each of the surface tethered cations via a harmonic restraining potential with an equilibrium distance $\sigma_{\mathrm{CA}} = 4.0$ Å. The chosen equilibrium distance mimic rather well the location of distribution maxima obtained with molecular dynamics simulations [238, 239]. In the case of micelles composed of phosphorylcholine–based surfactants (PBS), we simply exchanged the positive and negative zwitterion moieties. Hence, $\mathrm{A_{PBS}}$ is the species restrained by a potential which is identical in form to the one used to tether $\mathrm{C_{SBS}}$. The values for $\mathcal{Z}_{\mathrm{M}}$ and R_{M} are chosen so that the micelle is similar to what has been experimentally obtained when employing SBS with short ($\mathrm{C_{12}}$–$\mathrm{C_{14}}$) alkyl chains [239, 247, 248]. In fact, an aggregation number in the range of 55–62 molecules for 3–(Dimethyldodecylammonium)Propanesulfonate [247] or 3–(Dimethyltetradecylammonium)Propanesulfonate [239] has been reported, and a radius of roughly 20 Å has been indicated for micelles obtained with the second surfactant.

The strong polyelectrolyte species with their counterions (p-CIs) is, instead, composed of negatively charged monomers connected together by means of harmonic potentials with an equilibrium distance $\sigma = 3.85$ Å and an equivalent number of freely wandering p-CI. We mainly simulate linear polyanions composed of $L = 10$, 30 and 60 monomers; as a comparison, we also simulated a star–shaped species with $N_{\mathrm{arm}} = 6$ identical arms, each one containing $L = 10$ monomers. In the latter, the first bead of each arm in connected to a central bead via an harmonic potential with equilibrium distance $\sigma_{\mathrm{nuc}} = 2\sigma$ [36, 249].

All particles in the system are treated as soft spheres interacting with each other via a WCA potential ($\sigma = 3.85$, Å, $\epsilon = k_{\mathrm{B}}T$). When the star nucleus is

involved, σ_{nuc} is used instead of σ.

Charged particles interact with each others via a pairwise Coulomb potential (see Equation 2.7) screened by an uniform dielectric medium with a dielectric constant $\epsilon_r = 78.3$ identical to the one of water at room temperature. Notably, the approach indicated does not take into account the fact that both chain [133,183, 250,251] and micelle core [252] may have a dielectric constant much lower than the one of water, or that even the dielectric constant of the solution may depend on the local composition [128,253]. For our specific cases, it seems that predicting the impact of accounting for dielectric discontinuities or its composition-dependent changes with respect to results obtained with an uniform permittivity could be fairly complicated due to opposing effects. For instance, one would expect a lower chain adsorption probability upon introducing monomers "image charges" inside the micelle core, whereas the high local concentration of charged groups inside the zwitterionic corona may decrease ϵ_r strengthening the interaction between the polyelectrolyte and C_{SBS}. With our modeling effort being the first attempt, as far as we know, of addressing the issues mentioned in the Introduction, we feel that is presently not necessary to further complicate the matter, and we shall thus accept the limitation imposed by Equation 2.7, at least for the time being.

The scheme in Figure 6.1 provides a visual representation for the surfactants and micellar models. For convenience of discussion, we dub the system composed of a linear polyanion with L monomers and interacting with a micelle formed by X =SBS or PBS surfactants as $\mathcal{L}(1, L, X)$; the systems containing the star-like polymer is instead dubbed $\mathcal{S}(6, 10, X)$.

We performed classical Monte Carlo simulations, sampling the canonical thermal density matrix of the system. Monomers, counterions, and zwitterionic moities are displaced randomly along three orthogonal directions with a maximum attempted step and random displacements are accepted using the classical Metropolis-Hastings rule Equation 2.30). Apart from random monomer displacements, a series of cluster moves (see Section 2.2.1.4) are also attempted on the polyanions; these are: (i) entire species translations; and (ii) pivot moves. In the end, each Monte Carlo step consists of the attempted translation of each particle in the system, one rigid chain translation and one pivot move.

As the osmotic pressure π_{abs} (*vide supra*) is an extremely local quantity, it required quite extensive MC sampling to obtain reasonably precise values for an

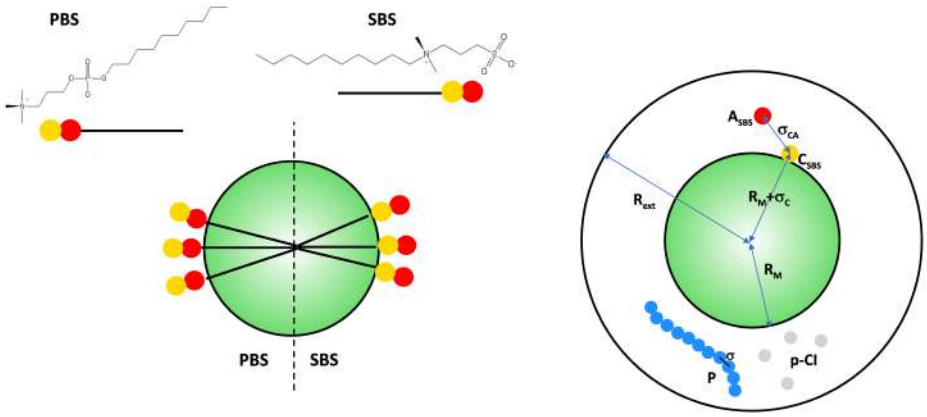

Figure 6.1: Structure and schematic representation for SBS and PBS, as well as for the model micelle investigated in this work. Color scheme: impenetrable micelle core in green, headgroup's cations in light orange, headgroup's anions in red, polyelectrolyte monomers in blue, polyelectrolytes counterions in light gray.

insightful discussion. Thus, all our simulations have been run until a relative standard error of 5% compared to the associate average value π_{abs} was obtained. As a positive byproduct, nearly all other physical quantities for the systems investigated have reached a statistical accuracy of, at least, 1 part for thousands; we thus avoided to show statistical errors completely (exception made for the Helmoltz energy and average potential profiles, *vide infra*).

6.2.1 Helmholtz energies calculation

For estimating changes in surfactant critical concentration, we needed to compute the change in Helmholtz energy, $\Delta_{\text{mix}}A$, due to mixing zwitterionic micelle (M) and polyelectrolyte (P) solutions of initial (i) concentration $C_S^{(\text{i})}$ and volume $V_S^{(\text{i})}$ ($S = \text{M}$ or P) into a final (f) system of volume $V^{(\text{f})} = V_{\text{M}}^{(\text{i})} + V_{\text{P}}^{(\text{i})}$ and concentrations $C_S^{(\text{f})} = C_S^{(\text{i})} V_S^{(\text{i})} / V^{(\text{f})}$ (here, we assume that $C_{\text{P}}^{(\text{f})} = C_{\text{M}}^{(\text{f})} \equiv C_{\text{MP}}^{(f)}$); to this end, we exploited the "function of state" nature of A by selecting a computationally convenient path to estimate it. Such path is composed of the following steps to be carried out in sequence (see also Figure 6.2 for a graphical representation):

1. **Neutralization of the polyanion isolated in its own cell.**
   The change in A associated with such step ($\Delta_{\text{neut}}A$) is estimated exploiting the relationship between ($\partial A/\partial \text{pH}$) and the average ionization degree (see

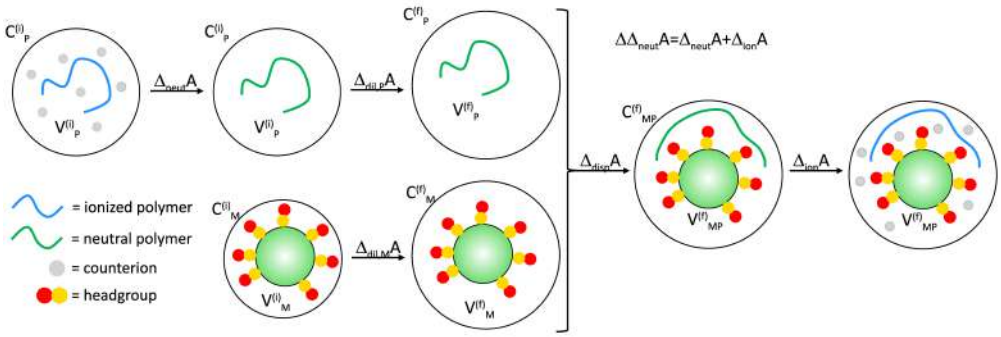

Figure 6.2: Thermodynamic path followed to estimate the change in Helmholtz energy due to mixing ($\Delta_{\mathrm{mix}}A$) micelle and polyelectrolyte solutions, each with the initial concentration $C_{\mathrm{S}}^{(\mathrm{i})}$ (S = M or P) into a solution with final concentration $C_{\mathrm{MP}}^{(\mathrm{f})}$ for both species. The other changes in Helmholtz energy indicated in the scheme refer to polyanion neutralization ($\Delta_{\mathrm{neut}}A$), the dilution ($\Delta_{\mathrm{dil}}A$) of both neutralized polymer and micelle to the final concentration, the displacement ($\Delta_{\mathrm{disp}}A$) of the polymer into the micelle cell, and the re-ionization ($\Delta_{\mathrm{ion}}A$) of the polymer to reintroduce p-CIs. The impenetrable micellar core is depicted in gray.

Reference [240] and Equation 2.35) by temporarily assuming that polyelectrolyte monomers behave as weak acids; here, $\langle q_i \rangle$ is the average charge of monomer i. This approach necessitates of the constant-pH method (see Section 2.2.2). We selected to apply this step in order to avoid difficulties related with the diffuse nature of the p-CIs while transferring the polyanion into the cell containing the micelle.

2. **Diluition of both micelle and polyanion to their final concentration in the mixed solution.**
   This step involves computing the change in Helmholtz energy due to increasing the radius of both cells from $R_{\mathrm{ext}}^{(i)} = [3\times10^{27}/(4\pi C^{(\mathrm{i})}\mathcal{N}_A)]^{1/3}$ Å) to the common $R_{\mathrm{ext}}^{(f)} = [3\times10^{27}/(4\pi C^{(\mathrm{f})}\mathcal{N}_A)]^{1/3}$ Å). Here, $\mathcal{N}_A$ is Avogadro's number. For the micelle, if $C^{(\mathrm{i})}$ is sufficiently low so that the electrostatic field generated by a micelle does not reach another one (i.e., the second term in the virial expansion of π is zero), the change in Helmholtz energy due to dilution is only due to an increase in translational entropy and it can be estimated as $\Delta_{\mathrm{dil,M}}A = RT\ln[C_{\mathrm{M}}^{(\mathrm{f})}/C_{\mathrm{M}}^{(\mathrm{i})}]$. In the case of neutralized polyanion, instead, the mobility of the latter may bring it sufficiently close to the cell boundary to impact on its conformations and thus modify its internal energy. We thus opted for simulating the change in C_{P} ($\Delta_{\mathrm{dil,P}}A$) via the same approach we employed to gauge the free energy of absorption

in spherical cavities [37] despite the fact that the magnitude of such effect ought to increase with polymer size.

3. **Displacement of neutralized polyanion from its simulation cell into the micelle one.** The change in Helmholtz energy due to this step ($\Delta_{\rm disp}A$) can be estimated either via the Widom's insertion method [254], with conformations for micelle and neutralized polyanion generated by stochastic simulations in separate (but identical) cells, or via the free energy perturbation (FEP) method [255]. In the latter, one may assume as a reference state one with non-interacting micelle and neutralized polyanion: the final state would, instead, have their interaction potential fully switched on. Given the analytic form of our model potentials, FEP is fundamental akin to computing the ratio between the accessible configurational space volume for the complete system, and the same quantity for a fictitious system without M/P interactions. In the end, we opted for implementing the FEP approach schematically indicated for mere convenience of programming.

4. **Complete reionization of the polyanion in the final (mixed) solution.** In this step, p-CIs are reinserted to generate the complete M/P system titrating the fictitious polyacid until pH $\gg$ pK_a; the associate Helmholtz energy change ($\Delta_{\rm ion}A$) is estimated as in the first step of this list. Compared to the neutralization of an isolated polyanion, $\Delta_{\rm ion}A$ would contain also contributions from the Coulomb interactions between p-CIs and micelle, ionized monomer and micelle, as well as to changes in the electrostatic screening of all charged species due to the change in composition of the environment [240].

In order to interpret $\Delta_{\rm mix}A$ results obtained with the procedure just discussed, we also collected the radial distribution of the polyanion center of mass (CoM) with respect to the micelle center to produce radial Helmholtz energy profiles, as well as the average value of the system total potential over narrow intervals along the same coordinate.

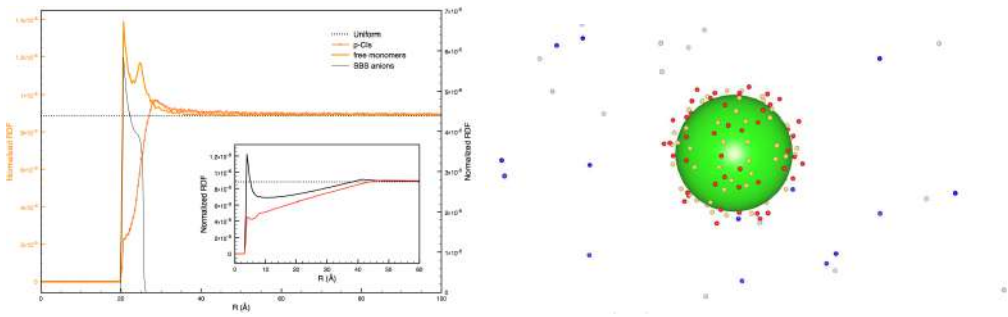

Figure 6.3: Left panel: normalized distributions for 60 charged free monomers, their p-CIs and A_{SBS}. The dashed line represents the distribution for uniformly distributed species; the right axis relates to the A_{SBS} distribution. Distributions for monomer/C_{SBS} (black) and CIs/A_{SBS} (red) pairs are also shown in the inset. The normalization is such that $\int D(R)R^2\mathrm{d}R = 1$. Right panel: configuration sampled for the system whose distributions are shown in the upper panel. Color scheme: negatively charged monomers in blue; p-CIs in gray; A_{SBS} in red; C_{SBS} in light orange. The impenetrable micellar core is depicted in green.

6.3 Results and discussion

To facilitate the discussion of differences in behavior induced by connecting anions into polyanions, we begin the presentation of our results with the ones obtained for systems composed of a zwitterionic micelle and N_{mono} monovalent ion pairs (i.e, N_{mono} monomers and a correspondent amount of p-CIs).

6.3.1 Zwitterionic micelle in presence of simple 1:1 electrolytes

The left panel of Figure 6.3 shows micelle-centered distributions for negatively charged monomers, p-CIs and A_{SBS} for $N_{\mathrm{mono}} = 60$. Results for the cases $N_{\mathrm{mono}} = 10$ and 30 have also been obtained, and they closely match the ones shown. As all charge bearing species share an identical value for σ, which defines their excluded volume, the results discussed in this Section can also represent the ones for PBS micelles upon exchanging labels between monomers and p-CIs, C_{SBS} and A_{PBS}, and A_{SBS} and A_{PBS}.

Comparing distributions with the case of uniformly distributed species, we notice that both monomers and p-CIs present a higher concentration, albeit slightly, than the nominal one in the vicinity of a micelle. Their distributions, however, differ substantially. Thus, monomer distribution displays a multimodal nature with its highest maximum (roughly 1.5 higher than the average concentration) being located close to the micellar core surface, and with the second maximum

being generated by the fact that the solvent accessible surface area of the micellar core is limited by A_{SBS}, which often lie in the vicinity of a C_{SBS} belonging to a different headgroup (see left panel of Figure 6.3). This characteristic would limit the lateral access to C_{SBS} by the negatively charged beads, thus imposing C_{SBS} and monomers to coordinate with the latter remaining distant from the surface; in fact, the location of the secondary maximum for the latter nicely agrees with the sum between σ_C and σ.

As for the p-CIs, instead, their distribution peaks lie just outside the range of distances spanned by the A_{SBS} of the zwitterionic corona. According to Gauss' Law, there should be no radial electric field outside the corona region due to the charge neutrality of an isolated micelle. Thus, the presence of a maximum in the p-CIs distribution ought to be ascribed to the overall negative charge acquired by the micelle following the adsorption of anions. This idea is well supported by the fact that p-CIs appear able to penetrate the headgroup layer despite the opposing field, as well as by the fact that the distribution for the p-CIs/A_{SBS} pair presents a maximum well below the uniform concentration value at distances compatible with the pair direct coordination. In fact, if the root cause for the maximum in p-CIs distribution was the electrostatic attraction with A_{SBS}, the maximum in pair distribution ought to be higher than the average p-CIs concentration.

6.3.2 Zwitterionic SBS micelles in presence of strong polyanions

We begin the presentation of simulations on polyelectrolyte/micelle composite by discussing results for the isolated $\mathcal{L}(1, L)$ systems with $L = 10$, 30 and 60 reported in Table 6.2, as these represent a reference for the interacting M/P complexes. From the average values obtained for isolated polyanions, we notice that, as expected, both the gyration radius $\sqrt{\langle R_g^2 \rangle}$ and the "end to end" distance $\sqrt{\langle r_{1N}^2 \rangle}$ (see Equations 2.13 and 2.14) increase upon increasing N_{mono}. Independently of the latter, $\phi = \sqrt{\langle R_g^2 \rangle}/\sqrt{\langle r_{1N}^2 \rangle} \simeq 2.87$, which suggests that polyelectrolytes are fairly elongated. In spite of this, polyanions do not act as rigid rods, as it is indicated by the average angle between two consecutive bonds, $\langle \theta \rangle \sim 125°$, and the persistence length $l_p = \sqrt{\langle R_{mm}^2 \rangle/(1 + \langle \cos\theta \rangle)}$, which suggest that the chain needs only slightly more than two bond lengths to make a "sharp turn" (here, $\langle R_{mm}^2 \rangle$ is the root mean squared distance between bonded monomers). In

L	$\langle\theta\rangle$	l_p (Å)	$\sqrt{\langle R_g^2\rangle}$ (Å)	$\sqrt{\langle r_{1N}^2\rangle}$ (Å)
		$\mathcal{L}(\mathbf{1},\mathbf{L})$		
10	124.9(2)	8.27(6)	7.9(5)	22.6(1)
30	127.1(1)	8.84(4)	21.7(5)	63.11(5)
60	127.3(1)	8.66(2)	38.1(9)	110.0(1)
		$\mathcal{L}(\mathbf{1},\mathbf{L},\mathbf{SBS})$		
10	125.0(1)	8.20(1)	7.9(6)	22.75(1)
30	127.4(41)	8.74(1)	24.5(1)	65.9(1)
60	127.0(1)	8.58(3)	38.6(7)	107.0(1)
		$\mathcal{L}(\mathbf{1},\mathbf{L},\mathbf{PBS})$		
10	125.2(1)	8.24(1)	7.9(5)	22.4(1)
30	127.4(1)	8.75(1)	21.2(2)	62.6(1)
60	127.3(1)	8.67(1)	40.2(3)	121.7(1)

Table 6.2: Average conformational properties for isolated polyanions ($\mathcal{L}(1, L)$), and polyanions interacting with SBS ($\mathcal{L}(1, L, \text{SBS})$) and PBS micelles ($\mathcal{L}(1, L, \text{PBS})$).

other words, whereas the inter-monomer repulsion is responsible for the deviation from a random coil behavior (in such a case $\langle\theta\rangle = 90°$ and $\phi = 2.45$), it is not sufficiently strong to force the complete extension of the polyelectrolytes. This finding is in line with what previously found with similar models and attributed to the effect of the localization of p-CIs on the polyelectrolyte [9, 30, 256]. At a higher level of detail, we also notice that both $\langle\theta\rangle$ and l_p increase upon increasing N_{mono}, possibly a consequence of a somewhat stronger inter-monomer repulsion due to the increased chain length.

Moving to M/P interacting systems, the upper panel of Figure 6.4 shows the distribution results for $\mathcal{L}(1, L, \text{SBS})$ systems with $L = 10$, 30 and 60.

The distributions for $\mathcal{S}(6, 10, \text{SBS})$ are instead shown in Figure 6.15 in the Appendix 6.5; a comparison with the $\mathcal{L}(1, 60, \text{SBS})$ highlights that only minor differences in behavior are indeed present between linear and star-like polyelectrolyte.

From monomer distributions shown in Figure 6.4, it is evident that the polyanion penetrates, at least partially, the zwitterionic corona for all three the L values, frequently reaching its innermost part. This picture is supported by the pair distributions between monomers and C_{SBS} (see the inset), which displays both a sharp maximum located at $R \sim \sigma$ proving the contact between the two species,

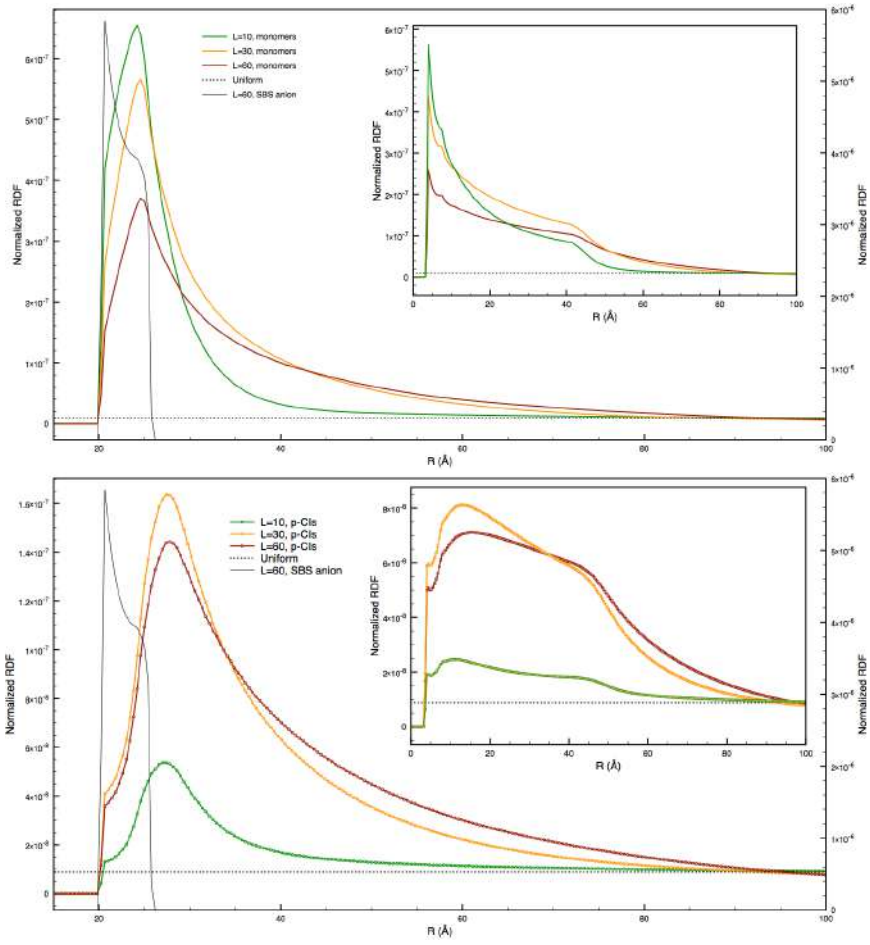

Figure 6.4: Radial distributions for $\mathcal{L}(1, L, \mathrm{SBS})$ with $L = 10$, 30 and 60. The dashed line represents the distribution for uniformly distributed species. The right axis related to A_{SBS} distribution only. Upper panel: distributions from the micelle center for charged monomers; the distributions for the monomer/C_{SBS} pairs are also shown in the inset. Lower panel: distributions from the micelle center for p-CIs; the distributions for p-CIs/A_{SBS} pairs are also shown in the inset.

and indications of a secondary structure positioned at $\sim 2\sigma$, probably due to the regular monomers spacing in the polyelectrolyte. Worth noticing, the local concentration for the chain beads inside the corona is 20–40 times higher than the one shown in Figure 6.3 for freely wandering monomers, showing that the increase in charge density due to their connectivity has a massive impact on the propensity toward localization on the micelle. Bearing in mind that all distributions are normalized to unity (i.e. their relative height should scale by 1:3:6 to represent the relative concentration for $L = 10$, 30 and 60), we notice that the amount of monomers lying inside the corona appears to grow with N_{mono}, thus suggesting that some form of "many-body effect" should be at play. Besides, all three distributions are characterized by long tails located well outside the micellar corona, a finding that may indicate thatsome chain segment are not adsorbed on the micelle, and/or that the polyion frequently detaches on the whole from the zwitterionic corona and freely wanders in solution.

p-CIs distributions for the $\mathcal{L}(1, L, \text{SBS})$ system are shown in the lower panel of Figure 6.4. Similarly to the free monomers' counterions (see Figure 6.3), p-CIs distributions show a peak just outside the zwitterionic corona and appear able to penetrate the latter reaching the micelle core despite the repelling C_{SBS} moieties located in its vicinity. The intensity of these effects is, however, an order of magnitude higher than shown in Figure 6.3, suggesting that it may be the polyanion that acts as a vector capable of drawing p-CIs inward. This idea is supported also by the similarity in width between monomer and p-CIs distribution, as well as by the fact that only weak maxima are present at short distances in the pair distributions between p-CIs and anionic moieties in the zwitterionic corona (see inset in Figure 6.4). This observation can be exploited, for instance, to speed up reactions between species bearing the same charge as p-CIs with species partitioning at the interphase of SBS micelles more than it would be possible when only monovalent anions were present [257] and exploiting the fact that the law of mass action relates the rate of a reactive encounter to the local concentration of the involved reactants. This may, thus, further extend the application of zwitterionic micelles to the speeding up of reactions, which is already a well-studied occurrence when corona-adsorbing anions are among the reactants (e.g. in S_N2–type nucleophilic processes [258]), to include reactions with electrophilic compounds [257] such as H^+.

N_{mono}	$\langle N^{\text{ads}}_{\text{mono}} \rangle$	$P^{\text{ads}}_{\text{chain}}$	$\langle \max[N^{\text{ads}}_{\text{mono}}] \rangle$
		M(SBS)/P system	
10	1.48(9)	0.26(2)	9.6(2)
30	4.0(2)	0.56(2)	21.5(3)
60	4.79(9)	0.68(2)	21.1(2)
		M(PBS)P system	
10	0.13(1)	0.036(3)	8.3(3)
30	1.06(5)	0.21(1)	18.2(3)
60	1.67(2)	0.33(3)	16.4(8)

Table 6.3: Values for the average number of adsorbed monomers ($\langle N^{\text{ads}}_{\text{mono}} \rangle$), the adsorption probability for a chain ($P^{\text{ads}}_{\text{chain}}$) and the average value of the maximum number of adsorbed monomers $\langle \max[N^{\text{ads}}_{\text{mono}}] \rangle$ for polyanions interacting with SBS micelles (M(SBS)/P system) and PBS micelles (M(PBS)/P system).

Apart from the possible rate enhancement effect just discussed, substituting monovalent anions with a polyanion may also impact on the effectiveness that positive counterions demonstrate in screening the negative charge acquired by the micelle, that is on the "Chameleon effect" [257]. In fact, comparing the relative height of monomers and p-CIs distribution obtained for $\mathcal{L}(1, L, \text{SBS})$ and the case with free monomers (see Figure 6.3), one may suspect that the "stealth" nature of SBS zwitterionic micelles may be compromised, at least partially, by the presence of polyelectrolytes. To check whether or not this is the case, and eventually the reasons involved, we computed the average fractional charge unbalance (or local charge density) within a distance from the micelle center for all the cases discussed so far. The results are shown in Figure 6.5 and clearly indicate that the negative charge due to the adsorption (albeit temporary) of a polyanion remains unbalanced over a very wide range of distances (i.e., beyond the polyanion average extension), and that its magnitude is one hundred times higher compared to the case in which monovalent anions are involved. Interestingly, the spatial extension of the effect suggest that it may be mainly due to the fact that a sizable fraction of p-CIs (and thus their charge) is dispersed in solution whereas the polyanion charge is more concentrated, an idea neatly supported by the adsorbed configurations shown in Figure 6.6 (*vide infra*).

An alternative representation for the interaction between SBS micelles and linear polyanions is provided by quantities averagely gauging the "contact" between the two species. For sake of simplicity, we consider that chain (or arm) is

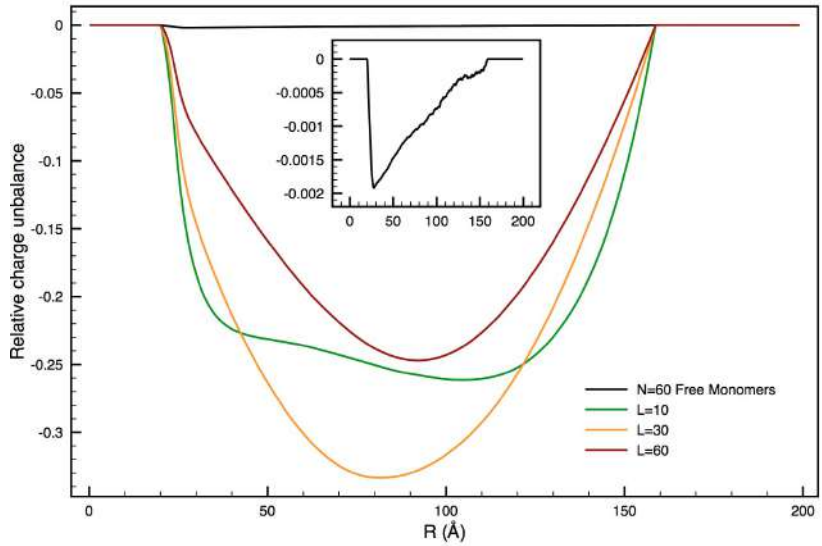

Figure 6.5: Relative charge unbalance within a distance R from the micelle center, $\left(4\pi \int_0^R [\rho_+(r) - \rho_-(r)]r^2 \mathrm{d}r\right)/N_{\mathrm{mono}}$, for the $\mathcal{L}(1, L, \mathrm{SBS})$ and free monomers cases discussed in the main text. Here, $\rho(r)$'s are the local concentration of monomers and p-CIs. Notice the two orders of magnitude difference in this quantity for the polymeric and simple ion (also in the inset) systems. The presence of a substantially non-compensated negative charge in the vicinity of the micelle when polyanions "visit" the corona region is made clearly evident by the behavior at short R.

adsorbed when at least one of its monomers is adsorbed; a monomer is considered adsorbed when lies at a distance shorter than 7 Å (roughly the Bjerrum length value in diluted aqueous solutions at room temperature) from the positive zwitterionic moieties. Thus, Table 6.3 shows the average number of adsorbed monomers ($\langle N^{\mathrm{ads}}_{\mathrm{mono}} \rangle$), the adsorption probability for a chain ($P^{\mathrm{ads}}_{\mathrm{chain}}$) and the average value of the maximum number of adsorbed monomers $\langle \max[N^{\mathrm{ads}}_{\mathrm{mono}}] \rangle$ per chain. The latter has been computed averaging a set of values for the maximum number of adsorbed monomers, each recorded during simulations spanning 2.5×10^6 MC steps.

As for $\langle N^{\mathrm{ads}}_{\mathrm{mono}} \rangle$, our data indicate that, in average, only a minor fraction of monomers lie sufficiently close to a cationic headgroup moiety to be considered adsorbed. In spite of this, the probability for a chain to be found adsorbed is substantially higher than the ratio $\langle N^{\mathrm{ads}}_{\mathrm{mono}} \rangle / N_{\mathrm{mono}}$, and it increases markedly with N_{mono}. This suggests, in turn, that polyanions dwell in the vicinity of the micelle despite the limited mean number of close contacts. Moreover, the fact that $\langle \max[N^{\mathrm{ads}}_{\mathrm{mono}}] \rangle / \langle N^{\mathrm{ads}}_{\mathrm{mono}} \rangle > 4$ suggests that the systems, overall, ought to be

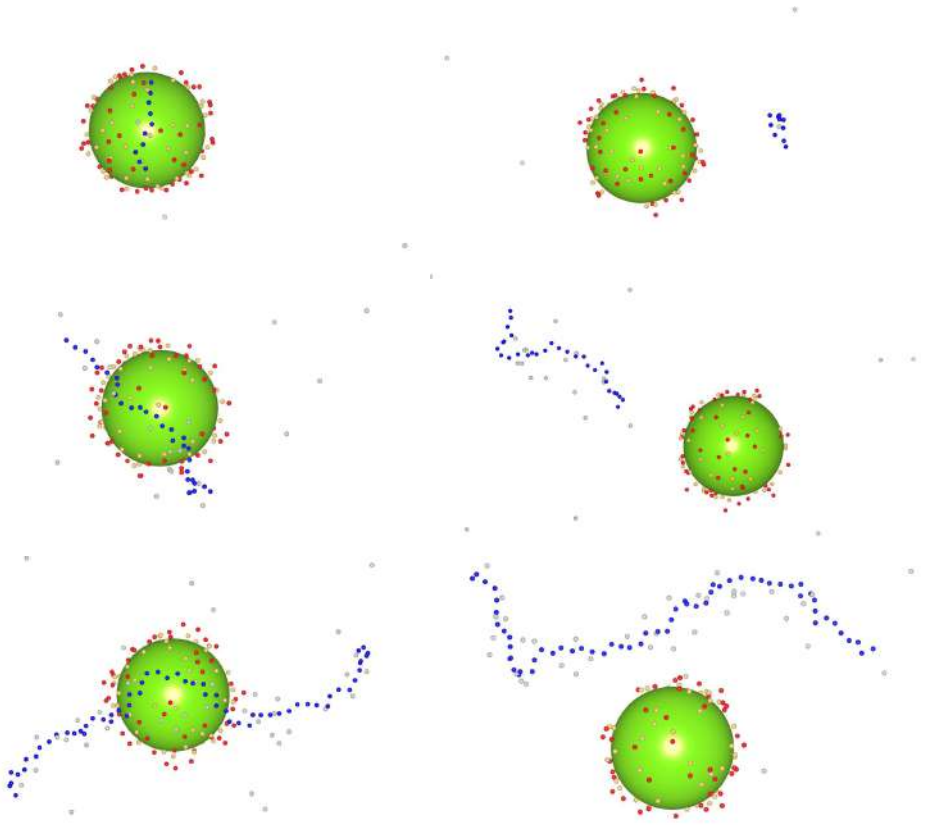

Figure 6.6: Adsorbed (left) and desorbed (right) configurations sampled for the $\mathcal{L}(1, L, \mathrm{SBS})$ systems with $L = 10$ (top), 30 (middle) and 60 (bottom). The color scheme is the same as in Figure 6.1

quite fluxional, with chains that are capable of adsorbing a large fraction of their monomers even though they can easily desorb due to the influence of thermal energy. The tendency of long chains (i.e., $\sqrt{\langle r^2_{1\mathrm{N}}\rangle} > R_{\mathrm{M}}$) seems, however, to not wholly adsorb on the micelle, an idea also supported by the expectation values describing polyelectrolyte conformations reported in Table 6.2 for the case of interacting M/P systems. In brief, the data suggest that the interaction between micelles and polyanion has, at most, a weak impact on the latter conformations. Even so, we mention the presence of a slightly lower l_p for both M/P systems, and a sizable increase of $\sqrt{\langle R^2_g\rangle}$ and $\sqrt{\langle r^2_{1\mathrm{N}}\rangle}$ for $\mathcal{L}(1, 30, \mathrm{SBS})$.

To rationalize the findings just discussed, Figure 6.6 shows a few configurations sampled during the simulation of $\mathcal{L}(1, L, \mathrm{SBS})$ systems. At first sight, it becomes apparent that the long tail of the distributions previously discussed is due to both the not complete adsorption of all the polyelectrolyte monomers

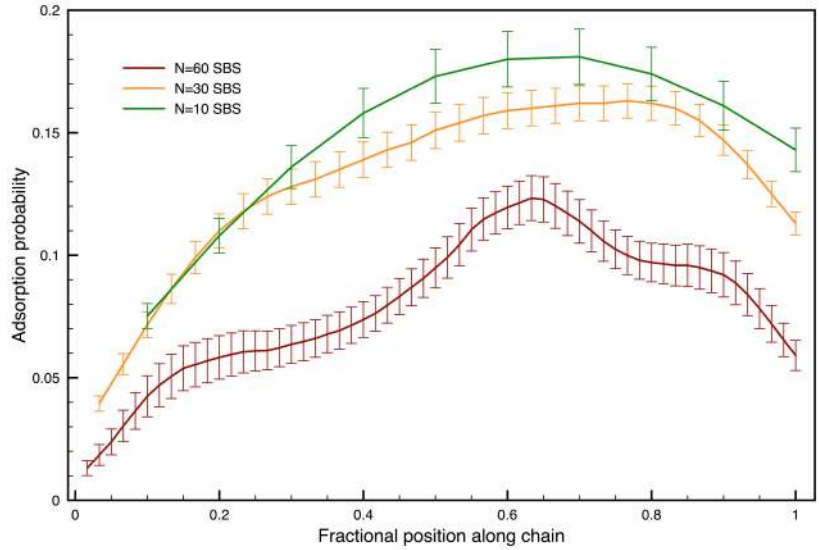

Figure 6.7: Monomer adsorption probability on SBS micelles versus their fractional position along the chain.

when $L \geq 30$, with chains remaining nearly tangent to the micellar core, which increases the likelihood of dissociating the aggregate. Such possibility is expected to lead to a frequent chain "tangential shift" so that sections lying close to the core surface may change in time. This conclusion is supported by the values of the adsorption probability for each one of the monomers along a chain (see Figure 6.7), which are all statistically different from zero. Albeit with a caveat related to a slightly broken ergodicity that appears to be present for the longest polyanion, it also seems that chains are most likely to adsorb on a micelle around their midpoint, a finding probably due to the location of the minimum of the electric potential generated by the polyanions. This finding is similar to what previously evidenced by Stoll and co-workers [16, 259] in the case of positively charged nanoparticles.

At a closer inspection, one also notices that only a limited number of cationic moieties surround the portion of an adsorbed polyanion and are sufficiently close to be recognized as contact with a monomer. Thus, the low values for $\langle N_{\mathrm{mono}}^{\mathrm{ads}} \rangle$ appear related to the relative disposition of the headgroups with respect to the polyanion rather than connected to the fact that only a very limited number of monomers lie close to the surface. As for the origin of such geometrical disposition, which deviates from what commonly seen when positive nanoparticles are

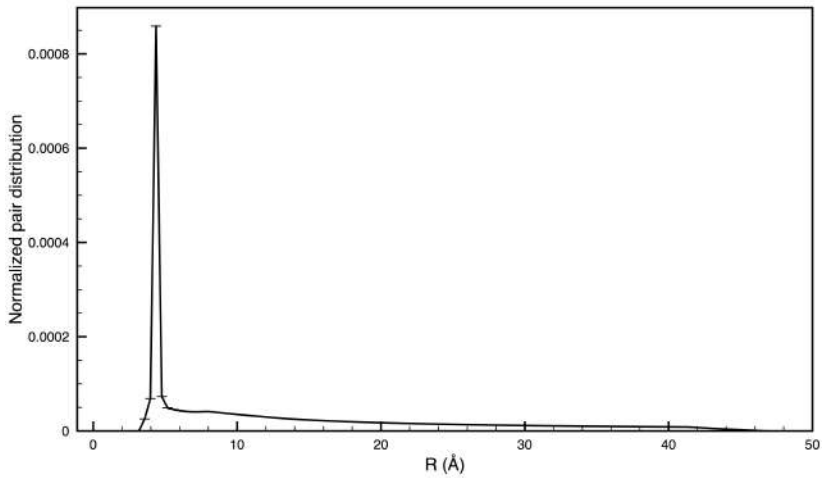

Figure 6.8: Normalized pair distribution function for the A_{SBS}/C_{SBS} couple in absence of other electrolytes in solution. Notice the intense peak at short R values representative of the pair interaction strength, which remains unchanged even after adding 60 monomer/p-CI pairs.

involved [12,249], we suggest that the C_{SBS} are more frequently bound to vicinal A_{SBS} than the counterions of positively charged micelles [238,239]; such interactions may need to be cleaved for a contact with a negatively charged monomer to form (see Figure 6.8 for the C_{SBS}/A_{SBS} pair distribution). Whereas the substitution may be isoenergetic due to the identical charge and size of chain beads and A_{SBS}, it is likely to have an entropic cost for the system, as it requires limiting the radial translational freedom of the polyanion, whereas no anionic moieties can be desorbed due to their covalent link with the cationic counterparts, so that there is no compensation for the entropic loss as it happens with the counterions of cationic micelles (*vide infra* Section 6.3.4).

As for the general impact on the osmotic pressure due to the solutes, previous studies on polyelectrolyte adsorption on charged nanoparticles [6, 8, 13–15, 249] highlighted that also p-CIs disperse in the solution upon the formation of M/P complexes, producing a sizable impact on mentioned property [249]. In this respect, configurations shown in Figure 6.6 showing adsorbed polyanions, *de facto*, suggest that a similar outcome may be expected also in the case of zwitterionic micelles, at least for the chain portion lying close to the core surface, as only a very limited number of p-CIs appear to be located near the chains. Such an effect is also evident in the monomer/p-CIs distributions, with the one for the $\mathcal{L}(1, L, \mathrm{SBS})$ systems presenting always a sensibly lower maximum (3-13%) than

the case involving isolated polyelectrolytes (see the upper panel of Figure 6.9). Despite the mentioned differences, the amount of p-CIs released ought to be expected lower than for the case involving cationic micelles. In absence of a clear minimum in the distribution indicating the size of the p-CIs coordination shell around a polyanion monomer and, hence, the average number of p-CIs localized on the chain, the latter inference can be supported only by computing the p-CIs "condensation index" on the polymer, $\gamma(R_l) = \frac{\int_0^{R_l} R^2\lambda(R)\mathrm{d}R}{\int_0^{\infty} R^2\lambda(R)\mathrm{d}R}$, and the differences in the osmotic coefficient Φ evaluated from our simulations for the various cases discussed so far. In the definition of γ, $\lambda(R)$ is the radial distribution between the monomers of a polyanion and their p-CIs, whereas $R_l = 7$ Å is the distance that, somewhat arbitrarily, defines whether a ion is condensed or not on a chain. In this case, R_l is chosen similar to the Bjerrum length at the simulation conditions

As for Φ, we found that the differences between the three $\mathcal{L}(1, L, \mathrm{SBS})$ systems and their counterpart in absence of the SBS micelle are of the same magnitude of the associated statistical errors (e.g., $\Phi = 0.349(3)$ and $0.348(3)$, respectively, for the $L = 60$ cases). Conversely, γ presents more marked differences, as shown in the top inset of Figure 6.9. Disregarding the absolute values of γ for the three different L, which depends on the width of $\lambda(R)$, we notice that the condensation index is lowered by 3-12% in the presence of the SBS micelle compared to the cases of isolated polyelectrolytes. Obviously, the lower tendency in localizing p-CIs in the vicinity of a chain in presence of a SBS micelle supports the idea that the adsorbed portion of a polyanion loses p-CIs, at least partially. According to the absence of changes in Φ, the amount of p-CIs lost does not seem to impact on the total amount of "free ions"; they are thus likely to remain in the vicinity of the micelle, as also suggested by the lower panel of Figure 6.4. Keeping in mind the latter observation, we are led to conclude that the adsorption, albeit temporarily, of the polyanion on the SBS micelle produces a complex bearing a total charge similar to the one shown by isolated polyelectrolytes [144, 260], due to the fact that adsorbed polyions only minimally lose their p-CIs.

6.3.3 Zwitterionic PBS micelles in presence of strong polyanions

In principle, swapping $\mathrm{C_{SBS}}$ with $\mathrm{A_{SBS}}$ to produce PBS–type micelles may impact on the formation of M/P complexes due to the different configurational freedom

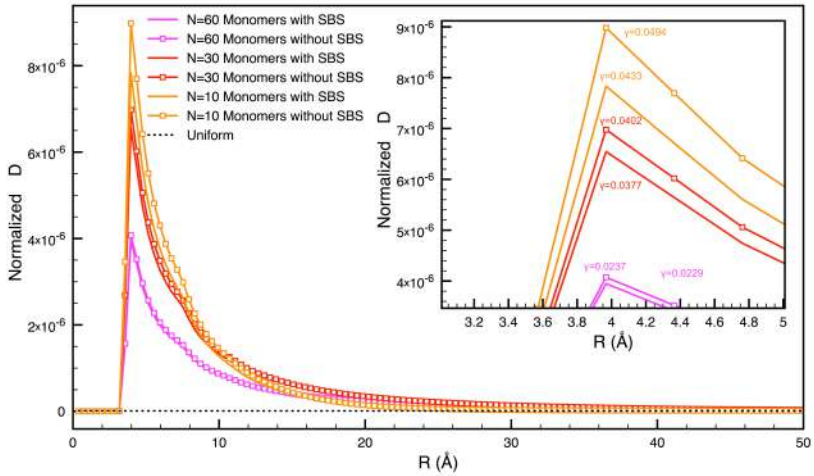

Figure 6.9: Normalized distributions for the monomer/p-CI pair ($\lambda(R)$) obtained simulating $\mathcal{L}(1, L, \mathrm{SBS})$ systems with $L = 10$, 30 and 60 (lines) and the isolated polyanions (lines with symbols). The inset zooms on the peak region; the "condensation index" γ for each case is also provided near the appropriate distribution.

afforded by the most external headgroup moieties ($\mathrm{A_{SBS}}$ or $\mathrm{C_{PBS}}$ in the two cases) and evidenced in Figure 6.3. To check if this is the case, Tables 6.2 and 6.3 provide average structural and adsorption-related quantities, whereas Figure 6.10 shows monomer and p-CI distributions with respect to the PBS micelle center. Pair distributions for the monomer/$\mathrm{C_{PBS}}$ and p-CIs/$\mathrm{A_{PBS}}$ are also shown in figure insets. Besides, the distributions for the $\mathcal{S}(6, 10, \mathrm{PBS})$ case are shown in Figure 6.15 in the Appendix 6.7.

Whereas, in general, polyanions conformational properties do not display substantial changes due to the interaction with PBS micelles, $\langle N^{\mathrm{ads}}_{\mathrm{mono}} \rangle$, $P^{\mathrm{ads}}_{\mathrm{chain}}$ and $\langle \max[N^{\mathrm{ads}}_{\mathrm{mono}}] \rangle$ are markedly impacted by substituting SBS with PBS. In fact, all such quantities decrease substantially as to indicate the presence of a weaker interaction between polyanions and micelles. That this is the case, it becomes even more evident from the distributions shown in Figure 6.10. As for the radial monomer distributions, they display maxima that are lower (by a factor 3–15) and located at larger distances (~ 29 Å) than in the case of SBS micelles. Besides, monomers do not appear to penetrate deeply inside the corona, a finding probably due to the repulsive interaction with the $\mathrm{A_{PBS}}$. In spite of this, the height of the peak in the monomers distributions is 5–14 times higher than when free monomers are involved (see the p-CIs distribution in Figure 6.3), stressing once

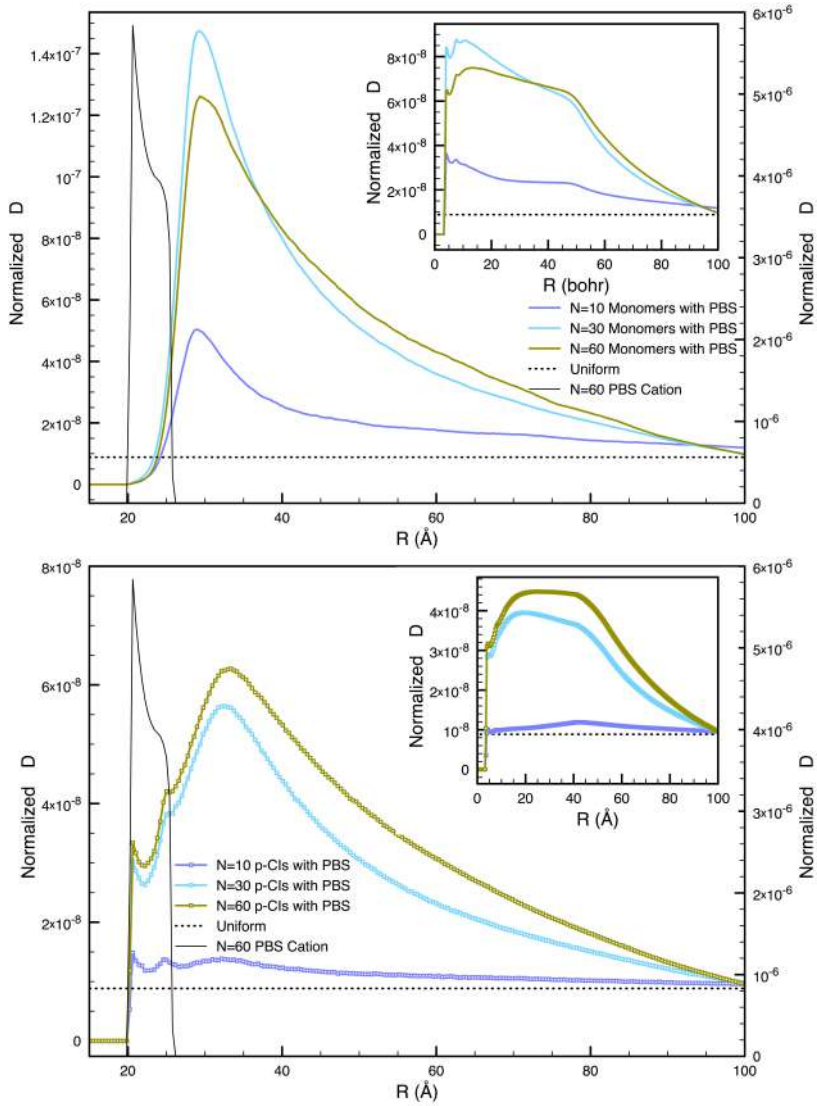

Figure 6.10: Radial distributions for $\mathcal{L}(1, L, \mathrm{PBS})$ with $L = 10$, 30 and 60. The dashed line represents the distribution for uniformly distributed species. The right axis relates to the C_{PBS} distributions only. Upper panel: distributions from the micelle center for charged monomers; the distributions for monomer/C_{SBS} pairs are also shown in the inset. Lower panel: distributions from the micelle center for p-CIs; the distributions for p-CIs/A_{SBS} pairs are also shown in the inset.

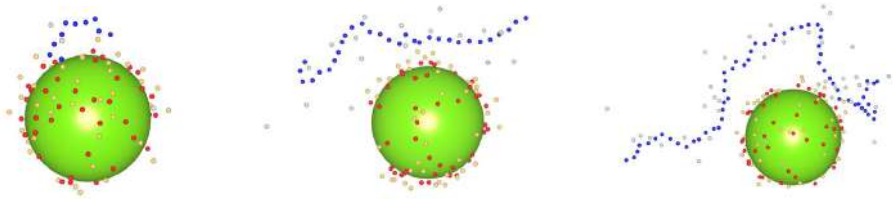

Figure 6.11: Adsorbed configurations sampled for the $\mathcal{L}(1, L, \mathrm{PBS})$ systems with $L = 10$ (left), 30 (center) and 60 (right). The color scheme is the same as in Figure 6.1.

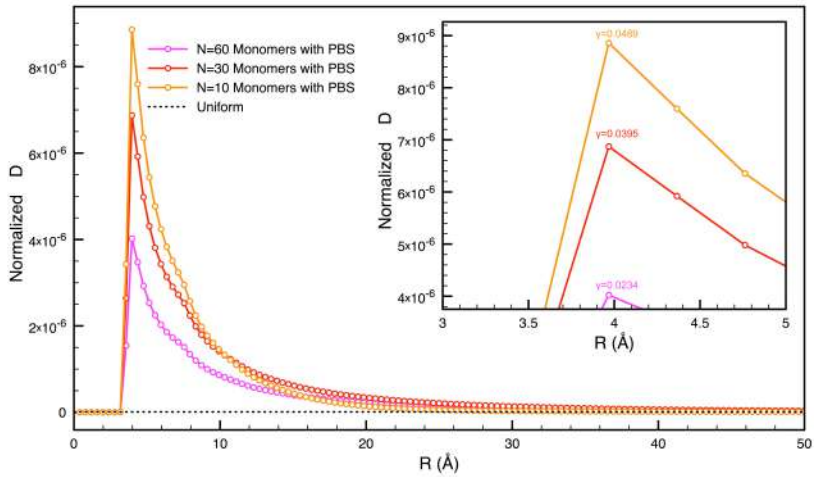

Figure 6.12: Normalized distributions (D) for the monomer/p-CI pair ($\lambda(R)$) obtained simulating $\mathcal{L}(1, L, \mathrm{PBS})$ systems with $L = 10$, 30 and 60 (lines) and the isolated polyanion (lines with symbols). The inset zooms on the peak region; the "condensation index" γ for each case is also provided near the appropriate distribution.

again the impact on the distribution of connecting charged species into polyanions. This conclusion is also supported by the monomer/C_{PBS} pair distributions shown as an inset in the upper panel of Figure 6.10, whose maxima around 4 Å are at least 10 times higher than the one seen in the inset in Figure 6.3.

Whereas the characteristics of monomers distributions may have been easily predicted, the situation appears more intricate and interesting for p-CIs distributions. Beginning with the shortest ($L = 10$) case, we notice that the distributions in the corona region closely resembles the one for the free monomers in Figure 6.3, the position and height of the two structures at short distance from the micelle surface being nearly identical in the two cases. A third maximum is also present around 32 Å, which seems to correlate rather well with the maximum in chain monomers distribution. We therefore suggest that the overall p-CIs distribution is the superposition of two contributions: the first one derives from p-CIs that,

dissociated from the chain, distribute as if the polyanion was not present; the second is instead due to p-CIs that are localized at the polymer/solvent interphase and produce the outmost peak. A consequence of the deep penetration of p-CIs into the corona and the presence of a surface maximum is the fact that the micelle acquires an overall positive charge due to the selective adsorption of such species. Clearly, this could be a component of the attraction between the polyanion and the zwitterionic corona leading to complex formation. We also notice that the height of all peaks increases upon increasing L to 30 and 60. This ought to be expected if one recalls that our distributions are normalized to unity and that there is a higher probability for both the polyanion to be adsorbed on the micelle (see Table 6.3) and of a p-CI to be localized at the polyion/solution interphase due to the higher form polymer charge (see Figure 6.9). The net effect of these characteristics is to lower the p-CIs density away from the micelle imposing an increase to the height of the features at short distance from the micelle. This notwithstanding, the surface maximum in the p-CI distribution for $\mathcal{L}(1, 30, \mathrm{PBS})$ and $\mathcal{L}(1, 60, \mathrm{PBS})$ is 3–4 times higher than the one of the free monomers for SBS micelle (see Figure 6.3), suggesting that a marked accumulation of positively charged species is induced by the two polyanions on the PBS–type micelle surface despite their limited penetration. As for p-CI surface concentration (i.e., considering also the total number of species in the simulation cell), $\mathcal{L}(1, 30, \mathrm{PBS})$ and $\mathcal{L}(1, 60, \mathrm{PBS})$ have the same or 2.5 times higher concentration than 60 free monomers in Figure 6.3. This suggests that reactions requiring the localization of positive species on the micelle surface to take place may be sped up by substituting the counterions of the latter with sufficiently long polyanions. Thus, the rate of acid catalyzed hydrolysis of 2–(p–heptoxyphenyl)–1,3–dioxolane might be increased by substituting chloride anions with soluble polyanions so that the overall concentration of negative charges is maintained [261]. This effect may even be magnified if negative groups on the polyanion weakly coordinate water in their first solvation shell as the perchlorate anion does.

To provide a pictorial representation for the cases in which a complex between PBS micelles and polyanions may be considered formed, Figure 6.11 displays configurations sampled during our Monte Carlo simulations and presenting, typically, polyanions at a distance from the micellar surface compatible with the maxima in Figure 6.10. From such configurations, it neatly emerges that, first, only a

limited portion of each chain approaches the micellar corona, and, second, the interaction between the species is characterized by a local polarization of C_{PBS}. In fact, the latter groups appear located further away from the micelle in regions of its surface that are approached by a portion of the polyanion. A consequence of such behavior appears in the monomer/C_{PBS} pair distribution, which peaks at distances just beyond σ, while it does not emerge from C_{PBS} distributions due to the limited number of groups implicated.

Differently from what seen when SBS micelles are involved, the proximity between chain monomers and the headgroups seems not to induce the release of p-CIs from the polyanion/solution interface. One would thus expect that $\lambda(R)$, γ and Φ would be quite close to the same quantities for the isolated polyelectrolyte cases. That this is exactly so for both $\lambda(R)$, and γ, it appears in the lower panel of Figure 6.9, where the mentioned quantities are shown for the $\mathcal{L}(1, L, \mathrm{PBS})$. Indeed, the difference between γ values for isolated chains and the ones for $\mathcal{L}(1, L, \mathrm{PBS})$ is roughly 1 part for hundreds, i.e. at least 4 times lower than the difference in γ for $\mathcal{L}(1, L, \mathrm{SBS})$. As in the latter case, Φ values obtained for $\mathcal{L}(1, L, \mathrm{PBS})$ and $\mathcal{L}(1, L)$ differ less than their statistical errors.

6.3.4 Impact of the Polyanion Size and Headgroup Structure on the Helmholtz energy change associates to mixing ($\Delta_{\mathrm{mix}}A$)

The results discussed in the preceding sections have highlighted that, albeit the formation of M/P complexes is indeed possible, the impact of the latter on the average properties of each constituent is substantially weaker than what expected for cationic micelles [36, 249]. If so, one would expect a very weak impact on the minimum concentration needed for a surfactant to aggregate forming a micelle in presence of a polyelectrolyte (i.e., the critical aggregation concentration, "cac") compared to the case without it (i.e., the critical micelle concentration, "cmc"). Indeed, a similar observation has emerged from previous experiments involving soluble polyelectrolytes such as sodium polyacrylates [244], even though the possible reasons for such behavior has not been investigated yet.

To verify whether or not our model systems behave in accord with the experiments before drawing any inference of the experimental findings from our results, we computed the change in Helmholtz energy ($\Delta_{\mathrm{mix}}A$) upon mixing solutions

L	$\Delta\Delta_{\text{neut,ion}}A$	$\Delta_{\text{dil,P}}A$	$\langle P_{\text{disp}}\rangle$	$\Delta_{\text{disp}}A$	$\Delta_{\text{mix}}A$
		M(SBS)/P system			
10	-0.12(1)	-0.955(3)	0.9914(2)	0.0051(1)	-1.43(1)
30	-0.41(3)	-1.045(3)	0.9848(3)	0.0091(2)	-1.58(3)
60	-0.93(5)	-1.146(3)	0.9734(3)	0.0160(2)	-2.06(5)
		M(PBS)/P system			
10	-0.03(1)	-0.955(3)	0.9914(2)	0.0051(1)	-1.33(1)
30	-0.28(2)	-1.045(3)	0.9848(3)	0.0091(2)	-1.55(2)
60	-0.38(3)	-1.146(3)	0.9734(3)	0.0160(2)	-1.87(3)

Table 6.4: Values for changes in Helmholtz energy ($\Delta_{\text{mix}}A$) associated to the process of mixing solutions containing already formed micelles and polyanions. Energies are expressed in kcal/mol. $\Delta_{\text{dil,M}}A = -0.136$ kcal/mol for a micellar solution that has the same concentration in surfactants as twice the cmc of SB 3–12 (3.4 mmol/kg). [244]

containing already formed micelles and polyelectrolyte. Table 6.4 provides the results for the quantities indicated in the scheme of Figure 6.2 and needed to estimate such energy change. Importantly, we selected as values for $C_{\text{M}}^{(\text{i})} = 1.21\times10^{-4}$ mol/l and $C_{\text{P}}^{(\text{i})} = 5\times10^{-4}$ mol/l for, respectively, micelles and polyelectrolytes. The latter are compatible with the concentration of stock solutions employed in Reference [244] to evaluate cmc and cac of SBS micelles.

Among the quantities reported in Table 6.4, the most interesting one is perhaps the sum between the change in Helmholtz energy upon neutralizing the polyanion in absence of micelle and the one due to the re-ionization computed using Equation 2.35 (*vide* Appendix 6.6) and indicated as $\Delta\Delta_{\text{neut,ion}}A = \Delta_{\text{neut}}A + \Delta_{\text{ion}}A$. In general, we notice that such quantity is negative but comparable in magnitude with the thermal energy, which in our cases is $k_{\text{B}}T = 0.594$ kcal/mol ($T = 299$ K); hence, the electrostatic interaction between micelle and polyanion appears to impact only weakly on the composite system energetics. $\Delta\Delta_{\text{neut,ion}}A$ appears to increase in magnitude upon increasing L, positively correlating with the probability for a chain of forming a M/P complex. Also, $\Delta\Delta_{\text{neut,ion}}A$ appears to depend on the structure of the zwitterionic headgroups, the SBS micelles impacting more on the polyelectrolyte energetics as it would have been expected basing one the distributions previously shown [244].

The dilution process for both micelle and neutral polyion is common to both SBS and PBS cases, as they involve simply a change in the cell volume inside which the two species are contained (i.e., there is not dependency on the charge

distribution in the micelle), and their change in Helmholtz energy are slightly negative as expected due to the entropic gain. *De facto*, $\Delta_{\mathrm{dil,P}}A$ presents a weak dependency on the chain length, becoming more negative upon increasing N_{mono}. Comparing the $\sqrt{\langle r_{1\mathrm{N}}\rangle}$ values in Table 6.2 with the radius of the simulation cell in which a chain is confined when $C_{\mathrm{P}}^{(\mathrm{i})} = 5\times10^{-4}$ M (i.e., 92.5 Å), it clearly appears that the latter is sufficiently small to have an impact on the conformations of long chains. As there are no intra-chain interactions other than monomer excluded volume, the change in $\Delta_{\mathrm{dil,P}}A$ as a function of N_{mono} ought to be mainly due to an increase in entropic work needed to confine progressively longer chains into a specific volume.

Finally, $\Delta_{\mathrm{disp,P}}A = -RT\ln[\langle P_{\mathrm{disp}}\rangle]$ estimates the change in Helmholtz energy associated with mixing neutral polyion and micelle systems into the final cell, with $\langle P_{\mathrm{disp}}\rangle$ (the insertion probability for a neutral polyion) being the ratio between the partition function of the M/P system with the complete system potential and the one for the M/P system when the interaction potential between the micelle and the polyion is set to zero. As it appears, $\langle P_{\mathrm{disp}}\rangle$ decreases upon increasing N_{mono} as a consequence of the increase in volume occupied by the chain, so that the change in A associated to the process is positive; however, $\langle P_{\mathrm{disp}}\rangle$ never deviates more than 3 parts per hundreds from the unity, so that $\Delta_{\mathrm{disp,P}}A \leq 0.016$ kcal/mol. In other words, the final solution is sufficiently diluted so that the simple mixing process, whose change in A is given by $\Delta_{\mathrm{dil,M}}A + \Delta_{\mathrm{dil,P}}A + \Delta_{\mathrm{disp,P}}A$, is, overall, spontaneous due, primarily, to the polymer dilution (i.e. to the negative sign of $\Delta_{\mathrm{dil,P}}A$).

Overall, $\Delta_{\mathrm{mix}}A$ is negative in all cases investigated in this work, as it was for positive micelle/flexible polyanion complexes studied previously [9–11]. However, $\Delta_{\mathrm{mix}}A$ appears at least 25 times larger when cationic micelles are involved than for either SBS or PBS aggregates, so that the ratio between cac and cmc estimated with data for the former species [9] via the formula $\mathrm{cac/cmc} = \exp[\Delta_{\mathrm{mix}}A/(N_{\mathrm{agg}}RT)]$ was, roughly, 0.02 (here, N_{agg} is the surfactant aggregation number). With $\Delta_{\mathrm{mix}}A$ values from Table 6.4, we, instead, estimate that the interaction between SBS or PBS–type micelles and polyanions may only slightly lower such ratio for these species, the lowest value of which ($\mathrm{cac/cmc} = 0.96$) being found for the $\mathcal{L}(1, 60, \mathrm{SBS})$ case. The latter results is in excellent agreement with the experimental analysis carried out on SB 3–12 and SB 3–14 interacting

with the sodium salt of poly(acrylic acid)$_{30}$ in Reference [244], where no impact on the micellization concentration was evidenced.

With our model appearing to be in agreement with the experiments as far as cac/cmc for hydrophilic polyanions is concerned, we thus feel entitled to use the results discussed in previous sections in order to suggest a rationale for the limited impact that (Na acrylate)$_{30}$ had on SBS–type micelles compared to the cases involving cationic micelles [9–11]. In particular, we highlight the relevance for the cac/cmc ~ 1 datum of the limited number of monomers adsorbed, the tangential orientation of the chain with respect to the micelle, and the fact that $P_{\text{chain}}^{\text{ads}} < 1$ even when $L = 60$. We are tempted to attribute such findings to the limited ability of the zwitterionic macroaggregate in displacing p-CIs from the polyion/solution interphase by substituting them with C_{SBS} or C_{PBS}, as the latter are involved in close–contact interactions with, respectively, A_{SBS} or A_{PBS} of different headgroups. Such interactions are entropically more favorable as the headgroup anions cannot escape the zwitterionic corona.

To investigate whether or not such conclusions may be sensible, we computed both the Helmholtz energy profile, $A(R)$, and the average value of the total potential, $V(R)$, along the distance R between the centers of mass of a chain and the micelle for the $\mathcal{L}(1, L, \text{SBS})$ systems ($L = 10$, 30 and 60), which displayed the strongest propensity to form complexes for each L value. The results are shown in Figure 6.13. The same quantities for the system $\mathcal{S}(6, 10, \text{SBS})$ are shown in Figure 6.17 in Appendix 6.5.

As for $V(R)$, these are characterized by a (local) minimum at short distances, a maximum in the range $50 < R < 90$ Å, and by decreasing values upon increasing R further. The steepness of such decrease appears to increase with L, so that the maximum appears quite shallow for $L = 10$. Besides, the location of the maxima (R_{max}) appears also to increase with L. As for the $R < R_{\text{max}}$ region, $V(R)$ increases more rapidly upon increasing R the shortest is the chain, so that the difference in value of $V(R)$ between the maximum and the minimum (ΔV_{max}) is highest for the shortest chain, $L = 10$.

Taken all together, the behavior of $V(R)$ for the three systems is compatible with the idea of stabilizing (hence attractive) M/P interactions at short range, and whose intensity decreases upon increasing R. This may be due to the increase in distance between the central segment of the chain (i.e., the part where the field

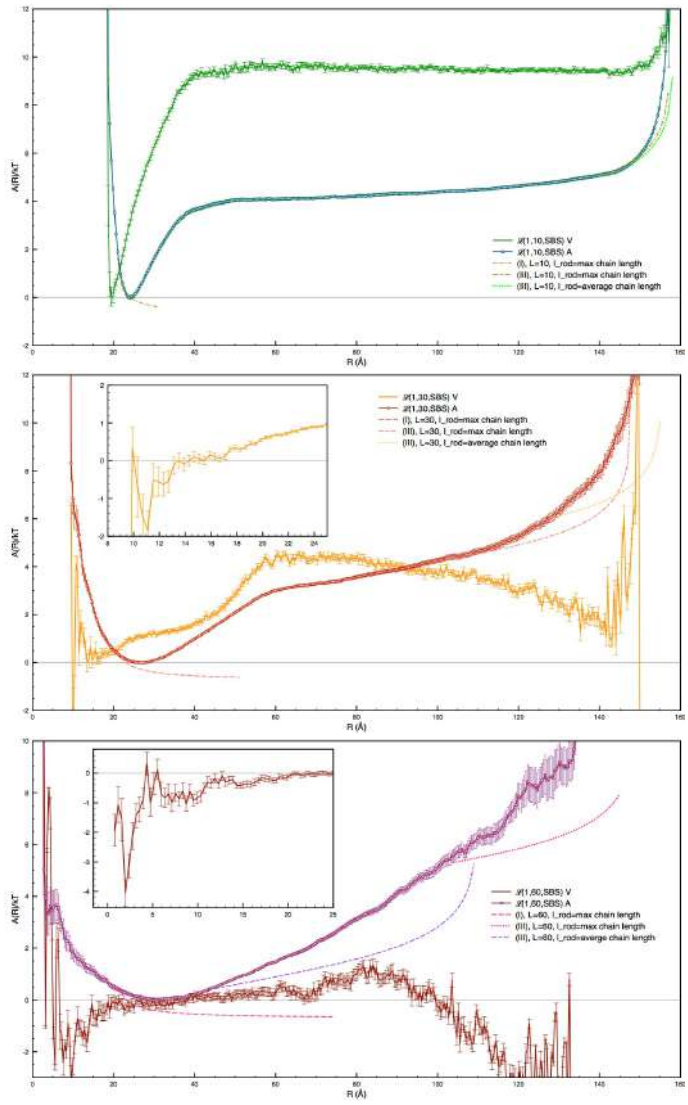

Figure 6.13: Helmholtz $A(R)$ and potential $V(R)$ energy profiles along the M/P center of mass distance for $\mathcal{L}(1, L, \mathrm{SBS})$ systems with $L = 10$ (upper panel), 30 (middle panel), and 60 (lower). The insets show $V(R)$ as sampled on a narrower R range to improve statistics. $A_{\mathrm{rod}}(R)$ (see Appendix 6.7) is also shown; two cases ($l_{\mathrm{rod}} = (L-1)\sigma$ or $\langle r_{\mathrm{1N}}^2 \rangle$) are presented for a comparison at large R values.

due to the polyanion charge is the strongest) and the headgroups upon increasing R. Figure 6.7 in the Appendix supports such view. Due to the relative value of $\sqrt{\langle r_{1N}^2 \rangle}$ for the three systems (see Table 6.2), the distance needed to completely detach the two species increases with L, so that the location of the maximum is displaced at a larger R value the longer the chain.

The length of the polyanion is also likely to impact on the slope of $V(R)$ at short R values as the longer the chain, the slower is the decrease of the chain electric field moving away from the polymer middle section. This idea, however, does not appear sufficient to quantitatively justify the difference in $\Delta V_{\max}$ values for the three systems, as the final part of the detachment process should be nearly identical for all L values. A more robust justification can, however, be proposed if one remembers that the osmotic coefficient Φ of linear polyelectrolytes decreases upon increasing the chain length [202] due to an increase ability in localizing p-CIs at the polyion/solution interphase. This appears true also in our $\mathcal{L}(1, L, \mathrm{SBS})$ cases, as we obtained $\Phi \simeq 0.72$, 0.46 and 0.35 respectively for $L = 10$, 30 and 60. Obviously, the stronger the localization of p-CIs on the charged chain, the weaker the M/P interaction ought to be, thus lowering the work needed to detach the two components of the complex.

The p-CIs localization around the chain plays a role also in the rationalization of the relative $V(R)$ slope as a function of L when $R > R_{\max}$. Thus, assuming that the lower than unity Φ value for our systems is only due to the latter phenomenon, we can easily estimate the effective charge (formal polyanion charge minus the fraction of condensed p-CI, Q_{eff}) for $L = 10$, 30 and 60, which roughly are 7.2, 13.8, and 21.0. Thus, the repulsive Coulomb potential due to the chain charge and felt by the most external A_{SBS} moieties at R values just above $R_{\max}$ during the detachment ought to be higher in magnitude the longer the polyanion. To show that this is indeed the case, we report the ratio $Q_{\mathrm{eff}}/R_{\max}$, which increases from 0.144, to 0.212, and reaches 0.247 (in units of electronic charge/Å) upon increasing L. One should, hence, expect a more marked decrease in $V(R)$ upon increasing $R > R_{\max}$ the higher L is.

Whereas $V(R)$ provides us with insights on the strength of the interaction between the two species as a function of R, the results for $A(R)$ shown in Figure 6.13 completely characterize the relative adsorption probabilities as a function of L. Before discussing the detail of our results, it is however advantageous to

present the behavior of $A(R)$ for the much simpler case represented by a thin neutral rigid rod of length l_{rod}. For the latter, which is akin to a linear rigid rotor rotating around its center of mass, it is possible to obtain analytical results for the classical partition function as a function of R (hence for $A_{\mathrm{rod}}(R)$), and the derivation is shown in the Appendix 6.7. Importantly for our intent, it is shown that:

(I) $A_{\mathrm{rod}}(R)$ increases upon reducing R if $R < R_{\mathrm{M}} + l_{\mathrm{rod}}/2$;

(II) $A_{\mathrm{rod}}(R)$ increases upon increasing R if $R > R_{\mathrm{ext}} - l_{\mathrm{rod}}/2$;

(III) $A_{\mathrm{rod}}(R)$ remains constant in the remaining range of accessible R values.

Such behavior is due to the restraints imposed on the rod rotation by the micelle core at short R and the simulation cell surface at large R. Obviously, the conformations of our polyanions are only grossly represented by a thin rigid rod, especially for the longest species, as shown by the samples presented in Figures 6.6 and 6.11. Nevertheless, $A_{\mathrm{rod}}(R)$ indicates that some limiting behavior ought to be expected for our systems even in absence of any interactions apart from the excluded volume, and these must be taken into account when discussing the $A(R)$ results.

Beginning with the $L = 10$ case, we notice that the overall behavior of $A(R)$ resembles the one for $V(R)$, albeit the work needed to reversibly detach $\mathcal{L}(1, 10, \mathrm{SBS})$ from the micelle is roughly half ΔV_{max}, and its minimum (24.2 Å) is located 5 Å further away. This is, of course, the effect of the rotational entropy, which decreases upon decreasing R due to the restraints imposed by the micelle. This is well supported by the good agreement between the simulation results and the analytical ones at short R if one chooses $l_{\mathrm{rod}} = l_p$ and the effective radius of the micelle to be slightly longer than R_{M}, i.e. 20.9 Å. Indeed, the need for a such longer radius can be easily justified as due to the $\mathrm{C_{SBS}}$ and $\mathrm{A_{SBS}}$ excluded volume, whereas the overall agreement may be due to the markedly stretched conformations of our shortest polyanion. At larger R, we notice that the $A(R)$ increases more rapidly than $V(R)$ due to the reduction in rotational entropy imposed by the cell surface. The contribution of $V(R)$ to $A(R)$ in the long R range is, however, important as shown by the fact that the Helmholtz energy increases more rapidly even than $A_{\mathrm{rod}}(R)$ when $l_{\mathrm{rod}} = l_{\mathrm{max}} = (L-1)\sigma$ for

$L = 10$. The overall contribution of the entropic term $-T\Delta S$ to $A(R)$ appears, thus, to be positive or, at most, negligible, indicating that no or only limited gain in A are afforded by polyion releasing p-CIs when in close interaction with the zwitterions. This, of course, is in agreement with the fact that statistically identical values of Φ for $\mathcal{L}(1, 10, \mathrm{SBS})$ and $\mathcal{L}(1, 10)$ have been obtained (*vide supra*). Finally, it is important to stress that the work needed to decompose the M/P complex is roughly 4 times the thermal energy, a finding that fully justifies the low adsorption probability for $\mathcal{L}(1, 10, \mathrm{SBS})$.

As for the $L = 30$ system, we notice a much slower increase in $A(R)$ upon decreasing R than seen for $\mathcal{L}(1, 10, \mathrm{SBS})$, which is due to the possibility that the center of mass of the chain may be located at R shorter than R_{M} as a consequence of the possible curvature of the chain. The location of the $A(R)$ minimum (roughly 27 Å) is also further away from the micelle than for $L = 10$, a finding due to both the increased chain length (hence, ideally, of l_{rod}), which positions the onset of $A_{\mathrm{rod}}(R)$ at longer R , and the less rapid change of $V(R)$ upon increasing R. In the range of R where the polyanion rotation may be hindered by the cell surface (e.g., $R > R_{\mathrm{ext}} - l_{\mathrm{max}}/2 \simeq 102$ Å if one assumes complete chain extension), $A(R)$ increases more rapidly than $A_{\mathrm{rod}}(R)$, while $V(R)$ decreases steadily until $R \simeq 145$ Å. This peculiarity suggests that another effect contributes to the decrease in entropy of the overall system besides the hindrance of rotation upon increasing R, and this is related to a limitation of the translational freedom of those p-CIs that are not localized on the chain. For them, the more the chain is close to the cell boundary, the less is the space available to distribute around the polyanion in order to optimize the relative values of inter–p-CIs repulsion and p-CI/chain attraction. Obviously, the effect just described plays a role also in the range of R where $A_{\mathrm{rod}}(R)$ is constant, leading to the slow increase in $A(R)$ seen when $60 < R < 102$ Å; a similar, albeit much weaker effect, could be seen also for $L = 10$. Finally, we point out that the increase in $A(R)$ upon going from its minimum to the location of the maximum in $V(R)$ (i.e. where the two species detach and a change in slope is observed for $A(R)$) is statistical equal to $\Delta V_{\mathrm{max}} \simeq 3k_{\mathrm{B}}T$, thus indicating the absence of entropic effects due to the release of p-CIs upon complexation.

Comments similar to the ones for $\mathcal{L}(1, 30, \mathrm{SBS})$ could be made also for $\mathcal{L}(1, 60, \mathrm{SBS})$, apart from the changes induced by its increased length. Thus, the polymer center

of mass samples R values close to the center of the micelle, the minimum is around 30 Å and the curvature of $A(R)$ around it is lower than for shorter polyanions due to the flat behavior of $V(R)$ until $R \simeq 80$ Å and the fact that polymer rotation remains hindered until its center of mass, at least, reaches $R \simeq 75$ Å. Besides, the quantitative effects due to the restriction imposed on p-CIs motion appear more marked due to the higher number of non–localized p-CIs.

6.4 Conclusions

In this work we have theoretically studied colloidal systems composed of a zwitterionic micelle, bearing on the surface either models for sulfobetaine (SBS) or phosphorylcholine (PBS) headgroups, and a strong polyanionic systems with 10–60 monomers. Our interest laid in determining how the interactions between the two constituents modifies their respective properties and whether or not a complex between them could be formed. This interest descends from both the possible impact on cmc and the so called "chameleon effect" [257], the latter possibly being magnified by the higher charge density of polyanions.

As for the issue of micelle/polyanion complex formation, we found that the probability for the chain to be adsorbed on a micelle is an increasing function of the polyanion size and that it also markedly depends on headgroups structure, sulfobetaine-like surfactants inducing, at least, a probability of adsorption twice larger than phosphorylcholine-like ones. Given the decrease in the height of the potential barrier toward dissociation upon increasing the polyanion size (see Figure 6.13), the positive correlation between adsorption probability and the latter is mainly due to a higher number of possible configurations with at least a monomer adsorbed for the longer chains. The dependency of the probability of forming a complex on the choice of headgroups can, instead, be rationalized as due to the relationship between headgroups structure and the electric field intensity attracting the anionic polyelectrolyte, which should be much weaker when the positive moiety dangles, in the average, further away from the surface (i.e. in the PBS case, see Figure 6.3). *De facto*, the adsorption of polyanions on PBS–based micelle would be predicted to be absent if one assumes a capacitor-like structure for the corona*, an idea suggesting that the non–zero value of

*If the zwitterionic corona structure were assumed to be akin to a spherical capacitor (e.g.

the adsorption probability may be exclusively due to charge correlation effects. This conclusion is well supported by the pair distributions between anionic chain monomers and cationic moieties in the headgroups (Figure 6.10), which present a maximum around their Lennard–Jones radius.

The less than unity adsorption probabilities found for all studied systems has a counterpart in the low average number of chain monomers adsorbed, and hence in the conformations assumed by the polyelectrolyte when in contact with the micelle. For sufficiently long chains, most of the latter stretches into the solution, possibly functioning as "antenna" and fundamentally maintaining their counterions localized on itself. The consequence of such behavior becomes apparent analyzing the osmotic coefficient for all studied polyanions, which does not vary despite the presence of a micelle. Notice, however, that the fact that chains maintain their elongated conformation despite being (temporarily) adsorbed on a micelle may lead to bridging between two or more micelles if the concentration of the latter is sufficiently high (i.e. the distance sufficiently short) [15] compared to the polymer "end to end" distance, $\sqrt{\langle r_{1N}^2 \rangle}$ In turn, this may foster self–assembly of advanced materials composed of weakly interacting (because zwitterionic) micelles kept together by a relatively weak binding (if taken per chain) provided by polyelectrolytes. A similar possibility was previously investigated for charged micelles interacting with weak polyacids controlling the interaction strength via the pH [16], and it thus seems worth exploring in the near future.

In the context framed by previous studies [242–246], the absence of interactions between monomers and the hydrophobic micellar core makes our primitive polyelectrolytes able to model only sodium polyacrylates, i.e. a highly soluble and hydrophilic chain. In this, the experimental and theoretical results show an excellent agreement, the computed change in Helmholtz energy due to solution mixing ($\Delta_{\text{mix}}A$) being so small in magnitude not to impact on the critical surfactant concentration. This result is mainly due to the weak enthalpic effects related to the process. In spite of this, the presence of polyanions markedly impact on mobile ion distributions surrounding the micelles compared to the case of simple monovalent ions, increasing, for instance, the concentration inside the

as in Reference [236]) bearing uniformly distributed charges, the field present externally to the corona ought to be identically zero. Even so, the possibility of accumulating charged species with a charge of opposite sign with respect to the one closed to the surface is expected to generate a finite charge on the micelle, which, in turn, would induce a non zero external electric field.

micellar corona of both positive and negative ions (disregarding the charge sign of the innermost headgroup moieties). In spite of this propensity, we showed that the tendency to partially neutralize and screen of the negative charge acquired by SBS micelles due to cations layering just outside the corona (also known as "Chameleon Effect") is markedly reduced by the more concentrated charge of polyelectrolytes. Apart from being a result likely to be easily tested [234], the increased ionic concentration in the corona region may as well be exploited for chemical purposes, as it may enhance reaction rates between anions and organic species with limited water solubility thanks to the law of mass action.

6.5 Appendix: Results for star polyelectrolytes

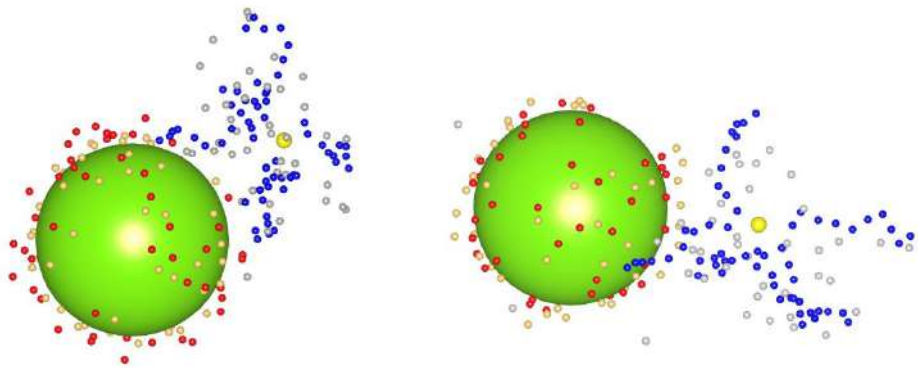

Figure 6.14: Adsorbed configurations sampled for the $\mathcal{S}(6, 10, \mathrm{SBS})$ (left) and $\mathcal{S}(6, 10, \mathrm{PBS})$ (right) systems. The color scheme is maintained from Figure 6.1

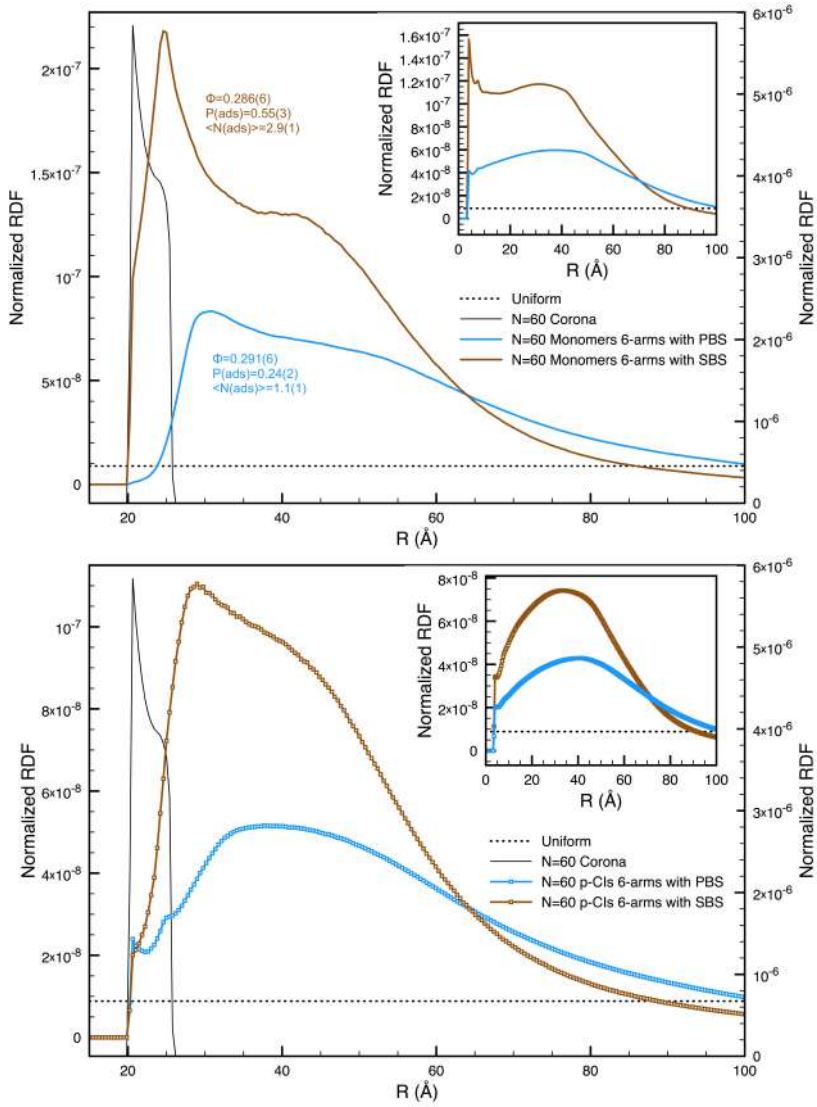

Figure 6.15: Radial and pair distribution functions for $\mathcal{S}(6, 10, \mathrm{SBS})$ and $\mathcal{S}(6, 10, \mathrm{PBS})$. The dashed line represents the RDF for uniformly distributed species; the right axis related to the zwitterion anion RDF. Upper panel: RDF from the micelle center for the charged monomers, together with the results for the osmotic coefficient Φ, the probability of polyelectrolyte adsorption, and the average number of adsorbed monomers; the RDF for the monomer/cationic moiety pairs are also shown in the inset. For the isolated $\mathcal{S}(6, 10)$, $\Phi = 0.32(2)$. Lower panel: RDF from the micelle center for the p-CIs; the RDF for the p-CIs/anionic moiety pairs are also shown in the inset.

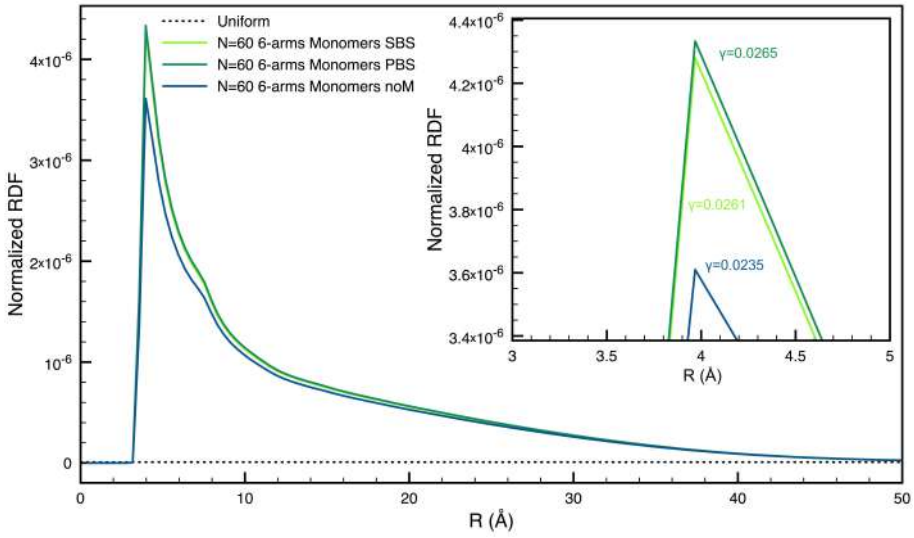

Figure 6.16: Normalized distributions for the monomer/p-CIs pairs obtained simulating $\mathcal{S}(6, 10, \mathrm{SBS})$ and $\mathcal{S}(6, 10, \mathrm{PBS})$ systems and the isolated polyelectrolytes $\mathcal{S}(6, 10)$ (labeled "noM"). The inset shows a zoomed view of the peak region; the "condensation index" γ for each case is also provided near the related distributions.

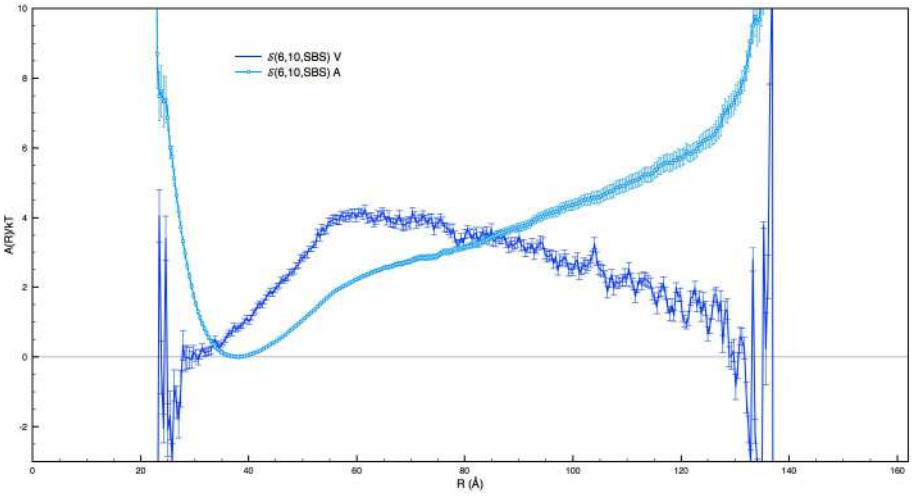

Figure 6.17: Helmholtz ($A(R)$) and potential ($V(R)$) energy profiles along the P/M centers of mass distance for $\mathcal{S}(6, 10, \mathrm{SBS})$ system.

6.6 Appendix: Change in Helmholtz energy during the titration of a weak polyacid

In this Chapter we exploited Equation 2.35 to investigate how the presence of a micellar system impacts on the electrostatic energy of polyanions exploiting the titration curves obtained in presence or absence of the latter. Notice, however, that we are only interested in differences involving two states of complete ionization, so that, in this case, pH is only a convenient variable allowing to connect states of interests. Indeed, alternative paths to gauge the energetics involved in processes we aim to describe may be devised (e.g., see Reference [9]). Thus, differences in titration behavior are studied to decompose the energetics associated with the formation of M/P complexes in the way described in the main text. As final technical note, we mention that the values of α in Equation 2.35 when $\mathrm{pH} - \mathrm{p}K_a < -5$ were represented with an exponential function interpolating the last two computed values.

6.7 Appendix: Helmholtz energy profile for a thin rigid rod inside a spherical cavity with a central spherical object

In this Appendix, we address the calculation of the Helmholtz energy profile for a linear object of length l_{rod}, which rotates around its center of mass inside a spherical cell of radius R_{ext}. Centered inside the cell, there is also a spherical impenetrable object of radius $R_{\mathrm{M}} < R_{\mathrm{ext}} - l_{\mathrm{rod}}$. As $A = -k_{\mathrm{B}}T\ln(Z)$ for the canonical ensemble, with Z being the partition function for the system under study, the free energy profile as a function of R is simply given by

$$A_{\mathrm{rod}}(R) = -k_{\mathrm{B}}T\ln\int\int\int\int \mathrm{d}\theta\mathrm{d}\phi\mathrm{d}p_\theta\mathrm{d}p_\phi \exp\left[-(p_\theta^2 + p_\phi^2/\sin^2\theta)/(2Ik_{\mathrm{B}}T)\right] \tag{6.1}$$

where I is the inertia moment of the rod, θ and ϕ are the angles defining its orientation with respect to the vector connecting the cell origin and its center of mass, whereas p_θ and p_ϕ are their respective conjugate momenta in the Hamiltonian formulation of classical mechanics. Importantly for our purposes, the R–dependency

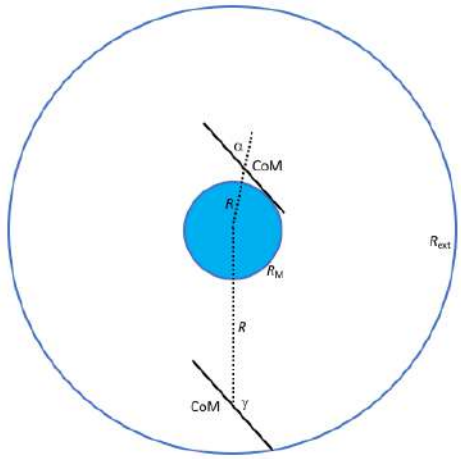

Figure 6.18: Geometrical analysis to determine the amplitude of the rotation along the spherical angle θ defining the orientation of the rod of length $l_{\rm rod}$ with respect to vector joining its center of mass with the micelle (and cell) center.

of the quadruple integral descends from the angular limit imposed on θ by the central sphere and the external cell surface, limits that can be analyzed as shown in Figure 6.18.

From such analysis, one derives the ranges of accessible θ values as a function of R, which are:

$$\begin{cases} \theta \in [\gamma; \pi - \gamma] \text{ if } R > R_{\rm ext} - l_{\rm rod}/2 \\ \theta \in [\alpha; \pi - \alpha] \text{ if } R < R_{\rm M} + l_{\rm rod}/2 \\ \theta \in [0; \pi] \text{ otherwise,} \end{cases} \tag{6.2}$$

where

$$\gamma = \arccos\left[\frac{R^2 + (l_{\rm rod}/2)^2 - R_{\rm ext}^2}{R l_{\rm rod}}\right],$$
$$\alpha = \arcsin\left[R_{\rm M}/R\right].$$

Splitting the results for the angular/conjugated momenta integral over the three mentioned regions, one easily obtains

$$\frac{A_{\rm rod}(R)}{k_{\rm B}T} = \begin{cases} -\ln\left[4\pi^2 I k_{\rm B}T\right] - \ln\left[\cos(\pi - \gamma) - \cos(\gamma)\right] & \text{if (I)} \\ -\ln\left[4\pi^2 I k_{\rm B}T\right] & \text{if (II)} \\ -\ln\left[4\pi^2 I k_{\rm B}T\right] - \ln\left[\cos(\alpha) - \cos(\pi - \alpha)\right] & \text{if (III)} \end{cases} \tag{6.3}$$

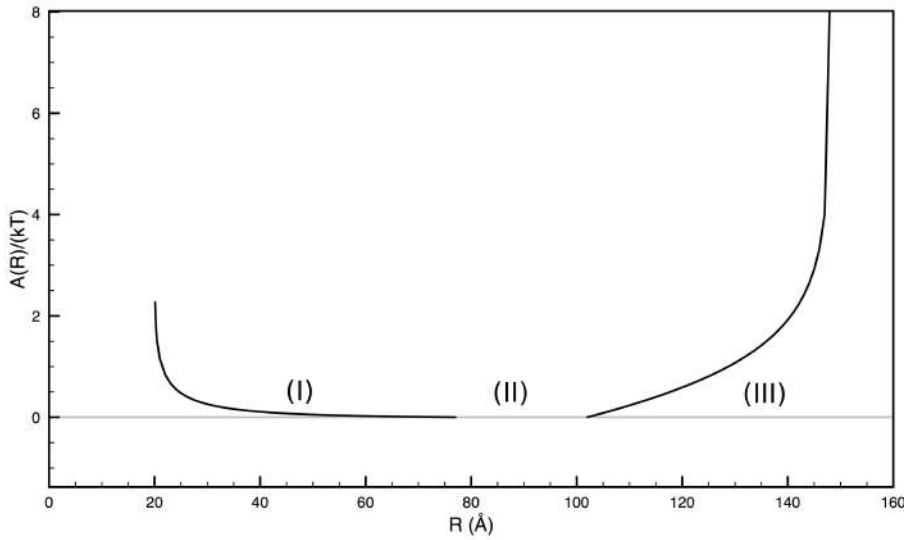

Figure 6.19: $A_{\mathrm{rod}}(R)/(k_{\mathrm{B}}T)$ (see Equation 6.3) for $R_{\mathrm{M}} = 20$ Å, $l_{\mathrm{rod}} = \sigma(L-1)$, $L = 30$, and $R_{\mathrm{ext}} = 159$ Å. The function has been shifted upward by $\ln\left[4\pi^2 I k_{\mathrm{B}}T\right]$ to obtain a representation independent of the rod mass.

$$\text{(I)} \qquad R_{\mathrm{M}} \le R < R_{\mathrm{M}} + l_{\mathrm{rod}}/2$$

$$\text{(II)} \qquad R_{\mathrm{M}} + l_{\mathrm{rod}}/2 \le R \le R_{\mathrm{ext}} - l_{\mathrm{rod}}/2$$

$$\text{(III)} \qquad R_{\mathrm{ext}} - l_{\mathrm{rod}}/2 < R \le \sqrt{R_{\mathrm{ext}}^2 - (l_{\mathrm{rod}}/2)^2}$$

Figure 6.19 shows the results for the case $R_{\mathrm{M}} = 20$ Å, $l_{\mathrm{rod}} = \sigma(L-1)$ (i.e., the maximum equilibrium extension for $L = 30$), and $R_{\mathrm{ext}} = 159$ Å; this is representative of one of the cases we simulated.

Chapter 7

Interface Counterions Localization Induces Switch Between Tight and Loose Configurations of Knotted Weak Polyacid Rings Despite Intermonomer Coulomb Repulsions*

7.1 Introduction

The relationship between ionization degree α and weak polyelectrolyte conformations has been the subject of many previous experimental [137, 138, 160, 262–271] and theoretical [29–31, 272–274] studies. On the whole, there is general consensus on the fact that polyelectrolyte persistence length increases upon increasing α [42, 274], unless chemically specific interactions (e.g. charged hydrogen bonds [12, 26, 27, 37, 249] – see Chapters 3 and 4 – or complexation/coordination of multivalent ions [6, 33, 45, 131, 132, 170]) may be formed as a consequence of polymer ionization.

Despite the current situation, the role of oppositely charged ions (either polyelectrolyte counterions, CIs, related to its titration or due to background salts) is yet to be completely understood quantitatively. Thus, original simulations by Ullner and Woodward [30] suggested that explicit monovalent ions modify

*This chapter has been adapted with permission from Tagliabue A., Izzo L., Mella M., *Journal of Chemical Physics B* 2020, 124, 14, 2930–2937. Copyright 2020 American Chemical Society. All rights reserved.

chain conformations compared to results obtained with screened potentials. To investigate in depth this finding, recent simulation works analyzed CIs partitioning between strong polyelectrolytes vicinal or distal regions detecting the presence of dynamical clusters of CIs at the polymer chain–solution interface, with characteristics depending on polymer topology (i.e. linear versus ring versus star-like, etc) [144, 260]. Also, the impact on conformations of introducing selective ion–solvent or polyelectrolyte–solvent interactions in the force field was interpreted as an indication that the thermodynamical preference of the medium toward a specific system component may play a role [275]. A positive correlation between gyration radius, R_g, and the fraction of interface localized CIs was also detected [275], suggesting that the CIs distribution may respond to chain conformations. Obviously, this should be expected to happen also with weak polyelectrolytes at relatively high α.

Albeit with the limitation implicit in a description based on screening potentials and the lack of explicit CIs, indications for a relationship between the conformations of topologically more complicate knotted ring strong polyelectrolytes and ion localization were put forward in Reference [276]. There, it was shown that an equilibrated tight knot (i.e. with the topological feature localized on a very small portion of the chain) loosens if one simply decreases the solution Debye screening length, λ_D; this behavior was rationalized via the competition between electrostatic long- and short-range contributions to the total energy and the thermal component of chain entropy. Support for this viewpoint emerged from simulations with model intra-chain monomer interactions [277], where the presence of long range attractions (or the reduction of repulsion) was, *de facto*, able to induce knot swelling. It may thus happen that the interfacial localization of CIs, and their stabilizing Coulomb forces, are able to induce differences in knotted polyelectrolyte conformations between simulations with or without explicit CIs; hints that it may be so are present in Reference [260].

Compared to strong polyelectrolytes, weak polyacids are known to locally adapt monomer ionization [14, 15] thanks to charge mobility; in presence of a topological feature such as knots, this may, in principle, lead to an interesting conformational behavior related to a local charge depletion in the knot region. If so, the pH-responsive nature of weak polyacid rings may be exploited for technological applications requiring, for instance, switching on/off a pulling force as

Abbreviation	Meaning
CI	Counterion

Table 7.1: List of abbreviations commonly used in this chapter

a function of pH. Thus, it is the aim of our work to investigate how solution parameters (i.e., pH, CIs description, background ionic strength, solvent quality and topological complexity) impact on conformations when a knot is tied into a weak polyacid ring.

7.2 Methods and Model

Our system consists of a single ring polyelectrolyte simulated in a cubic box of length L, the latter value chosen in order to have a concentration of monomers $C_{\text{mono}} = 10^{-2}$ M, with periodic boundary conditions in all the three dimensions. The polyelectrolyte is simulated via a coarse-grained "beads and springs" primitive model, and it consists in $N_{\text{mono}} = 120$ weak acidic (hence, titratable) monomers bonded together to form a circular chain via FENE potentials (see Equation 2.5) employing the following parameters values: $k_{\text{bond}} = 30\epsilon$, $\Delta r_{\max} = 3\sigma$, $\sigma = 3.55$ Å and $\epsilon = k_{\text{B}}T$ ($T = 298$ K). Monomers have a mass $m = 1$ and are treated as soft spheres, their excluded volumes simulated via WCA potentials (see Equation 2.3). Polyelectrolyte conformations are sampled via Langevin dynamics ($\gamma = \sigma^{-1}/\sqrt{(m/\epsilon)}$, see Equation 2.42), integrating the trajectories via a velocity Verlet algorithm with a time step $\delta t = 0.01\sqrt{\sigma(m/\epsilon)}$ (see Sections 2.2.3 and 2.2.4).

In order to take into account the weak acidic nature of the monomers, beside the Langevin dynamics we implemented the constant-pH method [32, 42, 55] (see 2.2.2). In a few simulations, we also added a certain amount of mono- and divalent salt ($z = 1$, $q_{\text{S}} = \pm 1$ and $z = 2$, $q_{\text{S}} = \pm 2$, respectively) in order to simulate the system in presence of a background ionic force. As the monomers, also CIs and salt ions are treated as soft spheres, and, hence, they're subjected to the same WCA potential. Coulomb interactions are simulated via the P3M method and implicit solvent, the latter assumed to be water at room temperature unless otherwise indicated. Hence, the Bjerrum length of the system is $l_B = 2.0\sigma = 7.10$

Å. All simulations have been performed with the software package ESPResSo [326].

7.2.1 Simulation protocol

For each pH - pK_a value investigated, the system has been warmed up for a time $t = 5 \cdot 10^4$, attempting $10N_{\text{mono}}$ dissociation/protonation reactions every 10^3 integration steps. Then, the system has been integrated for $t = 5 \cdot 10^5$, attempting N_{mono} reactions every 10^3 integration steps. System properties have been collected every 10^3 integration step. We performed a blocking analysis in order to verify that samples were uncorrelated.

7.2.1.1 Simulations without the insertion of counterions

Simulations without the insertion of CIs have been performed disabling the electroneutrality checks in ESPResSo [326] and replacing the insertion/deletion of CIs with the insertion/deletion of neutral dummy particles with a negligible excluded volume.

7.2.1.2 Simulations of polyelectrolytes with quenched charges

We performed a few simulations with polyelectrolytes bearing a certain amount of quenched charges (uniformly distributed along the chain); these species behave as strong polyacids with a certain amount of non-titratable neutral monomers.

7.3 Results and Discussion

As conformations may depend on polyelectrolyte topology, we simulated rings with 4 different prime knots X_n (see Figure 7.1): 0_1, i.e. unknotted; 3_1 "trefoil" knot; 4_1, "figure-eight" knot; 5_1, "pentafoil" knot. Figure 7.2 shows the behavior of the radius of gyration R_g^2 versus α (left panel) and pH - pK_a (right panel). An increase in knot complexity results in a decrease of R_g^2 regardless of α, [279] which, in turn, ought to impact on the polyelectrolyte dissociation behavior. This is, in fact, true, as the acidity is depressed by the shorter average distance of the dissociating groups (see Figure 7.3). More interestingly, the behavior of R_g^2 versus α depends on ring topology. So, R_g^2 for 0_1 monotonically increases upon increasing

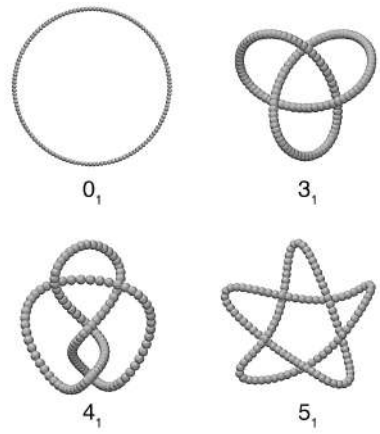

Figure 7.1: Pictorial illustration of the prime knots X_n simulated in our work; these are: 0_1, unknotted polyelectrolyte; 3_1, "trefoil knot"; 4_1, "figure-eight knot"; 5_1, "pentafoil knot".

α due to Coulomb repulsion paralleling linear and star-like polyelectrolytes, or even nanogels [280]. Conversely, R_g^2 of the other rings initially increases with α until $\alpha \simeq 0.75 \div 0.85$, and it decreases at higher ionization.

In order to allow a direct comparison with results obtained via mean-field calculations by Dommersnes et al., [276] the upper x-axis of Figure 7.2 reports $\lambda_D/(N_{mono}^{1/2} r_e)$, where $\lambda_D(\alpha) \cong \lambda_D$, is computed using the canonical formula

$$\lambda_D = \frac{1}{\sqrt{4\pi l_B \sum_i C_i q_i^2}}; \tag{7.1}$$

here, C_i is the concentration of the i-th species, with the index i that runs only over mobile species, whereas r_e is the average equilibrium distance between bonded monomers. We observe the transition from "tight" to "delocalised" knotted conformations appearing at $\lambda_D/(N_{mono}^{1/2} r_e)$ values which are roughly 3.5 times higher than what reported by Dommersnes et al., a clear evidence that charge correlation plays a fundamental role in defining the conditions determining the equilibrium conformation of the polyelectrolyte.

To analyze such unexpected findings, Figure 7.4 shows the normalized distributions of R_g^2 for the three non-trivial knots at various pH - pK_a and selected trajectory snapshots; results for 0_1 are instead shown in Figure 7.5. At variance with the latter case, whose distributions appears Gaussian-like and shift to higher R_g^2 values as the pH increases, the distributions for the other cases display a shift

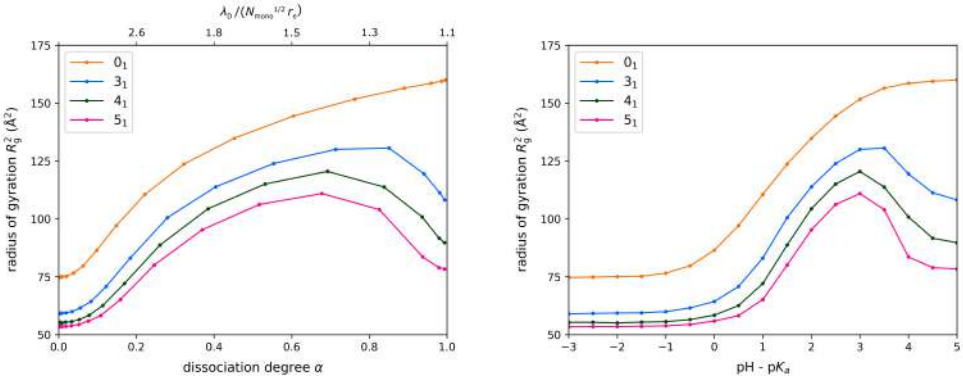

Figure 7.2: Radius of gyration R_g^2 as function of α (left panel) and pH - pK_a (right panel).

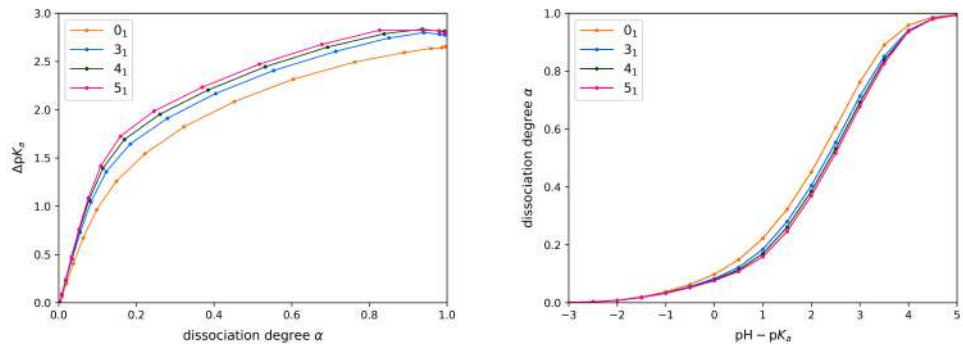

Figure 7.3: Left panel: ΔpK_a as a function of α. Righ panel: α as a function of pH - pK_a for polyelectrolytes presenting different knots. Notice the curve crossing at high pH and α.

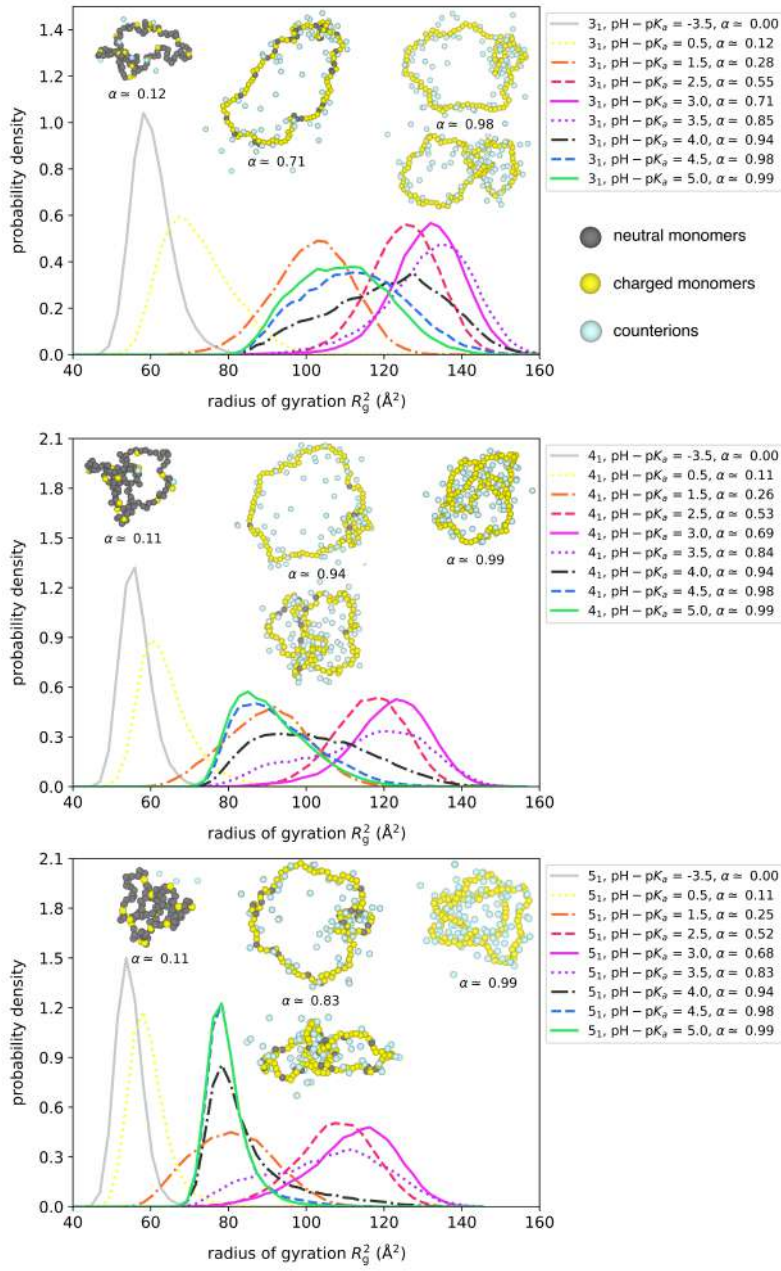

Figure 7.4: Probability density of R_g^2 as a function pH - pK_a for the 3 non-trivial knots: (top) 3_1, (middle) 4_1, (bottom) 5_1. Selected trajectory snapshots are also provided.

toward higher R_g^2 on going from pH - pK_a = -3.5 ($\alpha = 0$) to 3.5 ($\alpha \simeq 3.5$) and a backward displacement upon increasing pH - pK_a above 4.0. The appearance of a marked left shoulder, which turns into a peak with a extended right tail upon increasing α, is also noticeable.

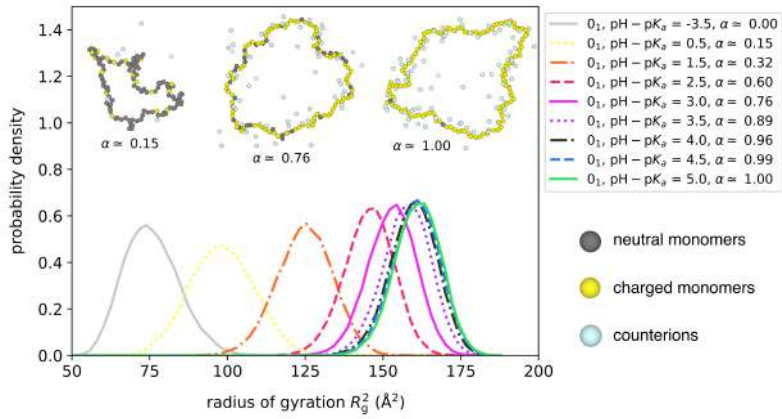

Figure 7.5: Probability density of the radius of gyration R_g^2 as a function of pH - pK_a for un unknotted circular polyelectrolyte.

A rationalization for the discussed findings is provided by trajectory snapshots. At $\alpha \simeq 0$, ring conformations are determined exclusively by monomers excluded volume and entropy, the knot resulting, in average, loose and localized over a wide portion of the chain ("loose knot" conformations) [†]. This result nicely agrees with the analysis carried out by Coronel *et al.* [281] for neutral polymers of varying stiffness. Upon increasing the chain charge, the persistence length also increases due to Coulomb repulsion, initially inducing the polyelectrolyte swelling. This results in circularly shaped polymers with the knot concentrated on a very small portion of the chain ("tight knot" conformations) to lower the energy as suggested by Dommersnes et al. for strong (i.e. fully dissociated) polyelectrolytes [276]. The decrease in R_g^2 upon increasing further α is, instead, explained by the polyelectrolyte assuming conformations in which the knot returns to be delocalized ("delocalized knot" conformations) while monomers try to remain as far as possible from each other. Notice that the systems become quite fluxional at ionizations intermediate between the ones characterizing the "tight knot" and "delocalized knot" conformations, all knotted rings managing

[†]The looseness of the knot induces the presence of chain "loops" composed of many monomers.

to populate all extreme conformational states with a frequency depending on α itself. From Figure 7.4, it is also evident that the trend reversal happens at lower α the more complex is knot topology. Thus, we observe very broad distributions already at pH - pK_a = 3.5 for the 4_1 and 5_1 cases. Notice, also, that knots topology had no impact on their tightness in absence of CIs [276], the behavior emerging from our simulations not being rationalized by the simple increase in local density of repelling monomers inside the knot volume (*vide infra* for further discussion).

De facto, our results suggest a strong interplay between ionized monomers Coulomb repulsion and the explicit presence of "condensable" CIs in defining the conformations of flexible polyacid rings. Playing some role in quantitatively determining this interplay, there may also be the "annealing" nature of monomer charges, the "tight knot" conformations possibly concentrating neutral beads inside the knot itself to reduce its energy. As first step to provide support for these ideas, we performed a simulation on 3_1 without inserting explicit CIs during the titration, the results (see Figure 7.6) showing a monotonic increase of R_g^2 and Gaussian-like R_g^2 distributions also at intermediate-high pH - pK_a values. Apart from proving the CIs presence to be key in defining the behavior of R_g^2, we also notice that this finding substantially extends what shown in Reference [276] demonstrating that, in absence of any screening effects, "tight knot" conformations dominate the equilibrium conformations even at quite low ionizations, i.e. $\alpha \gtrsim 0.25$.

From a more quantitative point of view, Figure 7.7 (left panel) shows the fractional amount of interphase localized CIs, φ_{CI}, as a function of α. We define φ_{CI} as the number of CIs that lie at a distance equal or less than the system Bjerrum length (l_B = 7.10 Å) from at least one monomer divided by the total number of CIs in solution (we arbitrary set the value of φ_{CI} equal to 0 in case of no CIs in solution, i.e. completely undissociated polyelectrolyte). As expected, φ_{CI} monotonically increases as the polyelectrolyte dissociates, the CIs feeling a progressively increasing electrostatic attraction and, hence, localizing near the chain despite their mutual repulsion. For a chosen α, φ_{CI} is higher the more complex is knot topology, a result attributable to an increase in charge density going from 0_1 to 5_1 due to their relative sizes (see Figure 7.2). We also notice a "kink" in the φ_{CI} curves of the knotted species around $\alpha \simeq 0.85$, a value roughly

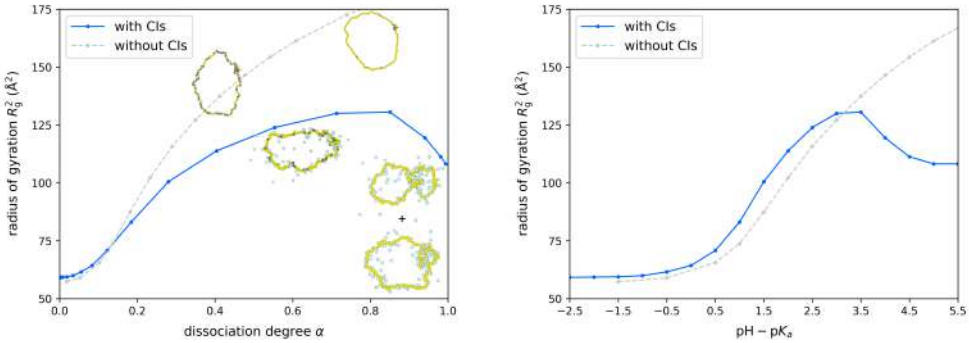

Figure 7.6: Radius of gyration R_g^2 and selected trajectory snapshots as a function of α (left panel) and pH - pK_a obtained with simulations with and without the explicit treatment of CIs for the 3_1 case. The lower R_g^2 values observed at very low dissociation degrees are due to the use of a slightly higher value of the FENE bond constant in the simulation without CIs in order to prevent knot disentanglements.

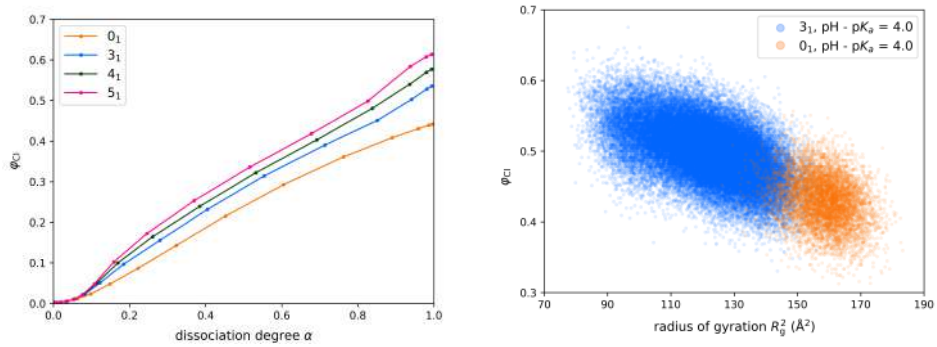

Figure 7.7: Right panel: Fraction of condensed CIs, φ_{CI}, as a function of the dissociation degree α for polyelectrolytes presenting different type of knots. Left panel: scatter plot representation of instantaneous values of R_g^2 and φ_{CI} for the 0_1 and 3_1 systems at near complete ionization. The pH value has been chosen to allow the 3_1 ring to fluctuate between "delocalized" (low gyration radius) and "tight" (high R_g^2) knot conformations. A marked negative correlation between interphase localized CIs and R_g^2 is clearly seen for the 3_1 species, whereas it is absent for the unknotted one.

corresponding to the dissociation degree at which we observe the beginning of the transition between the "tight knot" and the "delocalized knot" conformation. This supports the suggestion for a strong correlation between these properties. An even stronger support is found in the 2D-distributions of instantaneous (R_g^2, φ_{CI}) pairs sampled at pH values where conformations convert easily (see the right panel Figure 7.7); from these, we notice that high R_g^2 corresponds to a lower fraction of condensed CIs, or vice versa.

Analyzing from the viewpoint of thermodynamics, the aspects playing a role in defining the conformations dependent free energy are:

i) the increase in "global" average repulsion and, hence, also "local" chain stiffness due to monomer ionization compared to the neutral system;

ii) the decrease in CIs entropy due to the interphase localization itself;

iii) the decrease in average energy due to CIs interphase localization, with a concomitant reduction of the ionization induced local stiffness compared to the same chain without explicit CIs, consequently to the lowering of the long-range Coulomb repulsion due to CIs chain adsorption/screening;

iv) the much faster decrease in chain entropy connected to knot tightening as a consequence of the increasing stiffness, as also suggested by the thermal analysis by Dommersnes et al. [276]

From the results discussed above, it is evident that contributions iii) and iv) ought to vary their relative importance for a ring to invert the naively predicted increase of R_g^2 versus α. In fact, 0_1 continuously increase R_g^2, as does 3_1 when simulated without inserting CIs. In the latter case, this is mainly due to the absence of "knot loosening" (or knot size increase) effectively induced by reducing long range repulsion evidenced in Reference [277]. The latter effect appears magnified for our systems upon increasing the knot complexity (i.e. the knot turn "loose" at lower α), likely due to the higher average amount of interphase localized CIs.

As for the impact of the annealed nature of chain charges, Figure 7.8 (upper panel) compares R_g^2 distributions for 3_1 at $\alpha \simeq 0.55$, 0.71, 0.85 (see Figure 7.4) to the ones of a similarly knotted strong polyelectrolyte whose ionization degree is made nearly identical by neutralizing uniformly spaced monomers. From this, it is

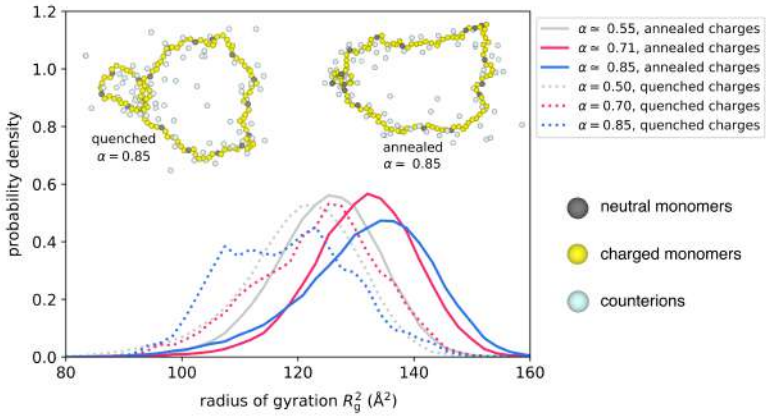

Figure 7.8: Radius of gyration R_g^2 and selected trajectory snapshots as a function of α for simulations on 3_1 type rings with weak ("annealed") and strong ("quenched") electrolytic behavior.

evident that knotted quenched polyelectrolytes loosen up at much lower α than annealed ones, suggesting that neutral monomers in the latter may be packed into the knot region to reduce the average energy and, consequently, lowering CIs localization on the knot itself. To prove that this is the case, Figure 7.8 (lower panel) shows the 2D probability density $p(d, R_g^2)$, with d being the distance between two neutral monomers, for 3_1 at a pH where inter-conversion between "tight" and "loose" knot configurations is possible ($\alpha = 0.94$). From this, it is evident that neutral monomers sit very close to each other despite their limited number (roughly 7), and tendency that is markedly stronger in the range of R_g^2 values typical of the "tight knot" configurations. Notice that the evidence that knot loosening induced by CIs condensation results also in a decreased size of the polyacid is also supported by the evidence that decreasing the stiffness (the latter a property that can be modulated, in our case, by the screening power of CIs, *vide infra*, the solvent Bjerrum length or the background ionic force) of neutral circular species results in conformations in which the knot is delocalized over a wider portion of the chain and, consequently, in a decreased polymer size [281].

If the mechanism suggested above for the knot loosening at high α is correct, its onset ought to happen at lower ionization the stronger is the CIs localization onto the chain. As the latter is modulated by the solvent Bjerrum length [159] l_B, we performed a series of simulations on the 3_1 system varying it; the results show that the non-monotonic trend of R_g^2 becomes either less evident (for $l_B = 10.65$ Å) or even disappears (for $l_B = 14.20$ Å) upon increasing l_B (see Figure 7.10).

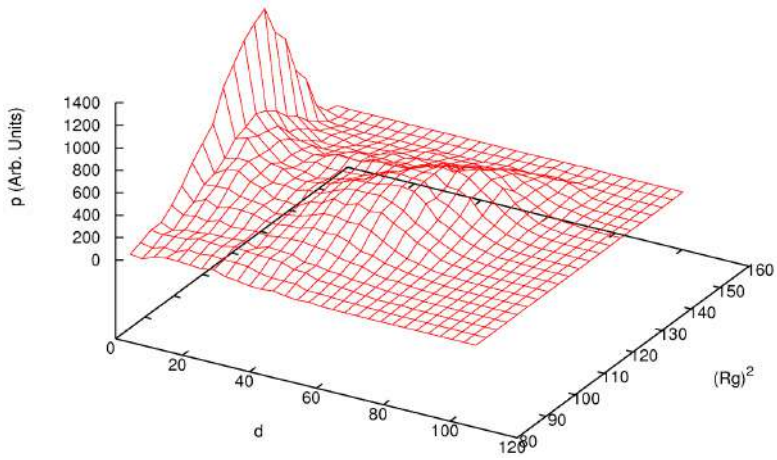

Figure 7.9: Probability density $p(d, R_g^2)$ (arbitrary units) at pH - p$K_a = 4.0$ for a 3_1 chain; d is the distance between neutral monomers in Å; R_g^2 in Å^2.

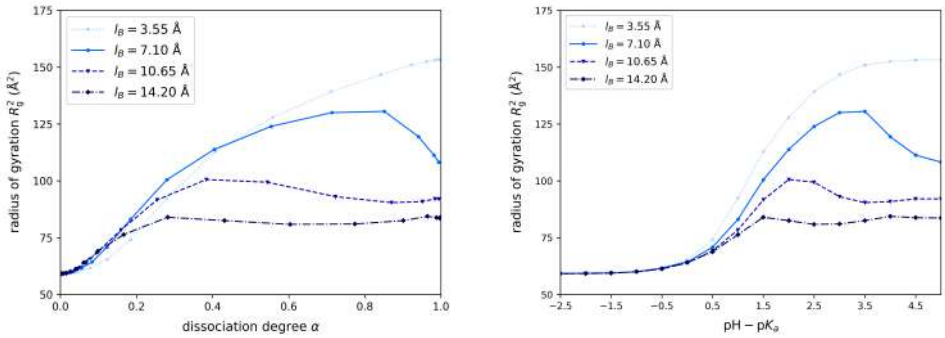

Figure 7.10: Radius of gyration R_g^2 as a function of α (left panel) and pH - pK_a (right panel) for simulations on 3_1 type rings employing various Bjerrum length l_B.

De facto, the "loose knot" conformations become more dominant at equilibrium (see Figure 7.11 for R_g^2 distributions) as the solvent screening power decreases, a fact that we attribute to a markedly enhanced CIs localization on the polyelectrolyte (Figure 7.13) and, consequently, in an increased acidity (in average) of the monomers (Figure 7.12). This phenomenon overcompensates the expected increase in chain stiffness due to the stronger Coulomb repulsion between neighbor and next-neighbor monomers. As expected, knot conformations switch from "loose" to "tight" at lower α (~ 0.3) upon decreasing l_B as the energetic gain obtained localizing CIs onto the chain is decreased, and more CIs wander in solution.

To conclude our presentation, we stress that our results indicate that the

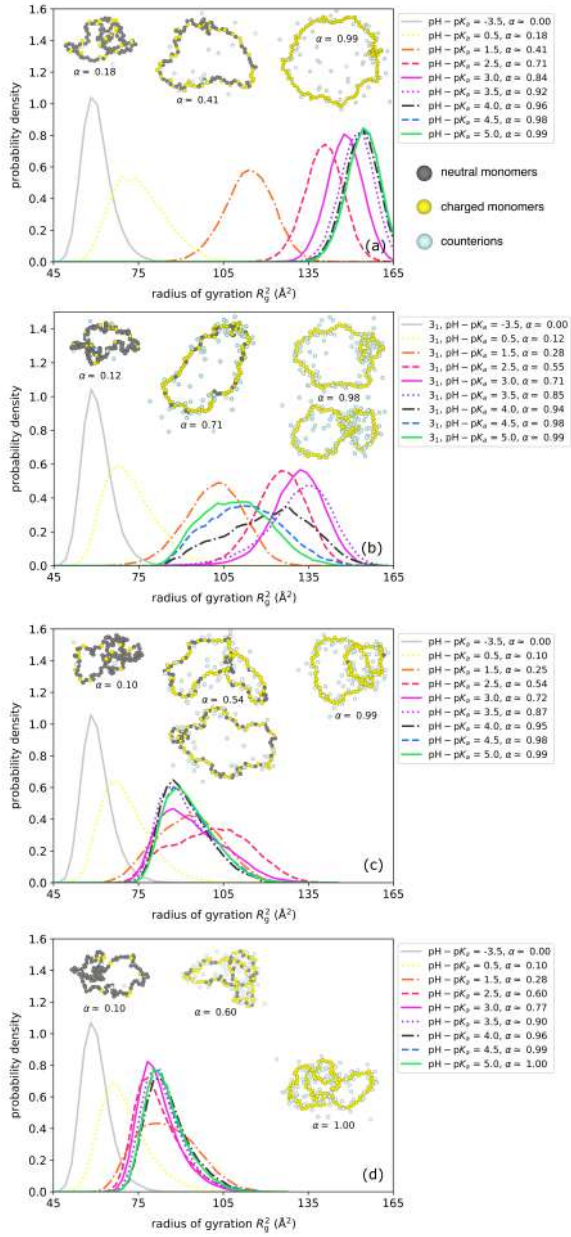

Figure 7.11: Probability density for the radius of gyration R_g^2 and selected trajectory snapshots are shown as a function of pH - pK_a for the 3_1 case and various l_B values: (a) $l_B = 3.55$ Å, (b) $l_B = 7.10$ Å, (c) $l_B = 10.65$ Å, (d) $l_B = 14.20$ Å.

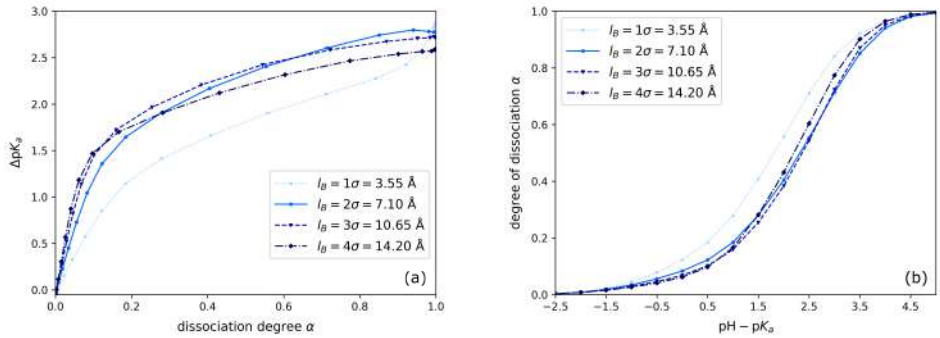

Figure 7.12: (a) ΔpK_a as a functions of α, and (b) α as a function of pH - pK_a for the 3_1 case and various l_B values.

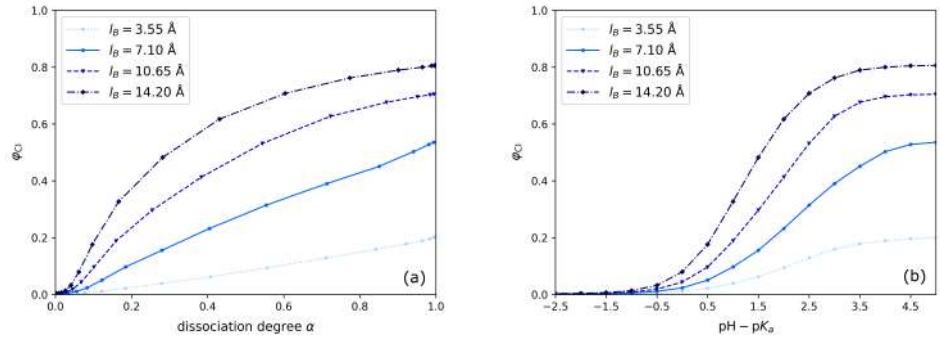

Figure 7.13: Fraction of "condensed" CIs, φ_{CI}, as a function of (a) α and (b) pH - pK_a for the 3_1 case and various l_B values. Notice the absence of "kinks" in φ_{CI} for $l_B \geq 10.65$ Å

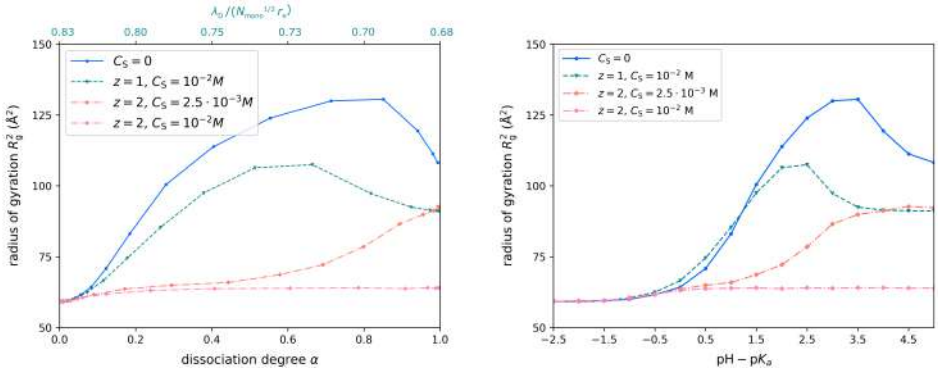

Figure 7.14: R_g^2 as a function of α (left panel) and pH $-$ pK_a (right panel) simulations on 3_1 rings in presence of 1:1 salts with monovalent or divalent ions and $l_B = 7.10$ Å; the upper x-axis refers to λ_D values calculated in presence of monovalent (i.e., $z = 1$) salts.

correlation between CIs and the polyelectrolyte charge plays a very important role in determining the latter conformations as originally pointed out by Ullner et al. [30], the quantitative aspects of this mechanism being finely controlled by the thermodynamics factors discussed above. In this respect, it would be possible to modulate the relative impact of CIs entropy (item 2) and adsorption (item 3) introducing a background salt. We thus investigated how the conformations of our 3_1 polyelectrolyte depends on salt valency, z, and concentration, C_S, in three different conditions[‡]: (a) $z = 1$, $C_S = 10^{-2}$ M; (b) $z = 2$, $C_S = 2.5 \cdot 10^{-3}$ M; (c) $z = 2$, $C_S = 10^{-2}$ M. The results are shown in Figures 7.14, 7.15, 7.16, and 7.17.

From the results, it is clear that salts decrease R_g^2 over the entire range of simulated pH due to the screening of charged monomers. More in detail, the non-monotonic trend of R_g^2 is maintained in presence of monovalent ions, albeit the curve maximum is shifted to lower α values by the increased amount of monovalent cations available to localize on the polyelectrolyte. *De facto*, the population of interphase localized cations is dominated by salt ones due to a straightforward mass effect (see Figure 7.17). Apart from reducing R_g^2, the presence of a background ionic force has another obvious effect. i.e. decreasing the Debye screening length of the solution. Comparing our simulations and results reported by Dommersnes et al., [276] we observe that, even in a moderately salty

[‡]The salt valences and concentrations we employed correspond to a ionic strength of $I = 10^{-2}$ M for (i) and (ii), whereas it is 4 times higher for (iii), i.e. $I = 4 \cdot 10^{-2}$ M. Notice that, given our simulation cell, a concentration of $C_S = 10^{-2}$ M is equivalent to 120 ion pairs, i.e. it is identical to C_{mono}.

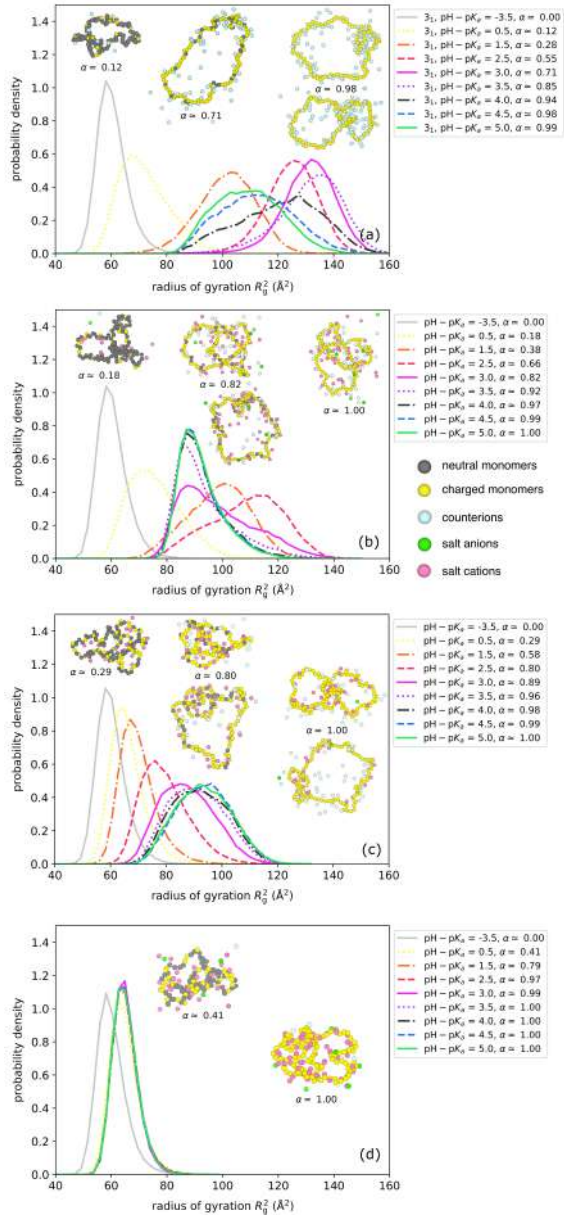

Figure 7.15: Probability density for the radius of gyration R_g^2 and selected trajectory snapshots as a function of pH - pK_a for the 3_1 case and various salt valencies z and concentrations C_S: (a) $C_S = 0$ M, (b) $C_S = 10^{-2}$ M, $z = 1$, (c) $C_S = 2.5 \cdot 10^{-3}$ M, $z = 2$, (d) $C_S = 10^{-2}$ M, $z = 2$.

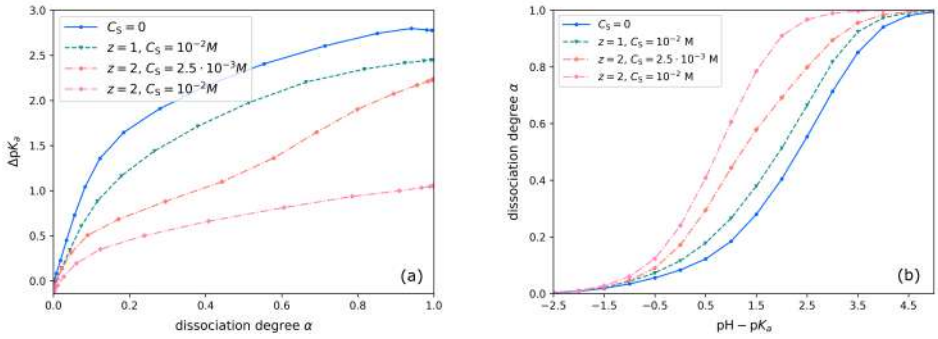

Figure 7.16: (a) ΔpK_a as a function of α, and (b) α as a function of pH - pK_a for the 3_1 case and various salt conditions.

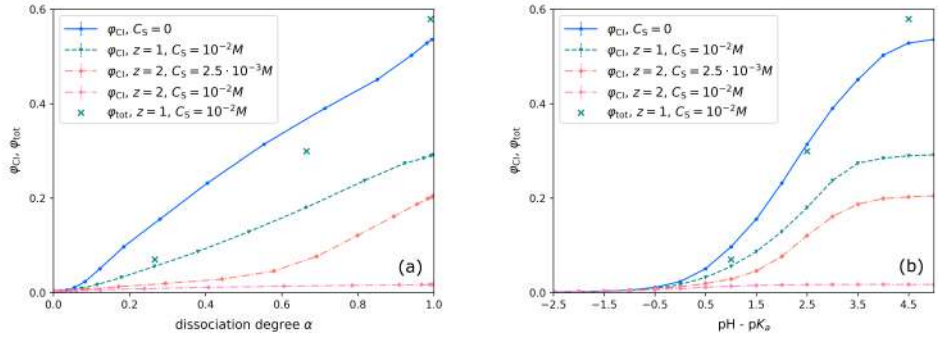

Figure 7.17: Fraction of "condensed" CIs φ_{CI} and fraction of total "condensed" cations φ_{tot} as a function of (a) α and (b) pH - pK_a for the 3_1 polyelectrolyte and various salt conditions.

solution $C_S = 10^{-2}$ M, the transition from "tight" to "delocalized" appear at a $\lambda_D/(N_{mono}^{1/2} r_e)$ value that is roughly twice the one reported in Reference [276].

We notice, instead, that R_g^2 remains very low and its behavior versus α turns monotonic in presence of divalent ions[§], finding due to the propensity of multivalent ions to go beyond a simple screening effect by coordinating onto sufficiently ionized polyelectrolytes via more than a single monomer [33].

Finally, we notice that R_g^2 barely varies upon increasing the pH (hence α) of the most concentrated solution of divalent salt; this is probably due to the fact that, for a knotted ring, cations coordinates not only on the chain loops replacing the monovalent CIs, but also become chelated inside the knot, which act as a cage able to sequestrate several divalent cations from the solution (see the snapshots

[§]Notice that the presence of salt cations, especially divalent ones, deeply impact on the polyelectrolyte titration curves as was originally evidenced in References [170] and [33].

reported in Figure 7.15 (d)).

7.4 Conclusion

In conclusion, our *in silico* simulations on weak polyacid rings have highlighted a non-monotonic behavior for the gyration radius R_g^2 versus the dissociation degree α for knotted species, such evidence opposite to the commonly expected ionization–repulsion–expansion scheme and related to a modified balance between entropic and energetic contributions compared to linear, star-like or even unknotted circular species. In other words, the average size, and hence the mechanical effects associated to it, of knotted rings is lower at both extremes of the ionization range. The key role played by CIs localization on a (partially) ionized chain has been thoroughly investigated by varying parameters such as the Bjerrum length l_B and the concentration and valence of inert salts. Comparing with strong polyelectrolytes of similar ionization degrees, it also emerges that the re-contraction of the gyration radius R_g^2 of knotted weak polyacid rings begins at higher α values thanks to the localization of undissociated monomers inside the knotted portion of the chain.

7.5 Appendix: Pair Distribution Functions

In this appendix we report all the pair distribution functions $g(r)$ calculated between all the species for each simulated system.

7.5.1 Varying knot complexity

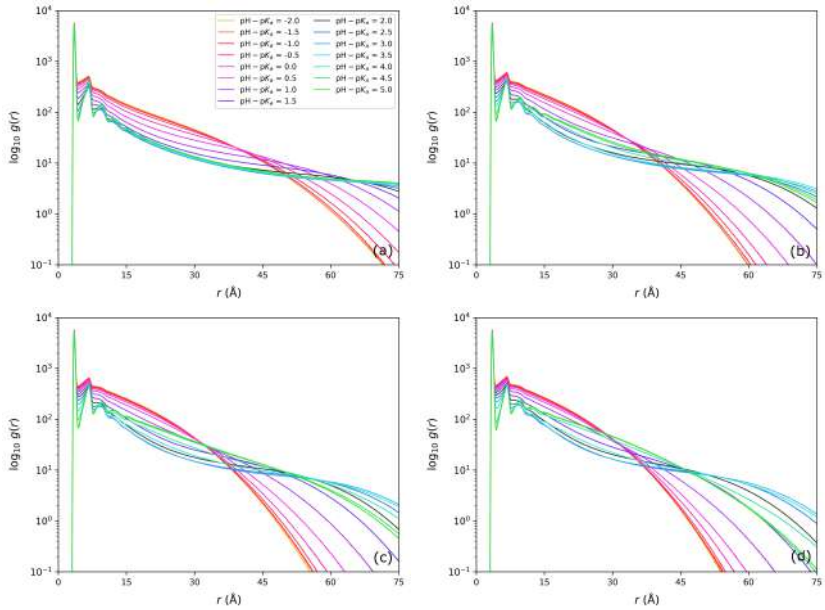

Figure 7.18: Monomer–monomer $g(r)$ as a function of pH - pK_a for the four topologies investigated: (a) 0_1, (b) 3_1, (c) 4_1, (d) 5_1.

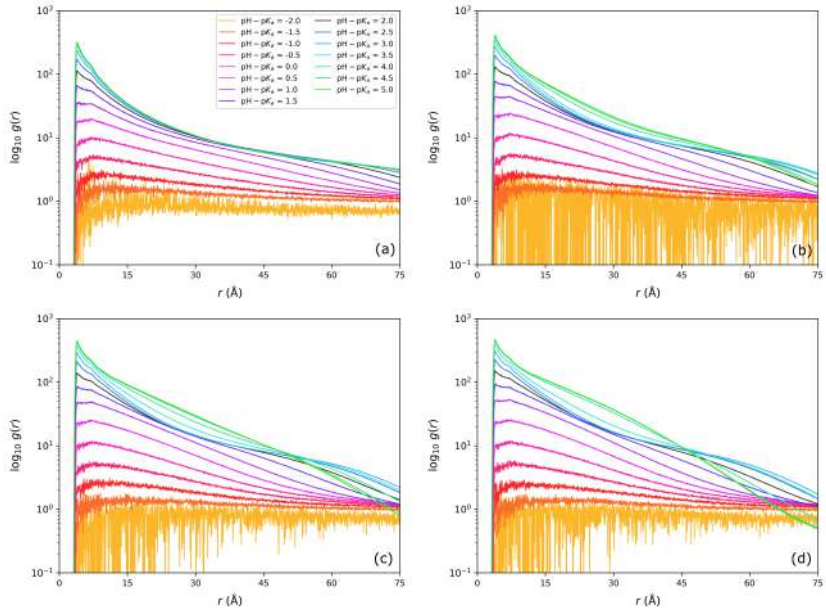

Figure 7.19: Monomer–CI $g(r)$ as a function of pH - pK_a for the four topologies investigated: (a) 0_1, (b) 3_1, (c) 4_1, (d) 5_1.

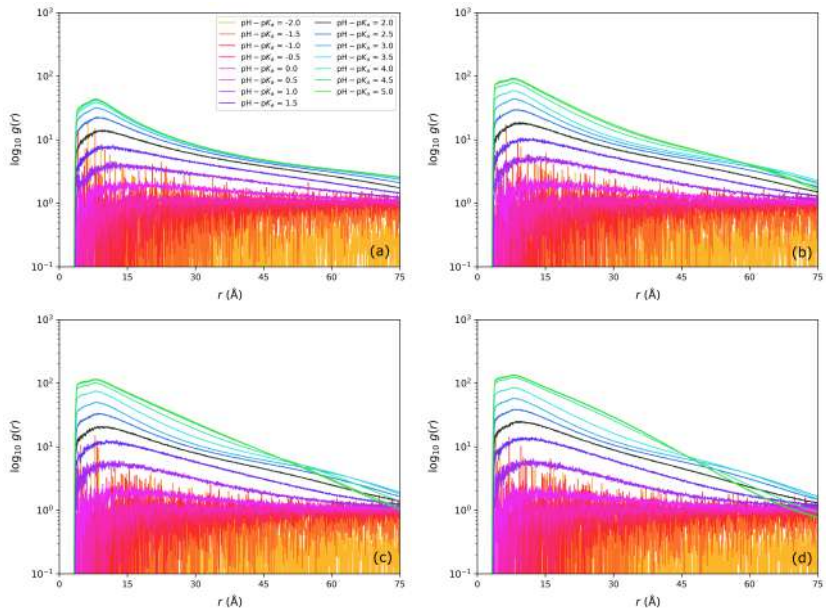

Figure 7.20: CI–CI $g(r)$ as a function of pH - pK_a for the four topologies investigated: (a) 0_1, (b) 3_1, (c) 4_1, (d) 5_1.

7.5.2 Impact of solvent Bjerrum length l_B

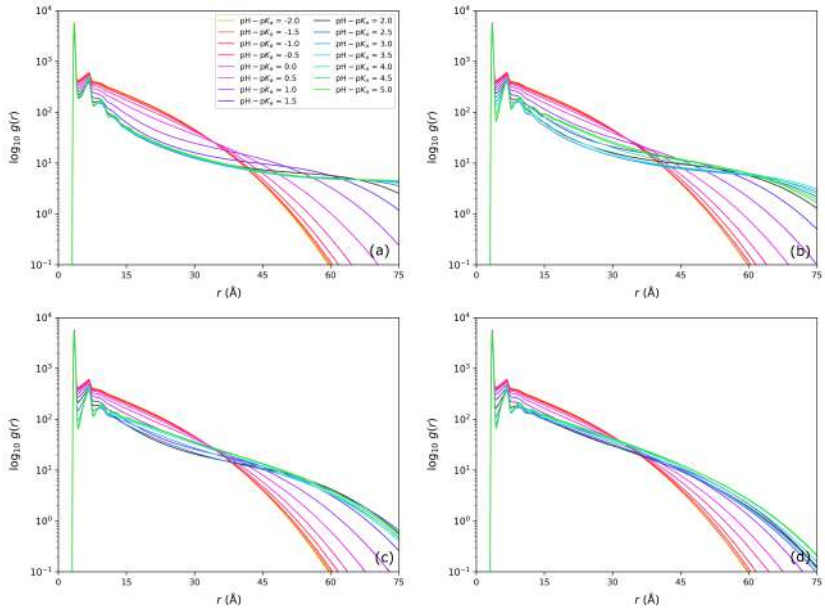

Figure 7.21: Monomer–monomer $g(r)$ as a function of pH - pK_a for various l_B values: (a) $l_B = 3.55$ Å, (b) $l_B = 7.10$ Å, (c) $l_B = 10.65$ Å, (d) $l_B = 14.20$ Å.

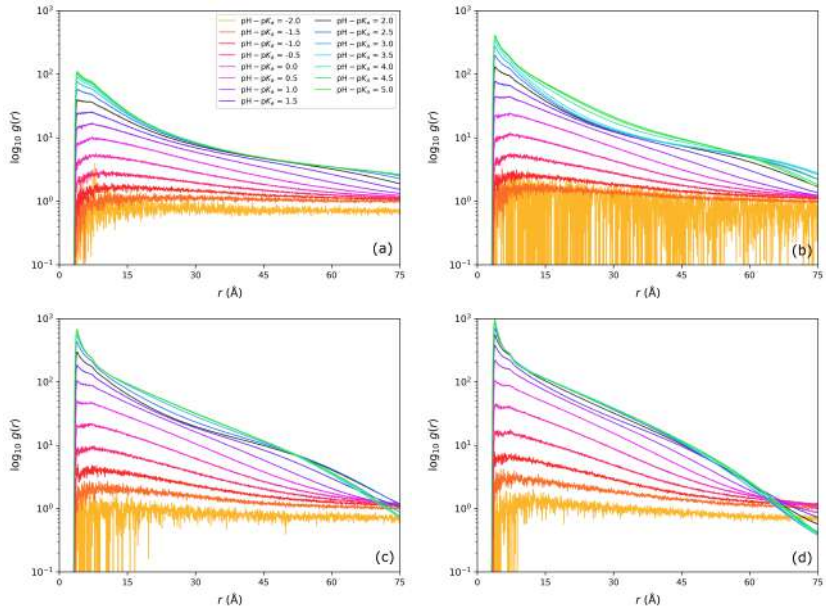

Figure 7.22: Monomer–CI $g(r)$ as a function of pH - pK_a for various l_B values: (a) $l_B = 3.55$ Å, (b) $l_B = 7.10$ Å, (c) $l_B = 10.65$ Å, (d) $l_B = 14.20$ Å.

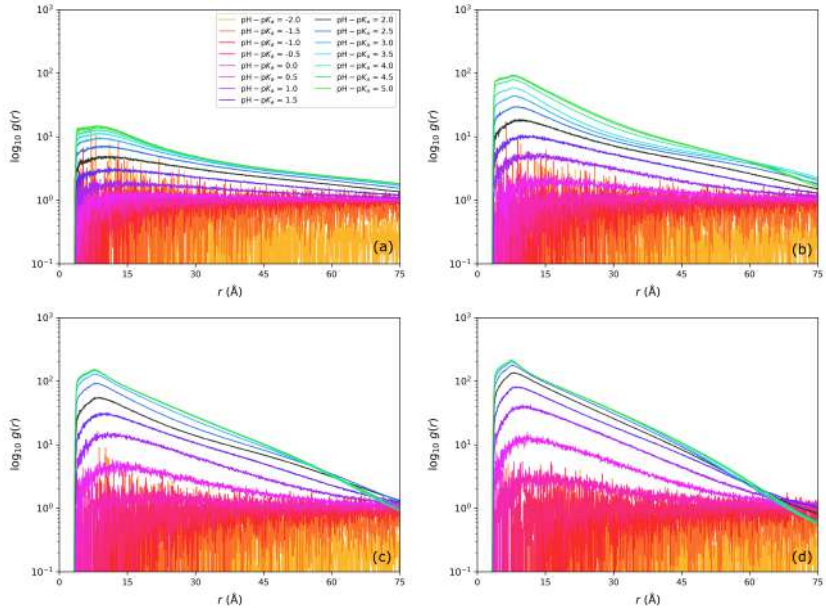

Figure 7.23: CI–CI $g(r)$ as a function of pH - pK_a for various l_B values: (a) $l_B = 3.55$ Å, (b) $l_B = 7.10$ Å, (c) $l_B = 10.65$ Å, (d) $l_B = 14.20$ Å.

7.5.3 Impact of solvent background inert salt

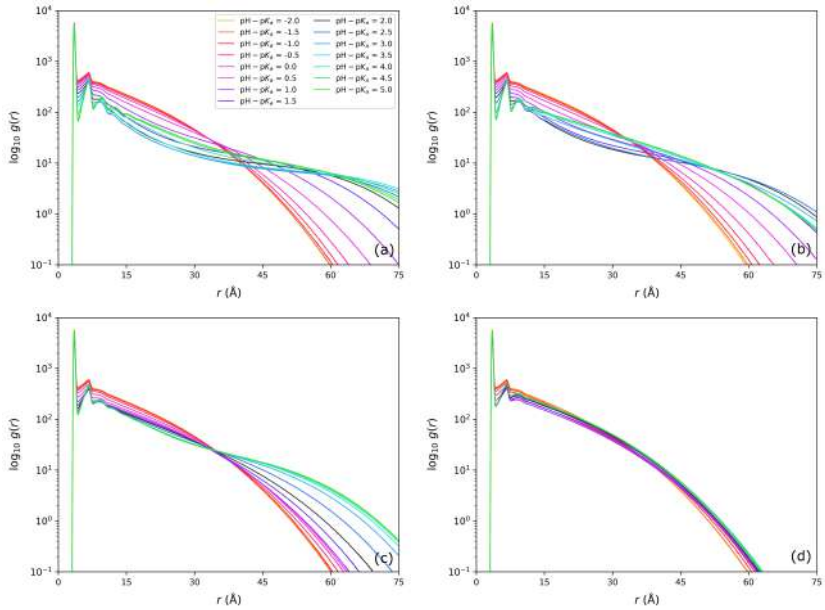

Figure 7.24: Monomer–monomer $g(r)$ as a function of pH - pK_a for various salt valencies z and concentrations C_S: (a) $C_S = 0$ M, (b) $C_S = 10^{-2}$ M, $z = 1$, (c) $C_S = 2.5 \cdot 10^{-3}$ M, $z = 2$, (d) $C_S = 10^{-2}$ M, $z = 2$.

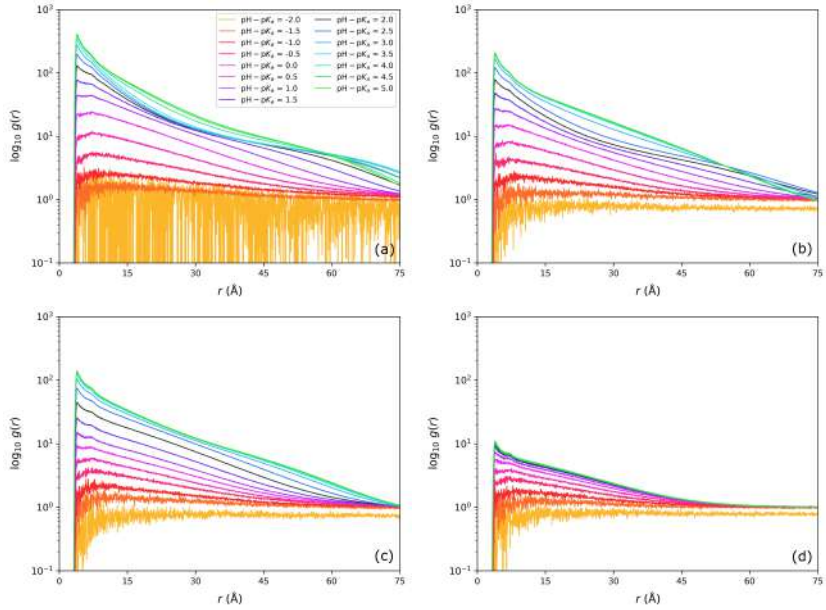

Figure 7.25: Monomer–CI $g(r)$ as a function of pH - pK_a for various salt valencies z and concentrations C_S: (a) $C_S = 0$ M, (b) $C_S = 10^{-2}$ M, $z = 1$, (c) $C_S = 2.5 \cdot 10^{-3}$ M, $z = 2$, (d) $C_S = 10^{-2}$ M, $z = 2$.

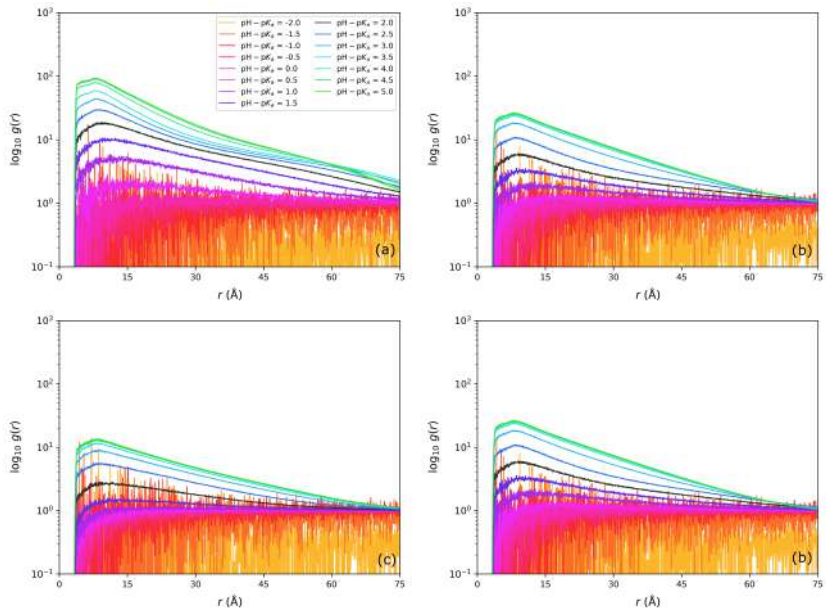

Figure 7.26: CI–CI $g(r)$ as a function of pH - pK_a for various salt valencies z and concentrations C_S: (a) $C_S = 0$ M, (b) $C_S = 10^{-2}$ M, $z = 1$, (c) $C_S = 2.5 \cdot 10^{-3}$ M, $z = 2$, (d) $C_S = 10^{-2}$ M, $z = 2$.

7.5.4 Simulations without CIs insertion

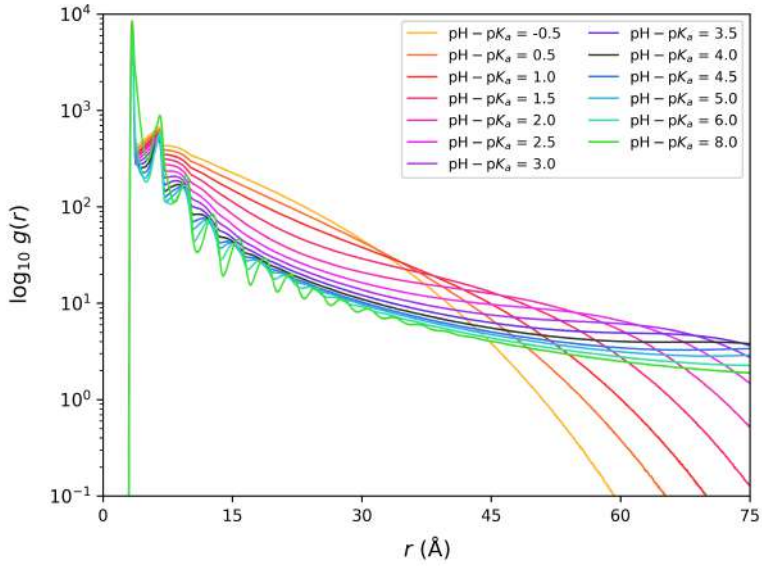

Figure 7.27: Monomer–monomer $g(r)$ as a function of pH - pK_a for the simulation of the 3_1 ring in absence of CIs.

Chapter 8

Can Oppositely Charged Polyelectrolyte Stars Form a Gel? A Simulational Study*

8.1 Introduction

If polyelectrolytes get chemically cross-linked they can form polyelectrolyte gels, and since they are water soluble one sometimes also calls them hydrogels. These gels possess a huge swelling capacity in aqueous solution and they can absorb water in amounts of up to a few hundred times their dry mass. This makes them ideal base materials for super-absorbers in hygiene products [282], biomedical [283–290] and agricultural [291–293] applications, and even for desalination purposes [294–297]. In contrast to bulk materials, polyelectrolyte micro- and nano-gels are being investigated as nano-reactors [298–300] or as carriers for controlled drug release [20–24].

Chemical cross-linking is not the only way to form a gel. There are so called physical gels that form via reversible bonds that can be based on various physical non-covalent interactions such as hydrogen bonds, $\pi - \pi$-stacking, hydrophobic forces, van der Waals or ionic interactions. The connectivity of the gel constituents is therefore partially or not at all fixed. This leads to the fact that physical gels are normally less structured [56–59] than chemical gels which are

*This chapter has been adapted from: Tagliabue A., Landsgesell J., Mella M., Holm, C., Can Oppositely Charged Polyelectrolyte Stars Form a Gel? A Simulational Study, *Soft Matter*, Accepted article (doi.org/10.1039/D0SM01617A),

often formed with tetra-functional nodes.

Physically cross-linked gels can have certain advantages; for example, a bond rupture event is reversible, and such gels can be to a certain degree self-healing. Of special interest could be ionic bonds, since they are tunable via many parameters. As an example, they can be formed and destroyed dynamically, and also their strength can be tuned by addition of salt, changes in the relative dielectric constant of the solution via adding co-solvents, or varying the solution pH if the dissociable groups are weak. For example, one could tune cargo encapsulation and a following release on changing some of the stimuli, e.g. the ionic strength.

The investigation of physically cross-linked networks by simulations are scarce. Exceptions worth mentioning are the investigations of associating polymers, so-called telechelic polymer chains [61, 301–305], as well as the investigation of ionomers [306–310], neutral block copolymers [60, 61], DNA nanostars [311, 312], or tetrahedral network liquids [313]; these, however, do not fall into the class of strongly swelling, ionically reversible cross-linked stars. Many theories also deal with the swelling of chemical gels, but much less with the swelling behavior of physical ones. As a notable exception we mention the works of Tanaka and others [314–319] on the properties of physically cross-linked ionic gels. Mixtures of oppositely charged polyelectrolytes can undergo an associative phase separation, known as a complex coacervate (see the review article by Sing and Perry [320]). The coacervate phase can be a liquid, a gel, or a glass, and sometimes special preparation techniques have to be employed to produce a hydrogel [321]. Since a popular way of synthesizing chemically cross-linked hydrogels with a low polydispersity is based on tetra-PEG ansatz from Sakai and co-workers [322], in this work we will investigate the physical gelation properties of four-armed polyelectrolyte stars, where one star species carries positively charged blocks, and the other star species carries negatively charged blocks. This could, in principle, lead to a regular tetra-functional network with matching charged blocks if the system is perfectly monodispersed. To our knowledge there have been no previous simulations performed with ionically bonded star polyelectrolytes. Investigations of regular charged polyelectrolyte copolymer networks using a thermodynamic model has been done by the group of Patrickios in a series of publications [323–325]. Their model predicts that such a network has a discontinuous transition from a homogeneous to a micellar phase. Such phases are similar to those known from di-block

copolymer melts. We therefore present the first exploratory simulation to study the gelation properties of an equimolar solution mixture of oppositely charged star polyelectrolytes. For the sake of simplicity, we avoid to add any salt ion or counterion in solution, and we treat the system as perfectly mono-dispersed.

This chapter is structured as follows: in Section 8.2 we will present our model and the used simulation methods, followed by our results in Section 8.3; we will conclude with a summary of our main results and an outlook for further studies in Section 8.4. Moreover, in Appendix 8.5 we present structural data calculated for all the isolated species investigated, in Appendix 8.6 we provide the technical information on the algorithms implemented to analyze networks structure and to detect the mechanisms lying under ionic bonds dynamics, and in Appendices 8.7.1 and 8.7.2 we present selected trajectory snapshots and movies.

8.2 Methods and Model

8.2.1 The model

Our system consists of a cubic simulation box of length L, with periodic boundary conditions in all the three dimensions, which contains $N_\mathrm{s} = 64$ star polymers. The latter are treated as a coarse-grained "bead & spring" model and consist of $N_\mathrm{a} = 4$ arms tethered to a common central monomer, or "nucleus". Each arm is composed of $N_\mathrm{mono}^{(\mathrm{a})} = 10$ monomers, so that the number of beads in each star-like polymer is $N_\mathrm{mono}^{(\mathrm{s})} = N_\mathrm{mono}^{(\mathrm{a})} N_\mathrm{a} + 1 = 41$, and the total number of monomers in the cell is $N_\mathrm{mono}^{(\mathrm{tot})} = 41 N_\mathrm{s} = 2624$. In the following, parameter and properties that refer to monomers, individual arms and stars are labeled with "mono", "a", and "s" as subscripts, respectively. Furthermore, during the discussion we will use italic capital letters (A, B, etc.) as star indexes, italic lowercase letters (i, j, etc.) as monomer indexes, and italic Greek lowercase ones (α, β, etc.) as arms indexes.

Each arm is structured as a AB-block copolymer, where "A" is the terminal part of the chain and is composed of Ω beads carrying each one quenched monovalent charge (i.e., they behave as strong electrolytes), whereas the part "A" is directly connected to the nucleus and is composed by $N_\mathrm{mono}^{(\mathrm{a})} - \Omega$ neutral beads; the nucleus is neutral itself. We provide a pictorial description of such

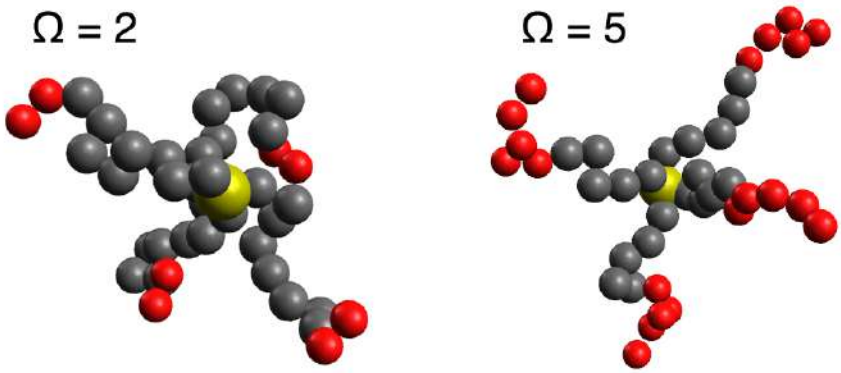

Figure 8.1: Models of tetra-functional strong polyelectrolyte stars simulated in this work. The snapshots were taken from simulations at very high dilution. Ω is the number of charged monomers at the end of each arm. Color scheme: neutral monomers in gray, (positively) charged monomers in red, central beads in yellow.

block copolymer model in Figure 8.1. Half of the stars in solution (N_s^+) carry positive charges, while the remaining half (N_s^-) is negatively charged, so that $N_s^+ = N_s^- = N_s/2 = 32$, and the system is overall electroneutral.

All monomers interact via a Weeks-Chandler-Anderson potential to simulate their excluded volume (see Equation 2.3), with $\epsilon = k_B T$; σ and $k_B T$ are both equal to 1 and represent, respectively, the internal units of measurement of length and energies. It immediately follows that $T = \epsilon/k_B = 1$. Bonds between adjacent beads are simulated via FENE potentials (see Equation 2.5), where $k_{bond} = 30\epsilon/\sigma^2$ and $r_{max} = 3\sigma$. Arms are connected to the central bead via the same FENE potential. No angular terms have been added to the total potential, so that the polymer chains are fully flexible, and tethered arms can easily rearrange around the nuclei. Electrostatic interactions are calculated by the P^3M method [65,66], with errors [67] set to 10^{-3}. The solvent is treated as a uniform dielectric. The Bjerrum length has the value $\lambda_B = e^2/(4\pi\varepsilon k_B T) = 2\sigma$, where e is the elementary charge and ε is the permittivity of the medium. Setting $\sigma = 3.55$ Å results in the typical Bjerrum length of the water at room temperature ($T = 298$ K), $\lambda_B = 7.10$ Å.

8.2.2 Simulation methods

Molecular dynamics simulations are performed in the canonical (NVT) ensemble using a Langevin thermostat (see Section 2.2.4), and integrating the equation of motion by integrated by a velocity Verlet algorithm (see Section 2.2.3) with a time step $\delta t = 0.01\sigma(m/\epsilon)^{1/2}$; thus our system time unit $\tau = \sigma\sqrt{m/\epsilon}$ contains 100 integration steps. All simulations have been performed with the software package ESPResSo [326]. In the following all length and time units are expressed in multiples of σ and τ, respectively, unless otherwise noted.

The equilibrium between the system and pure water is called "free-swelling equilibrium". In the canonical ensemble it is obtained at the minimum of the Helmholtz free energy F as a function of the volume V, that is $\partial F/\partial V = -P = 0$, where P is the volume averaged virial pressure, so that the equilibrium volume $V_{\mathrm{eq}} = L_{\mathrm{eq}}^3$ (and, consequently, the equilibrium concentration of the species $C_{\mathrm{s,eq}}$) is defined at V where the pressure P is equal to 0.

In order to identify L_{eq} as a function of the number of terminal charges, we performed a series of simulations varying the box length L for species with $\Omega = 1$, 2, 3, 4, and 5. For each system type, three different simulation protocols have been implemented; these are:

single-points protocol: for each value of the desired box length, $L \in [L_{\mathrm{min}}, L_{\mathrm{max}}]$, we simulate the system starting from a random solution of N_{s} stars. The system is initially thermalized for a time t_{therm}, then we take a time-average measure of all desired properties during a simulation time t_{sim}.

expansion protocol: we start simulating a random solution of N_{s} stars at a box length $L = L_{\mathrm{min}}$ and ensure ourselves that we have a positive volume average virial pressure P (e.g., *vide infra* Figure 8.2). The system is thermalized for a time t_{therm}, then properties are collected for a time t_{sim}. Once the simulation at $L = L_{\mathrm{min}}$ is done, we increase the box length L by a quantity ΔL (in order to obtain an isotropic expansion in V), we thermalize the last configuration obtained at the previous volume for a time t_{therm}, and then we collect properties for a time t_{sim}. The described process is then repeated until the system reach a desired box length $L = L_{\mathrm{max}}$.

compression protocol: we use the same scheme described for the "expansion"

Abbreviation	Meaning
CoS	Cluster of stars
CoA	Cluster of arms

Table 8.1: List of abbreviations commonly used in this chapter

simulations, but starting from a box length $L = L_{\max}$ and decreasing it by a quantity ΔL at each step until it reaches $L_{\min}$.

For all the cases, we set $L_{\min} = 16\sigma$, $L_{\max} = 50\sigma$, $t_{\text{therm}} = 10^5\delta t$ and $t_{\text{sim}} = 10^6\delta t$. We also chose $\Delta L = 2\sigma$ except for the ranges of box length values in which the systems are expected to be near the free–swelling equilibrium; in such ranges we increased the sampling resolution up to $\Delta L = 0.25\sigma$. For each simulated value of L, 50 independent simulations were performed in order to improve the sampling of possible configurations that may be hindered by high energy barriers. Our data represent averaged results accompanied by their standard errors. Subsequently, L_{eq} has been calculated by fitting the L values via a second-order polynomial, and we performed 50 independent simulations at L_{eq} ($t_{\text{therm}} = 10^5\delta t$, $t_{\text{sim}} = 10^6\delta t$) in order to collect information about structural and dynamical properties of aggregates in solution.

8.3 Results and discussion

8.3.1 Determining the free–swelling equilibrium

Figure 8.2 shows the behavior of the volume averaged virial pressure P of the system as a function of the box length L for species with a different number of terminal charged monomers, $\Omega = 1$, 2, 3, 4, and 5. Results are obtained implementing the "single–points" protocol described in Section 8.2.2. For $\Omega = 1$ (i.e., star polymers carrying only a monovalent terminal bead on each arm), we observe a positive pressure over all L ranges simulated. At low $L/L_{\max}$ values, i.e. at high concentration (see also the left panel of Figure 8.3), P starts to strongly increase due to the monomer excluded volume interactions, which oppose the compression preventing particles overlaps. As the box volume increases, the system becomes more diluted, and P tends to 0^+.

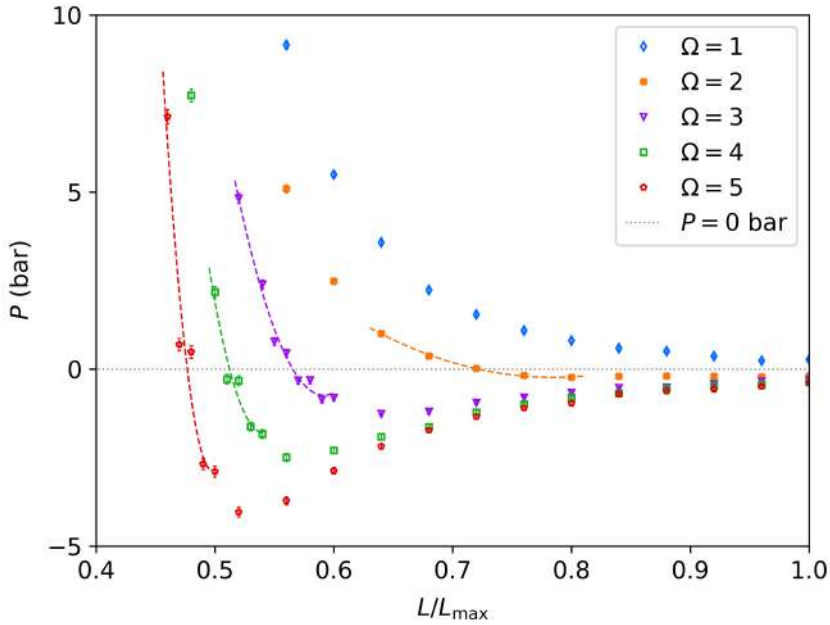

Figure 8.2: Isotropic pressure P (bar) vs $L/L_{\max}$ for different values of Ω obtained via the "single points" simulation protocol. The dashed lines are the quadratic fits performed in order to identify the L_{eq} values (the fitting parabolic function is used as the simplest option available and it has no physical significance). The dotted gray line is only a guide to the eye for discerning positive and negative pressure values. Standard error bars are included everywhere, but are sometimes smaller than the plot symbols.

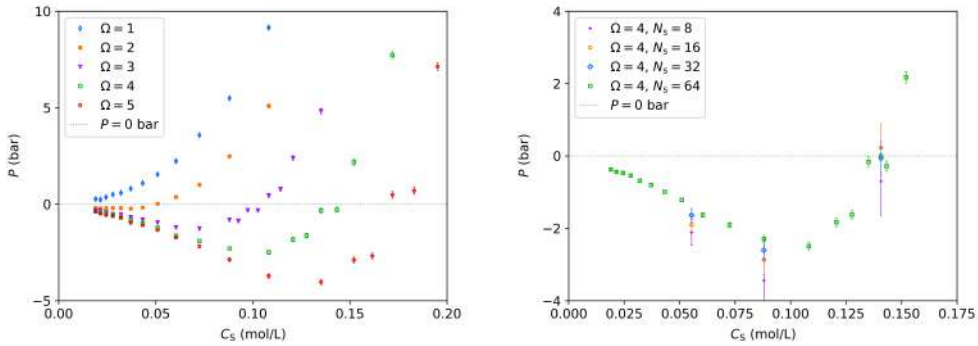

Figure 8.3: Isotropic P (bar) as a function of species concentration C_S (mol/L) for: the five Ω values (left panel); and the $\Omega = 4$ case and various number of stars in the cell (right panel).

For $\Omega \geq 2$ we observe a different behavior. As the number of terminal charges increases, P decreases for all simulated box lengths. We attribute this to the progressively stronger electrostatic attraction between the two oppositely charged species. At small box length values we observe, as for the $\Omega = 1$ case, positive values of P arising from the internal pressure generated by monomer excluded volumes. Unlike for the $\Omega = 1$ case, however, increasing the box volume results in non-monotonic P curves, and we find regions of negative pressure. As the system becomes more diluted, the isotropic pressure P asymptotically converges to 0 from below. We always find one box length L_{eq} for which $P(L_{\text{eq}}) = 0$ and that could be a candidate system to possess an equilibrium phase against a pure water system. In order to precisely determine L_{eq}, for each Ω value ($\Omega \geq 2$) we fitted the points near $P = 0$ with a parabolic function, weighting each data point with its respective statistical error (see the dashed lines in Figure 8.2). In this way we found $L_{\text{eq}}/\sigma = 36.07$, 28.27, 25.65, and 23.84 for Ω values 2 to 5, respectively. These correspond to species molar concentrations $C_{\text{s,eq}} = N^+/(N_{\text{A}}V)$ equal to $2.55 \cdot 10^{-2}$, $5.40 \cdot 10^{-2}$, $7.05 \cdot 10^{-2}$ and $8.75 \cdot 10^{-2}$ mol/l, respectively (in the formula, N_{A} is the Avogadro number and V is the volume in liters). Figure 8.4 displays selected snapshots for the various systems at free-swelling equilibrium.

In order to check if our *single-points* simulation protocol is able to correctly sample the system at equilibrium, i.e. that we do not run into metastable configurations, we performed the same simulations with the other two protocols described in section 8.2.2. Figure 8.5 displays the results for the three different schemes and various Ω. We can observe that, even for the worst case, the results

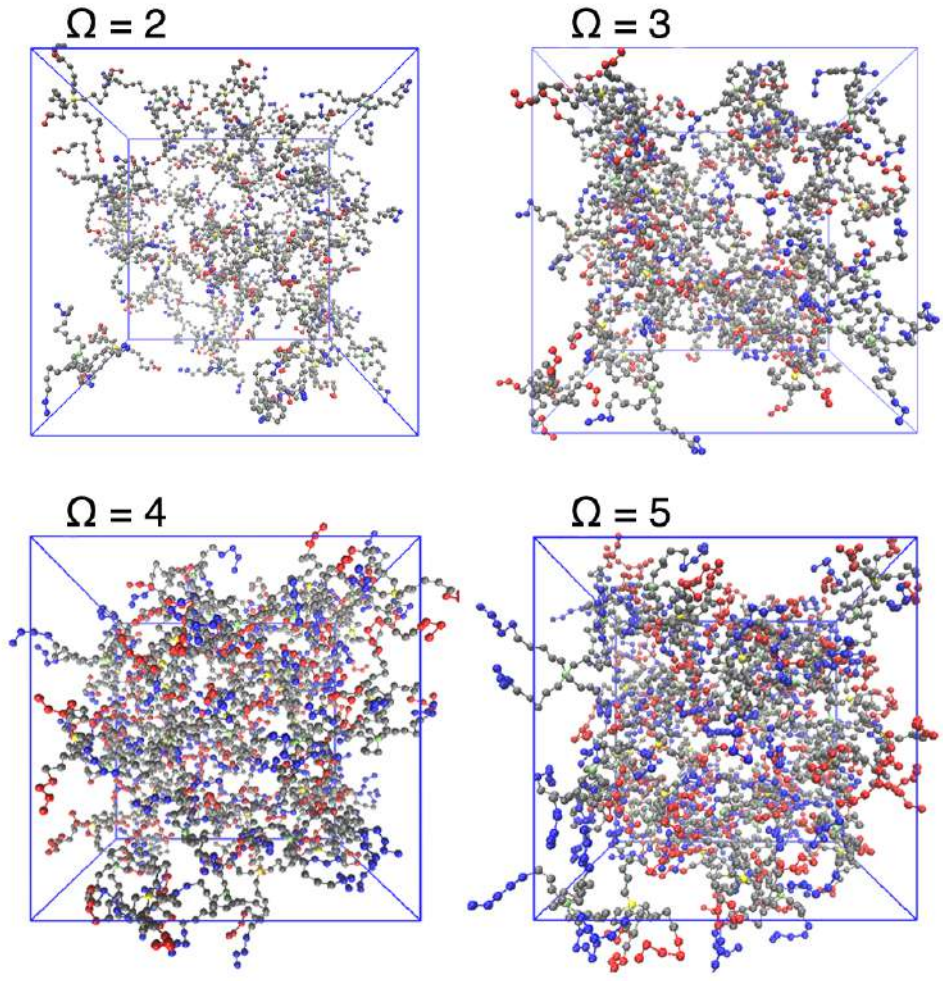

Figure 8.4: Snapshots for systems with various Ω values at the free-swelling equilibrium (notice that the box side length is different between the four snapshots, see Table 8.2). The diameter of all monomers has been reduced by roughly one half with respect to the real one in order to improve the clarity of the pictures. Color scheme: neutral monomers in gray, positively charged monomers in red, negatively charged monomers in blue, the nuclei of positive stars in yellow, the nuclei of negative stars in lime.

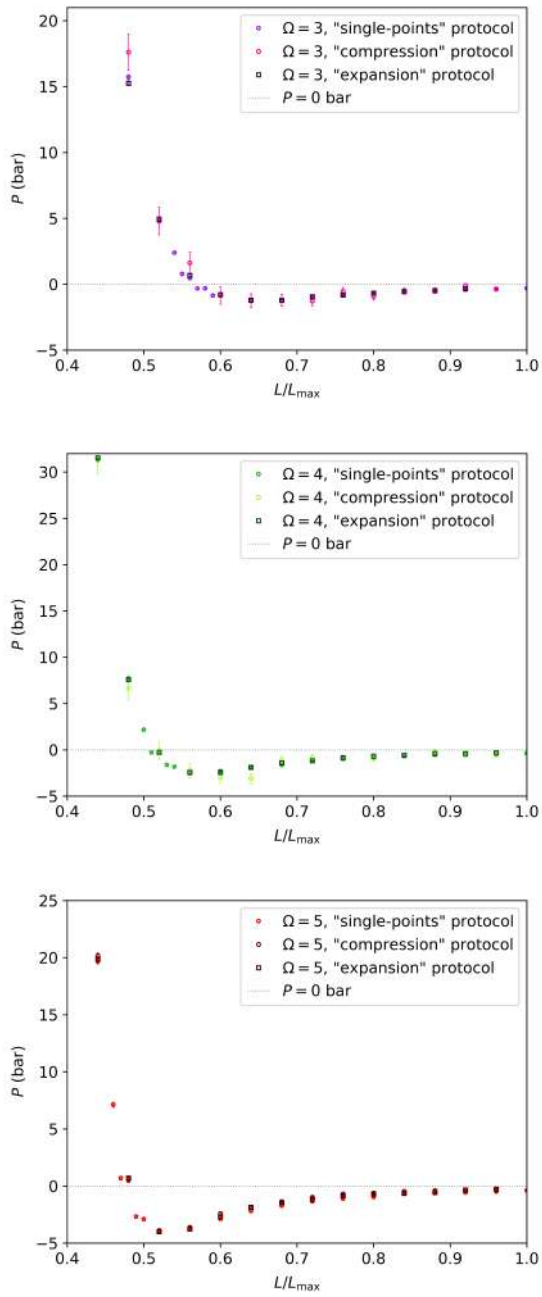

Figure 8.5: Comparison between the results obtained via the three different protocols described in Section 8.2.2 for various Ω. The dotted gray line is a guide to the eye to discern positive and negative pressure values. Standard error bars are included everywhere, but are sometimes smaller than the plot symbols.

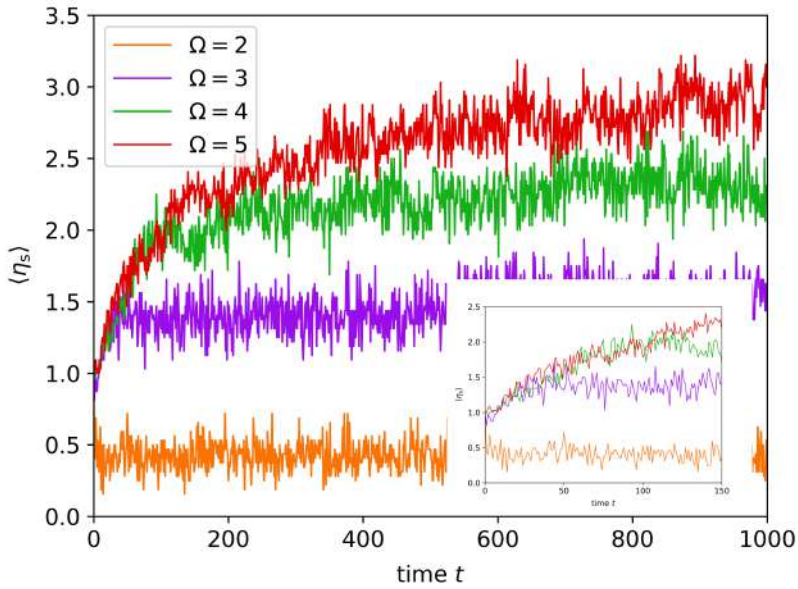

Figure 8.6: Average number of stars in contact with a given oppositely charged star η_s versus the simulation time t for different Ω values and starting from solutions of pre-equilibrated dimers. The inset shows the initial part of the simulation.

obtained via the three different protocols are in good agreement within standard error bars, hence we are confident that we are sampling the system in an ergodic way at each box length value.

Since, for the sake of simplicity, we simulated only systems with an equimolar mixture of oppositely charged, but otherwise identical stars, the smallest stable supramolecular aggregates in solution are expected to be dimers composed by two oppositely charged stars. Thus, in order to investigate the stability of the latter with respect to the aggregates observed at $P = 0$ (see Figure 8.4), we decided to monitor the evolution in time of a solution of 32 pre-assembled dimers.

To set up the system, for each Ω value we thermalized (for a time $t = 10^4$) a single dimer at very low concentration. Such dimers resulted stable for $\Omega \geq 2$, whereas for $\Omega = 1$ the two polyelectrolytes frequently dissociate and only transient dimeric interactions were observed during the simulation. Thus, for $\Omega \geq 2$ species, 32 pre-equilibrated random configurations of such dimers have been placed homogeneously (i.e., with their centers of mass regularly spaced inside the cell) inside a simulation box of side length $L = 42\sigma$ ($L/L_{\max} = 0.84$);

then, the system was simulated for a time $t = 10^4$.

To monitor the temporal evolution of the dimers, we define $\eta_{s,A}$ as the number of *oppositely* charged stars in contact with a given star A (*vide infra* Figure 8.7). Hence, in order to investigate the stability of the dimers with respect to clusters composed by more than 2 stars, we monitor the evolution of the value of $\eta_{s,A}$ averaged over all the stars in solution, $\langle \eta_s \rangle = \sum_A^{N_s} \eta_{s,A}$. We define a positive (negative) star A to be "in contact" with a negative (positive) star B if it is possible to find a pair of oppositely charged monomers i and j, belonging, respectively, to A and B, lying within a distance $r_{ij} < r_{cont} = 1.2\sigma$ from each other, where r_{cont} has been chosen as a reasonable distance to yield a sufficient binding strength. This value is only slightly higher than both the distance at which our WCA potential goes to zero (i.e., $r_{cut} = 2^{\frac{1}{6}}\sigma$, see Equation 2.2) and the distances at which we observe the main peaks in the pair distribution functions calculated between oppositely charged monomers at the free–swelling equilibrium (*vide infra* Figure 8.8). Despite the arbitrariness of the choice, we would like to stress that we explored alternative cutoff values, noticing that trends and behaviors which we report it this work stay preserved, and only small quantitative differences appeared.

Figure 8.6 shows the temporal evolution of $\langle \eta_s \rangle$ for system with different Ω values. Due to our initial set-up, all curves for $t = 0$ start at $\langle \eta_s \rangle = 1$ (see the inset in Figure 8.6), as one would expect in the presence of a solution of well-separated dimers in which each positively charged star is in contact with only one negative star, and *vice versa*. For $\Omega = 2$, we notice that $\langle \eta_s \rangle$ quickly drops to ~ 0.4, meaning that more than the 25% of the dimers dissociate, evidencing that the ionic bonds are not strong enough to balance the entropic forces of the stars that want to achieve a homogeneous distribution; hence, for $\Omega = 2$ the loss of contacts is "overcompensated" by the increase in system entropy due to dimers dissociation. For $\Omega = 3$, 4, and 5, instead, $\langle \eta_s \rangle$ initially rapidly increases with t and then it stabilizes around a value roughly equal to 1.4, 2.3, and 2.8, respectively, which means that clusters containing more than 2 stars start to form due to higher order multipole attraction. Moreover, we observe that the time needed to reach equilibrium increases with Ω, which is probably due to the progressive increase of the interaction strength between two stars bonded in a dimer, which in turn results in a higher potential barrier that must be overcome

to break the ionic bonds apart.

Finally, we simulated a few points of the PV curve for the $\Omega = 4$ system reducing the number of stars in the box ($N_s = 8, 16, 32$) in order to check for the presence of finite size effects. Results are reported in the right panel of Figure 8.3. Despite the larger error bars with respect to the $N_s = 64$ case (that are due to the fact that we simulated only 5 independent trajectories for the smaller systems), results with 64 and 32 stars are statistically equivalent. This, together with the fact that stars average size (*vide infra* Table 8.2) are at least ~ 3 times smaller than the smallest simulated box length ($L = 16\sigma$), gives us confidence that finite size effects can be neglected in this seminal study.

8.3.2 System structural properties at the free-swelling equilibrium

In this section we discuss the structural properties of the supramolecular aggregates observed at the free–swelling equilibrium (see Figure 8.4), with a particular focus on investigating the presence of percolating networks as function of Ω. Similarly to the number of contacts for a given star A, $\eta_{s,A}$, one can also define the number of contacts formed by an individual arm α, $\eta_{a,\alpha}$, and, consequently, the average value over all the chains in solution, $\langle \eta_a \rangle$. To do this, we use the same definition of "contact" introduced previously, that is two *oppositely charged* arms result linked if exist at least one pair of oppositely charged monomers lying at a distance which is less than the cutoff radius $r_{cont} = 1.2\sigma$ (see Figure 8.8). From such a definition it immediately follows that if two arms are in contact, then so are the stars to which they belong. Figure 8.7 displays an example of the calculation of such properties for an aggregate composed of 3 stars. Especially in the case of lower Ω values, a non-negligible fraction of stars (and, consequently, arms) may possess, at least transiently, no contacts in solution. Thus, we define an "isolated" star as a polyelectrolyte star A for which $\eta_{s,A} = 0$, and the average fraction of those as Δ_s. There will also be arms that do not have an ionic bond to any other arm, which we call in the following "dangling" arms, whose fraction is denoted by Δ_a. These are chains α for which $\eta_{a,\alpha} = 0$ (see Figure 8.7). Our results for the above discussed structural properties obtained for all systems are summarized in Table 8.2.

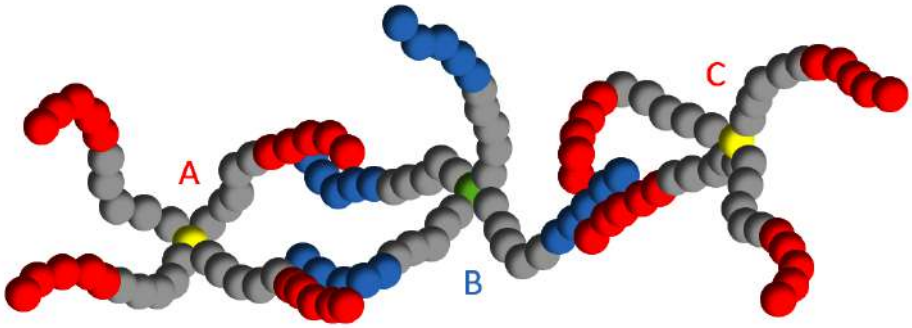

Figure 8.7: The picture represents a cluster of stars composed by 3 polyelectrolyte stars (i.e., $\mathscr{C}_{\rm s} = 3$), A, B and C ($\Omega = 5$) as an example. A: $\eta_{{\rm s},A} = 1$, $\sum_{\alpha=1}^{4} \eta_{{\rm a},\alpha} = 2$, 2 dangling arms; B: $\eta_{{\rm s},B} = 2$, $\sum_{\beta=1}^{4} \eta_{{\rm a},\beta} = 4$, 1 dangling arm; C: $\eta_{{\rm s},C} = 1$, $\sum_{\gamma=1}^{4} \eta_{{\rm a},\gamma} = 2$, 2 dangling arms. Here, α, β and γ are indexes that run over the four arms of A, B and C, respectively. For this specific system, we find $\langle \eta_{\rm s} \rangle = \frac{4}{3} \simeq 1.33$, $\langle \eta_{\rm a} \rangle = \frac{8}{12} \simeq 0.67$, $\Delta_{\rm s} = 0$ (no isolated stars), and $\Delta_{\rm a} = \frac{5}{12} \simeq 0.42$. The colour scheme is the same as in Figure 8.4.

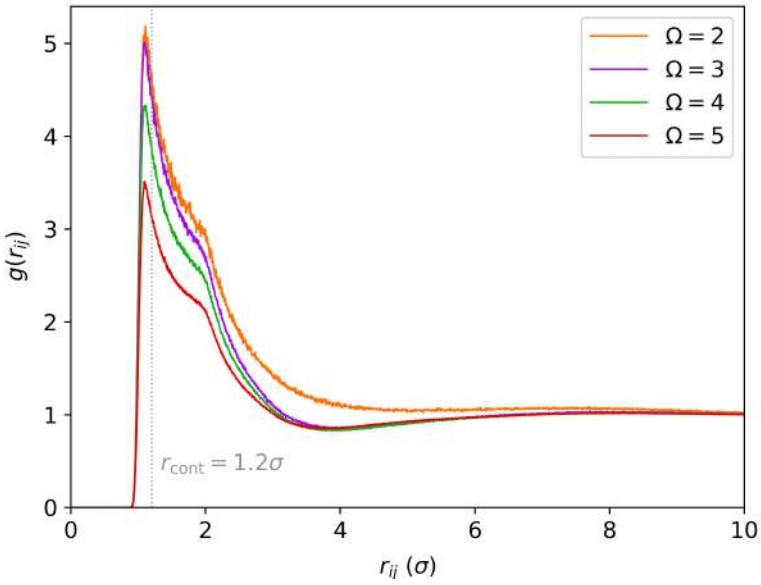

Figure 8.8: Pair distribution function calculated between positively and negatively charged monomers for polyelectrolytes with different Ω values. r_{ij} is the distance between the pairs. The gray dotted vertical line indicates the value of the cutoff radius $r_{\rm cont}$ used to define a "contact" (i.e., an ionic bond) between two oppositely charged stars (or arms).

Table 8.2: Table summarizing results for the structural properties of the system at the free-swelling equilibrium. The numbers in brackets indicate the statistical error in the last significant digit.

Ω	**2**	**3**	**4**	**5**
L_{eq} (σ)	36.07	28.27	25.65	23.84
$C_{\mathrm{s,eq}}$ (mol/l)	$2.55 \cdot 10^{-2}$	$5.40 \cdot 10^{-2}$	$7.05 \cdot 10^{-2}$	$8.75 \cdot 10^{-2}$
$\langle \eta_{\mathrm{a}} \rangle$	0.130(0)	0.481(0)	0.857(1)	1.21(0)
$\langle \eta'_{\mathrm{a}} \rangle$	1.01(0)	1.08(0)	1.21(0)	1.41(0)
$\langle \eta_{\mathrm{s}} \rangle$	0.500(1)	1.74(0)	2.89(0)	3.82(1)
$\langle \eta'_{\mathrm{s}} \rangle$	1.77(0)	1.92(0)	2.92(0)	3.82(1)
Δ_{a}	0.872(0)	0.553(0)	0.291(0)	0.141(0)
Δ_{s}	0.575(1)	0.091(0)	0.006(0)	0.0003(0)
$\langle R_{\mathrm{G}} \rangle$	3.35(1)	3.32(1)	3.33(1)	3.35(1)
$\langle R_{\mathrm{H}} \rangle$	6.56(0)	6.52(0)	6.55(0)	6.58(0)
$\langle r_{1\mathrm{N}} \rangle$	5.07(0)	5.06(0)	5.15(0)	5.22(0)

Figure 8.9 (upper panel) shows the behavior of $\langle \eta_{\mathrm{s}} \rangle$ and $\langle \eta_{\mathrm{a}} \rangle$ as a function of Ω at the free-swelling equilibrium. We notice that both observables scale linearly with the number of terminal charges carried by the stars in the range of Ω values investigated; however, we cannot give a physical explanation for this empirical observation. The increase in the number of contacts with Ω is due to the increased Coulomb attraction between the oppositely charged terminal end groups, which in turn results in a higher star concentration (and, hence, in a lower mean star–star distance) at free-swelling equilibrium (see Table 8.2 and Figure 8.3).

Figure 8.9 (lower panel) shows the fraction of isolated stars and dangling arms (Δ_{s} and Δ_{a}, respectively). As expected, both quantities decreases as Ω increases. For $\Omega = 2$, more than 3 arms out of 4 ($\sim 87\%$) result in no electrostatic bonding to other chains, evidencing that we are not in presence of a network phase. We also observe a very high Δ_{a} value for $\Omega = 3$ ($\sim 55\%$). This is in agreement with the observations that in this case each stars is on average connected with only 1.74 oppositely charged stars, and each arm possesses on average only ~ 0.5 contacts (see Table 8.2). Moving to the higher values of $\Omega = 4$ and 5, the fraction of dangling chains further decreases, but it remains, interestingly, higher than zero ($\Delta_{\mathrm{a}} \simeq 0.29$ and 0.14 for $\Omega = 4$ and 5, respectively). However, for these large values of Ω almost all stars participate in forming ionic bonds, hence clusters,

and Δ_s is approximately 0.

Nevertheless, we should be careful in interpreting the number of contacts provided by $\langle \eta_a \rangle$ and $\langle \eta_s \rangle$, since Δ_a and Δ_s show non-negligible values in the most of the analysed cases, hence the number of real contacts for non-isolated stars or and non-dangling arms is much larger. Therefore we recompute the averages of $\eta_{s,A}$ and $\eta_{a,\alpha}$ on the ensemble of stars A and arms α, respectively, that are involved in at least one contact (i.e., excluding from the averages all the isolated stars and all the dangling arms); we call these new observables $\langle \eta'_s \rangle$ and $\langle \eta'_a \rangle$, respectively. The renormalized contact data are contained in Table 8.2.

For $\langle \eta'_a \rangle$ we found that the probability for a chain to bind more than one arm increases with Ω, varying from 1.01 ($\Omega = 2$) to 1.41 ($\Omega = 5$). Thus, when Ω is large, the possibility for an individual star's ionic block to get in contact with two (or even more) oppositely charged blocks is higher; the latter arms can either belong to the same star or to different ones. The fact that $\langle \eta'_a \rangle$ increases with Ω can be explained bearing in mind that increasing Ω results in: (i) an increased electrostatic attraction between the chains; (ii) a higher star concentration; and (iii) an increase in the size of the terminal charged blocks of an arm, and, hence, in an enhanced ability to accommodate two (or even more) oppositely charged chains, without the latter being in contact with each other. As for $\langle \eta'_s \rangle$, we notice that for the $\Omega = 2$ and 3 cases, non–isolated polyelectrolytes tend to bind on average roughly 2 stars, whereas for $\Omega \geq 4$ our results do not considerably differ from those calculated including also the isolated stars in the averages, and this is obviously due to the negligible fraction of isolated stars found in solution.

To gain more insight into the architecture of supramolecular aggregates in solution, and in order to investigate if the systems percolate, we now look at the size distribution of aggregates composed by stars in solution. We define a "cluster of stars" (CoS) as the set of stars fulfilling the criterion that any of them is in contact with at least one other star that belongs to such a CoS. Furthermore, we define the size $\mathscr{C}_s$ of a CoS as the number of stars that belong to it (it follows that, e.g., dimers are CoS of size $\mathscr{C}_s = 2$).

Figure 8.10 shows the probability density for a given star to belong to a CoS of size $\mathscr{C}_s$ at the free-swelling equilibrium. This corresponds to the probability density to find a CoS with a certain size $\mathscr{C}_s$ in solution weighted by the size itself and renormalized. For $\Omega = 2$ we observe that most of the stars are bonded in

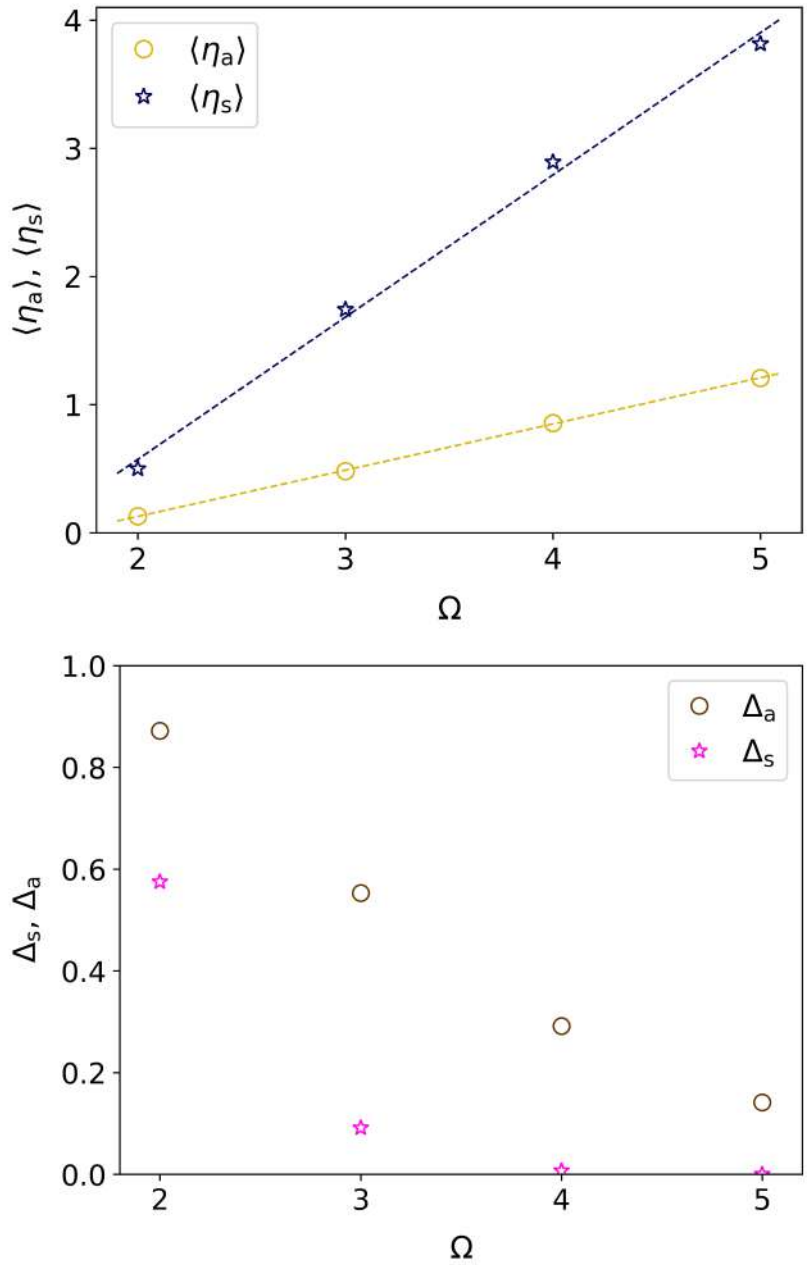

Figure 8.9: Upper panel: number of average contacts $\langle \eta_a \rangle$ and $\langle \eta_s \rangle$ as a function of Ω; lower panel: fraction of dangling arms Δ_a and isolated stars Δ_s as a function of Ω. Dashed lines in the upper panel represent linear fittings. Standard error bars are smaller than plot symbols.

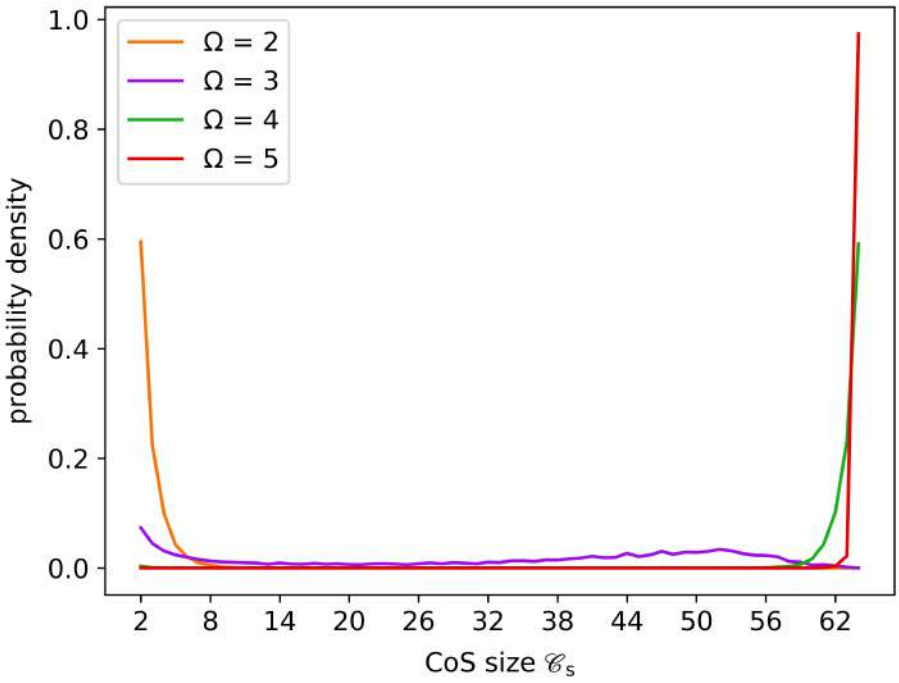

Figure 8.10: Probability density to find a given star in solution that belong to a CoS of size $\mathscr{C}_s$.

dimers, the probability to find CoS composed by a higher number of polyelectrolyte stars decreasing with $\mathscr{C}_s$, with only a few occurrences observed for $\mathscr{C}_s \geq 6$. Let us also recall that for $\Omega = 2$ roughly 58% of the stars are isolated in solution. Instead, for $\Omega = 3$ the majority of the stars belong to the same large CoS, the size of the latter varying approximately in the range $\mathscr{C}_s = 30$–64 (see the large peak which presents a maximum at $\mathscr{C}_s \simeq 53$), with non-negligible number of isolated polyelectrolyte stars (see lower panel of Figure 8.9) or belonging to very small CoS. For the systems with $\Omega = 4$ and 5, the vast majority of stars belong to a single very large CoS, with almost no isolated polyelectrolyte stars ($\Omega = 5$) or only a few ones ($\Omega = 4$). Supported by a visual inspection of the snapshots for the $\Omega = 4$ and 5 cases (see Figure 8.4, and see also the movies provided in Appendix 8.7.2), indicating that the box is completely filled by our polyelectrolyte stars, and also recalling the high number of contacts observed (see the upper panel of Figure 8.9), we are confident that we are observing a percolating gel.

In analogy with what was done for CoS, one can identify clusters formed by interacting individual arms. We define a "cluster of arms" (CoA) of size $\mathscr{C}_a$ as the set of $\mathscr{C}_a$ chains that fulfills the criterion that any of them is in contact with

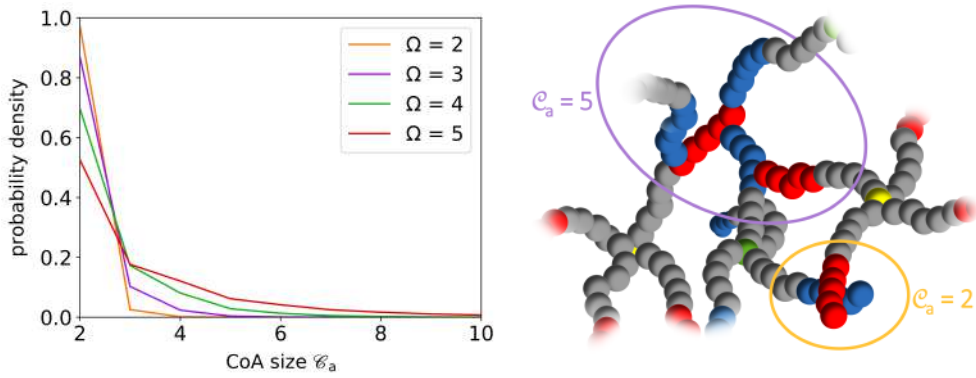

Figure 8.11: Left panel: CoA size distribution for the four Ω values. Right panel: examples of clusters formed by 5 (i.e., $\mathscr{C}_a = 5$, circled in violet) and 2 (i.e., $\mathscr{C}_a = 2$, circled in orange) arms. For these CoA, the "excess of arms" are $\mathscr{Q}_a = -1$ and 0, respectively. Notice that (i) arms that belong to the same CoA may not be directly in contact with each other, and (ii) arms that are tethered to the same central bead may belong to different CoA. The color scheme is the same as in Figure 8.4.

at least one other chain that belongs to the same CoA (definition very similar to the one used by Gârlea et al. in their work about the self-organization of soft patchy colloids [61]). Before discussing the results, let us stress here that the size of a CoA is *not* equal to the number of arms involved in a bond, and this is due to the fact that two chains belonging to the same CoA may not be in contact, but rather be far from each other; this is true especially for the systems with $\Omega = 4$ and 5, for which the charged block of each arm is "long" enough to accommodate more than one oppositely charged chain (we provide a pictorial illustration in the right panel of Figure 8.11).

The plot in Figure 8.11 shows CoA size distributions for all our simulated Ω values. When Ω is low, the vast majority of arms is involved in the formation of simple positive–negative contacts, or are dangling, whereas for higher values Ω values the CoA mean size increases, and we observe for $\Omega = 4$ and 5 that there is a non-zero probability to find CoA formed by 6 or more chains.

Since a CoA may not be charge-neutral we provide in Figure 8.12 heatmaps that show the probability density to find a CoA with a certain size $\mathscr{C}_a$ and an "excess of arms" $\mathscr{Q}_a$ in solution. We define $\mathscr{Q}_a$ as the excess charge carried by a CoA divided by Ω. At first glance, in all the panels we notice a very marked checkboard pattern; the latter is due to the fact that a CoA composed by an even (odd) number of arms must necessarily show an even (odd) $\mathscr{Q}_a$. A symmetry

shown in all the panels is that for a certain value of $\mathscr{Q}_a$ the probability density to observe $-\mathscr{Q}_a$ is almost identical (as it should be by the global symmetry of our monodispersed systems); we take this as another indication that our simulations sampled the phase space properly.

From the heatmaps we observe that, for a given size $\mathscr{C}_a$, the probability density decreases as $|\mathscr{Q}_a|$ increases. For $\Omega = 2$ (top left panel of Figure 8.12) we observe that most of the arms are involved in the simplest type of bond, that is, a positive-negative contact (hence, $\mathscr{Q}_a = 0$), with the probability to find contacts involving 3 chains being roughly two order of magnitude smaller. Nevertheless, it seems more probable to find a CoA with $\mathscr{C}_a = 3$ and $|\mathscr{Q}_a| = 1$, with respect to a neutral CoA in which 4 chains are involved. As Ω increases, we can also find larger sizes of CoA probably due to the ability of the large charge patches arms to bind to more than one oppositely charged chain. Furthermore, we observe several occurrences of CoA composed by a very large number of chains especially for $\Omega = 5$.

As a final comment, let us point out that the calculated sizes of both CoS and CoA could be slightly underestimated due to the fact that we never counted (i) two positive (or two negative) polyelectrolytes, or (ii) two stars that are in touch only via *neutral* monomers, as being in contact; although those situations seem to be very unlikely, they may occur due to thermal fluctuations especially in the case of low Ω values, or when star concentration is very high.

In the remainder of this section we investigate the mean values of the radius of gyration $\langle R_G \rangle$, the hydrodynamic radius $\langle R_H \rangle$ and the arm extension $\langle r_{1N} \rangle$ of stars as a function of Ω (see Equations 2.14, 2.15, and 2.13, respectively, for technical definitions)

As reported in Table 8.4, for isolated stars (i.e., single stars in condition of almost infinite dilution) the trends of all analyzed properties clearly show that the average size of stars increases with the number of terminal charges Ω, and this is due to the increased electrostatic repulsion between monomers. Similar trends are well known in literature for star-shaped weak polyelectrolytes. [327–329] Quite contrary, when oppositely charged stars interact with each other at free-swelling equilibrium, we observe that their size increases only slightly with Ω. At $\Omega = 3$, star polyelectrolytes even show a decrease in size with respect to the $\Omega = 2$ case, albeit the difference is very moderate; this fact is probably imputable to both, a lower species concentration and a higher number of isolated star for the

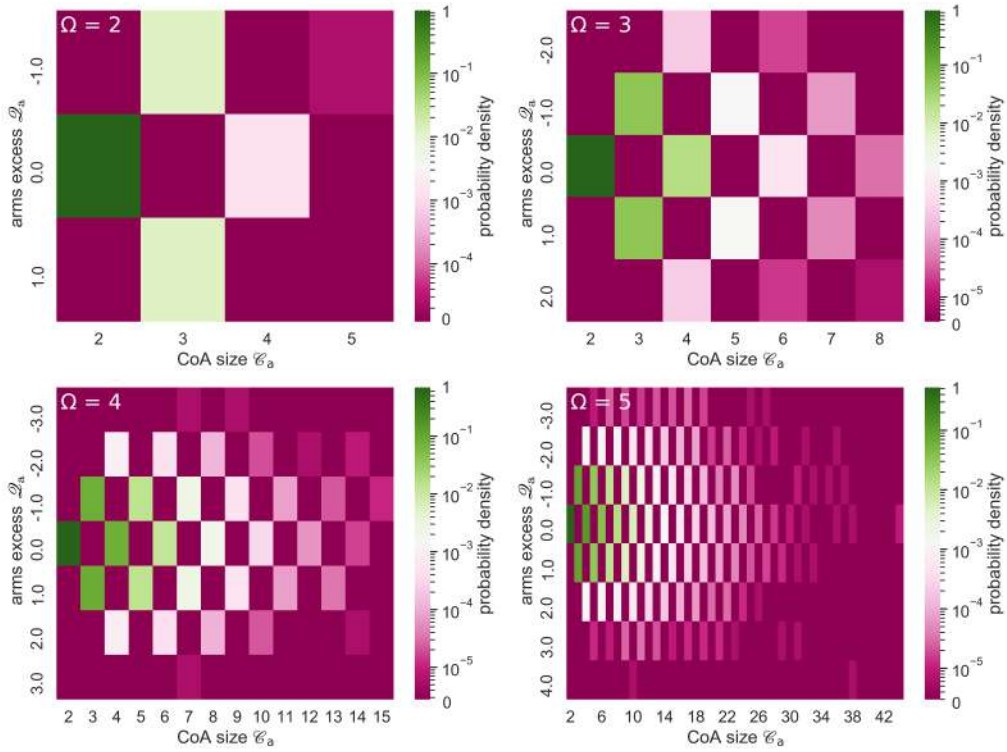

Figure 8.12: Heatmaps showing the probability density to find a CoA with a given size $\mathscr{C}_a$ and an excess of charges $\mathscr{Q}_a$ for $\Omega = 2$, 3, 4, and 5.

$\Omega = 2$ phase at equilibrium. Furthermore, $\langle R_G \rangle$, $\langle R_H \rangle$, and $\langle r_{1N} \rangle$ values at free-swelling equilibrium are about equal to those of neutral star polymers (i.e., $\Omega = 0$), demonstrating that stars at free-swelling equilibrium almost completely neutralize each other.

8.3.3 Ionic Bond Lifetimes

A visual inspection of the movies provided in Appendix 8.7.2 suggests that even the ionic bonds formed with $\Omega = 5$ are quite soft and allow for a continuous restructuring of the network. In order to gain a more quantitative understanding of the bond strengths and lifetimes we performed an analysis of the bond dynamics in time and investigated which mechanisms can lead to the breaking and subsequent reformation of such contacts.

We begin by defining a "contact time" τ_{bond} as the time a contact between two arms α and β persists in solution. The upper panel of Figure 8.13 shows the probability density $p(\tau_{bond})$ to observe a contact that breaks apart in the interval $(\tau_{bond};\ \tau_{bond}+\Delta\tau]$, with $\Delta\tau_{bond} = 0.05$. Contrary to the exponential decay expected, we notice that τ_{bond} displays a maximum around $\tau_{bond} \simeq 0.3$ for any Ω. As previously discussed by Bunker and Hase [330], this is a consequence of the "initial state selection" that derives from the orientation of the relative linear momentum for the two arms that have just come closer to be identified as a contact. Dissociation of the newly formed bond may, in fact, require some time to partially invert their relative velocity so that they can "wander back" to a distance at which the bond can be considered broken. Most likely, a properly oriented collision between the two approaching arms is needed to trigger such partial inversion, so that some degree of ballistic (hence, non–statistical) behavior may be present during the initial stages of the process. This notwithstanding, mean lifetimes ($\bar{\tau}_{calc} = \int_0^\infty \tau_{bond} p(\tau_{bond}) d\tau_{bond}$) have been computed with the shown $p(\tau_{bond})$, and these are 0.40, 0.50, 0.60, and 0.68 for $\Omega = 2$, 3, 4, and 5, respectively (see Table 8.3 for a summary). As one could have expected, the mean lifetime increase with Ω.

A mono-molecular event is formally described by the equation $\alpha\cdots\beta \longrightarrow \alpha + \beta$, where "$\cdots$" denotes a contact between two arms. As τ_{bond} deviates from the statistical behavior expected from such an event, also the fraction of surviving

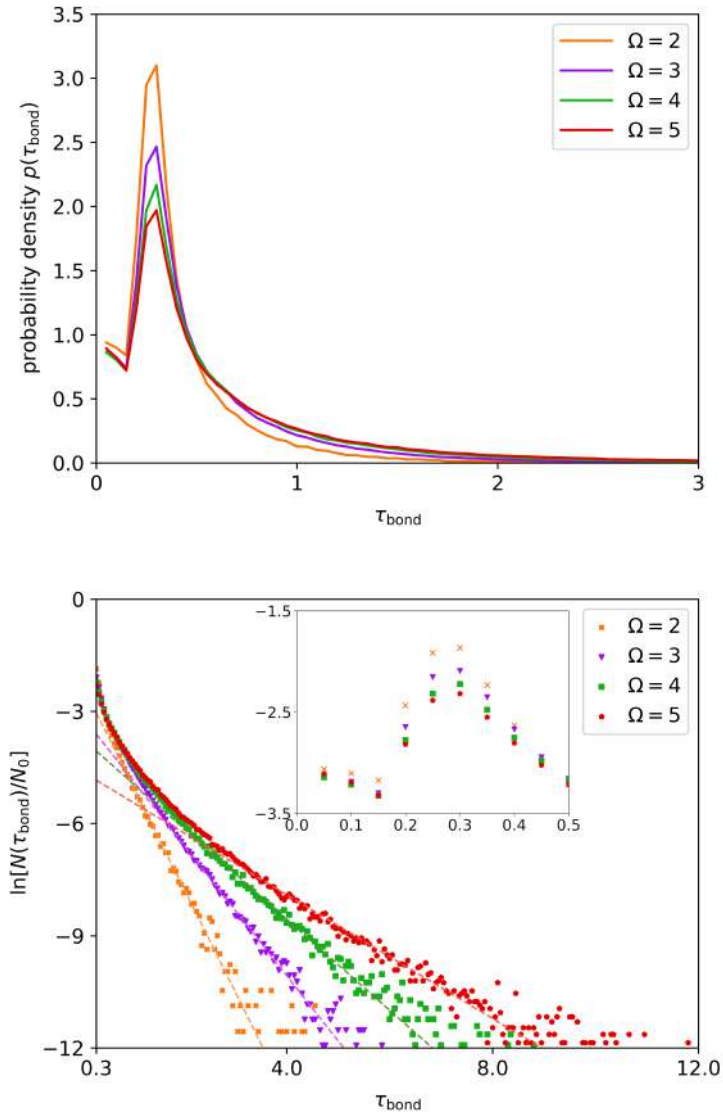

Figure 8.13: Upper panel: probability density $p(\tau_{\text{bond}})$ to observe a contact persisting in solution for a time τ_{bond}. Lower panel: natural logarithm of $N(\tau_{\text{bond}})/N_0$ versus the contact time τ_{bond}; here, dashed lines represent the linear fittings of the statistical part. The inset shows the short time behavior of $\ln[N(\tau_{\text{bond}})/N_0]$ versus τ_{bond}. τ_{bond} is in system time units.

contacts ($N(\tau_{bond})/N_0$) versus time should deviate from the exponential decay law $e^{-\tau_{bond}k_1} = e^{-\tau_{bond}/\tau_1}$ that are typical for such processes, where k_1 and τ_1 are the first–order rate constant and the corresponding mean lifetime. To prove this point we investigated the short time behavior of $N(\tau_{bond})/N_0$ (see the inset in the lower panel of Figure 8.13). At short times the lack of linearity displayed by $\ln[N(\tau_{bond})/N_0]$ shows a faster decay, indicating the presence of an intrinsically non–statistical (as in Rice–Ramsperger-Kassel–Marcus theory [331,332]) behavior for the dissociation process. This is characterized by an elevate population of fast dissociating states that are generated right after contact formation, leading to a high number of short time dissociation events. At longer times, $N(\tau_{bond})/N_0$ instead appears to decay exponentially, so that fitting the long time part of the scatter plot allowed us to compute the statistically derived mean lifetimes τ_1, which are 0.36, 0.57, 0.82, and 1.20 for $\Omega = 2$, 3, 4, and 5, respectively. As one would have expected, $\tau_1 > \bar{\tau}_{calc}$ for $\Omega \geq 3$, as the fitting process eliminates the majority of fast dissociation events. The fact that such inequality is not satisfied when $\Omega = 2$ is simply due to the limited sample of events collected and the related inaccuracy of the long time distribution. Also, the increase of the ratio $\tau_1/\bar{\tau}_{calc}$ upon increasing Ω seems to support the idea that the collision between two arms forming a contact are the cause of the high population of fast dissociating dimers. In fact, it is well known that it becomes increasingly less likely for a colliding pair to redistribute into internal modes a sufficiently large fraction of their relative kinetic energy so to allow the formation of a meta-stable dimer the higher the kinetic energy is [333]. Obviously, the latter increases upon increasing Ω due to stronger Coulomb interactions.

In order to better analyze the details of the discussed non–statistical effects and to investigate which other mechanism may be involved in restructuring the network of electrostatic bonds, we computed the relative frequency of three different mechanisms by means of which an arm α can loose a contact (that lasted for a time τ_{bond}) with an oppositely charged arm β, and switch the latter with a new arm γ after some time τ_{lag}. These three mechanisms are illustrated in Figure 8.14, and they are:

"intermittent bond" **($\mathcal{I}$):** a contact temporarily breaks reforming after a time τ_{lag} has elapsed (see Figure 8.14 (a))

Table 8.3: Contact times (in system time units) and relative frequencies for the three mechanisms ($\mathcal{I}$, $\mathcal{S}_{\rm ant}$, $\mathcal{S}_{\rm pos}$) and the non–classifiable ones ($\mathcal{O}$). $E_{\rm tot}$ is the relative total number of events observed calculated with respect to the $\Omega = 2$ case. The numbers in brackets indicate the statistical error on the last significant digit.

Ω	**2**	**3**	**4**	**5**
$\bar{\tau}_{\rm calc}$	0.401(0)	0.504(1)	0.601(1)	0.676(0)
τ_1	0.362(1)	0.573(9)	0.823(9)	1.20(1)
$\mathcal{I}$	79.7(1)%	68.3(1)%	52.3(1)%	41.1(1)%
$\mathcal{S}_{\rm ant}$	1.3(0)%	5.5(0)%	10.2(1)%	12.1(0)%
$\mathcal{S}_{\rm pos}$	17.1(1)%	17.9(1)%	20.6(0)%	21.2(0)%
$\mathcal{O}$	1.9(0)%	8.2(1)%	16.9(0)%	24.8(1)%
$E_{\rm tot}$	1.00	2.91	4.34	5.44

e.g., $\alpha\cdots\beta \underset{\tau_{\rm lag}}{\overset{\tau_{\rm bond}}{\rightleftharpoons}} \alpha + \beta$.

"anticipated partner switch" **($\mathcal{S}_{\rm ant}$):** a negative (positive) arm γ binds to an existing contact causing the detachment of another negative (positive) chain (see Figure 8.14 (b))
e.g., $\gamma + \alpha\cdots\beta \xrightarrow{\tau_{\rm lag}} \gamma\cdots\alpha\cdots\beta \xrightarrow{\tau_{\rm bond}} \gamma\cdots\alpha + \beta$.

"postponed partner switch" **($\mathcal{S}_{\rm pos}$):** an arm α loses a contact and then forms a new bond with a *different* chain after a time $\tau_{\rm lag}$ (see Figure 8.14 (c))
e.g., $\gamma + \alpha\cdots\beta \xrightarrow{\tau_{\rm bond}} \gamma + \alpha + \beta \xrightarrow{\tau_{\rm lag}} \gamma\cdots\alpha + \beta$.

Additionally, we classify all those mechanisms that cannot be included in the mentioned categories as "non-classifiable mechanisms" ($\mathcal{O}$). A more detailed discussion on the three mechanisms and the protocols implemented to categorize dissociation events is provided in Appendix 8.6.

Figure 8.15 and Table 8.3 show the results of our analysis. In the latter, we also report the relative frequency of events observed, $E_{\rm tot}$, with respect to the $\Omega = 2$ case. We notice that $E_{\rm tot}$ increases with Ω, which is probably related to the increase of the equilibrium concentration with Ω. For $\Omega = 2$, the vast majority of events ($\sim 80\%$, see Table 8.3) are classified as "intermittent contacts", which is probably due to the fact that stars are assembled in dimers or small CoS, so that mechanisms involving the exchange of arms are relatively rare, whereas temporary detachment due to thermal fluctuations are favored by the relatively low Coulomb attraction between oppositely charged chains. Roughly $\sim 17\%$ of

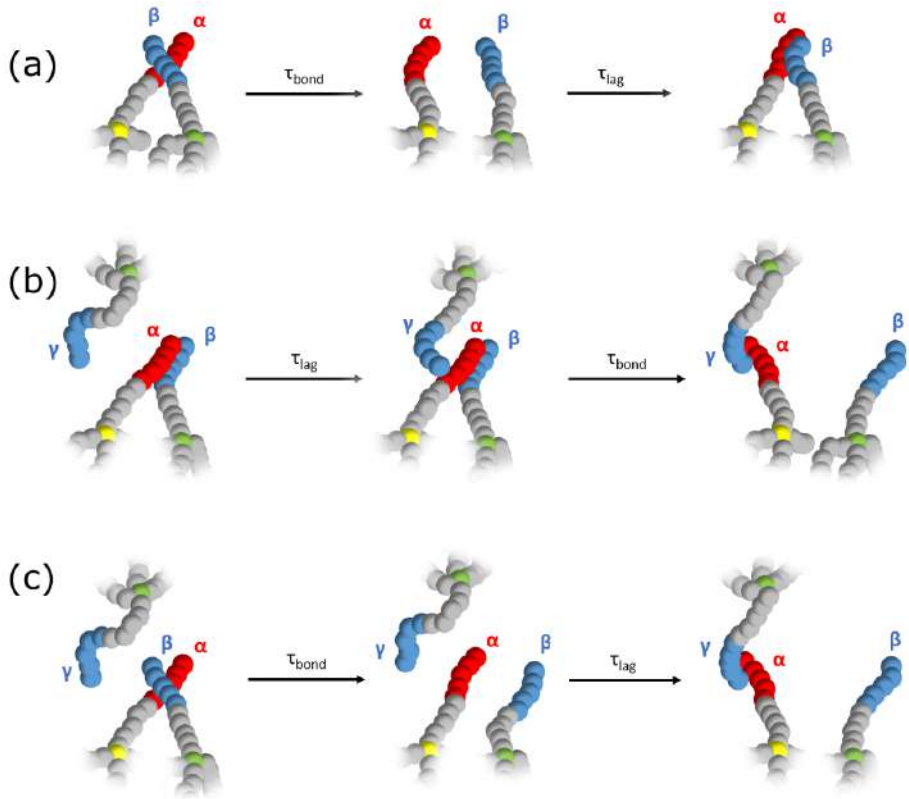

Figure 8.14: Pictorial description of the three mechanisms investigated: (a) $\mathcal{I}$; (b) $\mathcal{S}_{\text{ant}}$; (c) $\mathcal{S}_{\text{pos}}$.

the events result are "postponed partner switches", whereas the fraction of $\mathcal{S}_{\text{ant}}$ and $\mathcal{O}$ mechanisms results negligible.

As Ω increases, we observe an enhancement in the fraction of $\mathcal{S}_{\text{pos}}$, $\mathcal{S}_{\text{ant}}$, and $\mathcal{O}$ mechanisms, a clear evidence of the possibility for the network bonds to restructure themselves. Again, the increase in the number of $\mathcal{S}_{\text{pos}}$ may be rationalized by recalling that the equilibrium concentration increases with Ω; in fact, the denser the solution gets, the more likely it becomes for a positively (negatively) charged arm to replace a dissociating positive (negative) arm of a vicinal contact. As for the $\mathcal{S}_{\text{ant}}$ mechanism, also the increasing length of charged segments may play a role in increasing its frequency. The longer the charged block is, the higher is the probability for an arm α to "accommodate" more than one contact with oppositely charged segments (β, γ, etc.). This we attribute to the possibility for the charged portion of β and γ arms to stay further away from each other while being coordinated to the same α arm. Importantly, the 1 : 2 positive–negative (or *vice versa*) coordination mode is also expected to facilitate the detachment of, e.g., the β arm, as its binding energy with α ought to be lower due to the repulsive Coulomb interaction with γ.

As for the non–statistical behavior previously discussed, Figure 8.15 presents the plots of $\ln[N(\tau_{\text{bond}})/N_0]$ versus τ_{bond} for all Ω values and the three discussed mechanism. From these, one notices that fast dissociation events arise mainly as a consequence of the $\mathcal{S}_{\text{pos}}$ and $\mathcal{I}$ mechanisms, the latter invariably being the most likely whereas the former presenting a more marked fractional deviation from the statistical behaviour. Juxtaposing these results with similar ones concerning τ_{lag} (see Figure 8.16), it emerges that it takes more time for two free (e.g., α and β) arms to form a contact from a dissociated state than breaking an electrostatic bond already formed. Given the unhindered nature of the process forming a contact from dangling arms, we believe the previously discussed ballistic dynamics to be a robust justification for the non–statistical behavior evidenced by our data.

Finally, we mention that the increase in the fraction of $\mathcal{O}$–events upon increasing Ω is mainly due to an increase in the number of events that present multiple approaches or detachments taking place contemporary within the time window represented by our time resolution ($\Delta\tau = 0.05$). This is well supported by Figure 8.17, which shows the dependency of this fraction on $\Delta\tau_{\text{bond}}$ itself for

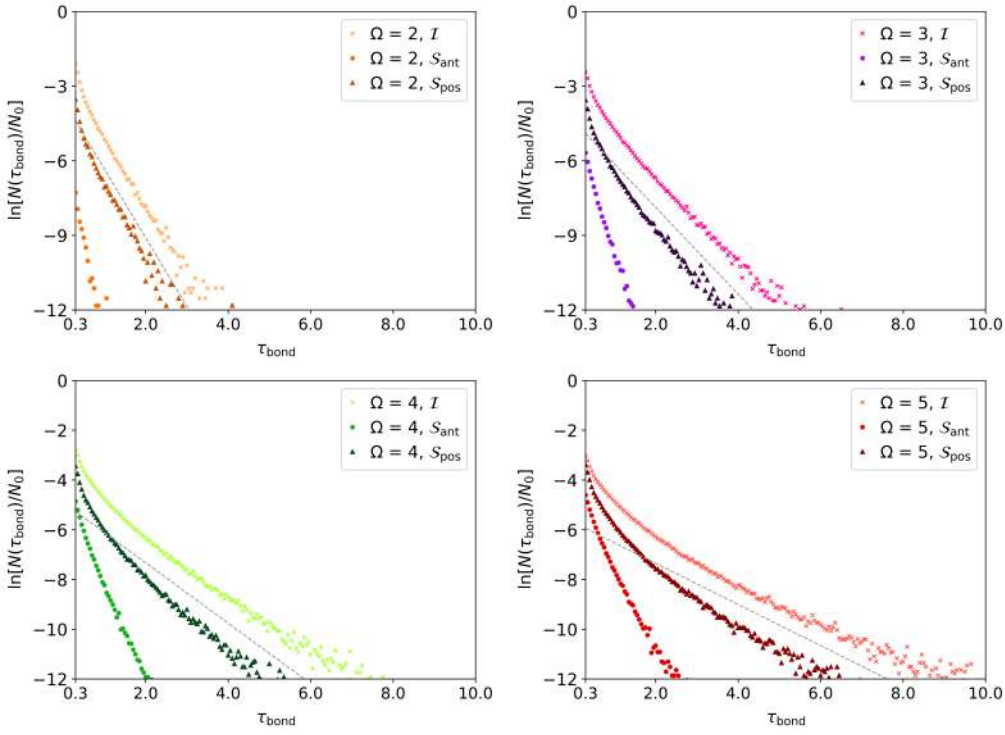

Figure 8.15: Natural logarithm of $N(\tau_{\text{bond}})/N_0$ versus τ_{bond} (system time units) for the three mechanisms and the four Ω values. We also report the linear fits (dashed grey lines) calculated in Figure 8.13 for a direct comparison.

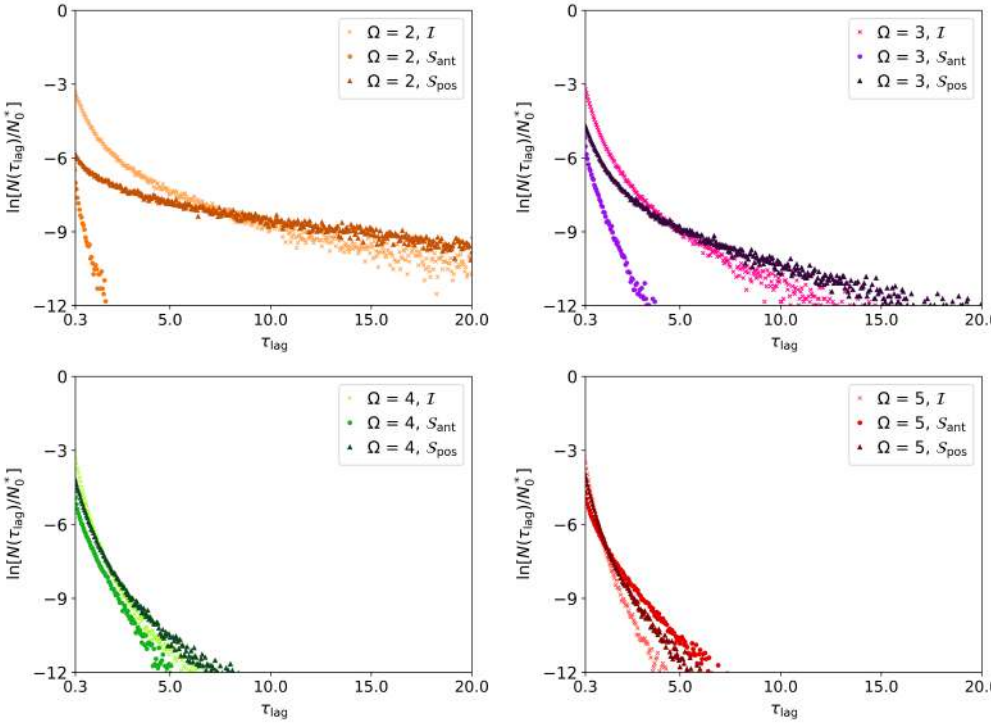

Figure 8.16: Natural logarithm of $N(\tau_{\text{bond}})/N_0^*$ versus τ_{lag} (system time units) for the three mechanisms at the four Ω values. N_0^* is the number of contacts who have just dissociated.

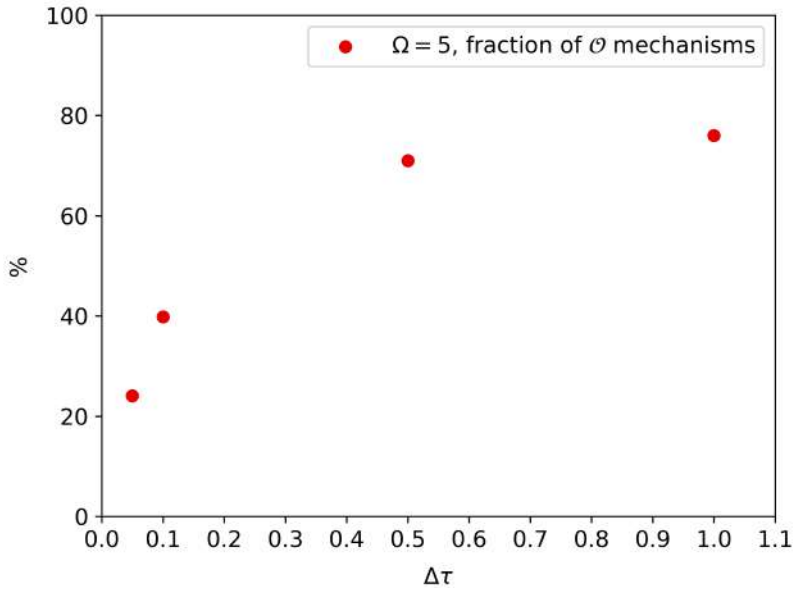

Figure 8.17: Fraction of non-classifiable mechanisms ($\mathcal{O}$) as a function of the time resolution $\Delta\tau$ for the $\Omega = 5$ case.

the case $\Omega = 5$. Obviously, if $\Delta\tau$ was infinitely small, only single dissociation or association events would be recorded.

To conclude this section, in Figure 8.18 we present the mean-squared displacement (MSD) calculated for star nuclei (top panel), and for neutral and charged monomers (middle and bottom panel, respectively) as a function of Ω. The nuclei MSD were evaluated as:

$$\langle \Delta r^2(t) \rangle = \frac{1}{N_s} \left\langle \sum_{n}^{N_s} [\mathbf{r}_n(t) - \mathbf{r}_n(0)]^2 \right\rangle, \tag{8.1}$$

where $\mathbf{r}_n$ is the position vector of the n-th nucleus. From Figure 8.18 we can observe that, as expected, the diffusion decreases with the number of terminal charges Ω; nevertheless, even when $\Omega = 5$ (the worst case, since both interaction strength and concentration are very high) stars are able to reach a diffusive regime (roughly after a time t = 500–800), hence we are not in an arrested gel. Finally, by comparing the time scales related to the star diffusion across the network phase (Figure 8.18) and contact dynamics (Figures 8.13 and 8.14) we observe that the latter is much faster than the former by roughly 3 orders of magnitude.

This suggests that most of the contact exchange events detected may take part between neighboring stars due to thermal fluctuations.

8.4 Conclusions

We performed a Langevin molecular dynamics study in order to investigate the possibility to create a supramolecular network by mixing equal amounts of oppositely charged di-block star-shaped polyelectrolytes under salt free conditions. Our polyelectrolyte stars consisted of four polymeric bead-spring chains tethered to a central common bead and carrying a tunable number Ω of (positively or negatively) charged monomers at their ends, using a polyelectrolyte primitive model in an implicit solvent [334].

We investigated systems with Ω values from 1 to 5 at different concentrations and determined from the P-V curves the equilibrium concentration with respect to a pure water phase. Our results yielded equilibrium concentrations for $\Omega \geq 2$ (see Figure 8.2 and 8.4). The reproducibility of our results for three different simulations protocols (see Section 8.2.2 and Figure 8.5), and the fact that also a solution of pre-thermalized dimers has relaxed (Figure 8.6) demonstrate that our simulations yield true equilibrium structures.

The observed phases at free–swelling equilibrium have been characterized via many structural parameters (see Table 8.2). We found that the number of contacts increases with Ω, with a non–zero probability to observe contacts involving more than two oppositely charged arms for $\Omega \geq 4$. Conversely, the fraction of dangling arms decreases with the number of terminal charges, but it remains interestingly non–zero even when $\Omega = 5$, for which we observe that $\sim 14\%$ of the arms are not involved in any ionic bond.

From an analysis of the cluster of stars (CoS) in solution we found that for the $\Omega = 2$ case only dimers and small oligomers can form, whereas for $\Omega = 4$ and 5 all stars are part of a single macro-aggregate (see Figure 8.10), the latter being identified as a percolating network spanning the whole box, i.e. a gel–like phase, after a visual inspection of snapshots and trajectory movies provided, respectively, in Appendices 8.7.1 and 8.7.2. The $\Omega = 3$ case turned out to be an intermediate one, in which most of the stars belong to a main CoS (the latter fluctuating in size), with a non–negligible number of stars being isolated in solution or belonging

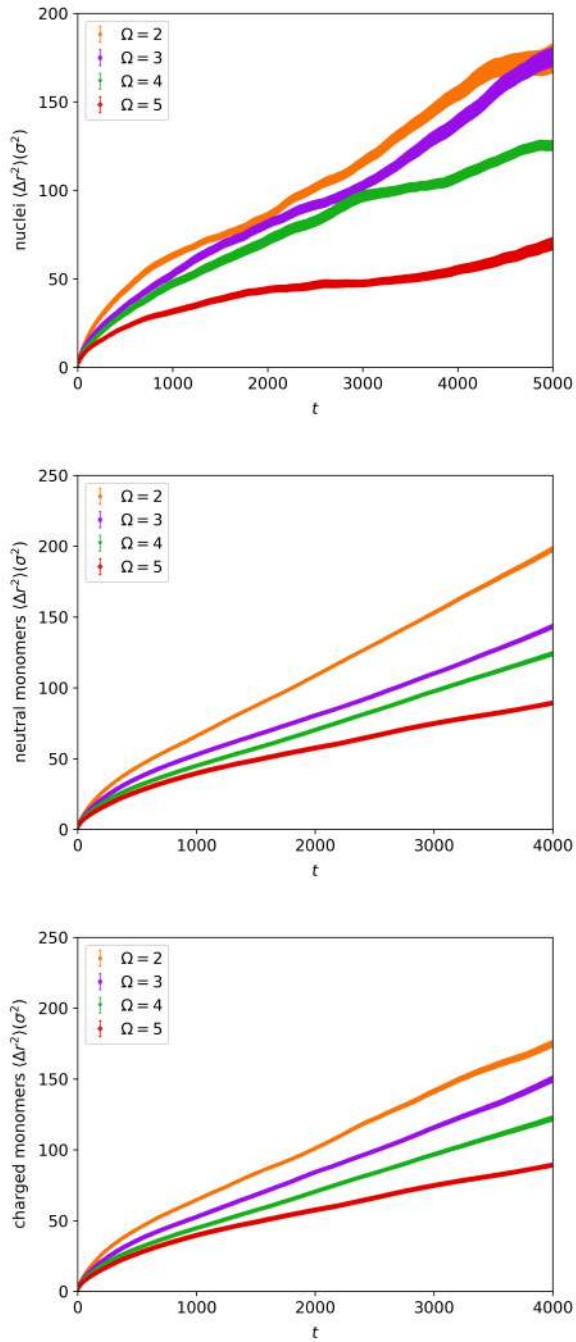

Figure 8.18: MSD for nuclei (top panel), neutral monomers (middle panel), and charged monomers (bottom panel).

to small oligomers or secondary CoS. An analogous analysis has been performed for clusters composed by individual arms (CoA), revealing that also in this case their size increases with Ω (see Figure 8.11). Furthermore, we found some CoA with an excess charge, whose probability of occurrence increases with Ω as well. Overall, the ionic cross-links structure is far from being trivial even for the case of equal charged terminal bonds. The simple picture of having mostly saturated ionic bonds is definitely not applicable.

In order to gain more insight in the dynamical processes of forming and dissolving ionic bonds, we analyzed the contact time of such bonds as function of Ω. As expected, the mean lifetime increases with the latter. Nevertheless, we found strong deviations from the expected statistical first–order dissociation kinetics, the latter underestimating the frequency of fast dissociation events for almost all cases (see Table 8.3). In this respect, the detailed analysis of the trajectories suggested that the latter finding is related to the ballistic nature of a large fraction of dissociation events. Moreover, we described various mechanisms leading to contact formations and ruptures, observing a non–zero probability (even for low Ω values) for an arm involved in a bond to be replaced by another chain with the same charge, a finding that clearly opens up the possibility for the network to restructure itself in time. The restructuring possibilities of the electrostatic bonds could lead to a reduced mechanical strength and to a low shear modulus. A more detailed investigation of the mechanical behavior of the star gels is left for future investigations.

8.5 Appendix: properties of single stars

In order to investigate single star conformational properties as a function of the number of their terminal charges, we simulated a single star in condition of very high dilution for each Ω value*. In table 8.4 we report the average radius of gyration $\langle R_G \rangle$ (Equation 2.14), the average hydrodynamic radius $\langle R_H \rangle$ (Equation 2.15), and the average arm extension $\langle r_{1N} \rangle$ of stars as a function of Ω (Equation 2.13). As expected, the value of all properties increases with the number of terminal charges carried by the polyelectrolyte.

*In practice, for each Ω value we simulated in a very large box a pair of oppositely charged stars kept separated one to each other by fixing their central beads ad a distance larger then

Table 8.4: Single star conformational properties as a function of Ω. The neutral case (Ω = 0) is also shown for comparison. The numbers in brackets indicate the statistical error in the last significant digit.

Ω	**0**	**1**	**2**	**3**	**4**	**5**
$\langle R_G \rangle$ (σ)	3.30(1)	3.34(1)	3.51(1)	3.69(1)	4.01(1)	4.24(1)
$\langle R_H \rangle$ (σ)	6.54(1)	6.58(1)	6.82(1)	7.06(1)	7.42(1)	7.75(1)
$\langle d_a \rangle$ (σ)	5.20(3)	5.10(3)	5.33(3)	5.84(4)	6.12(3)	6.76(3)

8.6 Appendix: methods implemented in determining the number of contacts per star/arm and the mechanisms lying under ionic bonds exchange dynamics

In this section we discuss in detail the computational protocol implemented to compute τ and to detect the ionic bond dissociation/formation mechanisms discussed in the main text.

At each time $t = t_0$, we define a "contact matrix" $\mathbb{H}_a(t_0)$ as

$$\mathbb{H}_a(t_0) = \begin{bmatrix} h_{11} & \dots & h_{1n} \\ h_{21} & \dots & h_{2n} \\ \dots & \dots & \dots \\ h_{m1} & \dots & h_{mn} \end{bmatrix} \tag{8.2}$$

Each element $h_{\alpha\beta}$ (with $\alpha = 1, 2, \dots, m$, where m is the total number of positively charged chains; and $\beta = 1, 2, \dots, n$, where n is the total number of negatively charged chains) is a binary variable that is equal to 1 if the two chains α and β are in contact with each other, and it is 0 otherwise. Computing $\mathbb{H}_a(t_0 = 0)$ and repeating process at regular time intervals $\Delta\tau$ allow us to build a 3D matrix $\mathbb{H}_a(t, \alpha, \beta) = \mathbb{H}_a$ (with size $\frac{t_{sim}}{\Delta\tau} \times m \times n$) that contains all the information about the time evolution of all the contacts. Thus, from $\mathbb{H}_a$ it is possible to compute the following structural properties at the time t_0:

100σ.

- the number of contact for a given arm α:

$$\eta_{\mathrm{a},\alpha}(t_0) = \sum_{\beta=1}^{n} h_{t_0\alpha\beta}. \tag{8.3}$$

- the fraction of dangling arms at a certain time t_0,

$$\Delta_{\mathrm{a}}(t_0) = \frac{1}{n+m}\left[\sum_{\alpha=1}^{m}\delta\left(\sum_{\beta=1}^{n} h_{t_0\alpha\beta}\right) + \sum_{\beta=1}^{n}\delta\left(\sum_{\alpha=1}^{m} h_{t_0\alpha\beta}\right)\right], \tag{8.4}$$

  where $\delta(x)$ is a function that returns 1 if $x = 0$, and 0 otherwise. Hence, $\Delta_{\mathrm{a}}(t_0)$ corresponds to the number of null rows plus the number of null columns of $\mathbb{H}_{\mathrm{a}}(t_0)$;

It is evident that is possible to build a similar matrix in order to analyse contacts between stars, i.e. $\mathbb{H}_{\mathrm{s}}(t, A, B) = \mathbb{H}_{\mathrm{s}}$, where $A = 1, 2, \ldots, M$ and $B = 1, 2, \ldots, N$; here, M and N are the total number of positive and negative stars, respectively). Thus, it immediately follows that from $\mathbb{H}_{\mathrm{s}}$ it is possible to calculate the number of isolated stars is solutions (Δ_{s}) and the number of contact for a given star A ($\eta_{\mathrm{s},A}$) in a similar way to what is done for the analogous properties of arms.

We also define the matrix $\mathbb{J}_{\mathrm{a}}$ at the time $t = t_0 + \Delta\tau$ as

$$\mathbb{J}_{\mathrm{a}}(t_0 + \Delta\tau) = \mathbb{H}_{\mathrm{a}}(t_0 + \Delta\tau) - \mathbb{H}_{\mathrm{a}}(t_0) = \begin{bmatrix} j_{11} & \ldots & j_{1n} \\ j_{21} & \ldots & j_{2n} \\ \ldots & \ldots & \ldots \\ j_{m1} & \ldots & j_{mn} \end{bmatrix} \tag{8.5}$$

In this case, $j_{\alpha\beta}$ is a variable that can assume three different values: $j_{\alpha\beta} = 1$ if a contact between two arms α and β is formed in the time interval $(t_0, t_0 - \Delta\tau]$; $j_{\alpha\beta} = -1$ if a pre–existing contact between two arms α and β broke in the interval $(t_0, t_0 - \Delta\tau]$; and $j_{\alpha\beta} = 0$ otherwise. For two generic ionically bonded chains α and β, the contact time τ_{bond} can be easily computed from $\mathbb{J}_{\mathrm{a}}$ identifying the time-frames at which the contact forms (t_{f}, $j_{t_{\mathrm{f}}\alpha\beta} = 1$) and breaks ($t_{\mathrm{b}}$, $j_{t_{\mathrm{b}}\alpha\beta} = -1$), so that $\tau_{\mathrm{bond}} = t_{\mathrm{b}} - t_{\mathrm{f}}$. From $\mathbb{J}_{\mathrm{a}}$ one can easily define, for a certain time $t = t_0$ and for a given arm α, the set of other chains in contact with α, the set of contacts formed by α in the time interval $(t_0, t_0 + \Delta\tau]$, and the set of contacts lost by

α in the interval $(t_0, t_0 - \Delta\tau]$. We call these sets $\mathbb{L}_\mathrm{f}(t_0, \alpha)$, $\mathbb{L}_\mathrm{b}(t_0, \alpha)$, $\mathbb{L}_\mathrm{c}(t_0, \alpha)$, respectively.

The mechanisms that could lead to the network restructuring are: (a) "intermittent bond", $\mathcal{I}$; (b) "anticipated partner switch", $\mathcal{S}_\mathrm{ant}$; and (c) "postponed partner switch", $\mathcal{S}_\mathrm{pos}$. Here we discuss more in detail these three mechanisms and the rules implemented to categorize the contact formation–dissociation events.

8.6.1 "Intermittent contact" ($\mathcal{I}$)

We classify as "intermittent" a contact that, after lasting in solution for a time $\tau = \tau_\mathrm{bond}$, it temporally breaks and then it reforms after a time τ_lag (see Figure 8.14 (a)). It can be described by the following equation:

$$\alpha \cdots \beta \underset{\tau_\mathrm{lag}}{\overset{\tau_\mathrm{bond}}{\rightleftharpoons}} \alpha + \beta. \tag{8.6}$$

Thus, it consists of three sub–events: (i) contact formation at time t_f; (ii) contact breaking at time t_b; and (iii) contact re–formation at time t'_f. It follows that $\tau_\mathrm{bond} = t_\mathrm{b} - t_\mathrm{f}$ and $\tau_\mathrm{bond} = t'_\mathrm{f} - t_\mathrm{b}$. The set of rules implemented to detect this type of event is:

1) $t_\mathrm{f} < t_\mathrm{b} < t'_\mathrm{f}$;

2) $\#\mathbb{L}_\mathrm{f}(t, \alpha) = 1$, $\#\mathbb{L}_\mathrm{b}(t, \alpha) = 0$ for $t = t_\mathrm{f}$, t'_f ("#" denotes the cardinality of the set);

3) $\#\mathbb{L}_\mathrm{f}(t, \alpha) = 0$, $\#\mathbb{L}_\mathrm{b}(t, \alpha) = 1$ for $t = t_\mathrm{b}$;

4) $\sum_{t=t_\mathrm{f}+\Delta\tau}^{t_\mathrm{b}-\Delta\tau} \#\mathbb{L}_\mathrm{f}(t, \alpha) - \sum_{t=t_\mathrm{f}+\Delta\tau}^{t_\mathrm{b}-\Delta\tau} \#\mathbb{L}_\mathrm{b}(t, \alpha) = 0$;

5) $\sum_{t=t_\mathrm{b}+\Delta\tau}^{t'_\mathrm{f}-\Delta\tau} \#\mathbb{L}_\mathrm{f}(t, \alpha) = 0$;

6) $\mathbb{L}_\mathrm{f}(t_\mathrm{f}, \alpha) = \mathbb{L}_\mathrm{f}(t'_\mathrm{f}, \alpha)$;

In other words, item 1) establishes the time sequence of the sub–events; items 2) and 3) states that no other contact formations/ruptures are allowed to taking place at times t_f, t'_f, and t_b); item 4) states that no net gain/lost of contacts is allowed in the time interval $(t_\mathrm{f}, t_\mathrm{b})$; item 5) states that no other contacts can be formed between t_b and t'_f; finally, item 6) checks that α get in touch with the same chain β at t_f and t'_f.

8.6.2 "Postponed partner switch" ($\mathcal{S}_{\rm pos}$)

We classify as "postponed partner switch" an event that is described by the following equation:

$$\gamma + \alpha\cdots\beta \xrightarrow{\tau_{\rm bond}} \gamma + \alpha + \beta \xrightarrow{\tau_{\rm lag}} \gamma\cdots\alpha + \beta. \tag{8.7}$$

Hence, it consists in three sub–events: (i) $\alpha\cdots\beta$ contact formation at time $t_{\rm f}$; (ii) $\alpha\cdots\beta$ contact breaking at time $t_{\rm b}$; and (iii) $\alpha\cdots\gamma$ contact formation at time $t'_{\rm f}$, with $\beta \neq \gamma$ see Figure 8.14 (c)) Also in this case, $\tau_{\rm bond} = t_{\rm b} - t_{\rm f}$ and $\tau_{\rm lag} = t'_{\rm f} - t_{\rm b}$. The set of rules describing the "postponed partner switch" is the same as those that describe an "intermittent contact", with the exception of item 6) that reads:

6) $\mathbb{L}_{\rm f}(t_{\rm f}, \alpha) \neq \mathbb{L}_{\rm f}(t'_{\rm f}, \alpha)$.

8.6.3 "Anticipated partner switch" ($\mathcal{S}_{\rm pos}$)

Finally, we classify as "anticipated partner switch" those events in which the dissociation of a contact $\alpha\cdots\beta$ is preceded by the formation of a contact $\alpha\cdots\gamma$ (see Figure 8.14 (b)); that is

$$\gamma + \alpha\cdots\beta \xrightarrow{\tau_{\rm lag}} \gamma\cdots\alpha\cdots\beta \xrightarrow{\tau_{\rm bond}} \gamma\cdots\alpha + \beta. \tag{8.8}$$

Once again, the event consists in three sub-events: (i) $\alpha\cdots\beta$ contact formation at time $t_{\rm f}$; (ii) $\alpha\cdots\gamma$ contact formation at time $t'_{\rm f}$; and (iii) $\alpha\cdots\gamma$ contact breaking at time $t'_{\rm f}$. Notice that in this case $t'_{\rm f} < t_{\rm b}$, so that $\tau_{\rm lag} = t'_{\rm f} - t_{\rm f}$ and $\tau_{\rm bond} = t_{\rm b} - t'_{\rm f}$. Thus, the rules implemented to identify these events are:

1) $t_{\rm f} < t'_{\rm f} < t_{\rm b}$;

2) $\#\mathbb{L}_{\rm f}(t, \alpha) = 1$, $\#\mathbb{L}_{\rm b}(t, \alpha) = 0$ for $t = t_{\rm f}, t'_{\rm f}$;

3) $\#\mathbb{L}_{\rm f}(t, \alpha) = 0$, $\#\mathbb{L}_{\rm b}(t, \alpha) = 1$ for $t = t_{\rm b}$;

4) $\sum_{t=t_{\rm f}+1}^{t'_{\rm f}-1} \#\mathbb{L}_{\rm f}(t, \alpha) = \sum_{t=t'_{\rm f}+1}^{t_{\rm b}-1} \#\mathbb{L}_{\rm f}(t, \alpha) = 0$;

We classify all those mechanisms that cannot be included in those three categories as "other mechanisms" ($\mathcal{O}$). Let us stress that $\Delta\tau$ plays a fundamental

role in classifying the mechanisms due to the fact that the algorithm is not able to discern the temporal order of two (or more) sub-events that take place in the same time interval $(t_0, t + \Delta\tau]$ (see Figure 8.17).

8.7 Appendix: trajectory snapshots and movies

8.7.1 Trajectory snapshots

Here we present a selection of trajectory snapshots for systems different number of terminal charges Ω taken at various box side lengths L. Snapshots taken at the free swelling equilibrium are labeled "$P = 0$". The diameter of all monomers has been reduced by roughly one half with respect to the real one in order to improve pictures "readability".

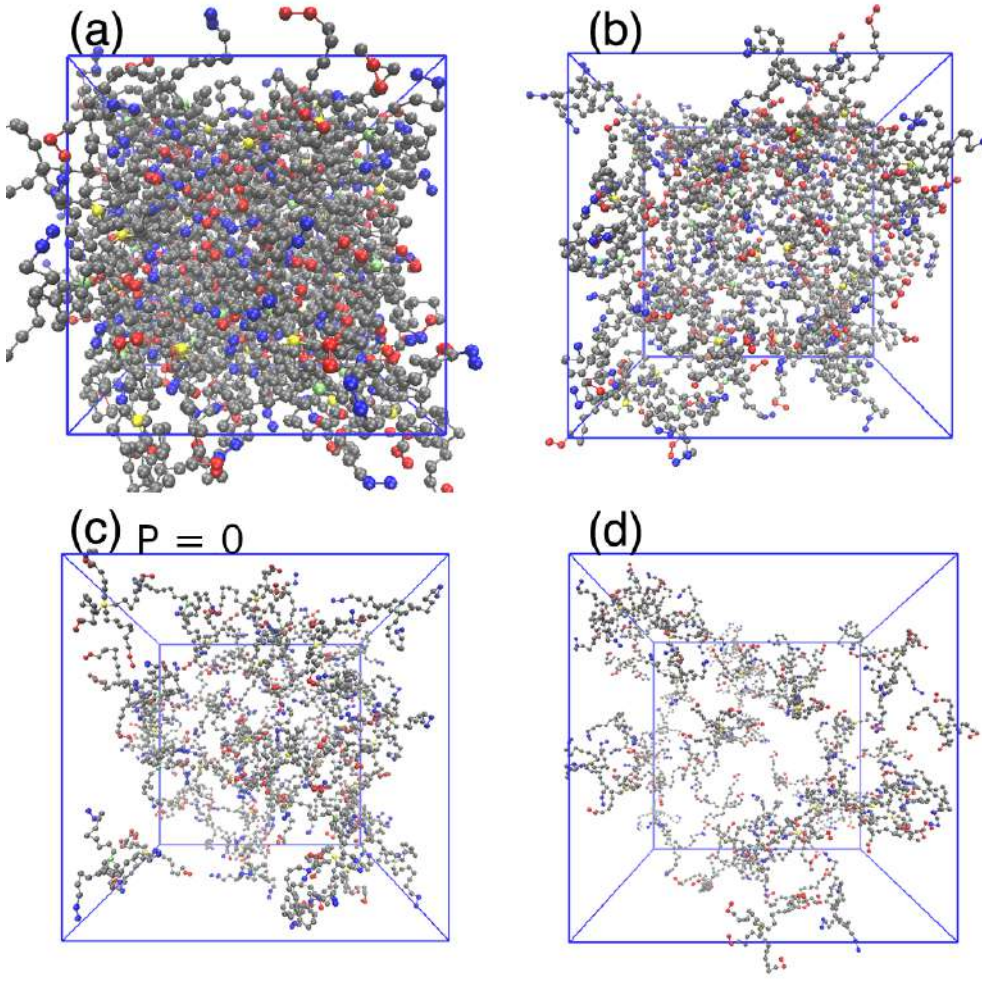

Figure 8.19: Trajectory snapshots for $\Omega = 2$ taken at different box length values: (a) $L = 16\sigma$, $L/L_{\max} = 0.36$; (b) $L = 26\sigma$, $L/L_{\max} = 0.56$; (c) $L = 36\sigma$, $L/L_{\max} = 0.72$, $P = 0$; (d) $L = 48\sigma$, $L/L_{\max} = 0.96$.

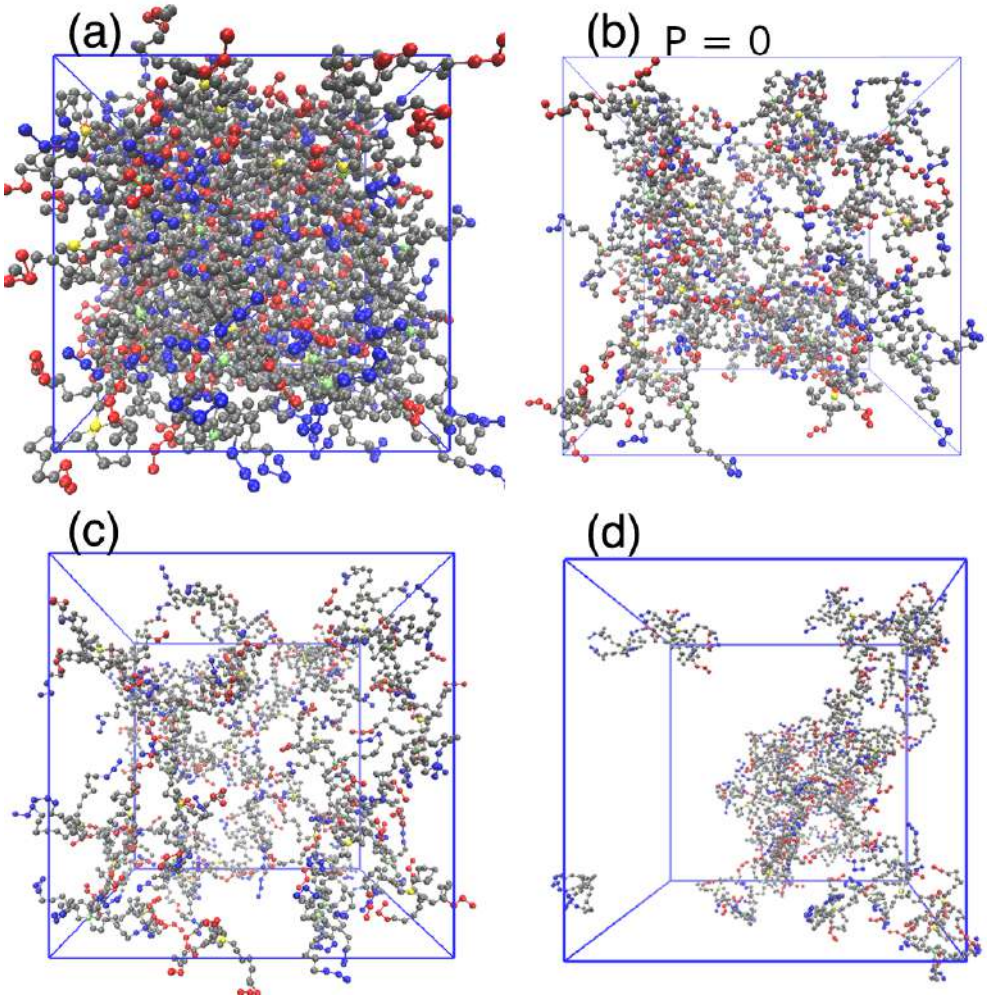

Figure 8.20: Trajectory snapshots for $\Omega = 3$ taken at different box length values: (a) $L = 18\sigma$, $L/L_{\max} = 0.36$; (b) $L = 28.27\sigma$, $L/L_{\max} = 0.56$, $P = 0$; (c) $L = 34\sigma$, $L/L_{\max} = 0.68$; (d) $L = 48\sigma$, $L/L_{\max} = 0.96$.

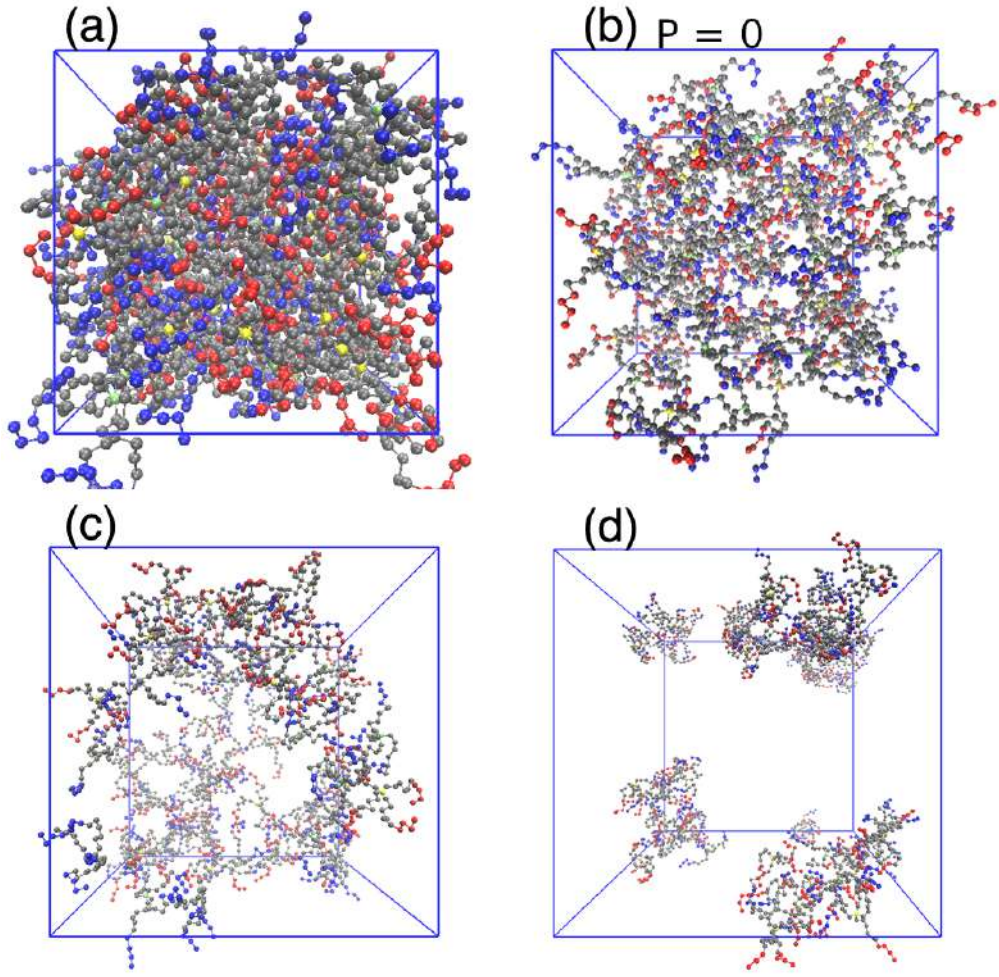

Figure 8.21: Trajectory snapshots for $\Omega = 4$ taken at different box length values: (a) $L = 16\sigma$, $L/L_{\max} = 0.36$; (b) $L = 25.65\sigma$, $L/L_{\max} = 0.51$, $p \simeq 0$; (c) $L = 36\sigma$, $L/L_{\max} = 0.72$; (d) $L = 48\sigma$, $L/L_{\max} = 0.96$.

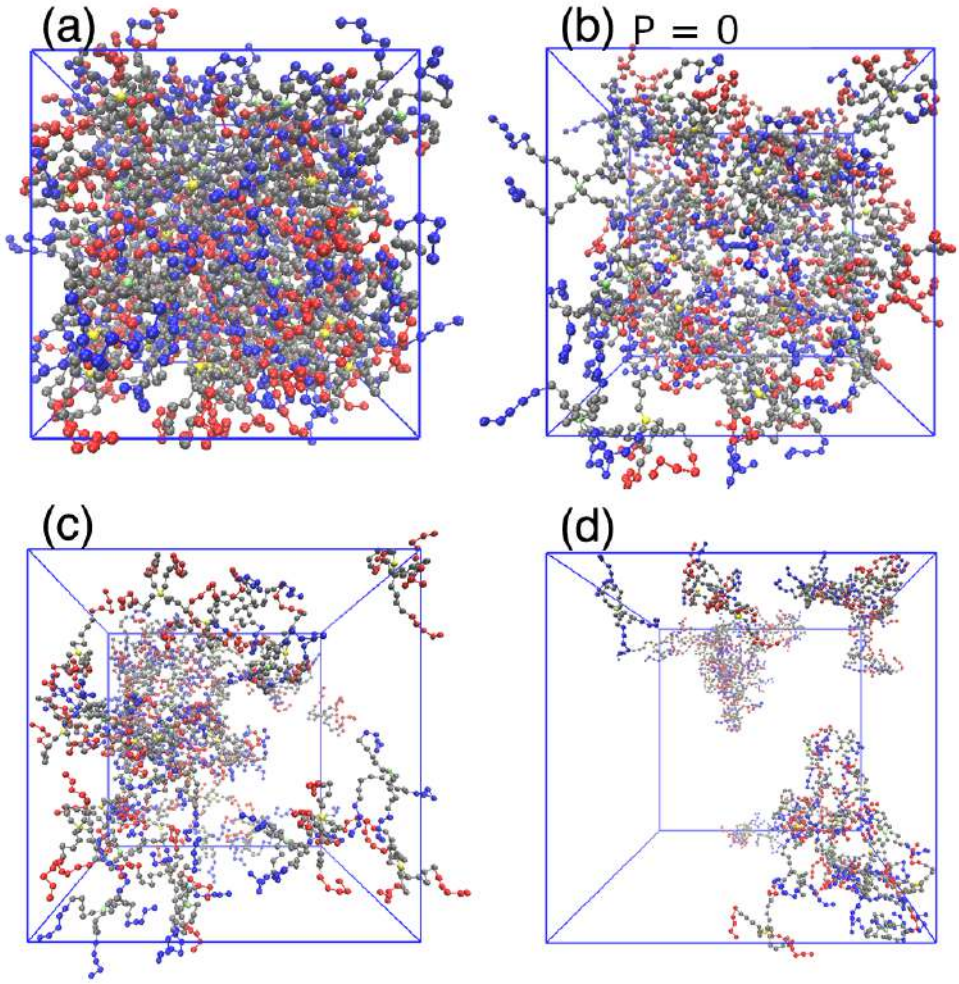

Figure 8.22: Trajectory snapshots for $\Omega = 5$ taken at different box length values: (a) $L = 18\sigma$, $L/L_{\max} = 0.36$; (b) $L = 23.84\sigma$, $L/L_{\max} = 0.48$, $P = 0$; (c) $L = 34\sigma$, $L/L_{\max} = 0.68$; (d) $L = 48\sigma$, $L/L_{\max} = 0.96$.

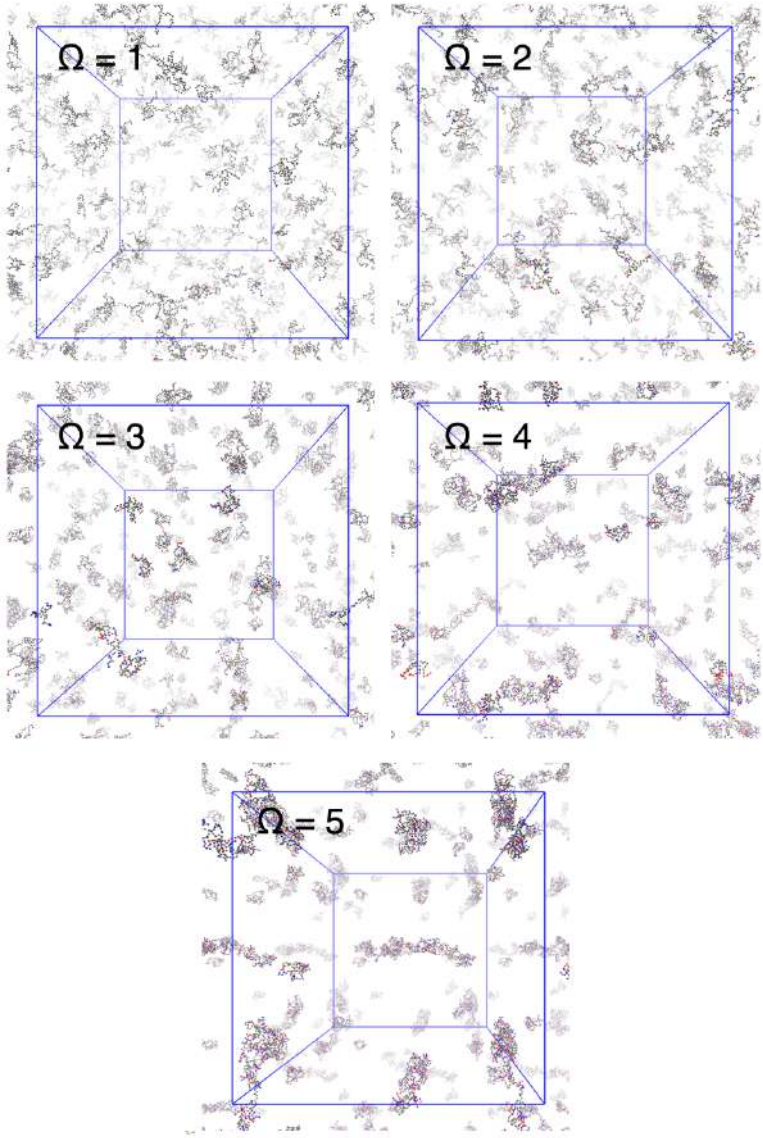

Figure 8.23: Trajectory snapshots for different Ω values taken at box length $L = 95\sigma$ ($L/L_{\max} = 1.90$, $C_S = 1.38{\cdot}10^{-3}$ mol/l). Periodic boundary conditions replicas are shown in some directions.

8.7.2 Trajectory movies

Here we provide the following movies taken from trajectories at the free–swelling equilibrium:

- S1_full_system_omega2.mp4
- S2_full_system_omega3.mp4
- S3_full_system_omega4.mp4
- S4_full_system_omega5.mp4
- S6_detail_omega3.mp4
- S7_detail_omega4.mp4
- S8_detail_omega5.mp4

"Full system" movies show the entire box cell with periodic replicas in some direction; here, the diameter of all monomers has been reduced by roughly one half with respect to the real one. In "detail" movies, instead, a few interacting stars are shown, whereas the other polyelectrolytes in the box are not visible.

Chapter 9

Conclusions

In this PhD project, stochastic coarse-grained simulations have been used in order to simulate various polyelectrolytes systems in aqueous solutions. We employed a restricted (poly)electrolytes primitive model, taking into account, when necessary, the dissociation equilibria of weak groups (i.e., weakly acidic or basic monomers) by means of the constant-pH method [32, 42, 55].

In Chapter 3, we have investigated titration behavior, conformations and energetics of weak polyelectrolytes confined inside capsids (i.e., spherical confining geometries permeable to mobile ions but not to the polyelectrolyte) as a function of pH, chain structure (linear versus star-shaped species) and rigidity and the possibility for monomers to interact via charged hydrogen bonds (c-H-bonds), thus extending previous works on confined strong polyelectrolytes to ranges of "annealed" ionization never investigated before and to species able to form c-H-bonds. The latter have been found to markedly impact not only on titration behavior and chain conformations, but also on the free energy needed to confine polyelectrolytes. In fact, the possibility to form c-H-bonds may impact positively on the polyelectrolyte partition constant not only compared to species unable to do that, but also with respect to the case of fully undissociated weak polyelectrolytes, at least over a range of pH values. Moreover, we introduced the explicit treatment of polyelectrolyte counterions (CIs), since the latter was missing in previous publications regarding the c-H-bond–mimicking many-body potential (References [12] and [37]).*

*The latter paragraph has been adapted from: Tagliabue A., Izzo L., Mella M., Absorbed Weak Polyelectrolytes: Impact of Confinement, Topology, and Chemically Specific Interactions on Ionization, Conformation Free Energy, Counterion Condensation, and Absorption Equilib-

Since charged hydrogen bonds revealed to have a marked impact also on solutions of short linear chains, in Chapter 4 we investigated how polyelectrolyte concentration, chain rigidity and the possibility to form inter- and intra-chain (c-H-bonds) can synergistically contribute to modify ionization and conformations of short linear polyacidic species, their CIs distribution and system Helmholtz energy. Worth noticing, a bimodal behavior in the end-to-end distributions at intermediate–high ionization degrees has been evidenced only when formation of c-H-bonds was allowed, a trait indicating the coexistence of two conformations, one folded (or clustered) and one unfolded, the transition between the two appearing first-order like. The evidence that two or more solvated polyelectrolytes may come sufficiently close to interact, e.g., via c-H-bonds, prompted us to perform window sampling (WS) simulations restraining their centers of mass distance. The latter allowed us to study how the distance between (the centers of mass of) two chains can affect their ionization behavior and conformations. For species unable to form c-H-bonds, as expected pK_a always increases as the distance diminishes; however, this is not true when c-H-bonds can be formed, especially in presence of semi-rigid chains. The formation of inter-chain c-H-bonds increases monomer acidity, modulates the local ionization behavior of monomers, and impacts on chains conformations and CIs distribution. Finally, potentials of mean force (PMF) extracted from window sampling simulations shed light on how chain rigidity and c-H-bonds modify the amount of reversible work (Δw) required to bring two chains at a certain distance. In detail, we found that increasing chain stiffness slightly lowers Δw when chain are unable to form c-H-bonds. Δw, instead, does not monotonically increase as pH increases when chains can form c-H-bonds and are close together, the chemically specific interactions giving rise to minima in PMF curves when chains are semi-rigid.[†]

Moving to the cases of polyelectrolytes interacting with charged colloids, in Chapter 5 we presented simulations of interacting systems composed by weak polyacids and an oppositely charged macroion, which invariably leads to the for-

rium, *Journal of Polymer Science Part B: Polymer Physics*, 57, 491-510 (2019).

[†]The latter paragraph has been adapted from: Tagliabue, A., Izzo L., Mella M., Impact of Charge Correlation, Chain Rigidity, and Chemical Specific Interactions on the Behavior of Weak Polyelectrolytes in Solution, *Journal of Physical Chemistry B*, 123, 42, 8872–8888 (2019).

mation of electrostatically–stabilized complexes between the two species when pH $\geq$ pK_a. Compared to previous works, we have extended substantially the families of investigated systems with respect to CIs' valence, polyelectrolytes structure (and number of chains/arms), as well as the nature and features of the colloid. The latter has been modeled in two different ways: (i) as a single colloid-centered total charge, or (ii) as surface-tethered mobile monovalent charges (the latter model thus representing a highly polarizable charged nanoparticle, or a micelle composed by both neutral and charged surfactants). Our results suggest that a strong polarization of surface charges may be induced upon adsorption of the star polyelectrolyte in such cases involving colloids formed by a mixture of ionic and non-ionic surfactants. Results described in Chapter 5 may bear importance not only for the formation of advanced materials and meta–materials, such as polyelectrolyte-NP composites [211], fluorescent [207] or magnetic [213] nanoparticle arrays, or patchy colloids [178, 214], but also on the bactericidal activity of insoluble weak polyelectrolytes [26, 27, 201], considering that the electrostatic interaction between the negatively charged bacterial wall with its double layer containing divalent ions and ionizable weak polybases closely resembles our models apart from charge inversion.[‡] Among the avenues of explorations upon which our results call attention with some immediacy, there are:

i. the possible impact of divalent colloid counterions coordination to charge bearing surface species (e.g. $Ca^{2+}(COO^-)_2$ [131, 132]) on polyelectrolyte adsorption;

ii. the impact of surfactant tail structure onto the segregation of ionic surfactants induced by star-polymer adsorption;

iii. the distance dependent effect of increasing colloid counterions valency on the ionization of adsorbing polyelectrolytes.

Similarly, colloidal systems composed of a zwitterionic micelle, bearing on the surface either models for sulfobetaine (SBS) or phosphorylcholine (PBS) headgroups interacting with a strong polyanionic systems are discussed in Chapter 6;

[‡]The latter paragraph has been adapted from: Mella M., Tagliabue A., Mollica L., Izzo L., Monte Carlo Study of the Effects of Macroion Charge Distribution on the Ionization and Adsorption of Weak Polyelectrolytes and Concurrent Counterion Release, *Journal of Colloid and Interface Science*, 560, 667-680, (2020)

this with the aim to understand how interactions between the two constituents modify their respective properties and whether or not a complex between them could be formed. Overall, results evidenced a mild impact of zwitterionic micelles on the conformation properties of polyelectrolytes. In spite of this, stark changes in charge distributions around the micelles were found upon linking anions into a polyanion compared with the cases of "free" anions, the maximum of the negative charge density in the micelle vicinity increased more than 30 folds with respect to the case inn which polyanions are present in solution. As for the issue of micelle/polyanion complex formation, we found that the probability for the chain to be adsorbed on a micelle is an increasing function of the polyanion size and that it also markedly depends on headgroups structure, sulfobetaine–like surfactants inducing, at least, a probability of adsorption twice larger than phosphorylcholine–like ones. Worth noticing, chains maintain an elogated conformation despite being (temporarily) adsorbed on a micelle, a fact that may lead to bridging between two (or even more) micelles if their concentration is sufficiently high; it thus seems worth exploring this eventuality in the near future. The computed change in Helmholtz energy due to solution mixing ($\Delta_{\mathrm{mix}}A$) is very small in magnitude so that the impact on the critical surfactant concentration can be considered negligible. Our results are in excellent agreement with experimental results regarding sodium polyacrylates, the latter highly soluble and hydrophilic chain. Nevertheless, to model systems in which interactions between monomers and the hydrophobic micellar core are important, our model needs to be refined. As an example, it would be worth to model chemically specific interactions between polyelectrolytes and corona components, e.g. the possibility for monomers to be coordinated via several headgroup moieties or the possible formations of (charged) hydrogen bonds between the micelle and the polyelectrolyte. Finally, the increased ionic concentration in the corona region may as well be exploited for chemical purposes, as it may enhance reaction rates between anions and organic species with limited water solubility thanks to the law of mass action.[§]

In Chapter 7, we discussed the titration behavior of circular weak polyelec-

[§]The latter paragraph has been adapted from: Mella M., Tagliabue A., Izzo L., On the Distribution of Hydrophilic Polyelectrolytes and their Counterions around Zwitterionic Micelles: the Possible Impact on the Charge Density in Solution *Soft Matter*, just accepted article (doi.org/10.1039/D0SM01541E), © Reproduced by permission of The Royal Society of Chemistry.

trolytes, highlighting an unexpected non-monotonic behavior for the gyration radius versus the dissociation degree for knotted species, such evidence opposite to the "canonical" ionization→repulsion→expansion scheme and attributable to a complex balance between entropic and energetic contributions compared to linear, star-like or even unknotted circular species. In other words, the average size, and hence the mechanical effects associated to it, of knotted rings resulted lower at both extremes of the ionization range. The key role played by CIs localization on a (partially) ionized chain has been thoroughly investigated by varying parameters such as the solvent Bjerrum length l_B and the concentration and valence of background inert salts. Comparing with strong polyelectrolytes of similar ionization degrees (but with quenched charges), it also emerged that the re-contraction of knotted weak polyacid rings begins at higher α values thanks to the localization of undissociated monomers inside the knotted portion of the chain.[¶] The evidence that knots tend to tighten and localize on the undissociated portions of a weak polyelectrolyte prompted us to investigate the possibility for a strong polyelectrolyte carrying a neutral segment on itself to confine the knot topological details on the latter. This hypothesis has been confirmed by looking at the probability density for a monomer to be part of the knotted segment as a function of its position along the co-polyelectrolyte chain, as shown in Figure 9.1 (see also the trajectory snapshots reported in Figure 9.2). As we can observe, even the presence of a few neutral monomers induce the knot confinement. This is observed also if the neutral segment is semi-rigid; moreover, the localization probability can be increased/decreased by tuning solvent properties (e.g., solvent quality for the neutral segment, or solution screening ability).

Finally, in Chapter 8 we investigated the possibility to obtain ionically cross-linked gel-like phases (in equilibrium with a solution of pure water) by mixing oppositely charged strong polyelectrolytes. We found that it is possible to obtain gel phases by tuning the number of terminal charges on star's arms (Ω), and we characterized such phases via many structural parameters (number of contacts per arm/star, number of " isolated "stars and dangling arms), excess of charges carried by clusters, etc.). From our analysis resulted that the simple picture of

[¶]The latter paragraph has been adapted from: Tagliabue A., Izzo L., Mella M., Interface Counterion Localization Induces a Switch Between Tight and Loose Configurations of Knotted Weak Polyacid Rings Despite Intermonomer Coulomb Repulsions, *Journal of Physical Chemistry B*, 124, 14, 2930–2937 (2020).

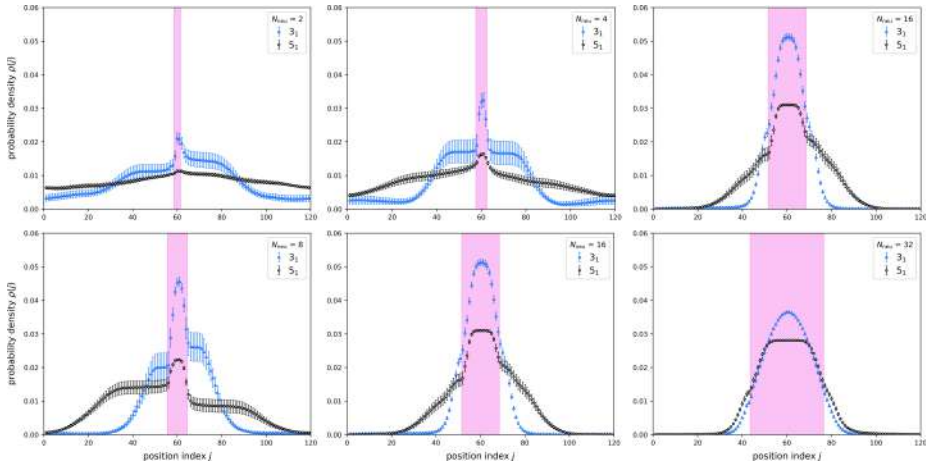

Figure 9.1: Probability density for a monomer to lie inside the knotted segment as a function of its position along the chain. Neutral monomers are highlighted in fuchsia.

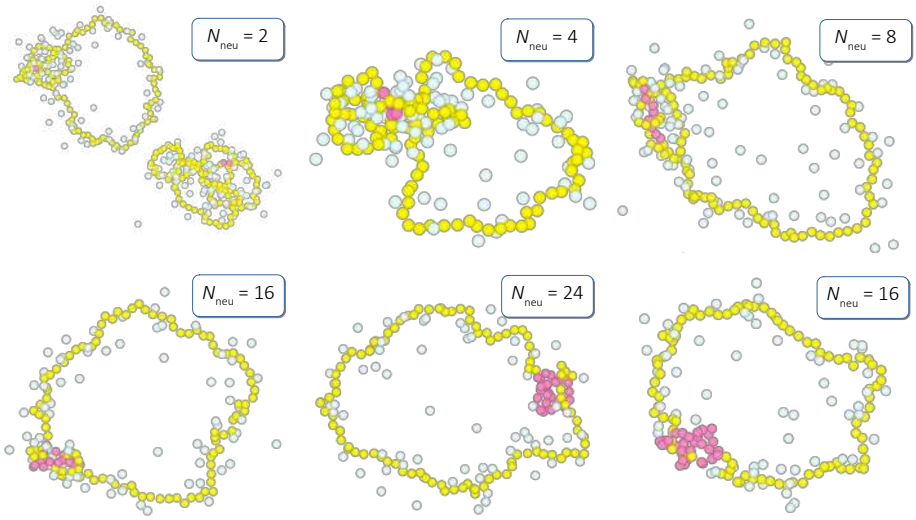

Figure 9.2: Trajectory snapshot for a 5_1–knotted circular strong polyelectrolyte with a neutral segment N_{neu} monomer long. Color scheme: charged (quenched) monomers in yellow, neutral (quenched) monomers in fuchsia, counterions in white.

having mostly saturated ionic bonds is definitely not applicable to the simulated cases. In order to gain more insight in the dynamical processes of forming and dissolving ionic bonds, we analyzed the contact time of such bonds as a function of Ω. Worth noticing, we found strong deviations from the expected statistical first-order dissociation kinetic, the latter underestimating the frequency of fast dissociation events for almost all the simulated cases. Moreover, we described various mechanisms leading to contact formations and ruptures, observing a non–zero probability for an arm involved in a bond to be replaced by another chain with the same charge, a finding that clearly opens up the possibility for the network to restructure itself in time, leading to a reduced mechanical strength and to a low shear modulus. This study has been so far restricted to a small parameter regime, most notably when counterions or background salt ions are absent. As such it should serve as a proof-of-principle that gel formation in mixtures of oppositely charged polyelectrolyte stars is possible. However, more complicated situations like adding different ion types as mono- or even multi-valent ions (e.g., in order to increase bond strengths by divalent ions bridging), changing the ionic block from being a strong polyelectrolyte to a weak polyelectrolyte and adding thus the possibility of the charged groups to respond to pH or to form reversible inter-molecular chemical interactions, or introducing polydispersity in arm length or in charged block length can easily be simulated with more refined models, and many of these systems are currently under investigation. The experimental realization of some of such systems is currently pursued in the group of F. H. Schacher.[‖]

Overall, our canonical and semi-grand canonical coarse-grained simulations highlighted that polyelectrolytes behavior in aqueous solutions often deviates form the expected canonical one, especially when in presence of factors like a strong charges correlation, complex chains architecture and topology, or the presence of chemical specific interactions have to be taken into account.

During this PhD project, the Candidate contributed to the following publications:

[‖] Work in progress.

1. **Tagliabue A.**, Izzo L., Mella M., Absorbed Weak Polyelectrolytes: Impact of Confinement, Topology, and Chemically Specific Interactions on Ionization, Conformation Free Energy, Counterion Condensation, and Absorption Equilibrium, *Journal of Polymer Science Part B: Polymer Physics*, 57, 491-510, **2019**. doi:10.1002/polb.24806
   The Candidate contributed in developing the software, carrying simulations, analyzing the results and writing the manuscript

2. **Tagliabue, A.**, Izzo L., Mella M., Impact of Charge Correlation, Chain Rigidity, and Chemical Specific Interactions on the Behavior of Weak Polyelectrolytes in Solution, *Journal of Physical Chemistry*, 123, 42, 8872–8888 **2019**. doi:10.1021/acs.jpcb.9b06017
   The Candidate contributed in developing the software, carrying out simulations, analyzing the results and writing the manuscript

3. Mella M., **Tagliabue A.**, Mollica L., Izzo L., Monte Carlo Study of the Effects of Macroion Charge Distribution on the Ionization and Adsorption of Weak Polyelectrolytes and Concurrent Counterion Release, *Journal of Colloid and Interface Science*, 560, 667-680, **2020**. doi:10.1016/j.jcis.2019.10.051
   The Candidate contributed in developing the software, analyzing the results and writing the manuscript

4. **Tagliabue A.**, Izzo L., Mella M., Interface Counterion Localization Induces a Switch Between Tight and Loose Configurations of Knotted Weak Polyacid Rings Despite Intermonomer Coulomb Repulsions, *Journal of Physical Chemistry B*, 124, 14, 2930–2937, **2020**. doi:10.1021/acs.jpcb.0c00620
   The Candidate ideated the study, carried out simulations, and contributed in analyzing the results and writing the manuscript.

5. Izzo L., Gorrasi G., Sorrentino A., **Tagliabue A.**, Mella M., Controlling Drug Release of Anti-inflammatory Molecules Through a pH-Sensitive, Bactericidal Polymer Matrix: Towards a Synergic and Combined Therapy. *Advances in Bionanomaterials II. BIONAM 2019. Lecture Notes in Bioengineering.* Springer, Cham., **2020**. doi:10.1007/978-3-030-47705-9_14
   The Candidate contributed in analyzing the results and writing the manuscript.

6. Mella M., **Tagliabue A.**, Izzo, L., On the Distribution of Hydrophilic Polyelectrolytes and their Counterions around Zwitterionic Micelles: the Possible Impact on the Charge Density in Solution, *Soft Matter*, advance article. doi.org/10.1039/D0SM01541E
   The Candidate contributed in developing the software, analyzing the results and writing the manuscript.

7. **Tagliabue A.**, Landsgesell J., Mella, M., Holm, C., Can Oppositely Charged Polyelectrolyte Stars Form a Gel? A Simulational Study, *Soft Matter* , accepted manuscript, **2020**. doi.org/10.1039/D0SM01617A. The Candidate carried out simulations, analyzed the results and wrote the manuscript.

Moreover, the Candidate contributed to the following manuscript that has been submitted to *Surfaces and Interfaces* (title and journal are provisional and may be subjected to changes):

8. Mella M., **Tagliabue A.**, Gorrasi G., Viscusi G., Izzo, L., How Chemical Structure and Composition Impact on the Release of Salt-like Drugs from Hydrophobic Matrices: Variation of Mechanism upon Adding Hydrophilic Features to PMMA. The Candidate carried out on-lattice MC simulations on self-assembling Janus nanoparticles, and contributed in analyzing the results and writing the manuscript.

Bibliography

[1] M. J. Zohuriaan-Mehr, H. Omidian, S. Doroudiani, K. Kabiri, *Journal of Materials Science* **2010**, *45*, 5711–5735. 1

[2] K. Kazanskii, S. Dubrovskii in *Polyelectrolytes Hydrogels Chromatographic Materials. Advances in Polymer Science, Vol. 104*, Springer Verlag, **1992**, pp. 97–133. 1

[3] X. Jia, K. L. Kiick, *Macromolecular Bioscience* **2009**, *9*, 140–156. 1

[4] J. Höpfner, T. Richter, P. Košovan, C. Holm, M. Wilhelm, *Intelligent Hydrogels* **2013**, 247–263. 1

[5] T. Richter, J. Landsgesell, P. Košovan, C. Holm, *Desalination* **2017**, *414*, 28–34. 1

[6] F. Carnal, S. Stoll, *J. Chem Phys.* **2011**, *115*, 12007–12018. 1, 76, 117, 121, 155, 172, 195

[7] S. Ulrich, A. Laguecir, S. Stoll, *Macromolecules* **2005**, *38*, 8939–8949. 1, 75, 117, 118

[8] S. Stoll, P. Chodanowski, *Macromolecules* **2002**, *35*, 9556–9562. 1, 117, 155, 172

[9] T. Wallin, P. Linse, *Langmuir* **1996**, *12*, 305–314. 1, 117, 147, 155, 156, 165, 180, 181, 191

[10] T. Wallin, P. Linse, *The Journal of Physical Chemistry* **1996**, *100*, 17873–17880. 1, 117, 180, 181

[11] T. Wallin, P. Linse, *The Journal of Physical Chemistry B* **1997**, *101*, 5506–5513. 1, 117, 180, 181

[12] M. Mella, L. Mollica, L. Izzo, *J. Pol. Sci. Pol. Phys.* **2015**, *53*, 650–663. 1, 2, 3, 14, 15, 16, 34, 36, 38, 66, 75, 76, 77, 78, 79, 82, 117, 118, 120, 123, 172, 195, 265

[13] A. Laguecir, S. Stoll, *Polymer* **2005**, *46*, 1359–1372. 1, 66, 117, 118, 121, 172

[14] M. Stornes, P. Linse, R. S. Dias, *Macromolecules* **2017**, *50*, 5978–5988. 1, 117, 118, 132, 172, 196

[15] M. Stornes, B. Shrestha, R. Dias, *J. Phys. Chem. B* **2018**, *122*, 10237–10246. 1, 117, 118, 172, 187, 196

[16] S. Ulrich, M. Seijo, A. Laguecir, S. Stoll, *The Journal of Physical Chemistry B* **2006**, *110*, 20954–20964, PMID: 17048913. 1, 118, 155, 171, 187

[17] A. A. C. C. Pais, M. G. Miguel, P. Linse, B. Lindman, *The Journal of Chemical Physics* **2002**, *117*, 1385–1394. 1, 33, 34

[18] S. C. C. Nunes, M. Skepö, A. A. C. C. Pais, *Journal of Computational Chemistry* **2015**, *36*, 1579–1586. 1, 33, 34, 35, 63

[19] D. A. Balazs, W. Godbey, *Journal of Drug Delivery* **2011**, *2011*, 326497. 1, 33

[20] J. K. Oh, R. Drumright, D. J. Siegwart, K. Matyjaszewski, *Progress in Polymer Science* **2008**, *33*, 448–477. 1, 221

[21] M. Hamidi, A. Azadi, P. Rafiei, *Advanced Drug Delivery Reviews* **2008**, *60*, 1638–1649. 1, 221

[22] K. Makino, R. Idenuma, T. Murakami, H. Ohshima, *Colloids and Surfaces B-Biointerfaces* **2001**, *20*, 355–359. 1, 221

[23] D. Tada, T. Tanabe, A. Tachibana, K. Yamauchi, *Journal of Bioscience and Bioengineering* **2005**, *100*, 551–555. 1, 221

[24] Q. Wang, S. Li, Z. Wang, H. Liu, C. Li, *Journal of Applied Polymer Science* **2009**, *111*, 1417–1425. 1, 221

[25] N. A. Peppas, P. Bures, W. Leobandung, H. Ichikawa, *European journal of pharmaceutics and biopharmaceutics* **2000**, *50*, 27–46. 1

[26] G. Vigliotta, M. Mella, D. Rega, L. Izzo, *Biomacromolecules* **2012**, *13*, 833–841. 1, 3, 34, 36, 119, 151, 152, 195, 267

[27] S. Matrella, C. Vitiello, M. Mella, G. Vigliotta, L. Izzo, *Macromol. Biosci.* **2015**, *15*, 927. 1, 3, 34, 36, 119, 151, 152, 195, 267

[28] J. Jagur-Grodzinski, *Polymers for Advanced Technologies* **2009**, *21*, 27–47. 1

[29] M. Ullner, B. Jönsson, B. Söderberg, C. Peterson, *J. Chem. Phys.* **1996**, *104*, 3048–3057. 2, 66, 75, 195

[30] M. Ullner, C. E. Woodward, *Macromolecules* **2000**, *33*, 7144–7156. 2, 75, 155, 165, 195, 210

[31] M. Ullner, B. Jönsson, P.-O. Widmark, *J. Chem. Phys.* **1994**, *100*, 3365–3366. 2, 66, 75, 195

[32] C. E. Reed, W. F. Reed, *J. Chem. Phys.* **1992**, *96*, 1609–1620. 2, 3, 8, 27, 29, 75, 122, 197, 265

[33] F. Carnal, S. Stoll, *J. Chem. Phys.* **2011**, *134*, 044909. 2, 75, 76, 195, 212

[34] O. Trotsenko, Y. Roiter, S. Minko, *Langmuir* **2012**, *28*, 6037–6044. 2, 75, 76

[35] F. Uhlík, P. Košovan, Z. Limpouchová, K. Procházka, O. Borisov, F. Leermakers, *Macromolecules* **2014**, *47*, 4004–4016. 2, 75

[36] A. Tagliabue, L. Izzo, M. Mella, *J. Pol. Sci. Pol. Phys.* **2019**, *57*, 491–510. 2, 29, 120, 123, 158, 178

[37] M. Mella, L. Izzo, *J. Pol. Sci. Pol. Phys.* **2017**, *55*, 1088–1102. 2, 14, 16, 17, 29, 34, 35, 36, 38, 39, 40, 41, 44, 64, 66, 75, 76, 77, 78, 79, 82, 83, 120, 123, 162, 195, 265

[38] V. Yadav, A. V. Harkin, M. L. Robertson, J. C. Conrad, *Soft Matter* **2016**, *12*, 3589–3599. 2, 75, 76

[39] L. Izzo, P. C. Griffiths, R. Nilmini, S. M. King, K.-L. Wallom, E. L. Ferguson, R. Duncan, *Int. J. Pharm.* **2011**, *408*, 213–222. 2, 75, 76, 117

[40] C. Heitz, M. Rawiso, J. François, *Polymer* **1999**, *40*, 1637 – 1650. 2, 75

[41] D. Sarkar, , P. Somasundaran, *Langmuir* **2004**, *20*, 4657–4664. 2, 75

[42] J. Landsgesell, L. Nová, O. Rud, F. Uhlík, D. Sean, P. Hebbeker, C. Holm, P. Košovan, *Soft Matter* **2019**, *15*, 1155–1185. 2, 3, 8, 27, 28, 29, 75, 195, 197, 265

[43] F. A. Plamper, A. Walther, A. H. E. Müller, M. Ballauff, *Nano Letters* **2007**, *7*, 167–171. 3

[44] D. Tolmachev, N. Lukasheva, G. Mamistvalov, M. Karttunen, *Polymers* **2020**, *12*, 1279. 3

[45] R. Staňo, L. Nova, F. Uhlik, P. Kosovan, *Soft Matter* **2020**, –, Advance article. 3, 195

[46] F. Plamper, H. Becker, M. Lanzendorfer, M. Patel, A. Wittemann, M. Ballauff, A. Müller, *Macromol. Chem. Phys.* **2005**, *206*, 1813–1825. 3

[47] F. A. Plamper, M. Ruppel, A. Schmalz, O. Borisov, M. Ballauff, A. H. E. Müller, *Macromolecules* **2007**, *40*, 8361–8366. 3

[48] L. Izzo, G. Gorrasi, *Journal of Macromolecular Science, Part B: Physics* **2014**, *53*, 474–485. 3, 34

[49] C. Garofalo, G. Capuano, R. Sottile, R. Tallerico, R. Adami, E. Reverchon, E. Carbone, L. Izzo, D. Pappalardo, *Biomacromolecules* **2014**, *15*, 403–415. 3, 34

[50] G. Gorrasi, M. Stanzione, L. Izzo, *Reactive and Functional Polymers* **2011**, *71*, 23–29. 3, 34

[51] L. Izzo, D. Pappalardo, *Macromolecular Chemistry and Physics* **2010**, *211*, 2171–2178. 3, 34

[52] F. A. Plamper, H. Becker, M. Lanzendörfer, M. Patel, A. Wittemann, B. Matthias, A. H. E. Müller, *Macromolecular Chemistry and Physics* **2005**, *206*, 1813–1825. 3, 34, 35, 39, 44

[53] F. A. Plamper, M. Ruppel, A. Schmalz, O. Borisov, M. Ballauff, A. H. E. Müller, *Macromolecules* **2007**, *40*, 8361–8366. 3, 34, 35, 39, 44, 75

[54] A. Schmalz, M. Hanisch, H. Schmalz, A. H. Müller, *Polymer* **2010**, *51*, 1213 – 1217. 3, 34, 35, 75

[55] J. Landsgesell, C. Holm, J. Smiatek, *Eur. Phys. J-Spec. Top.* **2017**, *226*, 725–736. 3, 8, 28, 197, 265

[56] S. Seiffert, J. Sprakel, *Chemical Society Reviews* **2012**, *41*, 909–930. 8, 221

[57] A. S. Hoffman, *Advanced Drug Delivery Reviews* **2012**, *64*, 18–23. 8, 221

[58] T. Rossow, A. Habicht, S. Seiffert, *Macromolecules* **2014**, *47*, 6473–6482. 8, 221

[59] S. Seiffert, *Polymer Chemistry* **2017**, *8*, 4472–4487. 8, 221

[60] L. Guo, E. Luijten, *Journal of Polymer Science Part B: Polymer Physics* **2005**, *43*, 959–969. 8, 222

[61] I. C. Gârlea, D. Jaramillo-Cano, C. N. Likos, *Soft Matter* **2019**, *15*, 3527–3540. 8, 222, 239

[62] F. Weik, K. Szuttor, J. Landsgesell, C. Holm, *The European Physical Journal Special Topics* **2019**, *227*, 1639–1655. 8

[63] J. D. Weeks, D. Chandler, H. C. Andersen, *The Journal of Chemical Physics* **1971**, *54*, 5237. 11

[64] K. Kremer, G. S. Grest, *Journal of Chemical Physics* **1990**, *92*, 5057–5086. 12, 13

[65] R. W. Hockney, J. W. Eastwood, *Computer Simulation Using Particles*, IOP, London, **1988**. 14, 224

[66] M. Deserno, C. Holm, *Journal of Chemical Physics* **1998**, *109*, 7678. 14, 224

[67] M. Deserno, C. Holm, *Journal of Chemical Physics* **1998**, *109*, 7694. 14, 224

[68] D. Wolf, *Phys. Rev. Lett.* **1992**, *68*, 3315–3318. 14

[69] D. Wolf, P. Keblinski, S. R. Phillpot, J. Eggebrecht, *The Journal of Chemical Physics* **1999**, *110*, 8254–8282. 14

[70] M. Mella, J.-L. Kuo, D. C. Clary, M. L. Klein, *Phys. Chem. Chem. Phys.* **2005**, *7*, 2324–2332. 14, 15

[71] M. Mella, A. Ponti, *ChemPhysChem* **2006**, *7*, 894–903. 14, 15

[72] M. Mella, *J. Chem. Phys.* **2007**, *126*, 204305. 14

[73] M. Mella, *Chem. Phys. Lett.* **2013**, *555*, 51 – 56. 14

[74] M. Meuwly, M. Karplus, *J. Chem. Phys.* **2002**, *116*, 2572–2585. 15, 76

[75] M. Mella, D. C. Clary, *J. Chem. Phys.* **2003**, *119*, 10048–10062. 15

[76] H. Wennerström, B. Jönsson, P. Linse, *The Journal of Chemical Physics* **1982**, *76*, 4665–4670. 17, 122, 157

[77] J.-Z. Zhang, X.-Y. Peng, S. Liu, B.-P. Jiang, S.-C. Ji, X.-C. Shen, *Polymers* **2019**, *11*, 295. 18

[78] N. Metropolis, A. W. Rosenbluth, M. N. Rosenbluth, A. H. Teller, E. Teller, *J. Chem. Phys.* **1953**, **21**, 1087. 24, 79

[79] H. L. Gordon, J. P. Valleau, *Molecular Simulation* **1995**, *14*, 361–379. 26

[80] W. R. Smith, B. Triska, *Journal of Chemical Physics* **1994**, *100*, 3019–3027. 28

[81] J. K. Johnson, A. Z. Panagiotopoulos, K. E. Gubbins, *Molecular Physics* **1994**, *81*, 717–733. 28

[82] J. Landsgesell, P. Hebbeker, O. Rud, R. Lunkad, P. Košovan, C. Holm, *Macromolecules* **2020**, *53*, 3007–3020. 28

[83] G. S. Grest, K. Kremer, *Physical Review A* **1986**, *33*, 3628–31. 31

[84] E. F. Casassa, *Journal of Polymer Science Part B: Polymer Letters* **1967**, *5*, 773–778. 33, 39, 64

[85] E. F. Casassa, Y. Tagami, *Macromolecules* **1969**, *2*, 14–26. 33, 39, 64

[86] X. Wang, M. Tang, Y. Wang, *Macromolecular Theory and Simulations* **2015**, *24*, 490–499. 33, 39, 64

[87] M. G. Davidson, U. W. Suter, W. M. Deen, *Macromolecules* **1987**, *20*, 1141–1146. 33, 39, 64

[88] J. Dayantis, J. Sturm, *Polymer* **1985**, *26*, 1631 – 1637. 33

[89] P. Cifra, T. Bleha, A. Romanov, *Polymer* **1988**, *29*, 1664 – 1668. 33

[90] T. Bleha, P. Cifra, F. E. Karasz, *Polymer* **1990**, *31*, 1321 – 1327. 33

[91] P. Cifra, T. Bleha, *Polymer* **2000**, *41*, 1003 – 1009. 33, 39, 64

[92] R. H. Boyd, R. R. Chance, G. V. Strate, *Macromolecules* **1996**, *29*, 1182–1190. 33

[93] I. Teraoka, *Macromolecules* **2004**, *37*, 6632–6639. 33

[94] W. Radke, *Macromolecular Theory and Simulations* **2001**, *10*, 668–675. 33

[95] A. A. Gorbunov, A. V. Vakhrushev, *Polymer* **2004**, *45*, 6761 – 6770. 33

[96] Z. Chen, F. A. Escobedo, *Macromolecules* **2001**, *34*, 8802–8810. 33

[97] P. Cifra, *The Journal of Chemical Physics* **2012**, *136*, 024902. 33

[98] H.-P. Hsu, K. Binder, *Soft Matter* **2013**, *9*, 10512–10521. 33

[99] Z. Škrinárová, P. Cifra, *Macromolecular Theory and Simulations* **2001**, *10*, 523–531. 33

[100] I. Teraoka, K. H. Langley, F. E. Karasz, *Macromolecules* **1992**, *25*, 6106–6112. 33

[101] Y. Wang, I. Teraoka, F. Y. Hansen, G. H. Peters, O. Hassager, *Macromolecules* **2010**, *43*, 1651–1659. 33

[102] Y. Wang, G. H. Peters, F. Y. Hansen, O. Hassager, *The Journal of Chemical Physics* **2008**, *128*, 124904. 33

[103] A. Milchev, W. Paul, K. Binder, *Macromolecular Theory and Simulations* **1994**, *3*, 305–323. 33

[104] Z. Škrinárová, T. Bleha, P. Cifra, *Macromolecules* **2002**, *35*, 8896–8905. 33, 39, 64

[105] C. M. Guttman, E. A. D. Marzio, J. F. Douglas, *Macromolecules* **1996**, *29*, 5723–5733. 33, 39, 64

[106] A. Cacciuto, E. Luijten, *Nano Letters* **2006**, *6*, 901–905. 33

[107] J. Z. Y. Chen, *Macromolecules* **2013**, *46*, 9837–9844. 33

[108] J. Gao, P. Tang, Y. Yang, J. Z. Y. Chen, *Soft Matter* **2014**, *10*, 4674–4685. 33

[109] P. Cifra, T. Bleha, Y. Wang, I. Teraoka, *The Journal of Chemical Physics* **2000**, *113*, 8313–8318. 33

[110] P. Cifra, *Macromolecules* **2005**, *38*, 3984–3989. 33

[111] J. M. Polson, A. F. Tremblett, Z. R. N. McLure, *Macromolecules* **2017**, *50*, 9515–9524. 33

[112] D. R. Tree, W. F. Reinhart, K. D. Dorfman, *Macromolecules* **2014**, *47*, 3672–3684. 33

[113] S. J. de Carvalho, R. Metzler, A. G. Cherstvy, *Soft Matter* **2015**, *11*, 4430–4443. 33, 34, 117

[114] J. Wang, M. Muthukumar, *The Journal of Chemical Physics* **2011**, *135*, 194901. 33, 34

[115] R. Kumar, M. Muthukumar, *The Journal of Chemical Physics* **2008**, *128*, 184902. 33, 34

[116] P. J. Park, M.-S. Chun, , J.-J. Kim, *Macromolecules* **2000**, *33*, 8850–8857. 33

[117] N. P. Lin, W. M. Deen, *Macromolecules* **1990**, *23*, 2947–2955. 33

[118] A. G. Cherstvy, *Biopolymers* **2012**, *97*, 311–317. 33, 34, 39, 64

[119] Y. G. Mishael, P. L. Dubin, R. de Vries, A. B. Kayitmazer, *Langmuir* **2007**, *23*, 2510–2516. 33, 39, 64

[120] D. G. Angelescu, R. Bruinsma, P. Linse, *Phys. Rev. E* **2006**, *73*, 041921. 33, 34, 63

[121] D. G. Angelescu, J. Stenhammar, P. Linse, *The Journal of Physical Chemistry B* **2007**, *111*, 8477–8485. 33, 34, 63

[122] M. Tagliazucchi, O. Azzaroni, I. Szleifer, *J. Am. Chem. Soc.* **2010**, *132*, 12404–12411. 34, 75

[123] M. Tagliazucchi, I. Szleifer, *Soft Matter* **2012**, *8*, 7292–7305. 34, 75

[124] M. Tagliazucchi, Y. Rabin, I. Szleifer, *Journal of the American Chemical Society* **2011**, *133*, 17753–17763. 34, 75

[125] F. Gilles, M. Tagliazucchi, O. Azzaroni, I. Szleifer, *J. Phys. Chem. C* **2016**, *120*, 4789–4798. 34, 75

[126] C. Qu, Y. Shi, B. Jing, H. Gao, Y. Zhu, *ACS Macro Letters* **2016**, *5*, 402–406. 35

[127] J. Klein Wolterink, J. van Male, M. A. Cohen Stuart, L. K. Koopal, E. B. Zhulina, O. V. Borisov, *Macromolecules* **2002**, *35*, 9176–9190. 35, 44, 47, 53, 75

[128] N. Rikkert, G. Peng, S. Igal, *J. Pol. Sci. Pol. Phys.* **2006**, *44*, 2638–2662. 35, 75, 159

[129] F. Uhlik, P. Kosovan, E. B. Zhulina, O. V. Borisov, *Soft Matter* **2016**, *12*, 4846–4852. 36, 53, 75, 76

[130] V. S. Rathee, B. J. Sikora, H. Sidky, J. K. Whitmer, *Mater. Res. Express* **2018**, *5*, 014010. 36, 44, 47, 53, 75

[131] R. J. Nap, S. H. Park, I. Szleifer, *Soft Matter* **2018**, *14*, 2365–2378. 36, 53, 76, 77, 91, 195, 267

[132] R. J. Nap, E. Gonzalez Solveyra, I. Szleifer, *Biomater. Sci.* **2018**, *6*, 1048–1058. 36, 53, 76, 77, 91, 195, 267

[133] J. D. Ziebarth, Y. Wang, *Biomacromolecules* **2010**, *11*, 29–38. 39, 78, 159

[134] A. A. Gorbunov, A. V. Vakhrushev, *Polymer* **2004**, *45*, 7303 – 7315. 39, 64

[135] P. Cifra, , T. Bleha, *Macromolecules* **2001**, *34*, 605–613. 39, 64

[136] M. Muthukumar, *Phys. Rev. Lett.* **2001**, *86*, 3188–3191. 40, 64

[137] F. A. Plamper, H. Becker, M. Lanzendörfer, M. Patel, A. Wittemann, M. Ballauff, A. H. E. Müller, *Makromol. Chem.* **2005**, *206*, 1813–1825. 44, 75, 146, 195

[138] F. A. Plamper, M. Ruppel, A. Schmalz, O. Borisov, M. Ballauff, A. H. E. Müller, *Macromolecules* **2007**, *40*, 8361–8366. 44, 75, 195

[139] V. Jadhao, F. J. Solis, M. Olvera de la Cruz, *The Journal of Chemical Physics* **2013**, *138*, 054119. 44

[140] P. Linse, L. Lue, *The Journal of Chemical Physics* **2014**, *140*, 044903. 44

[141] C. Qu, Y. Shi, B. Jing, H. Gao, Y. Zhu, *ACS Macro Lett.* **2016**, *5*, 402–406. 47, 75

[142] L. Nová, F. Uhlík, P. Košovan, *Phys. Chem. Chem. Phys.* **2017**, *19*, 14376–14387. 47

[143] C. Qu, B. Jing, S. Wang, Y. Zhu, *J. Phys. Chem. B* **2017**, *121*, 8829–8837. 47, 76, 117

[144] A. Chremos, J. F. Douglas, *MRS Advances* **2016**, *1*, 1841–1846. 56, 173, 196

[145] A. Jusufi, *The Journal of Chemical Physics* **2006**, *124*, 044908. 63

[146] R. P. Linna, P. M. Suhonen, J. Piili, *Phys. Rev. E* **2017**, *96*, 052402. 65

[147] W. Nowicki, G. Nowicka, J. Narkiewicz-Michałek, *European Polymer Journal* **2010**, *46*, 112 – 122. 65

[148] J. M. Polson, M. F. Hassanabad, A. McCaffrey, *The Journal of Chemical Physics* **2013**, *138*, 024906. 65

[149] S. Ulrich, A. Laguecir, S. Stoll, *J. Chem. Phys.* **2005**, *122*, 094911. 66, 76

[150] D. Wang, R. J. Nap, I. Lagzi, B. Kowalczyk, S. Han, B. A. Grzybowski, I. Szleifer, *J. Am. Chem. Soc.* **2011**, *133*, 2192–2197. 75

[151] P. Gong, T. Wu, J. Genzer, I. Szleifer, *Macromolecules* **2007**, *40*, 8765–8773. 75

[152] P. Gong, J. Genzer, I. Szleifer, *Phys. Rev. Lett.* **2007**, *98*, 018302. 75

[153] R. Nap, P. Gong, I. Szleifer, *J. Pol. Sci. Pol. Phys.* **2006**, *44*, 2638–2662. 75

[154] E. B. Zhulina, O. V. Borisov, *J. Chem. Phys.* **1997**, *107*, 5952–5967. 75

[155] M. Tagliazucchi, M. O. de la Cruz, I. Szleifer **2010**, *107*, 5300–5305. 75, 76

[156] R. J. Nap, M. Tagliazucchi, I. Szleifer, *J. Chem. Phys.* **2014**, *140*, 024910. 75

[157] T. Wu, P. Gong, I. Szleifer, P. Vlček, V. Šubr, J. Genzer, *Macromolecules* **2007**, *40*, 8756–8764. 75

[158] A. Z. Panagiotopoulos, *J. Phys-Cond. Mat.* **2009**, *21*, 424113. 75, 84, 88, 94

[159] L. Nova, F. Uhlik, P. Kosovan, *Phys. Chem. Chem. Phys.* **2017**, *19*, 14376–14387. 75, 84, 88, 94, 206

[160] W. Xu, I. Choi, F. A. Plamper, C. V. Synatschke, A. H. E. Müller, Y. B. Melnichenko, V. V. Tsukruk, *Macromolecules* **2014**, *47*, 2112–2121. 75, 76, 195

[161] G. Berghold, P. Van Der Schoot, C. Seidel, *J. Chem. Phys.* **1997**, *107*, 8083–8088. 75

[162] R. Dong, M. Lindau, C. K. Ober, *Langmuir* **2009**, *25*, 4774–4779. 76

[163] I. Borukhov, D. Andelman, R. Borrega, M. Cloitre, L. Leibler, H. Orland, *J. Phys. Chem. B* **2000**, *104*, 11027–11034. 76

[164] E. P. K. Currie, A. B. Sieval, M. Avena, H. Zuilhof, E. J. R. Sudhölter, M. A. Cohen Stuart, *Langmuir* **1999**, *15*, 7116–7118. 76

[165] A. P. Sassi, S. Beltrán, H. H. Hooper, H. W. Blanch, J. Prausnitz, R. A. Siegel, *J. Chem. Phys.* **1992**, *97*, 8767–8774. 76

[166] S. Uyaver, C. Seidel, *Europhys. Lett.* **2003**, *64*, 536. 76

[167] E. Raphael, J.-F. Joanny, *Europhys. Lett.* **1990**, *13*, 623. 76

[168] S. Uyaver, C. Seidel, *Macromolecules* **2009**, *42*, 1352–1361. 76

[169] S. Uyaver, C. Seidel, *J. Chem. Phys. B* **2004**, *108*, 18804–18814. 76

[170] F. Carnal, S. Ulrich, S. Stoll, *Macromolecules* **2010**, *43*, 2544–2553. 76, 195, 212

[171] M. Mella, *J. Chem. Phys.* **2006**, *124*. 77

[172] M. Mella, *J. Chem. Phys.* **2008**, *128*. 77

[173] M. Mella, *J. Chem. Phys.* **2009**, *130*. 77

[174] A. Zhuk, S. Sukhishvili, *Soft Matter* **2013**, *9*, 5149–5154. 117

[175] J. Landsgesell, L. Nová, O. Rud, F. Uhlík, D. Sean, P. Hebbeker, C. Holm, P. Košovan, *Soft Matter* **2019**, *15*, 1155–1185. 117

[176] A. Jusufi, M. Konieczny, C. Likos, *Zeitschrift fur Physikalische Chemie* **2012**, *226*, 585–596. 117, 142, 150

[177] R. Blaak, C. Likos, *Journal of Physics Condensed Matter* **2012**, *24*. 117, 150

[178] M. Konieczny, C. Likos, *Soft Matter* **2007**, *3*, 1130–1134. 117, 150, 267

[179] S. Ulrich, M. Seijo, S. Stoll, *Current Opinion in Colloid & Interface Science* **2006**, *11*, 268 – 272. 117, 118

[180] R. G. Winkler, A. G. Cherstvy, *Strong and Weak Polyelectrolyte Adsorption onto Oppositely Charged Curved Surfaces*, M. Müller (Ed.), Springer Berlin Heidelberg, Berlin, Heidelberg, **2014**, pp. 1–56. 117

[181] M. R. Bohmer, O. A. Evers, J. M. H. M. Scheutjens, *Macromolecules* **1990**, *23*, 2288–2301. 117

[182] P. M. Biesheuvel, M. van der Veen, W. Norde, *The Journal of Physical Chemistry B* **2005**, *109*, 4172–4180. 117

[183] A. G. Cherstvy, R. G. Winkler, *The Journal of Physical Chemistry B* **2012**, *116*, 9838–9845. 117, 159

[184] C. Narambuena, E. Leiva, E. Pèrez, *Colloids and Surfaces A: Physicochemical and Engineering Aspects* **2015**, *487*, 49 – 57. 117, 121

[185] V. M. de Oliveira, S. J. de Carvalho, *The European Physical Journal E* **2014**, *37*, 75. 117, 155

[186] L. Wang, H. Liang, J. Wu, *The Journal of Chemical Physics* **2010**, *133*, 044906. 117

[187] J.-M. Y. Carrillo, A. V. Dobrynin, *Langmuir* **2007**, *23*, 2472–2482. 117

[188] C. F. Narambuena, D. M. Beltramo, E. P. M. Leiva, *Macromolecules* **2008**, *41*, 8267–8274. 117, 121

[189] S. Y. Lee, M. A. Hubbe, *Colloids and Surfaces A: Physicochemical and Engineering Aspects* **2008**, *331*, 175 – 182. 117

[190] R. Dias, A. Pais, *Advances in Colloid and Interface Science* **2010**, *158*, 48 – 62, Polyelectrolytes. 117

[191] R. S. Dias, P. Linse, *Biophysical Journal* **2008**, *94*, 3760 – 3768. 117

[192] C. Fleck, R. R. Netz, H. H. von Grönberg, *Biophysical Journal* **2002**, *82*, 76–92. 117

[193] M. Goswami, J. M. Borreguero, P. A. Pincus, B. G. Sumpter, *Macromolecules* **2015**, *48*, 9050–9059. 117

[194] D. Li, N. J. Wagner, *Journal of the American Chemical Society* **2013**, *135*, 17547–17555. 117

[195] M. Gradzielski, I. Hoffmann, *Current Opinion in Colloid & Interface Science* **2018**, *35*, 124 – 141. 117

[196] D. Li, M. S. Kelkar, N. J. Wagner, *Langmuir* **2012**, *28*, 10348–10362. 117

[197] S. Ravindran, J. Wu, *Langmuir* **2004**, *20*, 7333–7338. 119

[198] R. Messina, C. Holm, K. Kremer, *The European Physical Journal E* **2001**, *4*, 363–370. 119

[199] M. L. Henle, C. D. Santangelo, D. M. Patel, P. A. Pincus, *Europhysics Letters (EPL)* **2004**, *66*, 284–290. 119

[200] K. Qamhieh, P. Linse, *The Journal of Chemical Physics* **2005**, *123*, 104901. 119

[201] L. Izzo, S. Matrella, M. Mella, G. Benvenuto, G. Vigliotta, *ACS Applied Materials & Interfaces* **2019**, *11*, 15332–15343. 119, 151, 152, 267

[202] M. Ullner, K. Qamhieh, B. Cabane, *Soft Matter* **2018**, *14*, 5832–5846. 144, 149, 183

[203] J. Gummel, F. Cousin, F. Boué, *Journal of the American Chemical Society* **2007**, *129*, 5806–5807. 146, 149

[204] V. S. Rathee, H. Sidky, B. J. Sikora, J. K. Whitmer, *Journal of the American Chemical Society* **2018**, *140*, 15319–15328. 149

[205] F. Plamper, Ph.D. dissertetion thesis. Last accessed: October 9th 2019. https://epub.uni-bayreuth.de/666/1/DissPlamper.pdf. 149

[206] B. P. Das, M. Tsianou, *Advances in Colloid and Interface Science* **2017**, *244*, 71 – 89, Special Issue in Honor of the 90th Birthday of Prof. Eli Ruckenstein. 150

[207] E. Glogowski, R. Tangirala, T. P. Russell, T. Emrick, *Journal of Polymer Science Part A: Polymer Chemistry* **2006**, *44*, 5076–5086. 150, 267

[208] J. Xiao, Y. Li, Q. Huang, *Advances in Colloid and Interface Science* **2017**, *239*, 31 – 45, Complex Coacervation: Principles and Applications. 150

[209] Y. Sakhawoth, L. Michot, P. Levitz, A.-L. Rollet, J. Sirieix-Plenet, D. H. Merino, N. Malikova, *Langmuir* **2019**, *35*, 10937–10946, PMID: 31318560. 150

[210] J. K. Gansel, M. Thiel, M. S. Rill, M. Decker, K. Bade, V. Saile, G. von Freymann, S. Linden, M. Wegener, *Science* **2009**, *325*, 1513–1515. 150

[211] G. Pandav, V. Pryamitsyn, J. Errington, V. Ganesan, *The Journal of Physical Chemistry B* **2015**, *119*, 14536–14550, PMID: 26473468. 150, 267

[212] F. Du, J. E. Fischer, K. I. Winey, *Phys. Rev. B* **2005**, *72*, 121404. 150

[213] S. Sun, C. B. Murray, D. Weller, L. Folks, A. Moser, *Science* **2000**, *287*, 1989–1992. 150, 267

[214] F. Tu, B. J. Park, D. Lee, *Langmuir* **2013**, *29*, 12679–12687, PMID: 24044808. 150, 267

[215] A. Tagliabue, L. Izzo, M. Mella, *Langmuir* **2016**, *32*, 12934–12946, PMID: 27809544. 151

[216] H.-Y. Lee, S. H. R. Shin, A. M. Drews, A. M. Chirsan, S. A. Lewis, K. J. M. Bishop, *ACS Nano* **2014**, *8*, 9979–9987, PMID: 25229312. 151

[217] A. Gröschel, F. H. Schacher, H. Schmalz, O. V. Borisov, E. B. Zhulina, A. Walther, A. H. E. Müller, *Nat Commun* **2012**, *3*, 710. 151

[218] L. Glavas, K. Odelius, A.-C. Albertsson, *Polymers for Advanced Technologies* **2015**, *26*, 880–888. 151

[219] M. Barrella, A. Di Capua, R. Adami, E. Reverchon, M. Mella, L. Izzo, *Supramolecular Chemistry* **2017**, *29*, 796–807. 151

[220] S. Villani, R. Adami, E. Reverchon, A. Ferretti, A. Ponti, M. Lepretti, I. Caputo, L. Izzo, *Journal of Drug Targeting* **2017**, *25*, 899–909. 151

[221] T. Katsu, H. Nakagawa, K. Yasuda, *Antimicrobial Agents and Chemotherapy* **2002**, *46*, 1073–1079. 151

[222] D. A. Pink, L. Truelstrup Hansen, T. A. Gill, B. E. Quinn, M. H. Jericho, T. J. Beveridge, *Langmuir* **2003**, *19*, 8852–8858. 151

[223] M. De Rosa, G. Vigliotta, A. Soriente, V. Capaccio, G. Gorrasi, R. Adami, E. Reverchon, M. Mella, L. Izzo, *Biomater. Sci.* **2017**, *5*, 741–751. 152

[224] Q. Shao, S. Jiang, *Advanced Materials* **2015**, *27*, 15–26. 153

[225] Y. Xiang, R.-G. Xu, Y. Leng, *Langmuir* **2018**, *34*, 2245–2257, PMID: 29361214. 153

[226] J. Ma, K. Kang, Q. Yi, Z. Zhang, Z. Gu, *RSC Adv.* **2016**, *6*, 64778–64790. 153

[227] J. Jiang, J. Li, B. Zhou, C. Niu, W. Wang, W. Wu, J. Liang, *Polymers* **2019**, *11*, 1019. 153

[228] J. Lu, H. Jia, L. Guo, G. Zhang, Y. Cao, H. Yan, K. Liu, *European Polymer Journal* **2015**, *66*, 376 – 385. 153

[229] G. Ridout, R. S. Hinz, J. J. Hostynek, A. Reddy, R. J. Wiersema, C. D. Hodson, C. R. Lorence, R. H. Guy, *Fundamental and Applied Toxicology* **1991**, *16*, 41 – 50. 153

[230] A. Michanek, N. Kristen, F. Höök, T. Nylander, E. Sparr, *Biochimica et Biophysica Acta (BBA) - Biomembranes* **2010**, *1798*, 829 – 838, A Surface View on Membrane Structure, Dynamics and Applications. 153

[231] V. Budker, A. Godovikov, L. Naumova, I. Slepneva, *Nucleic Acids Research* **1980**, *8*, 2499–2516. 153

[232] A. Khvorova, Y.-G. Kwak, M. Tamkun, I. Majerfeld, M. Yarus, *Proceedings of the National Academy of Sciences* **1999**, *96*, 10649–10654. 153

[233] P. D. Profio, R. Germani, A. Fontana, V. Canale, *Journal of Molecular Liquids* **2019**, *278*, 650 – 657. 154

[234] G. T. Silva, F. H. Quina, *Current Opinion in Colloid & Interface Science* **2019**, *44*, 168 – 176, Memorial Volume. 154, 188

[235] T. P. de Souza, H. Chaimovich, A. Fahr, B. Schweitzer, A. A. Neto, I. M. Cuccovia, *Journal of Colloid and Interface Science* **2012**, *371*, 62 – 72. 154, 155

[236] M. d. S. Baptista, I. Cuccovia, H. Chaimovich, M. J. Politi, W. F. Reed, *The Journal of Physical Chemistry* **1992**, *96*, 6442–6449. 154, 155, 187

[237] T. Okada, J. M. Patil, *Langmuir* **1998**, *14*, 6241–6248. 154, 155

[238] X. Jun, S. Wenqi, L. Ganzuo, Z. Gaoyong, *Chemical Physics Letters* **2007**, *438*, 326 – 329. 154, 156, 158, 172

[239] D. P. Santos, R. L. Longo, *The Journal of Physical Chemistry B* **2016**, *120*, 2771–2780, PMID: 26907972. 154, 156, 158, 172

[240] A. Tagliabue, L. Izzo, M. Mella, *The Journal of Physical Chemistry B* **2019**, *123*, 8872–8888, PMID: 31557036. 155, 156, 161, 162

[241] Y. Chevalier, N. Kamenka, M. Chorro, R. Zana, *Langmuir* **1996**, *12*, 3225–3232. 155

[242] M. S. Bakshi, G. Kaur, A. Kaura, *Colloids and Surfaces A: Physicochemical and Engineering Aspects* **2005**, *269*, 72 – 79. 156, 187

[243] R. K. Mahajan, K. K. Vohra, A. Shaheen, V. K. Aswal, *Journal of Colloid and Interface Science* **2008**, *326*, 89 – 95. 156, 187

[244] C. Brinatti, L. B. Mello, W. Loh, *Langmuir* **2014**, *30*, 6002–6010, PMID: 24823937. 156, 157, 178, 179, 181, 187

[245] R. Ribera, M. M. Velázquez, *Langmuir* **1999**, *15*, 6686–6691. 156, 187

[246] M. D. Merchán Moreno, M. M. Velázquez, *Colloids and Surfaces A Physicochemical and Engineering Aspects* **2010**, *366*, 12–17. 156, 187

[247] F. H. Florenzano, L. G. Dias, *Langmuir* **1997**, *13*, 5756–5758. 158

[248] A. Gerola, P. Costa, F. Nome, F. Quina, *Current Opinion in Colloid and Interface Science* **2017**, *32*, 48–56, cited By 12. 158

[249] M. Mella, A. Tagliabue, L. Mollica, L. Izzo, *J. Colloid Interf. Sci.* **2020**, *560*, 667 – 680. 158, 172, 178, 195

[250] H. Lee, S. H. Son, R. Sharma, Y.-Y. Won, *The Journal of Physical Chemistry B* **2011**, *115*, 844–860. 159

[251] T. Başţuğ, S. Kuyucak, *Biophysical Journal* **2003**, *84*, 2871 – 2882. 159

[252] F. L. B. da Silva, D. Bogren, O. Söderman, T. Åkesson, B. Jönsson, *The Journal of Physical Chemistry B* **2002**, *106*, 3515–3522. 159

[253] B. Hess, C. Holm, N. van der Vegt, *Phys. Rev. Lett.* **2006**, *96*, 147801. 159

[254] B. Widom, *The Journal of Chemical Physics* **1963**, *39*, 2808–2812. 162

[255] R. W. Zwanzig, *The Journal of Chemical Physics* **1954**, *22*, 1420–1426. 162

[256] M. J. Stevens, K. Kremer, *The Journal of Chemical Physics* **1995**, *103*, 1669–1690. 165

[257] D. W. Tondo, J. M. Priebe, B. S. Souza, J. P. Priebe, C. A. Bunton, F. Nome, *The Journal of Physical Chemistry B* **2007**, *111*, 11867–11869, PMID: 17894484. 167, 168, 186

[258] L. Marte, R. C. Beber, M. A. Farrukh, G. A. Micke, A. C. O. Costa, N. D. Gillitt, C. A. Bunton, P. Di Profio, G. Savelli, F. Nome, *The Journal of Physical Chemistry B* **2007**, *111*, 9762–9769, PMID: 17661510. 167

[259] S. Ulrich, A. Laguecir, S. Stoll, *Macromolecules* **2005**, *38*, 8939–8949. 171

[260] A. Chremos, J. F. Douglas, *Soft Matter* **2016**, *12*, 2932–2941. 173, 196

[261] J. P. Priebe, B. S. Souza, G. A. Micke, A. C. O. Costa, H. D. Fiedler, C. A. Bunton, F. Nome, *Langmuir* **2010**, *26*, 1008–1012, PMID: 19711953. 177

[262] A. Laguecir, S. Ulrich, J. Labille, N. Fatin-Rouge, S. Stoll, J. Buffle, *Eur. Pol. J* **2006**, *42*, 1135 – 1144. 195

[263] Y. Xu, S. Bolisetty, M. Drechsler, B. Fang, J. Yuan, M. Ballauff, A. H. Müller, *Polymer* **2008**, *49*, 3957 – 3964. 195

[264] H.-i. Lee, J. Boyce, A. Nese, S. Sheiko, K. Matyjaszewski, *Polymer* **2008**, *49*, 5490–5496. 195

[265] H.-i. Lee, J. Pietrasik, S. Sheiko, K. Matyjaszewski, *Progress in Polymer Science (Oxford)* **2010**, *35*, 24–44. 195

[266] P. Jia, Y. Gong, S. Wang, J. Zhao, *Chinese J. Chem.* **2012**, *30*, 2237–2240. 195

[267] S. Zhang, J. Yan, A. Qin, J. Sun, B. Tang, *Sci. China Chem.* **2013**, *56*, 1253–1257. 195

[268] J. Li, K. Zhao, *J. Phys. Chem. B* **2013**, *117*, 11843–11852. 195

[269] Q. Zhang, Q. Ran, H. Zhao, X. Shu, Y. Yang, H. Zhou, J. Liu, *Colloid Polym. Sci.* **2016**, *294*, 1705–1715. 195

[270] C. Dolce, G. Mériguet, *Colloid Polym. Sci.* **2017**, *295*, 279–287. 195

[271] A. Zaibudeen, J. Philip, *J. Mol. Liq.* **2018**, *252*, 30–39. 195

[272] J. Ziebarth, Y. Wang, *Biomacromolecules* **2010**, *11*, 29–38. 195

[273] G. Yao, J. Zhao, S. Ramisetti, D. Wen, *Ind. Eng. Chem. Res.* **2018**, *57*, 17129–17141. 195

[274] D. G. Mintis, V. G. Mavrantzas, *J. Phys. Chem. B* **2019**, *123*, 4204–4219. 195

[275] A. Chremos, J. F. Douglas, *Gels* **2018**, *4*. 196

[276] P. G. Dommersnes, Y. Kantor, M. Kardar, *Phys. Rev. E* **2002**, *66*, 031802. 196, 199, 202, 203, 205, 210, 212

[277] L. Dai, P. S. Doyle, *Macromolecules* **2016**, *49*, 7581–7587. 196, 205

[278] F. Weik, R. Weeber, K. Szuttor, K. Breitsprecher, J. de Graaf, M. Kuron, J. Landsgesell, H. Menke, D. Sean, C. Holm, *Eur. Phys. J-Spec. Top.* **2019**, *227*, 1789–1816.

[279] M. L. Mansfield, J. F. Douglas, *J. Chem. Phys.* **2010**, *133*, 044903. 198

[280] D. Sean, J. Landsgesell, C. Holm, *Gels* **2018**, *4*. 199

[281] L. Coronel, E. Orlandini, C. Micheletti, *Soft Matter* **2017**, *13*, 4260–4267. 202, 206

[282] M. J. Zohuriaan-Mehr, K. Kabiri, *Iranian Polymer Journal* **2008**, *17*, 451–477. 221

[283] N. A. Peppas, P. Bures, W. Leobandung, H. Ichikawa, *European journal of pharmaceutics and biopharmaceutics* **2000**, *50*, 27–46. 221

[284] G. V. Samsonov, N. P. Kuznetsova, *Advances in Polymer Science* **1992**, *104*, 1–50. 221

[285] X. Jia, K. L. Kiick, *Macromolecular Bioscience* **2009**, *9*, 140–156. 221

[286] J. Jagur-Grodzinski, *Polymers for Advanced Technologies* **2009**, *21*, 27–47. 221

[287] S. Meenach, K. Anderson, J. Hilt in *Safety of Nanoparticles*, of *Nanostructure Science and Technology*, T. J. Webster (Ed.), Springer New York, **2009**, pp. 131–157. 221

[288] H. Tamura, T. Furuike, S. Nair, R. Jayakumar, *Carbohydrate Polymers* **2011**, *84*, 820 – 824, Advances in chitin/chitosan science and their applications. 221

[289] A. Sannino, A. Esposito, A. D. Rosa, A. Cozzolino, L. Ambrosio, L. Nicolais, *Journal of Biomedical Materials Research Part A* **2003**, *67A*, 1016–1024. 221

[290] B. Zavan, R. Cortivo, G. Abatangelo in *Hydrogels*, Springer Milan, **2009**, pp. 1–8. 221

[291] M. J. Zohuriaan-Mehr, H. Omidian, S. Doroudiani, K. Kabiri, *Journal of Materials Science* **2010**, *45*, 5711–5735. 221

[292] K. Kazanskii, S. Dubrovskii in *Polyelectrolytes Hydrogels Chromatographic Materials. Advances in Polymer Science, Vol. 104*, Springer Verlag, **1992**, pp. 97–133. 221

[293] *Polyelectrolyte gels: Properties, Preparation, and Applications*, of *ACS Symposium Series No. 480*, American Chemical Society, Washington D.C., **1992**. 221

[294] J. Höpfner, C. Klein, M. Wilhelm, *Macromolecular Rapid Communications* **2010**, *31*, 1337. 221

[295] J. Höpfner, T. Richter, P. Košovan, C. Holm, M. Wilhelm in *Intelligent Hydrogels*, Vol. 140 of *Progress in Colloid and Polymer Science*, G. Sadowski, W. Richtering (Eds.), Springer International Publishing, **2013**, pp. 247–263. 221

[296] T. Richter, J. Landsgesell, P. Košovan, C. Holm, *Desalination* **2017**, *414*, 28–34. 221

[297] L. Arens, D. Barther, J. Landsgesell, C. Holm, M. Wilhelm, *Soft Matter* **2019**, *15*, 9949–9964. 221

[298] V. Kozlovskaya, E. Kharlampieva, S. Chang, R. Muhlbauer, V. V. Tsukruk, *Chemistry of Materials* **2009**, *21*, 2158–2167. 221

[299] Y. M. Mohan, K. Lee, T. Premkumar, K. E. Geckeler, *POLYMER* **2007**, *48*, 158–164. 221

[300] D. D. Diaz, D. Kuehbeck, R. J. Koopmans, *Chemical Society Reviews* **2011**, *40*, 427–448. 221

[301] O. Borisova, L. Billon, M. Zaremski, B. Grassl, Z. Bakaeva, A. Lapp, P. Stepanek, O. Borisov, *Soft Matter* **2011**, *7*, 10824–10833. 222

[302] C. Charbonneau, M. M. D. S. Lima, C. Chassenieux, O. Colombani, T. Nicolai, *Physical Chemistry Chemical Physics* **2013**, *15*, 3955–3964. 222

[303] J. S. Myung, F. Taslimi, R. G. Winkler, G. Gompper, *Macromolecules* **2014**, *47*, 4118–4125. 222

[304] D. Amin, A. E. Likhtman, Z. Wang, *Macromolecules* **2016**, *49*, 7510–7524. 222

[305] C. Tsitsilianis, G. Serras, C.-H. Ko, F. Jung, C. M. Papadakis, M. Rikkou-Kalourkoti, C. S. Patrickios, R. Schweins, C. Chassenieux, *Macromolecules* **2018**, *51*, 2169–2179. 222

[306] D. E. Williams, D. J. Houpt, *Acta Crystallographica Section B* **1986**, *42*, 286–295. 222

[307] I. A. Nyrkova, A. R. Khokhlov, M. Doi, *Macromolecules* **1993**, *26*, 3601–3610. 222

[308] A. R. Khokhlov, E. Y. Kramarenko, *Macromolecular Theory and Simulations* **1994**, *3*, 45–59. 222

[309] R. J. Varley, S. van der Zwaag, *Acta Materialia* **2008**, *56*, 5737–5750. 222

[310] Q. Chen, G. J. Tudryn, R. H. Colby, *Journal of Rheology* **2013**, *57*, 1441–1462. 222

[311] E. Locatelli, P. H. Handle, C. N. Likos, F. Sciortino, L. Rovigatti, *ACS Nano* **2017**, *11*, 2094–2102, PMID: 28157331. 222

[312] F. Spinozzi, M. G. Ortore, G. Nava, F. Bomboi, F. Carducci, H. Amenitsch, T. Bellini, F. Sciortino, P. Mariani, *Langmuir* **2020**, *36*, 10387–10396, PMID: 32787014. 222

[313] S. Roldán-Vargas, L. Rovigatti, F. Sciortino, *Soft Matter* **2017**, *13*, 514–530. 222

[314] F. Tanaka, S. Edwards, *Macromolecules* **1992**, *25*, 1516–1523. 222

[315] A. Semenov, J.-F. Joanny, A. Khokhlov, *Macromolecules* **1995**, *28*, 1066–1075. 222

[316] M. Rubinstein, S. Panyukov, *Macromolecules* **1997**, *30*, 8036–8044. 222

[317] M. Rubinstein, A. N. Semenov, *Macromolecules* **1998**, *31*, 1386–1397. 222

[318] A. N. Semenov, M. Rubinstein, *Macromolecules* **1998**, *31*, 1373–1385. 222

[319] Z. Mester, A. Mohan, G. H. Fredrickson, *Macromolecules* **2011**, *44*, 9411–9423. 222

[320] C. E. Sing, S. L. Perry, *Soft Matter* **2020**, *16*, 2885–2914. 222

[321] F. Luo, T. L. Sun, T. Nakajima, T. Kurokawa, Y. Zhao, K. Sato, A. B. Ihsan, X. Li, H. Guo, J. P. Gong, *Advanced Materials* **2015**, *27*, 2722–2727. 222

[322] T. Sakai, T. Matsunaga, Y. Yamamoto, C. Ito, R. Yoshida, S. Suzuki, N. Sasaki, M. Shibayama, U. i. Chung, *Macromolecules* **2008**, *41*, 5379. 222

[323] M. Vamvakaki, C. S. Patrickios, *The Journal of Physical Chemistry B* **2001**, *105*, 4979–4986. 222

[324] T. Georgiou, M. Vamvakaki, C. Patrickios, *Polymer* **2004**, *45*, 7341–7355. 222

[325] M. Karbarz, Z. Stojek, T. Georgiou, C. Patrickios, *Polymer* **2006**, *47*, 5182–5186. 222

[326] F. Weik, R. Weeber, K. Szuttor, K. Breitsprecher, J. de Graaf, M. Kuron, J. Landsgesell, H. Menke, D. Sean, C. Holm, *The European Physical Journal Special Topics* **2019**, *227*, 1789–1816. 198, 225

[327] F. Uhlík, P. Košovan, Z. Limpouchová, K. Procházka, O. V. Borisov, F. A. M. Leermakers, *Macromolecules* **2014**, *47*, 4004–4016. 240

[328] F. Uhlík, P. Košovan, E. B. Zhulina, O. V. Borisov, *Soft Matter* **2016**, 4846–4852. 240

[329] A. Tagliabue, L. Izzo, M. Mella, *Journal of Polymer Science Part B: Polymer Physics* **2019**, *57*, 491–510. 240

[330] D. L. Bunker, W. L. Hase, *The Journal of Chemical Physics* **1973**, *59*, 4621–4632. 242

[331] O. K. Rice, H. C. Ramsperger, *Journal of the American Chemical Society* **1927**, *49*, 1617–1629. 244

[332] L. S. Kassel, *The Journal of Physical Chemistry* **1928**, *32*, 225–242. 244

[333] M. Mella, *The Journal of Chemical Physics* **2009**, *131*, 124309. 244

[334] M. J. Stevens, K. Kremer, *Macromolecules* **1993**, *26*, 4717. 251